Small Scale Pumped Thermal Energy Storage

Modeling and Optimization

Ali A. Al Radi

Small Scale Pumped Thermal Energy Storage

Modeling and Optimization

by

Ali A. Al Radi

to obtain the degree of Master of Science
at the Delft University of Technology,
to be defended publicly on Friday August 25, 2023 at 09:30 AM.

Student number:	5238226	
Project duration:	November 7, 2022 – August 25, 2023	
Thesis Committee:	Prof. dr. ir. Sikke Klein,	TU Delft, supervisor
	Prof. dr. Rene Pecnik,	TU Delft, supervisor
	Prof. dr. Kamel Hooman,	TU Delft, examiner

TU Delft

Technische Universiteit Delft

Department of Process & Energy

The undersigned hereby certify that they have read and recommended to the Faculty of Mechanical, Maritime and Materials Engineering (3mE) for acceptance of the thesis entitled

Small Scale Pumped Thermal Energy Storage Modeling and Optimization

by

Ali A. Al Radi

to obtain the degree of Master of Science
at the Delft University of Technology,
to be defended publicly on Friday August 25, 2023 at 09:30 AM.

Supervisor

Prof. dr. ir. Sikke Klein,
TU Delft, supervisor

Supervisor

Prof. dr. Rene Pecnik,
TU Delft, supervisor

Examiner

Prof. dr. Kamel Hooman
TU Delft, examiner

TU Delft

Abstract

Variable green energy sources were sought to supply the growing demand for energy without impacting the environment. Wind and solar energy are at the forefront of the energy transition. However, their intermittent nature poses a challenge that necessitates the development of energy storage technologies. Several technologies were studied over the years including pumped hydro energy storage, compressed air energy storage, electrochemical energy storage, and pumped thermal energy storage.

Pumped thermal energy storage provides a mean to store excess electrical energy in the form of heat by employing a heat pump cycle during the charging process and a heat engine cycle during the discharging process. There are multiple variations of pumped thermal energy storage cycles of which Rankine and transcritical cycles. Unlike Brayton cycles, Rankine and transcritical cycles typically operate at low-temperature levels $< 200°C$ which facilitate their integration with low-temperature waste heat in order to boost their round trip efficiencies even beyond 100%. Therefore, the focus of this thesis was to model and optimize Rankine and transcritical thermally integrated small scale pumped thermal energy storage.

Critical to the storage system's efficacy are the performances of its key components: the compressor and expander. Geometric models were developed and validated for these components, facilitating the determination of their isentropic efficiencies and their variation with pressure ratio and rotation speed.

Additionally, a small-scale pumped thermal energy storage system model was developed to study the system performance. The choice of working fluid and operating parameters were guided by both a simplified optimization scheme and a multi-objective approach utilizing the Non-Dominated Sorting Genetic Algorithm-II (NSGA-II). This yielded $R13I1$ as the optimum working fluid with source temperature $T_{source} = 80°C$ and storage temperature $T_{storage} = 140°C$. This configuration led to a transcritical heat pump charging cycle and a subcritical heat engine discharging cycle employing pressurized water as the storage medium.

Consequently, the compressor and expander geometric models were integrated into the pumped thermal energy storage system model working with $R13I1$ at the source and storage temperature mentioned earlier which yielded a round trip efficiency of $\eta_{rt} = 93\%$, energy density $\rho_{en} = 12kWhr/m^3$, and exergy efficiency $\psi_{ex} = 29\%$.

Finally, a case study was demonstrated with the integrated cycle employed in a Dutch household solar system where dual electric and thermal panels are employed for the electrical and heat energy input in the pumped thermal energy storage. The system was developed for a $1kW$ electrical input from the solar system to be stored for further use during off peak hours.

Acknowledgement

With my journey at TU Delft coming to an end, I can't help but remember a quote " Time passes opposite to our wishes". It is bittersweet writing the acknowledgment part as it feels like yesterday that I bought my first bike and struggled to get it back home.

First and foremost, I would like to extend my thanks and appreciation to Prof. dr. ir. Sikke Klein, Prof. dr. Rene Pecnik, and Prof. dr. Kamel Hooman. Prof. Sikke and Prof. Rene for their continuous support and guidance throughout this thesis and for availing the time out of their busy schedule to meet and resolve, what seemed to be, never-ending doubts. Prof. Kamel for taking the time to go through the report and agreeing to be a member of the panel.

My incredible family, thank you for always being there and never doubting me even when I doubted myself. Your love and support kept my motivation going and made me who I am today. For that and more, I love you. P.S. I will get my car back, right?

Abduladheem, what a journey we had and continue to have together. The highlights of my life seem to always have you in them. You push me to become a better person every day. Further, to my friends back home, even when life kept us apart, your presence was always felt. Let's meet again and have some Haneeth together. To you, I am forever grateful.

Now to the friends whom I met along the way, we shared hardship together but most importantly we shared smiles and laughter. Ever since our first meeting in Delftse Hout, you've been an integral part of my life. Whether it is a casual talk during an F1 race, or a football game while enjoying a home-cooked meal (not couscous), or a deep heartfelt conversation atop of TU Delft library, or over a cup of chai, I cherish them all. You've asked me why am I doing this at the age of 33, and the answer is really simple, to meet all of you.

This brings me to my colleagues, thank you for allowing me to bother you when you were busy. I really can't list all the things that I had experienced over the course of two years but all of that wouldn't have happened without you. We even started a weekly volleyball game session which I hope you will continue and I get to play with you all again. Not only that, I became a member of Delftsche Dodgers through which I got to meet some awesome people whom helped me get through some tough time of my life. I was even presented with a best catcher trophy, would you believe that.

To my father, you were watching me during my bachelor graduation ceremony and I would like to believe that you are watching me now. I miss you and hope I made you proud.

To all, I hope I was a source of your smile as much as you were of mine. I hope that I was a good son, brother, friend, and colleague to all of you whom you would remember one day. If I wasn't, please forgive my wrongdoing.

THANK YOU

Best Wishes
Ali A. Al Radi

Nomenclature

Abbreviations

Abbreviations	Definition
A-CAES	Adiabatic Compressed Air Energy Storage
ASU	Air Storage Uni
B-PTES	Brayton Pumped Thermal Energy Storage
CAES	Compressed Air Energy Storage
CSP	Concentrated Solar Power
D-CAES	Diabatic Compressed Air Energy Storage
ECES	Electrochemical Energy Storage
GWP	Global Warming Potential
HE	Heat Engine
HEX	Heat Exchanger
HP	Heat Pump
I-CAES	Isothermal Compressed Air Energy Storage
LMTD	Logarithmic Mean Temperature Difference
LTES	Latent Thermal Energy Storage
ODP	Ozone Depletion Potential
ORC	Organic Rankine Cycle
PCM	Phase Change Material
PHES	Pumped Hydro Energy Storage
PTES	Pumped Thermal Energy Storage
RPM	Revolutions Per Minute
R-PTES	Rankine Pumped Thermal Energy Storage
SLM	Standard Litres per Minute
STES	Sensible Thermal Energy Storage
TES	Thermal Energy Storage
TI-R-PTES	Thermal Integrated Rankine Pumped Thermal Energy Storage
T-PTES	Transcritical Pumped Thermal Energy Storage
TSU	Thermal Storage Unit

Symbols

Symbol	Definition	Unit
ΔT	Temperature Difference	$[K]$
ΔT_{lm}	Logarithmic mean Temperature Difference	$[K]$
$\dot{m}$	Mass Flowrate	$[kg/s]$
$\dot{Q}$	Heat Transfer Rate	$[W]$
$\dot{V}$	Volumetric Flowrate	$[m^3\ s^{-1}]$
$\dot{W}$	Power	$[W]$
$\dot{E}$	Rate of Total Energy	$[W]$
$\dot{KE}$	Rate of Kinetic Energy	$[W]$
$\dot{PE}$	Rate of Potential Energy	$[W]$
$\dot{U}$	Rate of Internal Energy	$[W]$
γ	Ratio of Specific Heats = C_p/C_v	$[-]$
λ	Latent Heat	$[kJ\ kg^{-1}]$
ω	Angular Velocity	$[rad\ s^{-1}]$
ρ	Density	$[kg\ m^{-3}]$
τ	Torque	$[Nm]$
A	Area	$[m^2]$
A	Heat exchange area	$[m^2]$
c	Velocity	$[m\ s^{-1}]$
C_p	Specific Heat Capacity at Constant Pressure	$[kJ\ kg^{-1}\ K^{-1}]$
C_v	Specific Heat Capacity at Constant Volume	$[kJ\ kg^{-1}\ K^{-1}]$
E	Total Energy	$[J]$
$\dot{W}_{el,in}$	Electrical Inlet Power	$[W]$
$\dot{Q}_{in}$	Thermal Inlet Power	$[W]$
$\dot{W}_{el,out}$	Electrical Outlet Power	$[W]$
η_{rt}	Round-Trip Efficiency	$[-]$
g	Gravitational Acceleration	$[m\ s^{-2}]$
h	Specific Enthalpy	$[J\ kg^{-1}]$
h'	Ideal specific enthalpy	$[J\ g^{-1}]$
KE	Kinetic Energy	$[J]$
m	Mass	$[kg]$
M_W	Molecular Weight	$[kg\ mol^{-1}]$
p	Pressure	$[Pa]$
P	Power	$[W]$
PE	Potential Energy	$[J]$
Q	Heat Energy	$[J]$

Symbol	Definition	Unit
R	Universal Gas Constant	$[J\ mol^{-1}K^{-1}]$
s	Specific Enthalpy	$[J\ kg^{-1}\ K^{-1}]$
t	Time	$[s]$
T	Temperature	$[K]$
T'	Ideal temperature	$[K]$
U	Internal Energy	$[J]$
U	Overall heat transfer coefficient	$[W\ m^{-2}K^{-1}]$
V	Volume	$[m^3]$
X_e	Exit subscript	$[-]$
X_i	Inlet subscript	$[-]$
z	Height	$[m]$
Z	Compressibility Factor	$[-]$
$\eta_{is,c}$	Compressor Isentropic Efficiency	$[-]$
$\eta_{is,t}$	Turbine Polytropic Efficiency	$[-]$
COP_{hp}	Heat Pump Coefficient of Performance	$[-]$
η_{he}	Heat Engine Efficiency	$[-]$
T_{st}	Storage Temperature	$[K]$
T_{sk}	Sink Temperature	$[K]$
T_{sr}	Source Temperature	$[K]$
$\Delta T_{L_{hp}}$	Heat Pump Lift Temperature	$[K]$
$\Delta T_{L_{he}}$	Heat Engine Lift Temperature	$[K]$
E_{he}	Heat Engine Net Energy Output	$[J]$
E_{hp}	Heat Pump Net Energy Input	$[J]$
t_{ch}	Charging time	$[h]$
t_{dis}	Discharging time	$[h]$
$Q_{HT_{hp}}$	High Temperature Heat Pump Heat Output	$[J]$
ρ_{en}	Energy Density	$[J\ m^{-3}]$
ρ_{pw}	Power Density	$[W\ m^{-3}]$
η_{tot}	Total Efficiency	$[-]$
η_{th}	Thermal Storage Efficiency	$[-]$
p_{op}	Operation Pressure	$[bar]$
p_{atm}	Atmospheric Pressure	$[bar]$
T_{atm}	Atmospheric Temperature	$[K]$
T_{Bp}	Boiling Point Temperature	$[K]$
p_{crit}	Critical Pressure	$[bar]$
ϕ_{FF}	Filling Factor	$[-]$
$\dot{V}_{meas}$	Measured Volumetric Rate	$[m^3\ s^{-1}]$
$\dot{V}_{th}$	Theoretical Volumetric Rate	$[m^3\ s^{-1}]$

Contents

List of Figures

List of Tables

1

Introduction

Global energy consumption has experienced a substantial increase exceeding ninefold during the preceding seven decades. Notably, hydrocarbon sources, namely coal, crude oil, and natural gas, have dominated the energy sector, accounting for over 70% of the overall energy supply by the year 2021, as visually depicted in the accompanying figure 1.1[29].

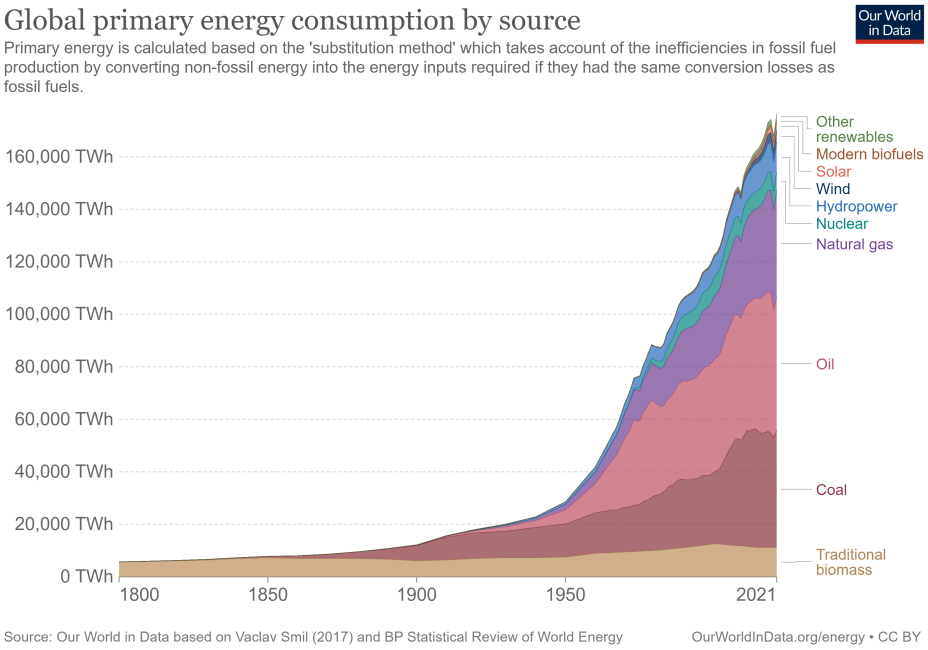

Figure 1.1: Global Energy Consumption for the Period from 1800 - 2021 Distributed by Energy Source [29]

Consequently, carbon emissions increased at an alarming rate of more than $(7X)$ over the same period [11]. Thus, over the past 20 years more focus was given to renewable energy sources resulting in a continuous growth of renewable energy sources with solar, wind, and hydro-power spearheading the energy transition [66]. Unlike hydropower, wind and solar suffer from intermittency where energy variation occurs daily as well as seasonally. Additionally, matching energy supply with load demand poses another challenge for renewable energies.

Hence, innovative energy storage systems became a necessity where excess energy from supply peak hours can be stored and then reused during high demand as modeled in figure 1.2 from one week in Minnesota in 2007 [30]. As can be seen in the graph, excess energy

from wind energy (green graph) can be stored during a charging period (orange graph) and then used during high demand (purple graph). Many energy storage methods have been studied over the years to resolve the storage challenge including pumped hydro energy storage (PHES), electrochemical energy storage (ECES), compressed air energy storage (CAES), and pumped thermal energy storage (PTES).

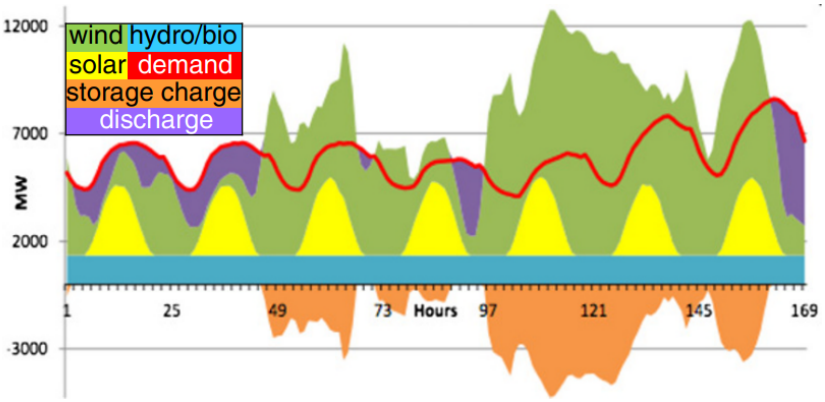

Figure 1.2: Minnesota Daily supply and demand with storage of renewable energy in 2007. Green: Wind Energy Supply. Red: Energy Demand. Orange: Excess Energy Storage. [30]

1.1. Energy Storage Methods

1.1.1. Classifications

Energy storage can be classified into four main types which are: (i) Mechanical, (ii) Electro-chemical, (iii) Electro-thermal, and (iv) chemical energy storage technologies [53] [27] as can be seen in figure 1.3.

i **Mechanical:** is the storage of excess electrical energy in the form of potential or kinetic energy with the most common examples being pumped hydro energy storage, compressed air energy storage, etc.

ii **Electro-thermal:** is the storage of excess electrical energy in the form of heat with the common example of pumped thermal energy storage, liquid air energy storage, etc.

iii **Electro-chemical:** is the storage of excess electrical energy in batteries where the electro-chemical potential of the materials is exploited. Typical examples are conventional solid-state Li-ion batteries, flow batteries, etc.

iv **Chemical:** is the storage of excess electrical energy by altering the chemical bonds of compounds like using excess electrical energy in an electrolyser to produce hydrogen H_2.

1.1.2. Comparison

Table 1.1 along with Figure 1.5 different aspects of the different storage technologies including round trip efficiency η_{rt} which is the ratio of energy output to the input energy, energy density ρ_{en} which is the ratio of delivered energy to the storage volume, and energy cost $\$/kWhr$ which is represented by the bubble size.

It can be seen that pumped hydro energy storage is the leading technology in large-scale energy storage as it has reached the commercial development stage with over $100GW$ installation as can be seen in figure 1.4 [52]. They have high output power and high round trip efficiency of $60-90\%$ [27] [53] which made them the benchmark in energy storage technologies.

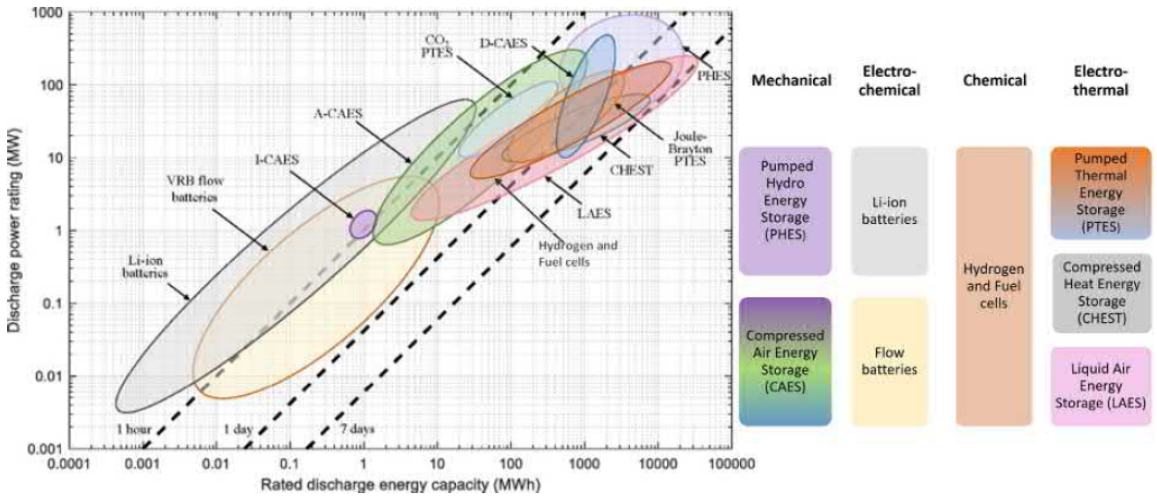

Figure 1.3: Energy Storage Technologies Comparison Based on Their Classifications [27] [53]

However, they suffer from high reliance on geography and topography as a consequence of their need for a high amount of water with sufficient elevation [65] in addition to their relatively low energy density of around $(0.2 - 2\ Whr/L)$.

Electrochemical energy storage is the second highest grid-scale energy installation [52] as it provides geographical independence but suffers from high installation costs, especially at large scale with a low lifetime of $10 - 15\ years$.

Chemical energy storage has high energy density with geographical independence but suffers from relatively low efficiency and high cost.

Even though electro-thermal energy storage is in the initial commercial deployment stage, it has gained attraction in recent years due to its relatively high energy density and round trip efficiency in addition to its low cost and geographical independence. Hence, it will be the focus of this thesis and will be referred to from now on as Pumped Thermal Energy Storage (PTES).

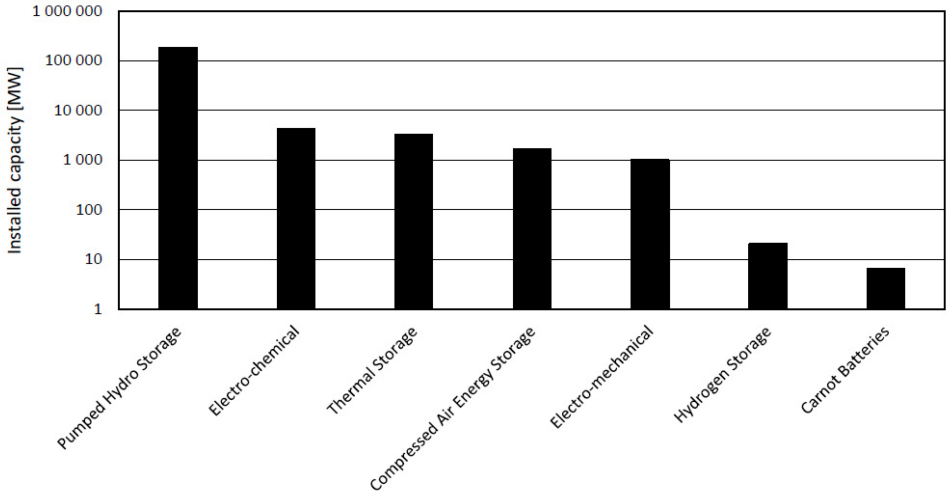

Figure 1.4: Global Deployments of Grid-Scale Electricity Storage Systems in 2020 [52]

Table 1.1: Technical Characteristics of Energy Storage Technologies Based on Their Classifications [27] [53]

Storage types	Mechanical		Chemical	Electro-chemical		Electro-thermal
Technology	PSH	CAES	H_2 production and fuel cells	Li-ion	Flow battery	TES
Development Stage	Commercialised	Initial commercialization	Pilot stage	Commercialised	Initial commercialization	Initial commercialization
Power output (MW)	100-5000	1-400	1e-6 - 50	0.1-50	1-200	0.1-300
Cost range	1504-2422 ($/kW) 150-242 ($/kWh)	973-1259 ($/kW) 97-126 ($/kWh)	2793-3488 ($/kW) 279-349 ($/kWh)	1410-1950 ($/kW) 350-490 ($/kWh)	2000-2440 ($/kW) 500-610 ($/kWh)	1700-1800 ($/kW) 20-60 ($/kWh)
Discharge Duration	several hours to days	several hours to days	several hours to months	minutes to few hours	several hours	several hours
Round Trip efficiency	60-90%	40-80%	20-70%	85-90%	55-85%	30-60%
Energy Density (Watt-hour/litre)	0.2-2	3-12	500-3000	200-600	16-60	50-500
Lifetime (years)	40	30	30	10	15	30
	suitable for large scale (>100 MWh)		suitable for large scale (>100MWh)	suitable for smaller scale (<10 MWh)		Better for industrial to large scale (>10 MWh)
	100% depth of discharge	limited depth of discharge	~50% depth of discharge	Limited depth of discharge		full depth of discharge
	Cheap on very large scale		cheap on large scale	often cheaper on smaller scale		Cheap on large scale
	possible storage losses		possible losses	no storage losses		1% loss per day
	Geographically dependent		location independent	No geographical limitations		location independent

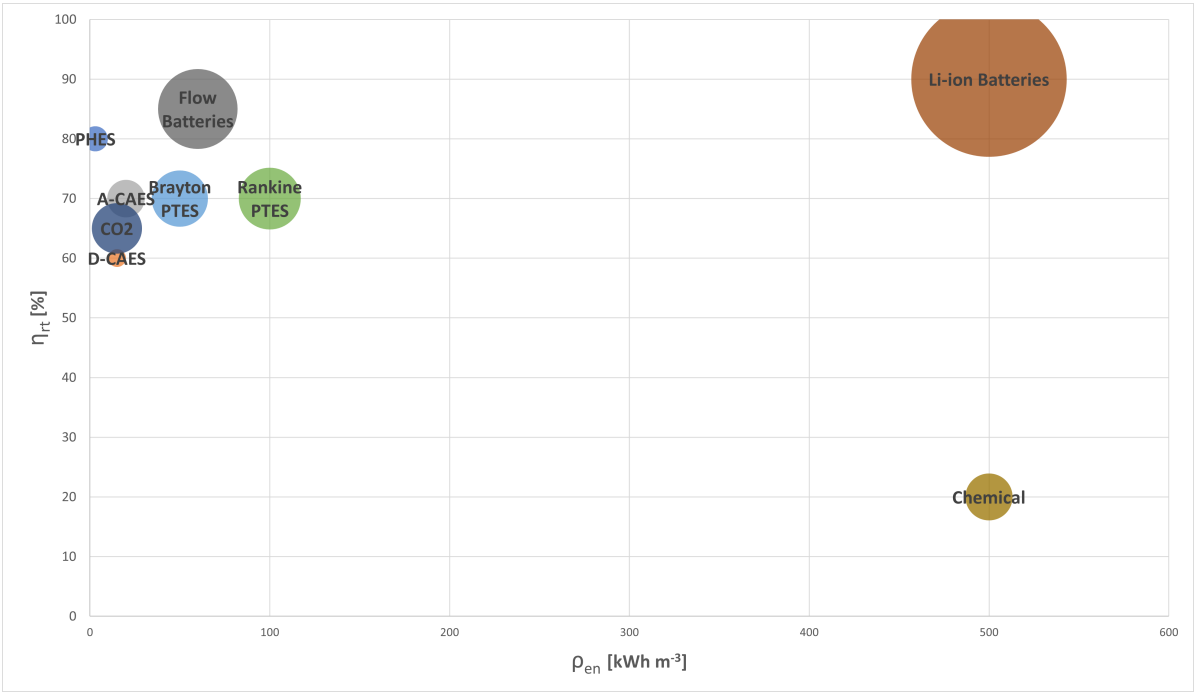

Figure 1.5: Energy Storage Technologies where the circle size represents the energy cost of Pumped Hydro Energy Storage (PHES), Diabatic Compressed Air Energy Storage (D-CAES), Adiabatic Compressed Air Energy Storage (A-CAES), Rankine Pumped Thermal Energy Storage (R-PTES), Brayton Pumped Thermal Energy Storage (B-PTES), Carbon Dioxide Pumped Thermal Energy Storage CO_2, Lithium Ion Batteries (Li-ion Batteries) and Flow Batteries [53] [27]

1.1.3. Electro-Thermal Energy Storage

Electro-thermal energy storage is referred to in many literature articles under different names like Carnot battery, pumped thermal energy storage, and pumped heat energy storage.

In any case, they refer to an emerging energy storage technology where excess electrical energy is stored in the form of heat by using the energy to heat a hot reservoir through a heat pump cycle working between low-temperature and high-temperature reservoirs [58]. Electric heated energy storage will also be included in this type as it uses excess electricity to directly heat the storage fluid through the electric heater [20]. The heat is then consumed in a heat engine cycle to generate power as depicted in figure 1.6a. There are three main categories of PTES: Brayton B-PTES, Rankine R-PTES, and transcritical T-PTES which will be detailed further in the following sections. The main advantage of PTES is their theoretical location independent while having a round trip efficiency of around $30 - 60\%$ and energy density $50 - 500 Whr/L$ as can be seen from Table 1.1. The main components in pumped thermal energy storage are the compressor, expander, heat exchangers, pump, and storage reservoirs as can be seen in Figure 1.6b [17]. Figure 1.6b demonstrate the main components for the Rankine and transcritical cycle, while the Brayton cycle has a similar layout with the valve replaced with an expander and the pump replaced with a compressor. Based on the employed cycle, interaction with the storage system can be either through sensible heat like in the case of Brayton and transcritical cycles with either direct or indirect contact, or phase change materials latent heat storage like in the case of Rankine Cycle which will be detailed further in the next chapter.

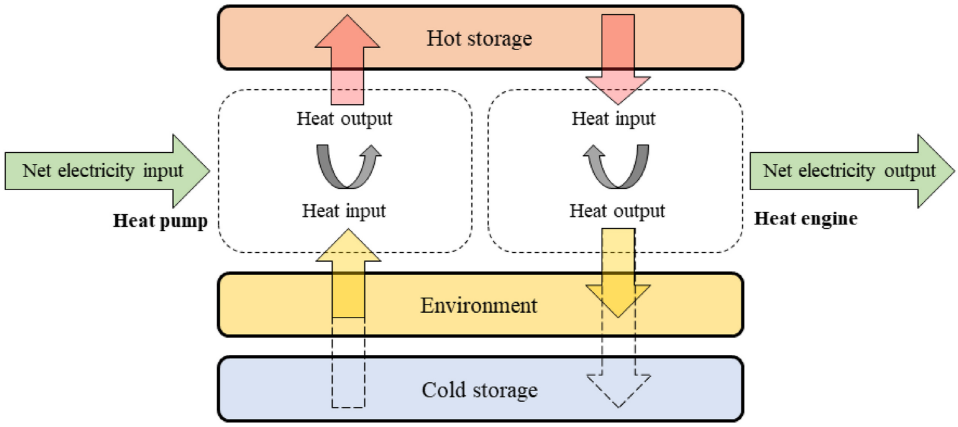

(a) Charging Heat Pump and Discharging Heat Engine Cycles in Pumped Thermal Energy storage [43]

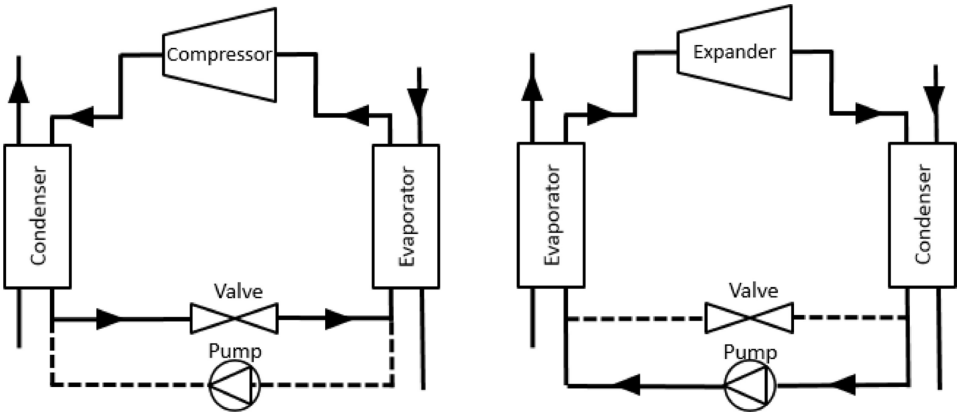

(b) Pumped Thermal Energy Storage Main Components [17]

Figure 1.6: Pumped Thermal Energy Storage Concept and Main Components. (a) Charging Heat Pump and Discharging Heat Engine Cycles. (b) Heat Pump and Heat Engine Main Components

1.2. Thesis Outline

The outline of the rest of the thesis is as follows:

- **Chapter 2** presents the literature review of the different pumped thermal energy storage technologies along with their major components and typical performances as depicted in the different literature.
- **Chapter 3** presents the work of modeling the major components of the pumped thermal energy storage namely the compressor and expander. A geometric model of a scroll compressor is presented in this chapter with their geometry, thermodynamic model, model validation, results, and discussion. A similar model is also presented for a scroll expander.
- **Chapter 4** will detail modeling of pumped thermal energy storage detailing the heat pump and heat engine cycles along with their sensitivity analysis. Additionally, fluid selection will be provided based on the fluids' properties as well as their performance in the cycle. Finally, a simple optimization scheme, as well as a multi-objective optimization scheme, will be detailed to determine the optimum working fluid as well as operating conditions.
- **Chapter 5** details the integration of the compressor and expander models into the pumped thermal energy storage model and provides a more reasonable storage performance based on the compressor and expander isentropic efficiencies. Additionally, a case study is proposed where the small scale pumped thermal energy storage system is integrated into a dutch household solar system. The solar system uses dual electric and heat solar panels where excess electric energy is used to drive the heat pump compressor and heat is used to provide the low temperature thermal integration to boost the system efficiency.
- **Chapter 6** finalize the thesis by providing a conclusion based on the previous chapters and recommendations for future work.

The structure of the thesis can be seen in figure 1.7

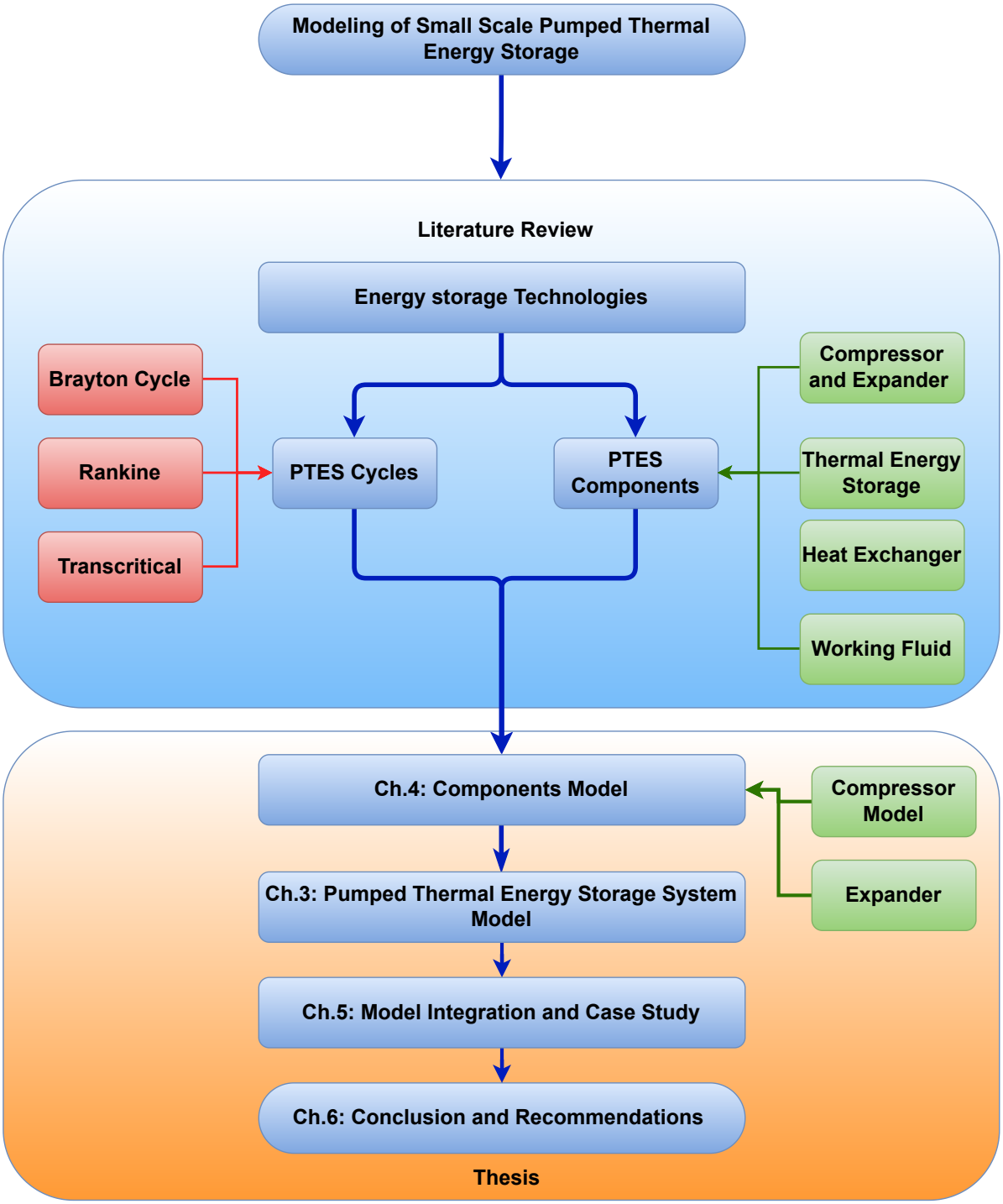

Figure 1.7: Thesis Structure

2

Literature Review

In this chapter, a literature review will be presented tackling the different parts of the thesis. First, a review of the different Pumped Thermal Energy Storage thermodynamic cycles will be detailed. Second, the different components that make up the cycle will be detailed like the compressor, expander, and heat exchanger. Third, the thermal energy storage system will be presented. Fourth, different working fluids will be discussed.

2.1. Basic Concept

PTES was first patented in 1934 by Fritz Marguerre under the name of Thermodynamic Energy Storage [25]. Ever since multiple variations of PTES have been studied that span a huge range of applications.

The basic concept work by having a heat pump charging cycle that uses excess electrical input to upgrade the temperature from a low-temperature reservoir to a high-temperature (Heat Storage) reservoir as can be seen in Figure 2.1. The stored heat is then consumed in a heat engine discharging cycle working between the high-temperature and low-temperature reservoirs to generate electricity.

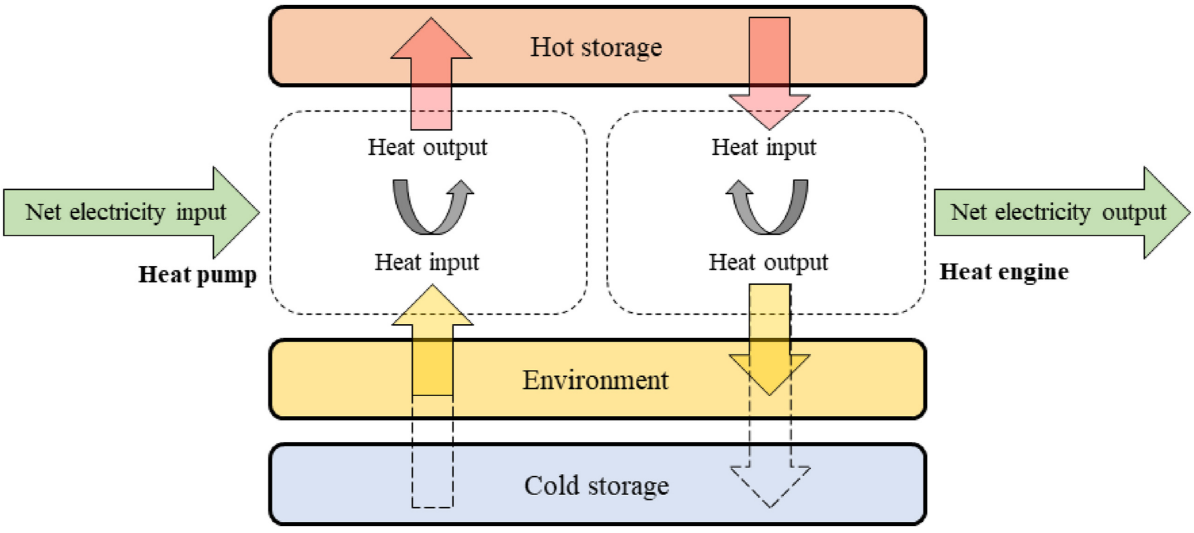

Figure 2.1: Pumped Thermal Energy Storage Basic Concept of Using Heat Pump in The Charging Cycle and Heat Engine In the Discharging Cycle [43]

Figure 2.2 shows different concepts of the cycle. In Figure 2.2a, electricity is used to directly

heat a storage medium which is then used to derive a HE cycle to generate electricity. Even though this is technically not a pumped thermal energy storage, it was included in this category for completeness. Figure 2.2b, HP and HE are used in a reversible cycle operating between cold temperature and hot temperature reservoirs. In Figure 2.2c, heat integration is introduced with hot storage where a hot source temperature is upgraded to a higher temperature in an HP cycle and stored in the hot storage T_{st} which is then used in a HE cycle to generate electricity. Finally, Figure 2.2d shows heat integration with cold storage where a refrigeration cycle is used to cool the low-temperature cold storage, and then heat from the high-temperature source is used in a HE cycle operating between the high-temperature source and low-temperature storage.

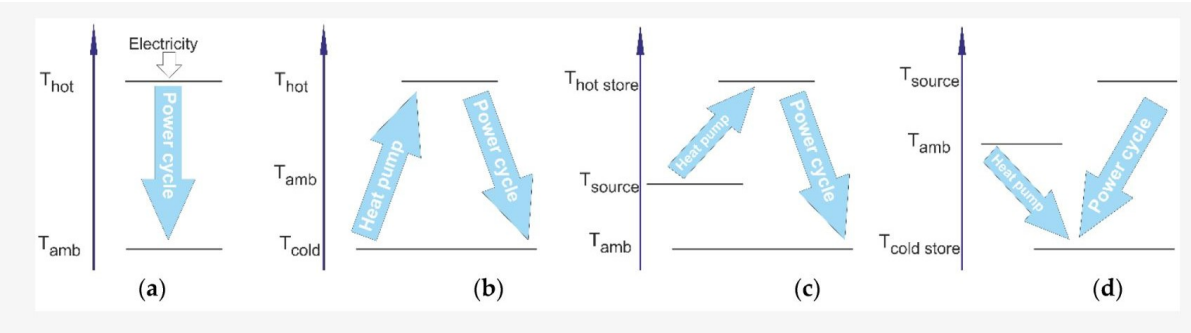

Figure 2.2: The main concept of PTES Systems (a) Electric Heater Heat Engine (b) Reversible PTES Working Between Cold and Hot Temperatures (c) Heat Integration with Hot Storage PTES (d) Heat Integration With Cold Storage PTES [52]

As mentioned in the previous chapter, there are three main categories of PTES based on the thermodynamic cycle employed which are Brayton (B-PTES), transcritical (T-PTES), and Rankine (R-PTES). The categorization is based on the state of the working fluid in the cycle. In B-PTES, the fluid is in a supercritical state throughout the cycle therefore no phase change occurs. While in R-PTES, the fluid is in sub-critical mode throughout the cycle with phase change occurring across an evaporator and a condenser. Finally in T-PTES, part of the cycle is supercritical while the other part is subcritical therefore phase change only occurs on the low-pressure side as demonstrated in figure 2.3.

Therefore, an overall categorization of PTES based on the concepts and the employed thermodynamic cycles can be seen in figure 2.4 which will be detailed in the following sections.

2.1.1. Brayton B-PTES

B-PTES refers to a Brayton cycle where the working fluid is in a supercritical single phase throughout the cycle. The main types of Brayton PTES are electric heater with heat engine cycle and heat pump with heat engine which will be detailed later.

2.1.1.1. Electric Heater with Heat Engine

K. Attonaty et al. [4] demonstrated the cycle where charging is done through an electric heater in which fan-driven air is heated up to $900°C$ and heat is stored in packed bed hot storage. However, the round trip efficiency is reported to be lower than the other types with $\eta_{rt} = 41\%$ in a $200\ MWh$ storage without the use of the combustion chamber as can be seen in Figure 2.5.

2.1.1.2. Heat Pump and Heat Engine

The basic Brayton cycle (heat pump and heat engine) is demonstrated by the work of [43] where the cycle configuration is shown along with the T-s Diagram which shows the charging

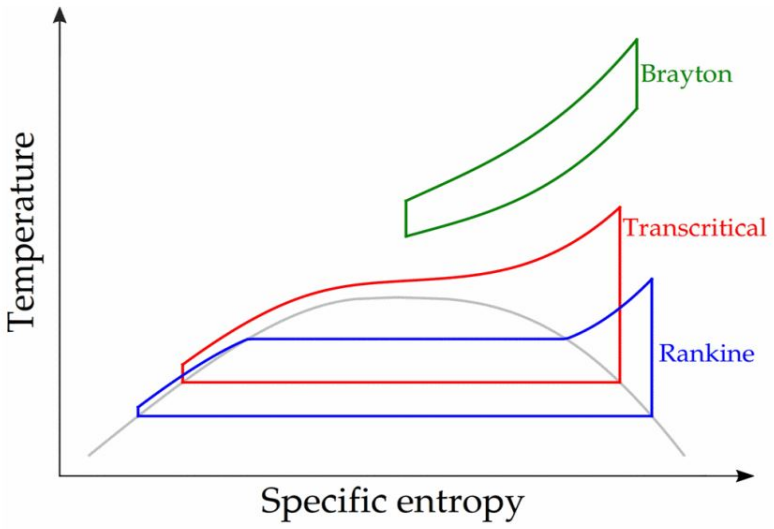

Figure 2.3: Brayton, Rankine and Transcritical Cycles [38]

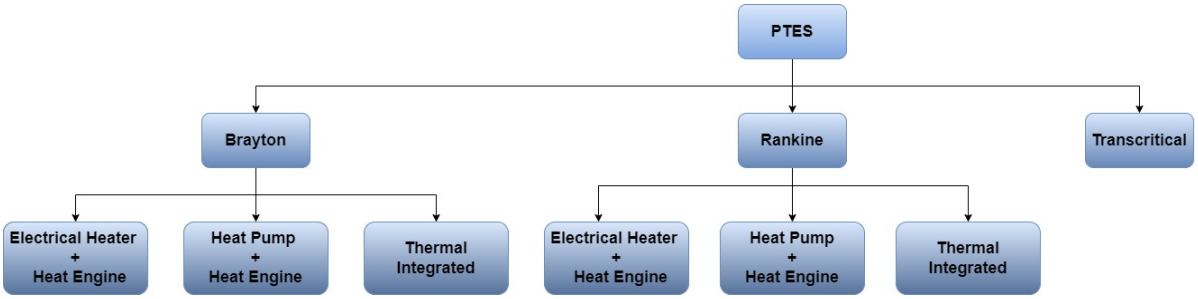

Figure 2.4: Overall PTES Categories

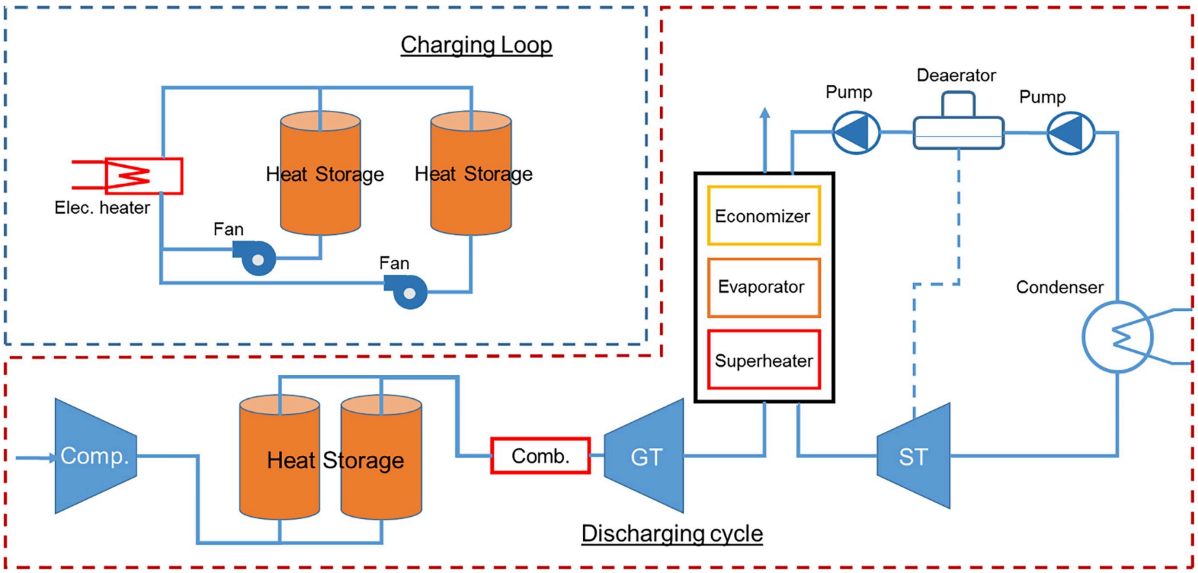

Figure 2.5: Electric Heater Charging Cycle with Brayton Heat Engine Discharging Cycle [4]

and discharging phases of the cycle as can be seen in Figure 2.6. During the charging phase designated by numbers (1-4) in figure 2.6, electrical excess energy is used to drive a HP with heat is stored in a thermal energy storage. The cycle is then reversed during the discharging phase (1'-4') where the stored energy is consumed to drive a turbine to generate electricity.

The working principle is that the working fluid is adiabatically compressed from low pressure and low temperature (1) to high-pressure high temperature (2) with a compressor driven by excess electricity. The heat is then isobarically removed and stored in the hot storage (3). The high-pressure low temperature (3) is then expanded in a turbine to reach the low-pressure low temperature at point (4) with the energy of the turbine being used to reduce the compressor load. Heat is then isobarically added from the cold storage to reach (1) where the cycle continues. This cycle is then reversed in the discharge phase as mentioned earlier with the expansion energy used to generate electricity.

The shown heat exchangers denoted as (HEX A and HEX B) are used to maintain temperature stability at the compressor and turbine inlets.

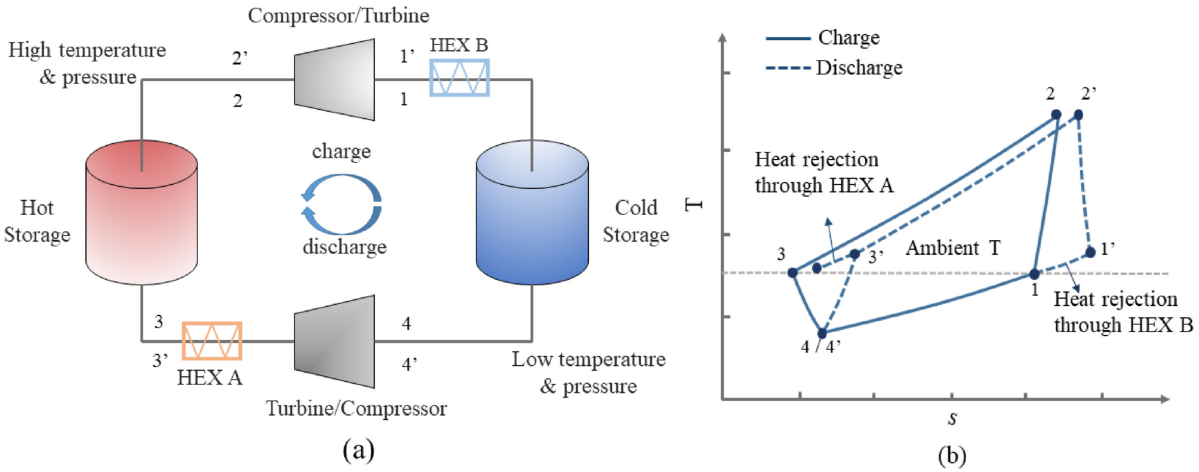

Figure 2.6: Brayton Cycle Heat Pump (charging) and Heat Engine (discharging) (a) Configuration and (b)T-s Diagram where (1-4) HP charging (1'-4') HE discharging [43]

There are two common cycles studied in literature based on the work of Isentropic ltd. and Malta Inc. as can be seen in Figure 2.7 [72]

A. White et al. [73] investigated the Isentropic Ltd. cycle using argon as the working fluid where they stressed the importance of the temperature ratio across the high-temperature storage $R = \frac{T_2}{T_3}$ where T_2 is storage temperature inlet and T_3 is storage temperature outlet in the performance of the cycle where energy density ρ_{en} increases with an increase of R. This is achieved by increasing the cycle pressure ratio PR. Additionally, the authors stressed the importance of the machine (compressor and turbine) polytropic efficiency $\eta_{pol,C}$ and $\eta_{pol,T}$ where higher values result in an increase of the cycle round trip efficiency η_{rt}. Similarly, J.D. McTigure et al. [45] studied the same cycle with a $2\ MW$ and $16\ MWh$ energy storage system working with argon as the working fluid with iron oxide Fe_3O_4 packed bed hot storage at a storage temperature of $T_s = 778K$. The study showed that a round trip efficiency is a strong function of machine polytropic efficiency where $\eta_{rt} = 70\%$ and $\eta_{rt} = 50\%$ can be achieved with $\eta_{pol} = 0.99$ and $\eta_{pol} = 0.9$ respectively. T.Desrues et al. [14] studied the cycle for large-scale energy storage of around $900MWh$ energy storage using argon as the working fluid. The paper reasoned that achieving high round trip efficiency of around $\eta_{rt} = 70\%$ can be done by either increasing the polytropic efficiency to around $\eta_{pol} = 0.94$ with low-temperature storage $T_s = 593K$ or by increasing the hot temperature storage to $T_s = 1323K$ with $\eta_{pol} = 0.84$.

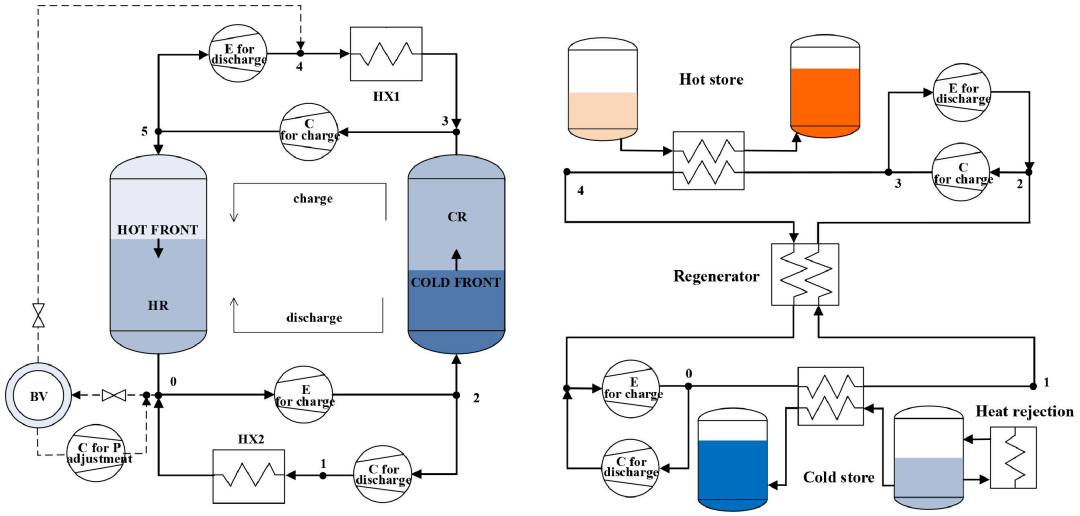

(a) Isentropic ltd (b) Malta Inc.

Figure 2.7: Different Brayton Cycles (a) Isentropic ltd. (b) Malta Inc. [72]

R. Laughlin [39] studied a basic Brayton cycle that resembled the one developed by Malta Inc. The cycle was working with argon as the working fluid with molten salt and liquid hydrogen as the high and low-temperature storage respectively. The high temperature storage of $823K$ and low temperature storage of $300K$ were employed with polytropic efficiencies of the compressor and expander $\eta_{pol,C} = 0.93$ and $\eta_{pol,T} = 0.93$ respectively which achieved a round trip efficiency of $\eta_{rt} = 75\%$.

M. Petrollese et al. [58] studied a thermally integrated cycle based on Malta Inc where a concentrated solar power was integrated into the cycle to boost its round trip efficiency as can be seen in Figure 2.8. However, only $\eta_{rt} = 60\%$ was reported with the heat integration with $\eta_{pol} = 0.90$ which is attributed to the inclusion of the solar exergy input in the efficiency calculation.

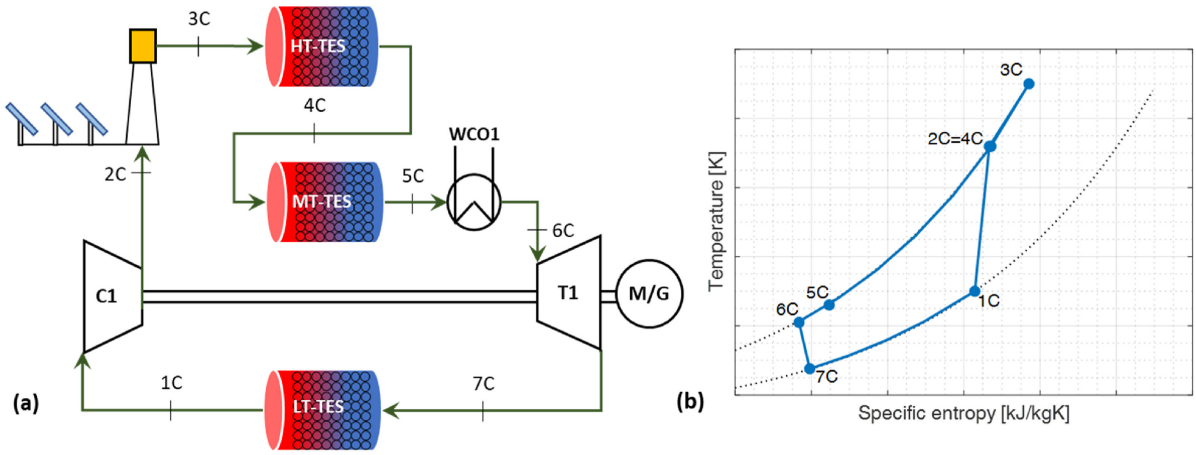

Figure 2.8: Concentrated Solar Power (CSP) Brayton PTES Charging Cycle Configuration and T-S Diagram [59]

2.1.2. Rankine R-PTES

Unlike Brayton PTES, Rankine PTES works in the subcritical state with phase change occurring at an evaporator and a condenser. The cycle was demonstrated by [43] which is

shown in figure 2.9 with a heat pump charging and heat engine discharging cycles similar to the one described in Brayton PTES. High efficiency of the cycle can be achieved by either a lower temperature lift in the heat pump cycle which targets improving HP COP_{hp}, or by increasing the temperature difference in the heat engine cycle which targets improving the HE η_{he}.

The working principle is slightly different than Brayton PTES. In the charging cycle, the vapor is adiabatically compressed from low pressure and low temperature (2) to high pressure and high temperature (3) utilizing the excess electrical energy. The heat of compression is removed and stored in hot storage through an isobaric condenser where the working fluid phase changes from vapor (3) to liquid (5). The high-pressure and low-temperature liquid at the outlet of the condenser is expanded in an expansion valve to low-pressure low temperature where two-phase occurs (1). The two-phase fluid enters the evaporator at (1) and exits at (2) as saturated vapor where heat is added to the fluid from cold storage or from atmospheric conditions and the cycle repeats. In the discharge cycle, the saturated liquid is pumped from low-pressure low temperature (1') to high pressure (2'). The hot storage is then consumed to heat the fluid to high pressure and high-temperature superheated vapor (4') through the evaporator. The superheated vapor is then expanded to low pressure and low temperature in a turbine to generate electricity (5') which is then cooled down in a condenser to saturated liquid at point (1') where removed heat can be stored in the cold storage or removed at the atmospheric condition and the cycle continues.

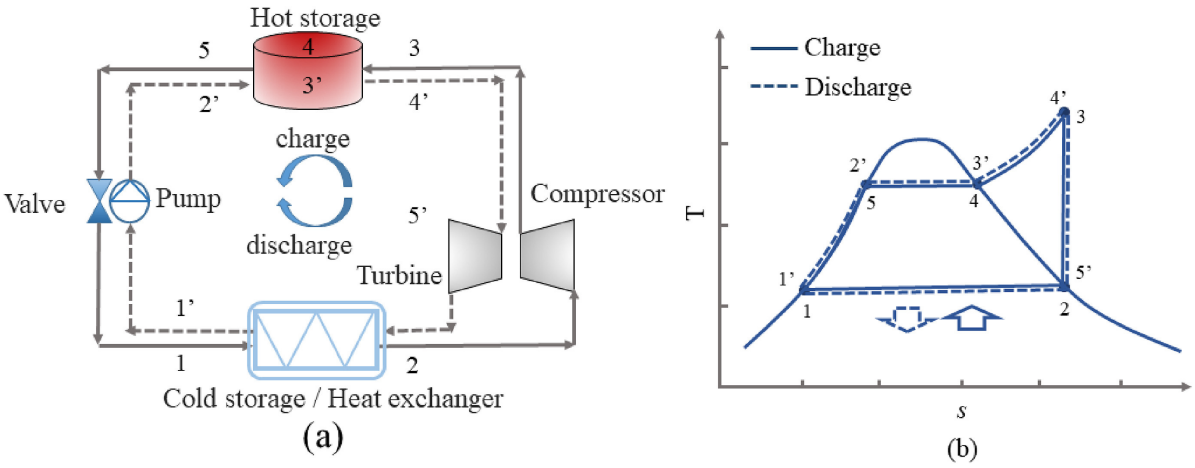

Figure 2.9: Ideal Rankine PTES (a) Configuration and (b) T-s Diagram (1-5) HP charging cycle (1'-5') HE discharging cycle Where Storage is Done Between (3-5) During Charging and (2'-4') During Discharging [43]

R-PTES has three main configurations which are heat pump and heat engine, thermal integrated Rankine cycle, and electric heater Rankine cycle. Additionally, several working fluids were reported like refrigerants, water, ammonia, and hydrocarbons [38].

2.1.2.1. Electric Heater Rankine Cycle

Electric heater Rankine cycle work by having a resistive heating element to heat the hot storage during the charging cycle which is then used in a Rankine cycle to generate electricity. SIEMENS Gamesa [36] proposed a plant working by heating air using electric heat which is then driven through a packed bed of rocks to store thermal energy at a maximum storage temperature between $500 - 800°C$ [20] during the charging cycle. In the discharging cycle, cold air is heated from the thermal storage unit which is then used to superheat steam in a Rankine heat engine cycle which is used to generate electricity as designed by the light and dark green lines in figure 2.10. SIEMENS Gamesa [36] are working to construct a commercial scale electric heated TES with a storage power of $100\ MW$ in Hamburg, Germany with an

outlook round trip efficiency of $\eta_{rt} = 50\%$ after their successful deployment of a demonstrator scale $5.4\ MW$ in 2019 which J.R. Eggers et al. anticipated that it had a round trip efficiency of $30\%–47\%$ [20].

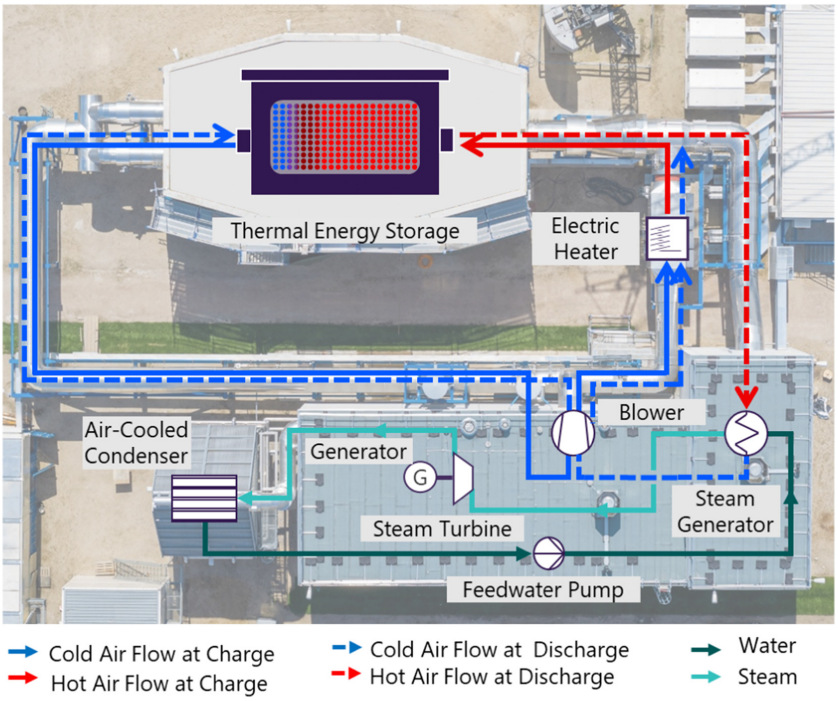

Figure 2.10: Electric Heater Rankine Cycle plant by SIEMENS Gamesa [20]

2.1.3. Heat Pump and Heat Engine

The basic heat pump and heat engine cycle Rankine cycle working without heat integration was rarely investigated which is attributed to its low efficiency. W.D. Steinmann [69] investigated the cycle using water as the working fluid which is operating at a low temperature of $25°C$ as can be seen in figure 2.11. Two cases were investigated by the paper with different high pressure $100\ bar$ and $140\ bar$ at storage temperatures of $400°C$ and $550°C$ respectively with reported round trip efficiencies of $\eta_{rt} = 38.6\%$ and $\eta_{rt} = 41.8\%$ respectively. Hence the paper concluded that the cycle efficiency can only achieve $\eta_{rt} = 40\%$. Consequently, R-PTES is normally investigated with the deployment of thermal integration.

2.1.3.1. Thermal Integrated Rankine Cycle

Thermal integration in R-PTES is the utilization of low temperature $< 200°C$ waste heat to increase the round trip efficiency of the storage system. This is achieved by decreasing the temperature lift across the heat pump charging cycle to improve the heat pump coefficient of performance COP_{hp}.

H. Jockenhöfer et al. [35] investigated heat integration from district heater smart solar system or shallow geothermal energy sources in a Rankine cycle using butane as the working fluid with a combined sensible (STES) and latent (LTES) thermal energy storage based on pressurized water and potassium nitrate phase change material (PCM) in order to match the temperature profile of the working fluid and cooling medium as can be seen in figure 2.12. The paper concluded that in order to achieve higher round trip efficiency, the source temperature T_{sr} in the charging cycle has to be increased and the sink temperature T_{sk} in the discharging cycle has to be decreased and demonstrated that a round trip efficiency of $\eta_{rt} = 125\%$ can

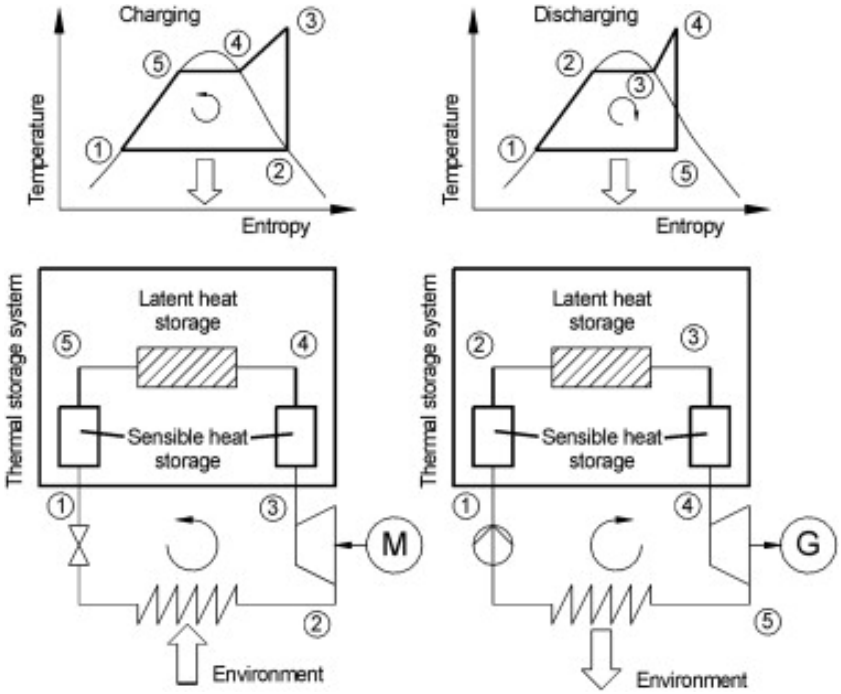

Figure 2.11: Ideal Heat Pump and Heat Engine Reversible Rankine Cycle [69]

be achieved with $T_{sr} = 100°C$ and $T_{sk} = 15°C$. The paper also stressed on maintaining a low pinch minimum temperature ΔT_{min} in the evaporator, condenser, and PCM heat storage to achieve high round-trip efficiency. Finally, the authors studied the main sources of exergy losses in the cycle and concluded that the HP evaporator, ORC (HE) condenser, and rotating machinery (compressor and expander) are the main sources of exergy loss as can be seen in Figure 2.13.

G.F. Frate et al. [23] investigated the influence of source and storage temperatures in a similar cycle working by varying the source temperature $T_{sr} = 80 - 110°C$ and the storage temperature $T_{st} = 110 - 200°C$ and the influence of different working fluids on the performance of the cycle. The paper concluded that R1233ZD(E) was the most suitable fluid based on performance, safety, and environmental considerations which achieved a round trip efficiency $\eta_{rt} = 130\%$ at $T_{sr} = 110°C$. Additionally, the paper concluded that increasing the storage temperature results in a decrease in round-trip efficiency due to increasing temperature lift in the HP cycle. Finally, the authors conducted a sensitivity analysis over the cycle and concluded that isentropic efficiencies of the rotating equipment have a high influence over round-trip efficiency.

G.F. Frate et al. [24] provided a multi-objective optimization scheme utilizing Pareto Front for thermally integrated pumped thermal energy storage with source temperature $T_{sr} \leq 80°C$ with respect to cycle parameters round trip efficiency η_{rt}, energy density ρ_{en}, and exergy efficiency ψ_{ut} as can be seen in Figure 2.14. Different scenarios to account for different weights of the parameters were studied as demonstrated below with and without the employment of a regenerator:

$$\begin{bmatrix} & \eta_{rt} & \psi_{ut} & \rho_{en} \\ W_1 & 1/3 & 1/3 & 1/3 \\ W_2 & 1/2 & 1/2 & 0 \\ W_3 & 1/2 & 0 & 1/2 \\ W_4 & 2/3 & 0 & 1/3 \end{bmatrix}$$

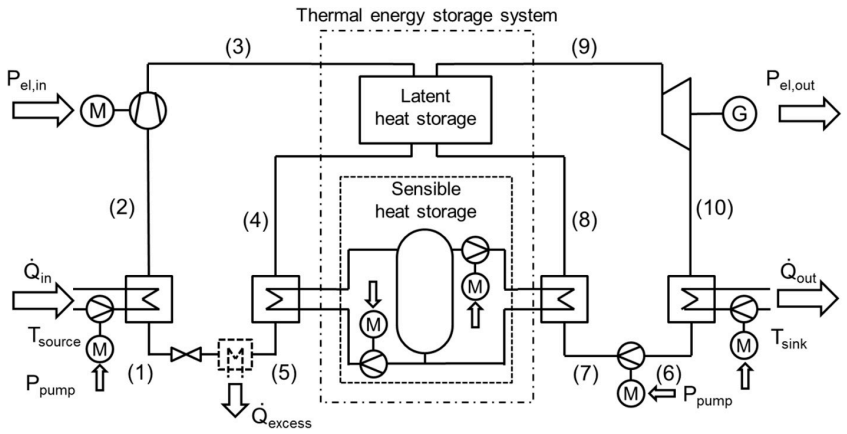

Figure 2.12: Thermal Integrated Rankine Pumped Thermal Energy Storage (TI-R-PTES) [35]

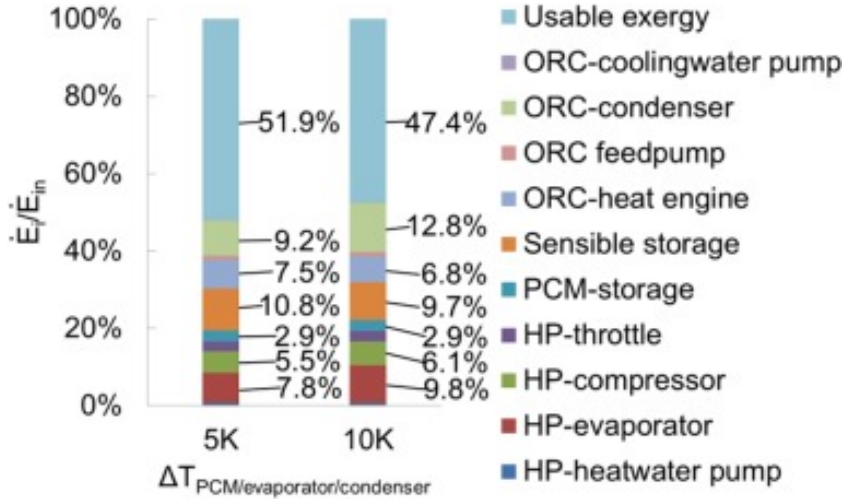

Figure 2.13: Main Components Responsible for Exergy Losses in Organic Rankine Cycle Heat Engine (ORC) and Heat Pump (HP) in District Heater Smart Solar Thermal Integrated Rankine Cycle [35]

The paper concluded that an energy density of $10 - 15\ kWh/m^3$ can be easily achieved which is much higher than PHES which has a typical value of $0.5 - 2\ kWh/m^3$ and CAES which has a typical value of $3 - 6\ kWh/m^3$. Additionally, a realistic round trip efficiency of $0.5 - 0.6\%$ can be achieved with the authors claiming that higher values are not realistic as they require inefficient exploitation of the waste heat source. Moreover, the paper demonstrated that energy density and round trip efficiency are competing in the cycle with maximizing one will require to minimize the other as can be seen in figure 2.15. For the case with a regenerator, the author reported having a high impact on exergy efficiency but a low impact on round-trip efficiency and energy density. For the fluid, Cyclopentane was reported to be the best fluid for maximizing round trip efficiency and exergy efficiency but it has low energy density while R245fa was reported to have the opposite effect.

Considering the promising results of the simulations, several experimental investigations were carried out like the work of O.Dumont et al. [19] who conducted an experimental investigation of heat integrated reversible Rankine cycle working with R1233ZD(E) as the working fluid and was able to demonstrate a round trip efficiency of $\eta_{rt} = 72.5\%$ as can be seen in figure 2.16. The author also claimed that a higher efficiency of around $\eta_{rt} = 100\%$ can be achieved with better optimization of the volumetric machine and the control and thermal insulation. The paper demonstrated the possibility of using the same equipment in the charging

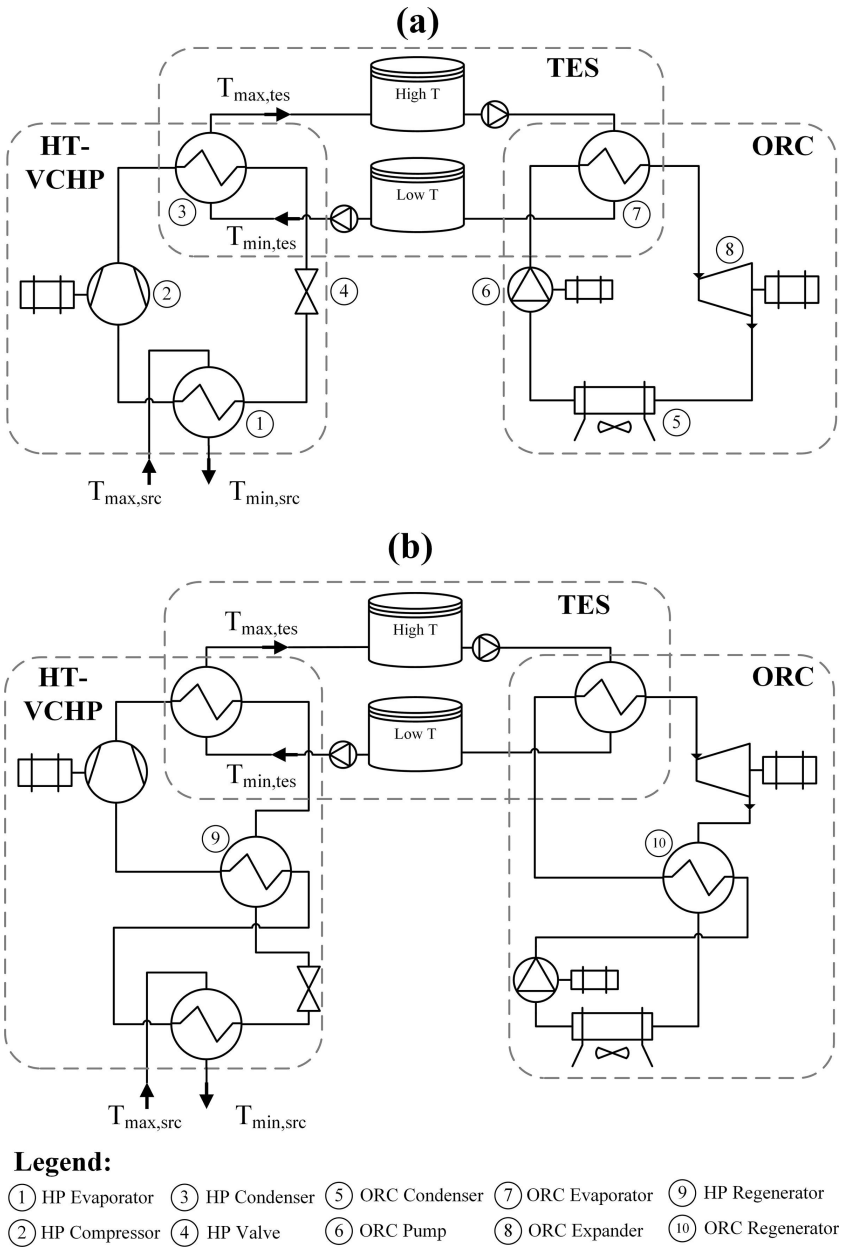

Figure 2.14: TI-PTES (a) without regenerator (b) with regenerator [24]

and discharging cycle with the compressor modified to work as an expander in the discharging cycle.

Even though high efficiency is reported, utilizing PCM in energy storage is still experimental. Having both a PCM and sensible require proper control to ensure the charging or discharging of both systems occurs at the same rate. Finally, using sensible heat only will result in a lower exergy efficiency as will be described later.

Finally, it is estimated that $1/3$ of waste heat in EU is in the range of $100 - 200°C$ as can be seen in figure 2.17 [55] which can be exploited in the pumped thermal energy storage.

2.1.4. Transcritical T-PTES

For transcritical PTES, the high-pressure side is in a supercritical state, and therefore phase change doesn't occur and the condenser in the R-PTES HP charging cycle is replaced

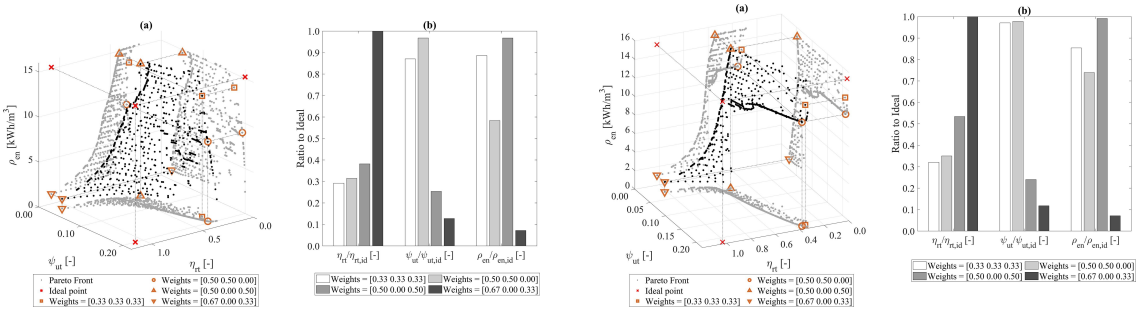

(a) Non Regenerator Cycle Competing Window (b) Regenerator Cycle Competing Window

Figure 2.15: Pareto Front for optimization of different configuration linearized against the ideal values value which are $\eta_{rt} = 1.08$, $\psi_{ut} = 0.2$, $\rho_{en} = 15.17\ kWh/m^3$[24]

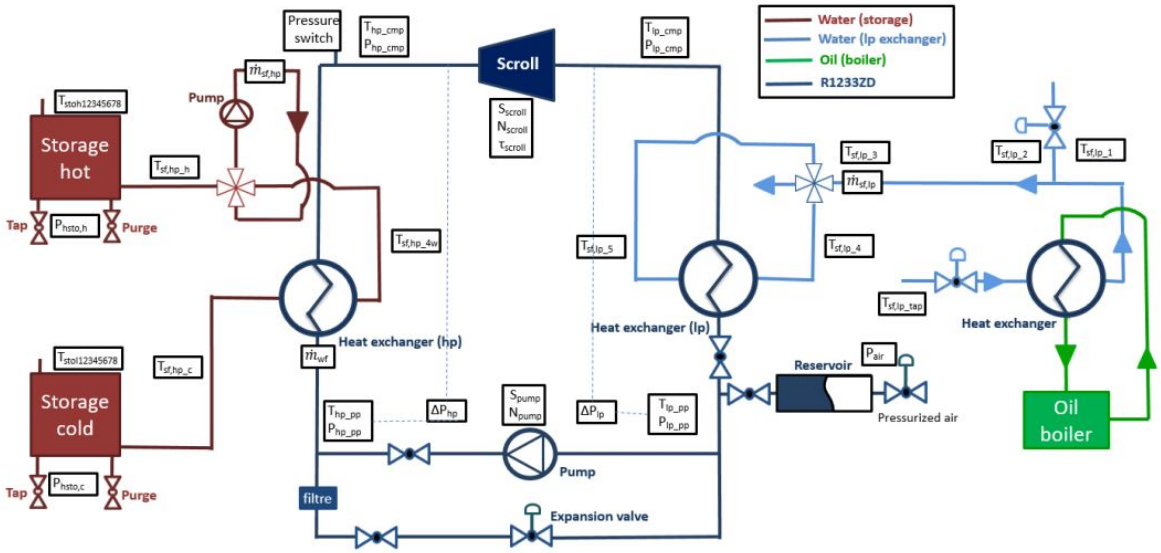

Figure 2.16: Schematic of the TI-R-PTES Experiment Done By University of Liage Which Demonstrated Utilizing the Same Scroll as a Compressor in the Charging Cycle and Expander in the Discharging Cycle [19]

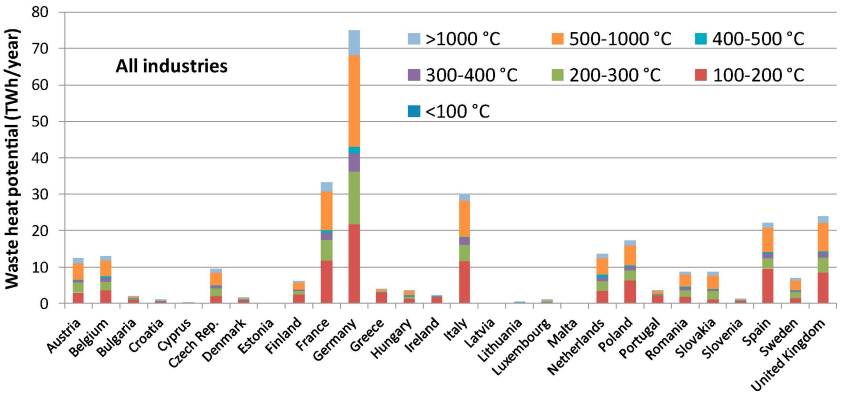

Figure 2.17: EU Industrial Waste Heat [55]

with a heat exchanger as can be seen in figure 2.18. The direction of the arrows in figure 2.18a represents the charging HP cycle which corresponds to figure 2.18b red lines from point (1 - 4) while the discharging HE cycle run in the opposite direction and represented by the blue

lines with corresponding numbers (1' - 4').

A. Koen et al. [38] investigated 176 working fluids in T-PTES cycle based on η_{rt}, ρ_{en} along with safety and environmental consideration with water, Therminol D12, and Therminol 66 as storage mediums. Ambient temperature is used as the lower temperature of the cycle. The paper demonstrated that Trifluoroiodomethane (R13I1) achieved the highest cycle round trip efficiency of $\eta_{rt} = 57.6\%$ as can be seen in figure 2.19. However, considering all parameters like ρ_{en}, sCO_2 and Ammonia were the best. Additionally, the authors studied the effect of storage temperature on the performance of the cycle and concluded that increasing the storage temperature (T_2) results in an increase in ρ_{en} but a decrease in the machine performance due to losses.

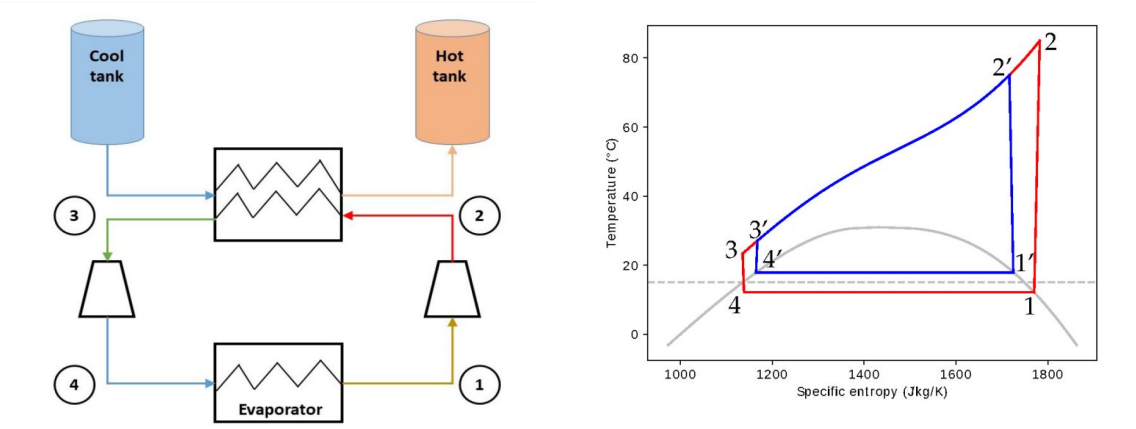

(a) Schematic of the T-PTES

(b) T-s Diagram of Ideal sCO_2 Cycle (red) charging (blue) discharging

Figure 2.18: Transcritical PTES Cycle Operating at Atmospheric Low Temperature (a) Schematic (b) T-s Diagram of the charging (Red) and Discharging (Blue) cycles [38]

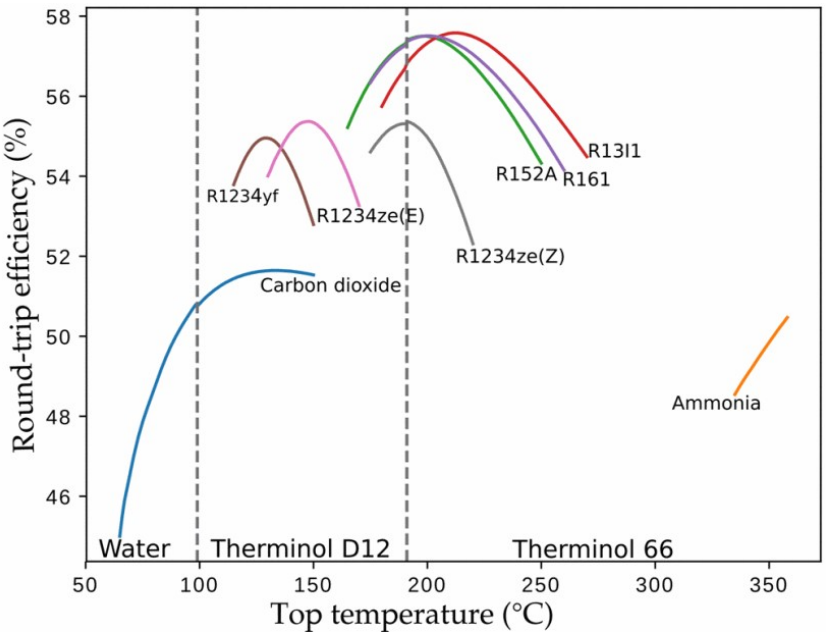

Figure 2.19: Maximum Round Trip Efficiency Achieved for Each Fluid with Their Corresponding Storage Temperature [38]

Consequently, most of the work in T-PTES revolves around supercritical carbon dioxide

sCO_2 as the working fluid. Hence, MAN energy solutions partnered with ABB Switzerland to build a T-PTES with CO_2 as the working fluid [12]. Accordingly, M. Morandian et al. [48] investigated the performance of the plant proposed by ABB using pressurized water for hot storage and ice slurry salty water for cold storage as can be seen in figure 2.25. A maximum of $\eta_{rt} = 60\%$ was demonstrated for $50\ MJ$ energy storage with isentropic efficiencies between $\eta_{is} = 0.85 - 0.88\%$. The authors highlighted that due to variations in heat capacity c_p around the critical point, multiple storage tanks are required to match the profile of working fluid and avoid exergy loss as can be seen in figure 2.21. Similarly, M. Mercangöz et al. [47] investigated the ABB plant for $1\ MW$ and $50\ MW$ pilot scale and commercial scale plants and concluded a round trip efficiency $\eta_{rt} = 51\%$ and $\eta_{rt} = 65\%$ respectively. The main contribution of the commercial scale efficiency increase is attributed to the increase in machine isentropic efficiency.

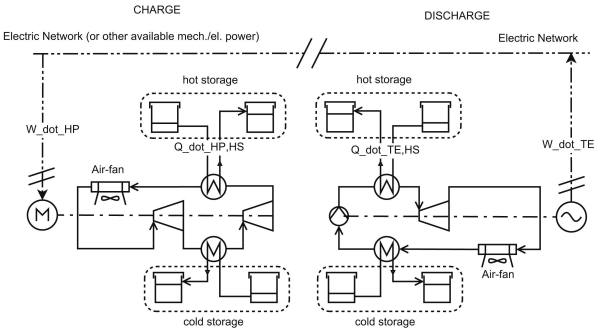

(a) Schematic of ABB T-PTES

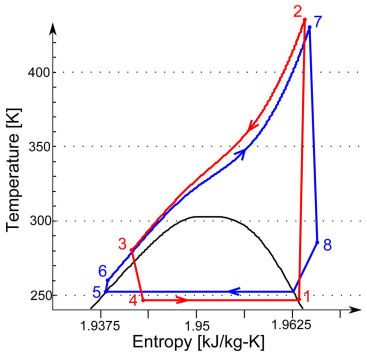

(b) T-s Diagram of CO_2 ABB plant (red) charging (blue) discharging

Figure 2.20: ABB CO_2 T-PTES (a) layout (b) T-s Diagram of the Charging (Red) and Discharging (Blue) Cycles [48]

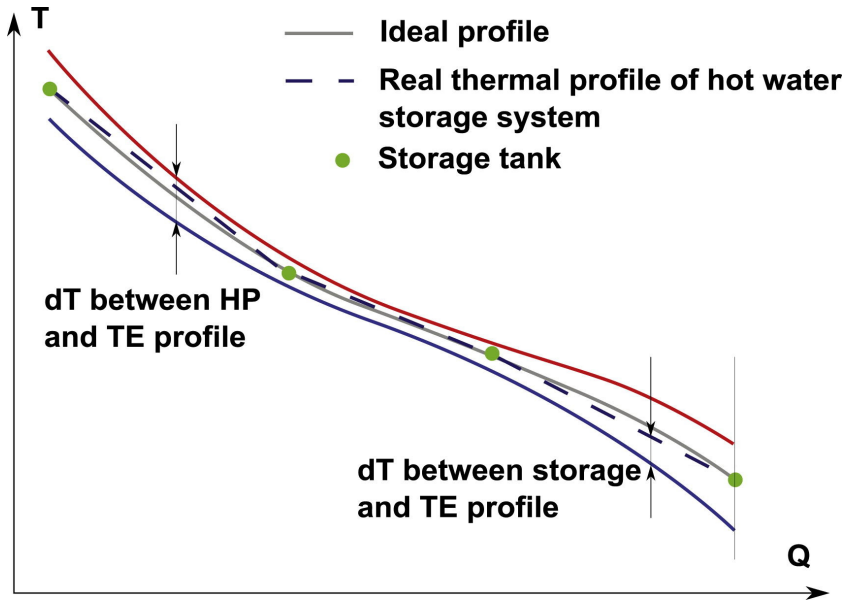

Figure 2.21: Thermal profile of hot water storage in T-PTES[48]

A summary of the studied cycles can be seen in table 2.1. From the table, it is clear that Brayton cycles generally operate at high temperatures $> 200°C$ which makes them not suitable for low temperature heat integration. Rankine and transcritical cycles operate at lower

temperatures than Brayton cycles with possible low temperature heat integration. With heat integration, high round trip efficiencies were reported even higher than 100%.

2.2. Components

The major components of PTES are compressor, expander, thermal energy storage, heat exchangers, and working fluids as can be seen in figure 2.22. Components' types, performance, and selection criteria will be detailed in the following sections.

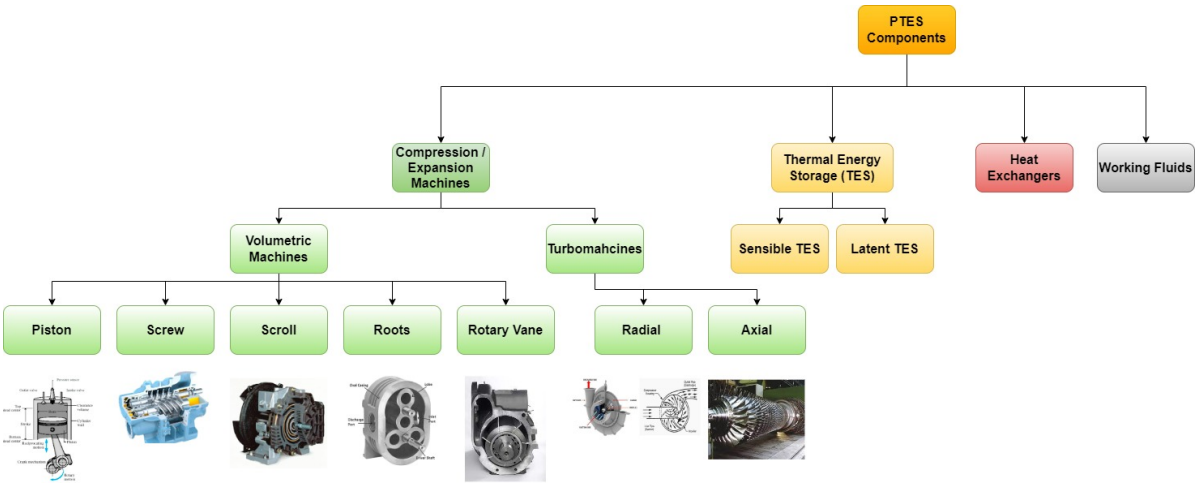

Figure 2.22: PTES Components; Piston [34] ; Screw [34] ; Scroll [13]; Roots [2]; Rotary Vane [60]; Radial [7]; Axial[8]

2.2.1. Compressor and Expander Machines

The compressor and expander are used in the heat pump and heat engine cycles. While compressors use electric power to increase the enthalpies of the working fluid, expanders work in reverse by consuming the fluid enthalpies to generate electric power. The main types of machines are volumetric and turbomachines.

2.2.1.1. Machine Selection

Volumetric machines generally are used for small-scale applications with power ranges ($< 1\ MW$) featuring low flow rate $10 - 100\ L/s$ and high-pressure ratios up to 200[43]. Alternatively, turbomachines are used for large-scale applications ($> 1\ MW$) handling high flow rate with low-pressure ratio per stage [43]. Therefore, for the purpose of this thesis, more focus on volumetric machines will be given.

O. Dumont et al. [18] investigated the performance of four different expander machines namely root, scroll, screw, and axial piston in small scale $< 5\ KW$ organic Rankine cycle (ORC) working with R245FA as the working fluid. The paper showed that higher rotation speed reduces internal leakage which improves the performance of all studied expanders as can be seen in figure 2.23 where filling factor ($\phi_{FF} = \frac{\dot{V}_{meas}}{\dot{V}_{th}}$) approaches $\phi_{FF} = 1$ at rotation speed $RPM > 3000$. Additionally, the scroll expander demonstrated the best isentropic efficiency among all expanders with an isentropic efficiency of $\eta_{is,T} = 76\%$ followed by screw and piston with $\eta_{is,T} = 53\%$ for both and finally root with $\eta_{is,T} = 47\%$. S. Quoilin et al.[42] investigated scroll, screw, and radial inflow single-stage turbines in an organic Rankine cycle. The author stressed the importance of the built-in volumetric ratio which is the ratio of the discharge volume to the suction volume with a maximum value $r_v = 4$ for the scroll and $r_v = 5$ for the screw.

Table 2.1: Summary of the Referenced Cycles

Category	Type	Electrical Power	Electric Energy	Working Fluid	Storage Medium	Temperature Range [$^{\circ}C$]	Round Trip Efficiency η_{rt}	Reference
Brayton Cycle	Electrical Heater with Heat engine	[-]	200 [MWh]	air	Packed bed	900	41%	[4]
	Heat pump and Heat Engine	2 [MW]	16 [MWh]	argon	Packed bed Fe_3O_4	LT: 396 HT: 778	70%@ $\eta_{is} = 0.99$ 50%@$\eta_{is} = 0.9$	[45]
	Heat pump and Heat Engine	[-]	900[MWh]	argon	Packed bed	LT: 500 HT: 1200	70%@$\eta_{pol} = 0.9$	[14]
	Heat pump and Heat Engine	[-]	[-]	argon	LT: Liquid hydrogen HT: Molten salt	LT: 27 HT: 550	75%@$\eta_{pol} = 0.93$	[39]
	Thermal integrated heat pump and heat engine	5 [MW]	[-]	argon	Packed bed	727	60%@$\eta_{pol} = 0.9$	[58]
Rankine Cycle	Heat pump and heat engine	100 [MW]	[-]	water	[-]	LT: 25 HT: 550	40%	[69]
	Electric Heater and Heat Engine	5.4 [MW]	[-]	water	Packed bed of rocks	HT: 500-800	$30 - 47\%$	[20]
	Thermal Integrated Heat pump and heat engine	[-]	[-]	Butane	STES: pressurized water LTES: potassium nitrate	$T_{sr} = 100$ $T_{sk} = 15$	125%	[35]
	Thermal Integrated Heat pump and heat engine	[-]	[-]	R1233zD(E)	[-]	$T_{sr} = 80 - 100$ $T_{st} = 110 - 200$	130%	[23]
	Thermal Integrated Heat pump and heat engine	1.5 [kW]	[-]	R1233zD(E)	Water	$\Delta T_{lifthp} = 8$ and $\Delta T_{lifthe} = 49$	72.5%	[19]
	Thermal Integrated Heat pump and heat engine	[-]	[-]	Propane	Ethylene Glyco	$T_{st} = -15$	65%	[57]
Transcritical cycle	Transcritical cycle	[-]	[-]	Multiple Fluids	Multiple Fluids	$T_{sr} = ambient$	$57.6\%$for R13I1	[38]
	Transcritical cycle	[-]	50 [MJ]	CO_2	HT: Pressurized water LT: ice slurry	Multiple tanks	60%	[48]
	Transcritical cycle	1 - 50[MW]	[-]	CO_2	HT: Pressurized water LT: ice slurry	$T_{st} = 123$ $T_{sk} = -3$	51% for $1MW$ and 65% for $50MW$	[47]

Additionally, the author recommended an operation power window which can be seen in figure 2.24 which shows that scrolls are the most suitable expander for small scale $< 10\ kW$.

For compressors, [43] summarized different off-the-shelf volumetric and dynamic compressors with the conclusion that scroll compressors have an adiabatic efficiency around $55-60\%$. However, [74] demonstrated that an isentropic efficiency of $\eta_{c,is} = 70\%$ is achievable as will be shown later.

Therefore, for the purpose of this thesis, a scroll compressor and expander will be used and therefore will be detailed.

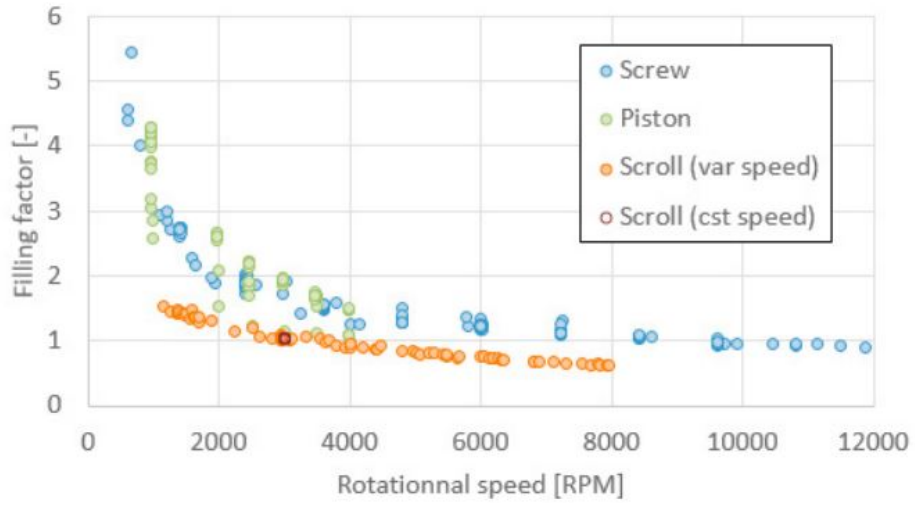

Figure 2.23: Expander filling factor ($\phi_{FF} = \frac{\dot{V}_{meas}}{\dot{V}_{th}}$) Variation with RPM Where $\phi_{FF} = 1$ is Favorable [18]

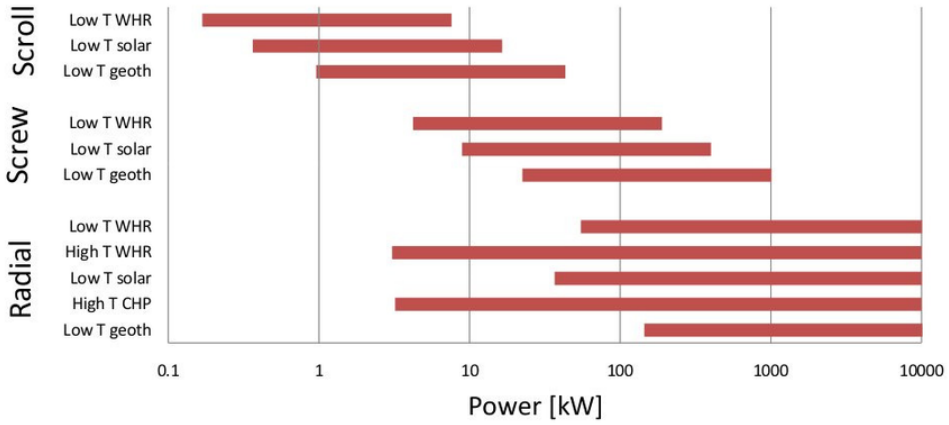

Figure 2.24: Expander Allowed Power Range for Low Temperature Waste Heat Recovery (Low TWHR); Low Temperature Solar (Low T solar); Low Temperature Geothermal (Low T geoth); High Temperature Waste Heat Recovery (High TWHR); High Temperature Combined Heat and Power (High T CHP) [63]

2.2.1.2. Modeling of Scroll Compressor and Expander

Several models were used to simulate the performance of the scroll compressor and expander which can be grouped into three methods which will be detailed later:

- **Geometric:** mathematical equations are used to simulate the geometric volumes of different champers and the different properties like pressure and temperature in order to

calculate the performance of the compressor and expander

- **Semi-Empirical:** parameters from both experimental and physical laws are used to model the performance of the compressor and expander
- **Polytropic:** general simple model based on ideal gas law with assumed constant efficiency

i Geometrical Model

In the geometrical model, conservation laws of mass, energy, and momentum are used to solve mathematical equations to simulate the performance of the scroll compressor and expander. The work involves mathematical equations to simulate the geometric volumes of different scroll champers as can be seen in figure 2.25a with the change of the chamber volume represented in terms of the rotation angle of the scroll as can be seen in figure 2.25b.

B. Wang et al.[71] provided a general geometrical model of a scroll compressor with leakage area consideration where the compressor was divided into three chambers (suction, compression, and discharge) to calculate the volumes of each chamber. Additionally, the leakage model was divided into two types radial (leak across the seal) and flank (leak across involute walls). The model was able to simulate the performance of the compressor within $\pm 2.5\%$, and $-2.0\ to\ +5\%$ for mass flow rate and power respectively.

The majority of the work around the scroll expander is done by altering a scroll compressor to work as an expander with the same simulation model working in reverse as demonstrated by E. Oralli et al.[54] who used B. Wang et al.[71] geometrical model to simulate the work of the compressor as well as the expander. The simulated model showed isentropic efficiencies of $\eta_{is,C} = 0.51$ and $\eta_{is,T} = 0.51$ for compressor and expander respectively.

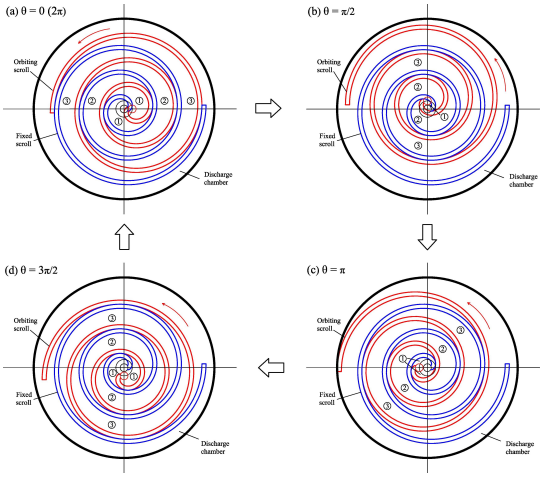

(a) Scroll Geometrical Model [38]

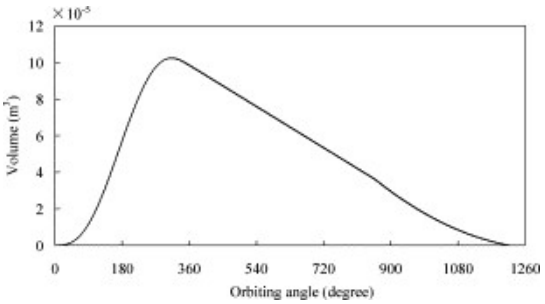

(b) Scroll Compressor Chomper Volume Change With Angle [71]

Figure 2.25: Scroll Compressor Geometric Model [38]

ii Semi-Empirical Model

In a semi-empirical model, parameters from both experimental and physical laws are used to model the performance of the compressor and expander. Even though an expander model is demonstrated in figure 2.26a, similar model can be used for scroll compressor as demonstrated by [74] in Figure 2.26b.

- **su →su,1:** Adiabatic pressure drop
- **su,1 →su,2:** Isobaric cooling down
- **su,2 →ad:** Adiabatic reversible expansion due to built-in volume ratio
- **ad →ex,2:** Adiabatic expansion at constant volume
- **ex,2 →ex,1:** Adiabatic mixing of main flow with leakage flow
- **ex,1 →ex:** Isobaric heating up

E. Winandy et al. [74] conducted an experimental investigation along with a semi-empirical investigation on a hermetic scroll compressor to predict the mass flow rate, electric consumption, ambient losses, and discharge temperature. The author concluded that an isentropic efficiency of about $\eta_{is,C} = 70\%$ is achieved at a built-in volumetric ratio of $r_{v,in} = 2.5$ based on the model. Additionally, the model was able to simulate the compressor performance of flowrate, power, and outlet temperature to an error of $(-3.5\% - 2.5\%)$, $(-2.5\% - 3\%)$, and $(-2.5K - +5K)$ respectively where these accuracy levels are comparable to ones attained with the geometric model.

V. Lemort et al.[42] provided an experimental and analytical assessment of scroll expander based on a semi-empirical model as can be seen in figure 2.26a. The semi-empirical model has 8 input parameters as can be seen in table 2.2 which are used to calculate mass flowrate, shaft power, and exhaust temperature as can be seen in figure 2.26c which are then compared with the experimental results where error ϵ is evaluated and parameters are updated if the error is high. The model was validated through an experimental set-up with three rotation speeds (1771,2296, and 2660) to an accuracy of $\pm 2\%$ for mass flowrate, $\pm 3K$ for exhaust temperature, and $\pm 5\%$ for shaft power. The maximum achieved isotropic efficiency was $\eta_{is,T} = 68\%$ at a power output $\dot{W}_t = 1.82\ kW$.

Table 2.2: Semi-empirical Parameters [42]

Parameter	Unit	Description
AU_{amb}	$W\ K^{-1}$	Heat transfer coefficient with the ambient
$AU_{su,n}$	$W\ K^{-1}$	Supply heat transfer coefficient
$AU_{ex,n}$	$W\ K^{-1}$	Exhaust heat transfer coefficient
$\dot{M}_n$	$kg\ s^{-1}$	Nominal mass flow rate
A_{leak}	m^2	Leakage area
$r_{v,in}$	$-$	Built-in volume ratio
$V_{s,exp}$	m^3	Swept volume
A_{su}	m^2	Supply port cross-sectional area
T_{loss}	$N\ m$	Mechanical loss torque

iii Polytropic Model

The Polytropic model is based on ideal gas law with the specific work of the machine represented by equation 2.1 which assumes a constant polytropic efficiency of the compressor and expander. The model is used for system-level simulation. However, the accuracy depends on real gas properties as it is based on idealistic behavior [43].

$$\Delta h = \eta_{pol} \frac{n}{n-1} R T_i \left[\left(\frac{p_o}{p_i} \right)^{\frac{n-1}{n}} - 1 \right] \tag{2.1}$$

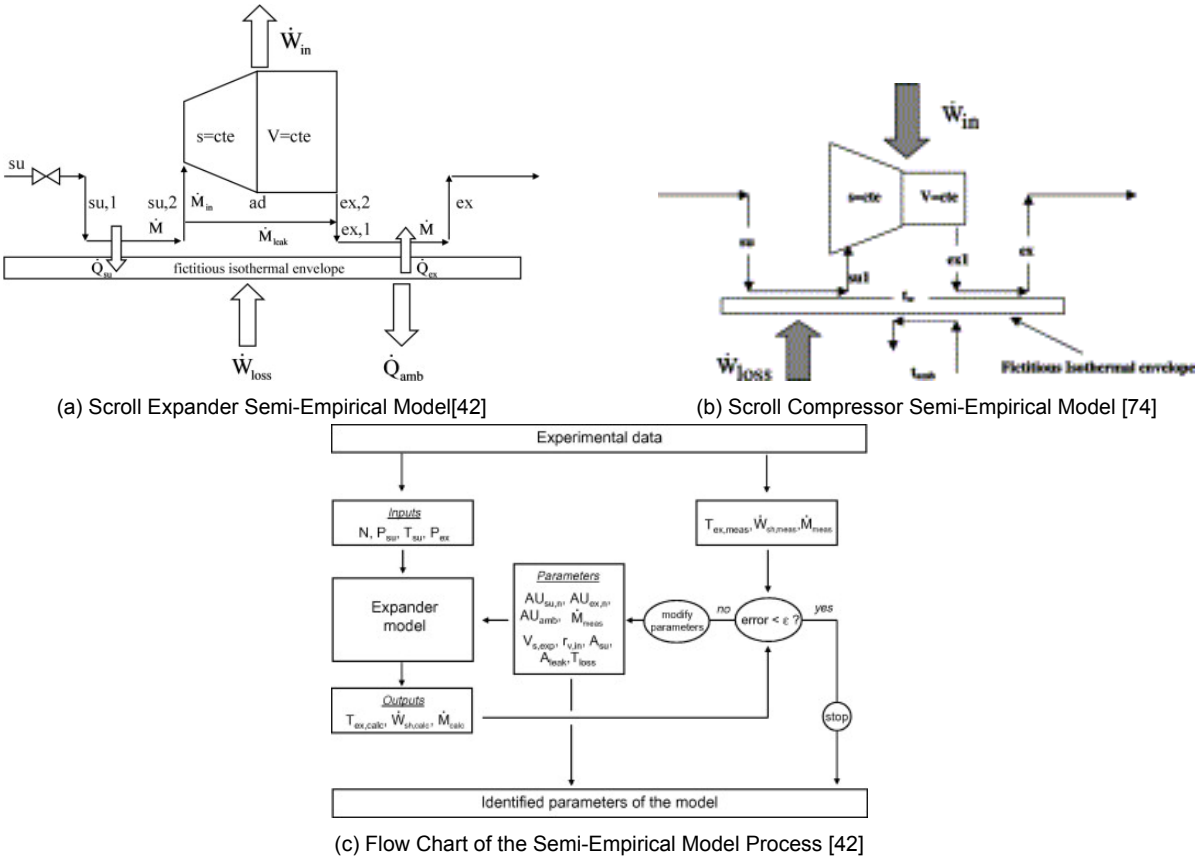

(a) Scroll Expander Semi-Empirical Model[42]

(b) Scroll Compressor Semi-Empirical Model [74]

(c) Flow Chart of the Semi-Empirical Model Process [42]

Figure 2.26: Scroll Compressor and Expander Semi-Empirical Model. (a) Scroll Expander Semi-empirical Model [42].(b) Scroll Compressor Semi-Empirical Model [74] (c) Flow Chart of the Semi-Empirical Model Process[42]

Since the semi-empirical model depends on experimental results to validate the parameters while having a similar accuracy to the geometric model, then a geometrical model will be used to simulate the performance of the compressor and expander in the detailed system model while polytropic efficiency will be used in the simple system models.

2.2.2. Thermal Energy Storage System

Thermal energy storage is a crucial part of PTES and therefore several technologies will be detailed to ensure the proper selection of the storage system. The TES systems can be divided into two categories Sensible Thermal Energy Storage (STES) and Latent Thermal Energy Storage (LTES). The STES can be subdivided into liquid and solid while LTES mainly have Liquid-Solid Phase Change Material (PCM) as can be seen in figure 2.27 and 2.28.

Depending on the cycle discussed earlier, the working fluid can have a phase change like in the case of the subcritical Rankine cycles where a condenser and evaporator are employed or a temperature glide like in the case of the high-temperature side of the transcritical cycle. Therefore, matching the temperature profile between the two mediums is crucial to the performance of the system as can be seen in figure 2.29. When the working fluid goes through phase change like in the (condenser/evaporator) of R-PTES, the use of PCM is advantageous to have a better temperature profile match as can be seen in figure 2.29 bottom right. The use of sensible heat storage when having a phase change in the working fluid will result in exergy losses and therefore less efficient storage. The different systems will be detailed below:

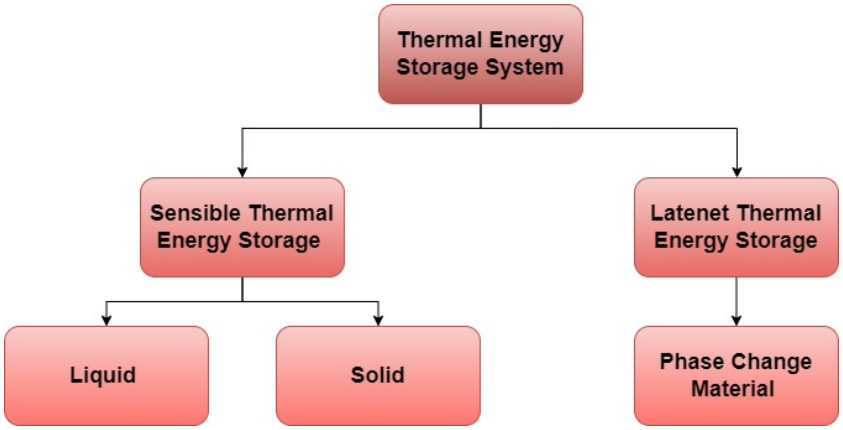

Figure 2.27: Thermal Energy Storage Overview

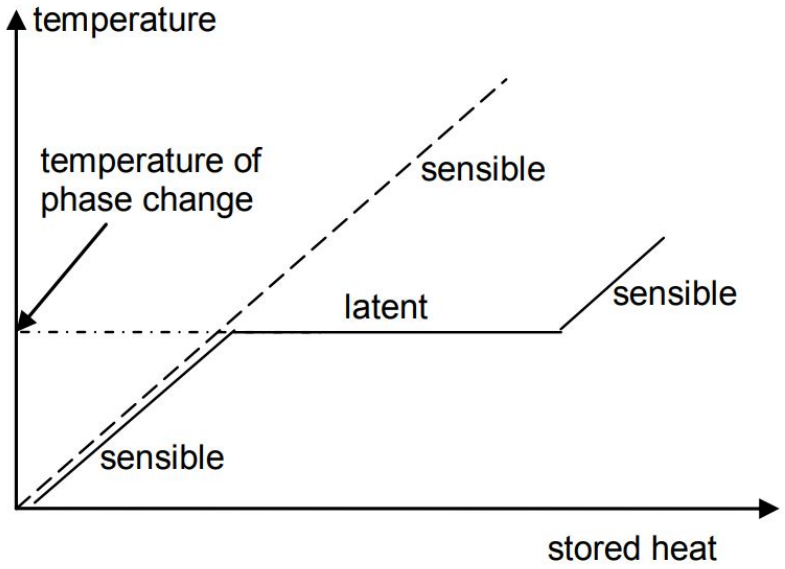

Figure 2.28: Latent (Solid Line) and Sensible (Dashed Line) Heat Storage. In latent heat, temperature increases before and after phase change temperature

2.2.2.1. Sensible Thermal Energy Storage

In STES, heat is stored by changing the temperature of the storage medium which is called temperature glide. The fluid need to have the following properties [33]:

- High thermal capacity c_p
- Stable under thermal cycling
- Low cost
- Compatible with other materials

The size of the system will be governed by the heat duty as can be seen in equation 2.2 where high duty will require high volume and vice versa. Additionally, the equation shows the importance of storage fluid density as higher density requires a smaller storage volume hence reduced cost [75].

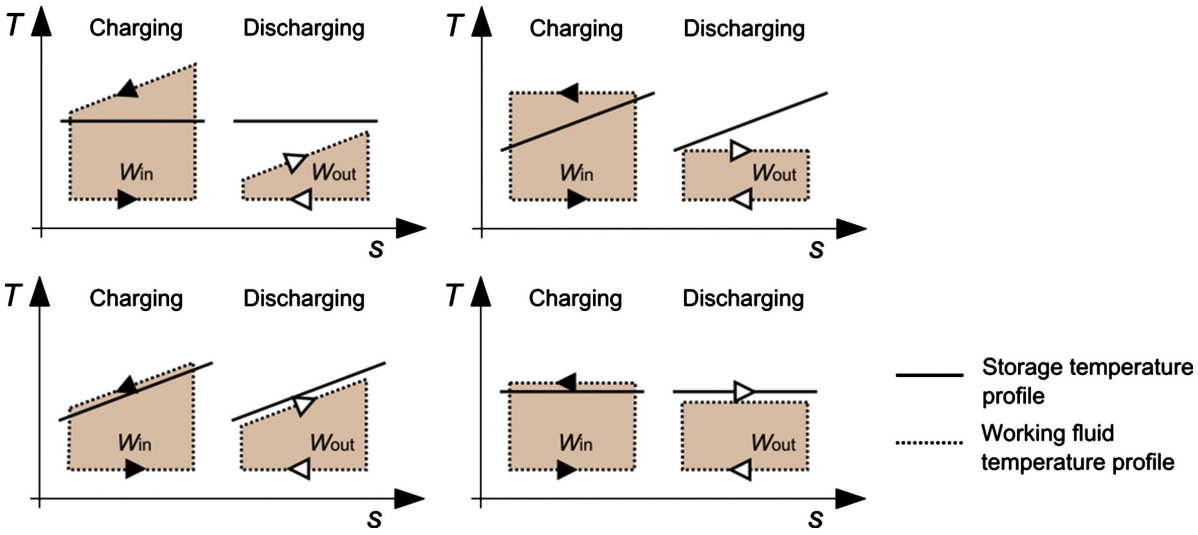

Figure 2.29: Bad and Good Temperature Profile where (top) bad match (bottom) good match and (bottom left) sensible (bottom right) latent) [47]

$$V = \frac{Q}{\rho c_p \Delta T} \tag{2.2}$$

There are two types used for STES which are Liquids and Solids. Vapors are not suitable for thermal storage due to their low specific volume and therefore high storage size. An overview of the temperature operating range of different systems is demonstrated in figure 2.30.

- **Liquids**

  The most common used storage medium is water [26] due to its high thermal capacity $c_p = 4.2\ kJ\ kg^{-1}\ K^{-1}$, low cost, and availability. However, it has limited operating temperature $25-90°C$ for unpressurized systems. With pressurized water, the operating temperature can be increased up to $200°C$ as used in [48] but that will increase the cost of the storage equipment. Other liquids include petroleum-based oils which can be used for higher temperature storage up to $350°C$ [33]. Additionally, molten salt can be used up to $800°C$ but suffer from being corrosive which impacts the equipment cost [33].

- **Solids**

  Solids can be used for high temperatures up to $1000°C$ with materials like rocks, metals, etc [33]. Since the Brayton cycle operates at high temperatures, solids are commonly used in the cycle like the use of a packed bed of iron oxide Fe_3O_4 in [45] and rocks in [36].

2.2.2.2. Latent Thermal Energy Storage

In LTES, heat is stored at a constant temperature based on the latent heat of fusion in Phase Change Material (PCM) with a typical example being water/ice. The latent heat like water $\lambda = 333\ kJ\ kg^{-1}$ is higher than the sensible heat capacity $c_p = 4.2\ kJ\ kg^{-1}\ K^{-1}$. This means that for the same heat energy Q, latent thermal storage volume can have a lower storage volume than sensible thermal storage for a given temperature range in the sensible heat as can be seen in equation 2.3 compared to equation 2.2. However, the concept of LTES is not mature as the majority of work is experimental and numerical due to the complexity of the system with limited understanding of the different technical aspects [46].

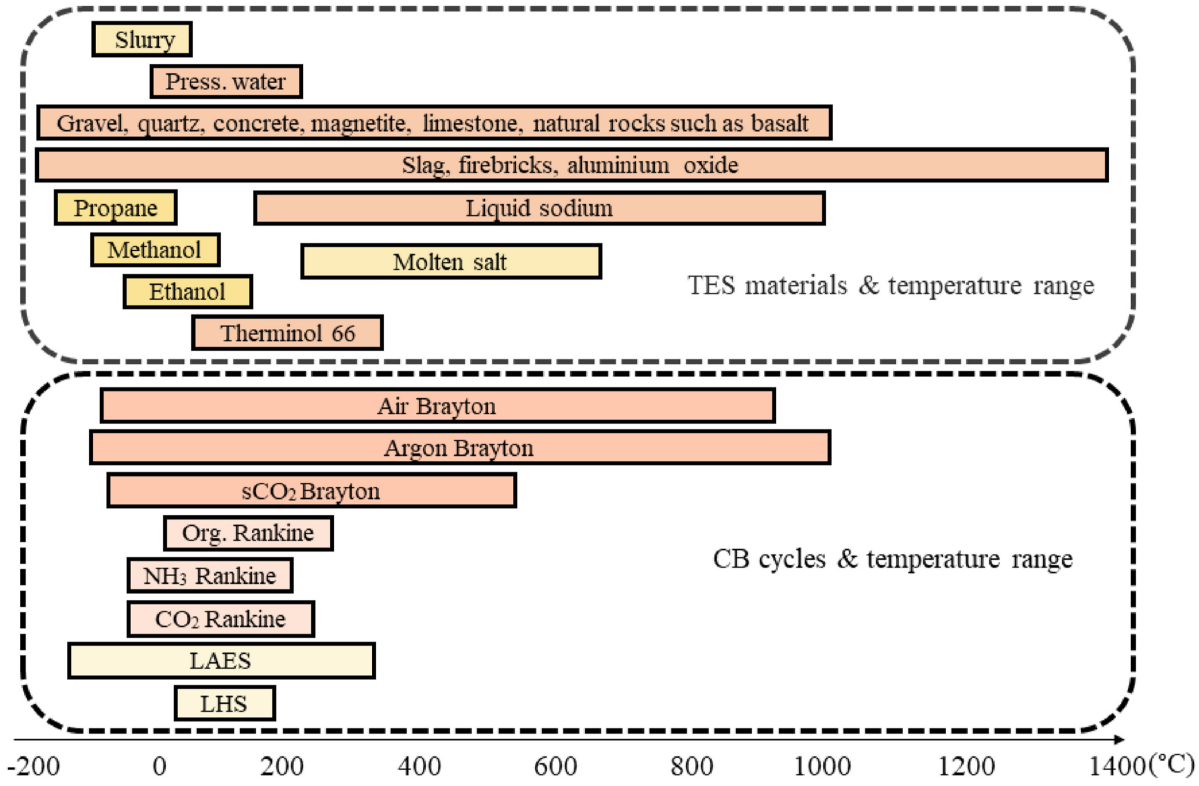

Figure 2.30: Sensible Thermal Storage System Materials and Operating Temperature Range in Comparison with Carnot Battery Cycles and Temperature Range [43] where Org. Rankine: Organic Rankine; sCo_2: supercritical CO_2; LAES: Liquid Air Energy Storage; LHS: Lamm-Honigmann storage

$$V = \frac{Q}{\rho\lambda} \tag{2.3}$$

Table 2.3 shows common materials used in a thermal storage system and their properties. Additionally, figure 2.30 shows different cycles with their typical operation temperature window and the corresponding storage medium. It is worth mentioning that liquid can be transported and stored without direct contact with the working fluid. On the other hand, solid and latent heat requires direct contact and therefore no transport of the storage medium occurs.

2.2.3. Heat Exchangers

When the storage medium selected is transferable, then a heat exchanger can be used to transfer heat between the working fluid and the storage fluid medium. Temperature difference works as the driving force where heat is transferred from the high-temperature medium to the low one. The most common types of heat exchangers are shell and tube HEX, plate HEX, and air cooler HEX [70]. Shell and tube heat exchangers are the most common type in the chemical industry [70] however they are not suitable for low flows as low flow velocity causes dead zones which increases the likely hood of fouling [40]. Air cooler HEX are highly dependent on ambient conditions, have low thermal efficiency attributed to air low conductivity, density, and thermal capacity, and require large space. Plate HEX however, can be used for low flows typically up to $(2500m^3\ h^{-1})$ with temperature and pressure typically of $(180°C\ and\ 20bar)$ for gasket type and $(450°C\ and\ 40bar)$ for brazed and welded type [31]. They have the perks of being compact, easy to clean for the gasket type, and small approach temperature difference as low as $1°C$ [70].

Table 2.3: Thermal Storage Material

Fluid	Density [$kg\ m^{-3}$]	Temperature Range [$^{\circ}C$]	$c_p[kJ\ kg^{-1}\ K^{-1}]$	Melting Temp [$^{\circ}C$]	Heat of Fusion [$kJ\ kg^{-1}$]
Solid Sensible Thermal Energy Storage [68]					
Sand-rock mineral	1700	200-300	1.30	-	-
Reinforced concrete	2200	200-400	0.85	-	-
Cast iron	7200	200-400	0.56	-	-
NaCl	2160	200-500	0.85	-	-
Cast steel	7800	200-700	0.60	-	-
Silica fire brick	1820	200-700	1.00	-	-
Liquid Sensible Thermal Energy Storage [68] [43]					
Unpressurized Water	L (1000); S (920)	0-100	4.19	0	333
Engine Oil	888	≤160	1.88	-	-
Calorie HT43	867	12 - 260	2.4	-	-
Isopentanol	831	≤148	2.2	-	-
Octane	704	≤126	2.4	-	-
Therminol 66	750	-3 - 345	2.1	-	-
Sunflower Oil	918	227	2.4	-	-
Soybean Oil	925	232	2.1	-	-
Synthetic Oil	900	-40-300	2.3	-	-
Pressurized Water	1000	0-200	2.19	-	-
Phase Change Material [15]					
$MgCl_26H_2O$	L (1450) S (1569)	-	-	117	168.6
$Mg(NO_3)_26H_2O$	L (1550) S (1636)	-	-	89	162.8
Paraffin wax	L (790) S (916)	-	-	64	173.6

The duty of the heat exchanger can be determined based on the heat transfer rate across the system as defined in equation 2.4:

$$\begin{aligned} \dot{Q} &= \dot{m} c_p \Delta T && \text{Sensible heat flux} \\ \dot{Q} &= U A \Delta T_{lm} && \text{Heat exchanger duty} \end{aligned} \tag{2.4}$$

The logarithmic mean temperature difference (LMTD) method as described in [70] can be used to size the heat exchanger where an iterative method is used to calculate the overall heat transfer coefficient as can be seen in figure 2.31.

2.3. Working Fluids

The working fluid is crucial for the performance of the system. Therefore, the criteria required to select the proper working fluid will be detailed. Table 2.4 shows common fluids with their respective properties [62].

- **Boiling Point:** The boiling point of the fluid shall be lower than the atmospheric temperature. This is to ensure that the fluid will be in the vapor phase without the employment of low temperature system $T_{Bp} < Tatm$. Figure 2.33c shows the boiling point of different fluids.

- **Density:** The density shall be high in order to have lower equipment size and therefore lower cost.

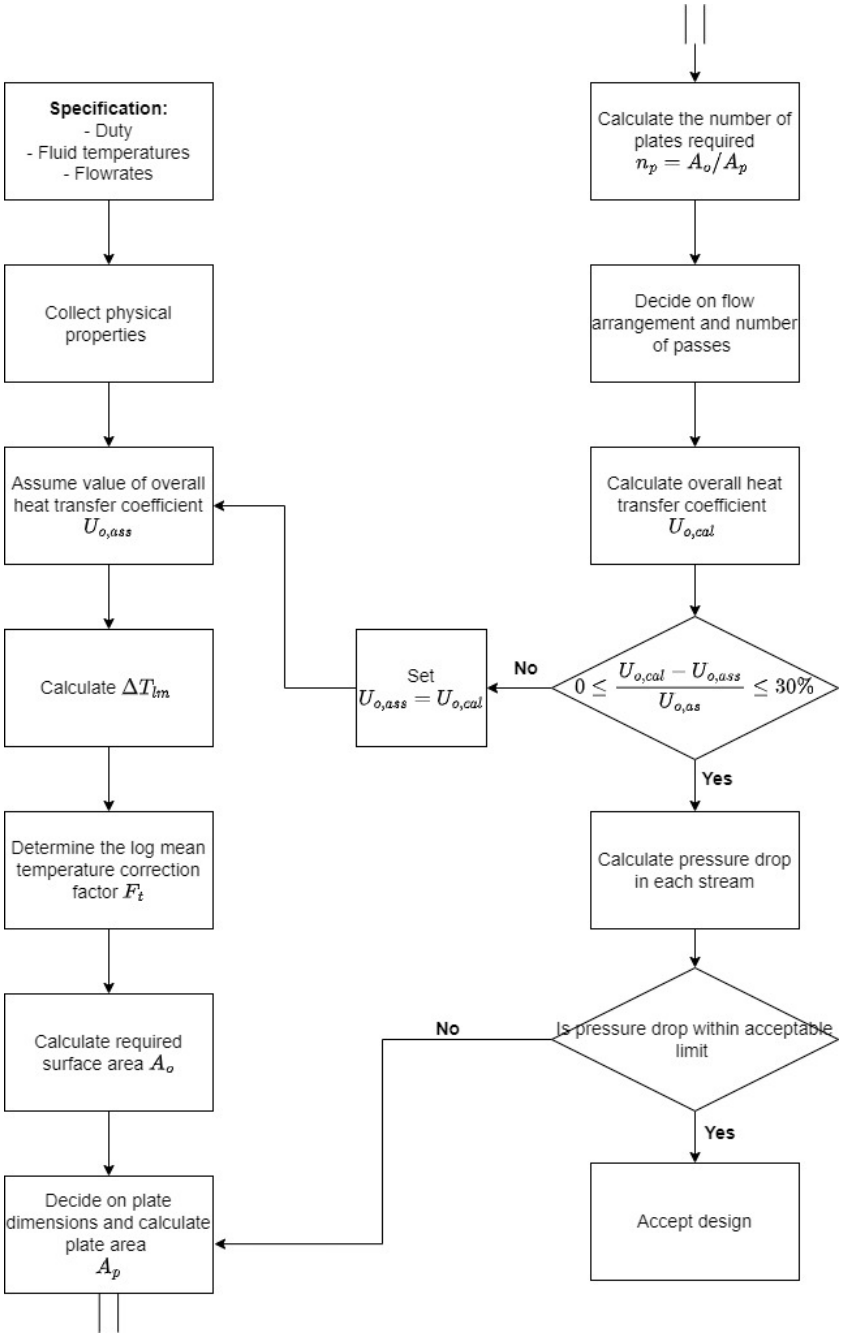

Figure 2.31: Plate Heat Exchanger Design Logic [70]

- **Viscosity:** The fluid shall have low viscosity to reduce friction losses.
- **Critical Pressure p_{crit}:** The critical pressure can be selected based on the cycle. When a transcritical cycle is employed, a lower value is desirable to have lower upper pressure which reduces equipment cost. However, if a sub-critical is employed, then a high value is desirable to have a high operation window. Figure 2.33b shows the critical pressure of the different fluids.
- **Critical Temperature T_{crit} :** Similar to the critical pressure, the critical temperature shall be high in sub-critical cycles while it shall be low in transcritical cycles. Figure 2.33a shows the critical temperature of the different fluids.

- **Safety:** The fluid shall be safe to handle which means that it shall be non-toxic, non-flammable, non-combustible, and chemically stable. ASHRAE safety index was used to describe the fluids' safety index where 'A' represents low toxicity and 'B' represent high toxicity and 1 - 3 represents lower to higher flammability [3]. Therefore, A1 is the most desirable fluid while B3 is the least desirable.
- **Environment:** The fluid shall have a low impact on the environment and therefore shall have null Ozone Depletion Potential (ODP) and low Global Warming Potential (GWP). Therefore, fluids with high GWP will not be selected like (R410A, R507A, and R134A, etc.).
- **Operation Pressure:** The operation pressure shall be higher than the atmospheric pressure to avoid air infiltration to the system. $p_{op} > p_{atm}$
- **Type of Fluids:** There are three types of fluids based on the slope of the saturation vapor curve which are dry (positive slope), wet (infinite slope), and isentropic (zero slope). Isentropic fluids are desirable to avoid liquid formation at the outlet of the compressor or expander without the need for a large superheat.

For the transcritical cycle, the most studied fluid is CO_2 as mentioned earlier. The critical pressure of CO_2 is high $p_{crit} = 73.8\ bar$ which will mandate additional cost for the high pressure. Pentane and R1234yf were identified as possible fluids for the transcritical cycle due to their lower critical pressure of around $p_{crit} = 33bar$. Additionally, R13I1 was reported by [38] as an optimum fluid for transcritical cycles based on round trip efficiency of $\eta_{rt}57.6\%$. Table

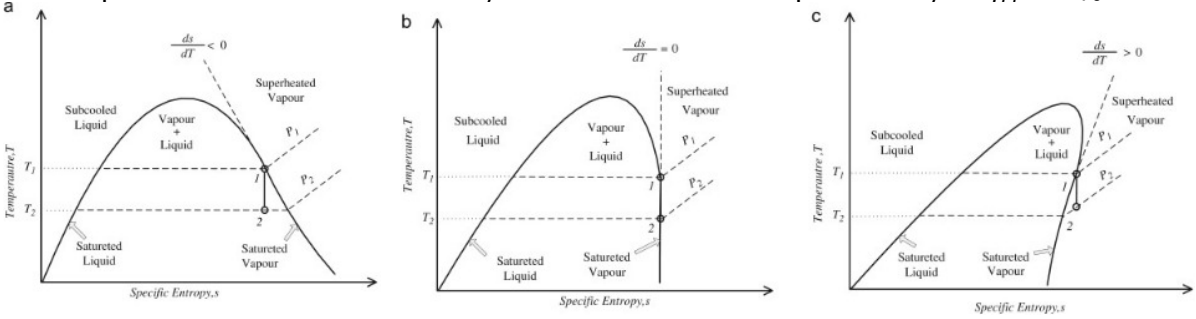

Figure 2.32: Working Fluid Types (a) Wet (b) Isentropic (c) Dry [5]

2.4. Thesis Objectives, Scope, and Goals

After reviewing the literature around the utilization of PTES, a case study was developed to study a small-scale thermally integrated pumped thermal energy storage with water as the storage medium.

Research Objective: Optimization of thermally integrated small-scale pumped thermal energy storage

The following **goals** will be achieved:

- Develop compressor and expander model and integrate them into the optimized cycle
- Develop an optimization scheme to determine the best operating conditions including the working fluids
- Explore possible application of the optimized pumped thermal energy storage where the cycle can be deployed

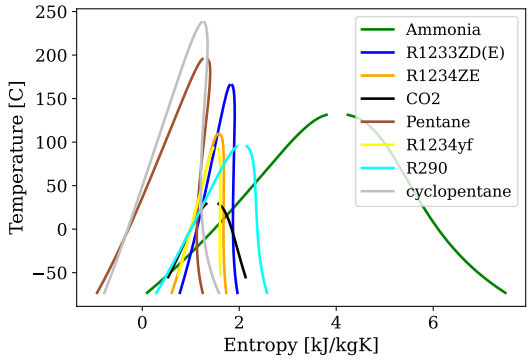

(a) Critical Temperature of Different Fluids

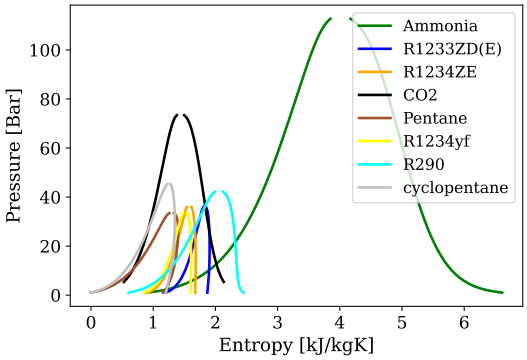

(b) Critical Pressure of Different Fluids

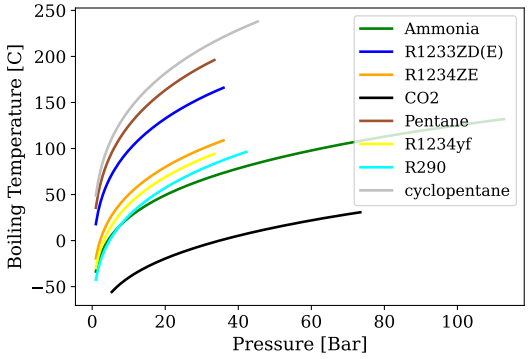

(c) Boiling Point of Different Fluids

Figure 2.33: Different Fluid Critical Properties. (a) Critical Temperature. (b) Critical Pressure. (c) Boiling Point

The **scope** of this thesis will be limited to small-scale applications with steady-state modeling.

Table 2.4: Fluid Properties [28][3],and REFPROP

Fluid	$T_{crit}[°C]$	$p_{crit}[bar]$	Density [kgm^{-3}]@ P=1.01 bar and $T = 15°C$	ODP	GWP	ASHRAE safety index
CO_2	31.3	73.8	L (-) ; V (1.9)	0.0	1.0	A1
Pentane	196.7	33.6	L (610.1) ; V (3.0)	0.0	11.0	A3
R13I1	123.3	39.5	L (2249.2) ; V (9.9)	0.0	1.0	A1
R507A	70.0	37.0	L (1317.04) ; V (5.57)	0.0	3985.0	A1
R1233ZD(E)	165.6	35.7	L (1279.12) ; V (5.7)	0	1.0	A1
Ammonia	131.9	113.3	L (681.7) ; V (0.9)	0	0.0	B2L
R410A	71.0	49.0	L (1349.8) ; V (4.2)	0.0	2088.0	A1
R134A	101.1	40.6	L (1376.9) ; V (5.2)	0.0	1400.0	A1
R1234ZE	109.4	36.4	L (1293.8) ; V (5.7)	0.0	6.0	A2L
R245FA	153.7	36.5	L (1365.3) ; V (5.9)	0.0	950.0	B1
R1234yf	94.7	33.8	L (1263.3) ; V (6.0)	0.0	4	A2L
Cyclopnetane	238.7	45.2	L (715.8) ; V (2.7)	0.0	0	-
Propane (R290)	96.7	42.5	L (581.0) ; V (2.4)	0.0	3	A3
R1336mzz(Z)	171.4	29.0	L (1390.4) ; V (3.5)	0.0	2.0	A1
R1224yd(Z)	155.5	33.4	L (1388.3) ; V (6.7)	0.0	0.9	A1

3

Components Model

Component models are crucial in the performance of the PTES system. In multiple studies, the performance of the different components like the compressor, the expander, and the pump is assumed to be constant. In reality, however, compressor and expander performance will vary depending on the operating condition of the system which heavily influences the performance of the storage system. In this chapter, different components models will be detailed starting from the compressor model followed by the expander model.

3.1. Compressor Model

A geometric scroll compressor model was developed to evaluate the performance of the compressor in energy storage. The scroll compressor has a built-in volumetric ratio associated with its geometry. In order to develop the model, firstly the scroll geometry will be detailed. Secondly, the thermodynamic model will be demonstrated. Thirdly, the model will be validated against the paper model and commercial software. Finally, results and discussion of the model will be provided. The compressor was modeled in Python with CoolProp being used as the thermophysical property database.

3.1.1. Geometry

A scroll compressor comprises two identical involutes one is stationary and the other is rotating as described in [76] with a $180°$ phase difference. The scroll geometry starts from the base circle with radius (a) and thickness (b) with two tangent lines formulate the inner involute (l_a) and outer involute (l_b) and scroll height (h). At the end of the inner involute, the radius continues with a radius of (r_a) as shown in equation 3.1 as can be seen in figure 3.1a.

$$\begin{aligned} l_a &= a(\phi_{inner} - \alpha) \\ l_b &= a(\phi_{outer} + \alpha) \\ \phi_{inner} &= [\phi_a, \phi_{end}] \\ \phi_{outer} &= [\phi_a - \pi, \phi_{end}] \\ \alpha &= b/2a \\ r_a &= a\left[\phi_a - \frac{\pi}{2} + \frac{1}{\phi_a - \frac{\pi}{2}}\right] \end{aligned} \tag{3.1}$$

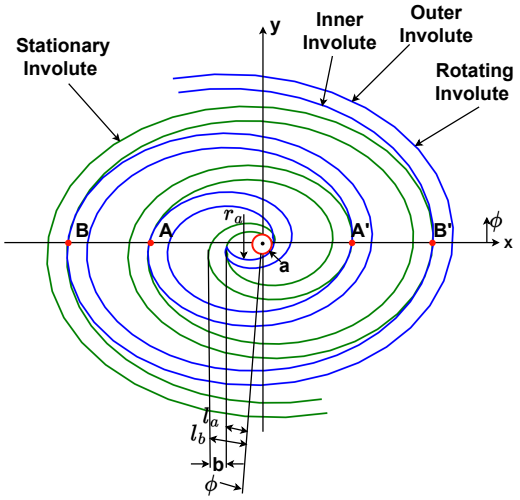

(a) Scroll Compressor Detailed Geometry Where Stationary Involute (Green) And Rotating Involute (Blue). (A,B,A',B') are Contact Points.
a: is Base Circle, l_a: is Inner Involute Length, l_b: is Outer Involute Length, r_a: Radius of Discharge Arc, and ϕ: is Involute Angle

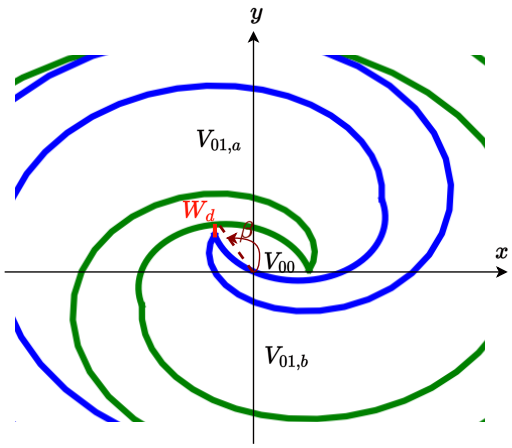

(b) Scroll Discharge Geometry
where W_d: is the Distance Between Tip and Inner Involute and β: is the Angle of the Tip

Figure 3.1: Geometry of Scroll Compressor where (a) Overall Compressor Geometry (b) Discharge Detailed Geometry

The rotating involute rotates with a radius of $(r = \pi a - b)$ and rotating angle (θ). With the rotation of the involute, the number of pairs of contact points (n) where the stationary meets the rotating involute is determined through equation 3.2. Through the number of contact points, the number of pairs of compression chambers (N) can also be determined.

$$n = INT\left[\frac{\phi_{end} - \theta - \phi_a}{2\pi} + 1\right]$$
$$N = n - 1 \tag{3.2}$$

The involute angle for the contact points (ϕ_i) is determined by equation 3.3 where i is the index of the contact point starting from the center of the scroll.

$$\phi_i = \phi_{end} - \theta - 2\pi(n - i) \tag{3.3}$$

3.1.1.1. Volume Development

Considering all the previous parameters, there are three types of chambers with each chamber having its own volume which are intake volume V_n, compression volume V_1 & V_2, and discharge volume V_0. The discharge process starts at discharge angle of (θ_d) before which there is two compression pairs V_1 & V_2 and one discharge chamber V_0 and after which there is only one compression V_1 and two discharge V_{00} & V_{01} as summarized in table 3.2. The gap length separating the tip of the rotating part and the inner of the stationary part in the discharge region is (W_d) with the tip formulating an angle (β) as can be seen in figure 3.1b. Finally, a clearance volume V_c is defined to account for the inner clearance between the rotating and stationary involutes. These chambers are determined with equation 3.4

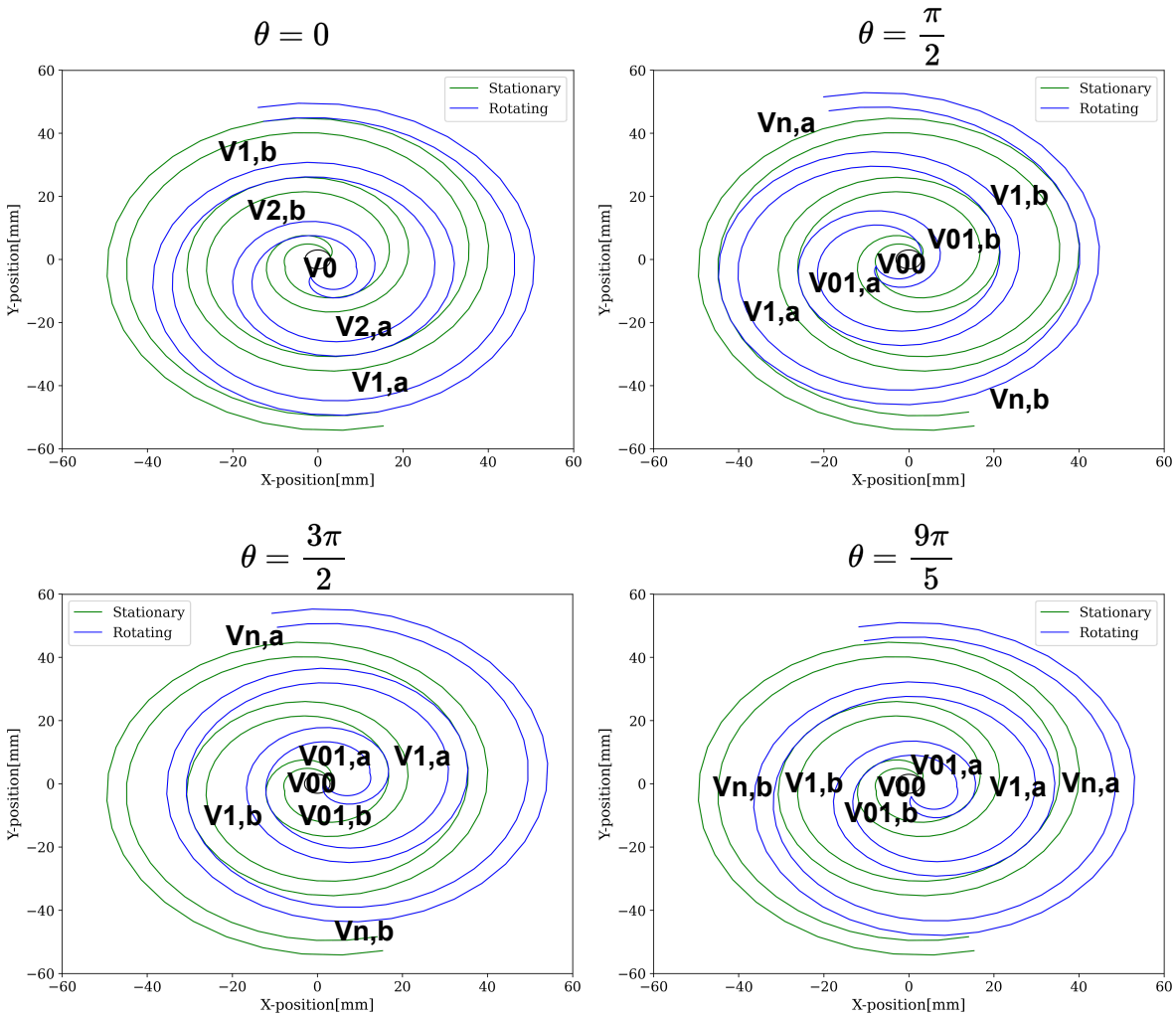

Figure 3.2: Scroll Compressor Chambers for Different Rotation Angles

Table 3.1: Scroll Compressor Chambers

	Chambers Numbers					
Condition	V_n	V_1	V_2	V_0	V_{00}	V_{01}
Before θ_d	X	X	X	X	-	-
After θ_d	X	X	-	-	X	X

$$
\begin{aligned}
V_n &= har[\theta(2\phi_{end} - \theta - \pi) - 2(\phi_{end} - \pi + \alpha)\sin\theta \\
&\quad - (\frac{\pi}{2} - \alpha)\sin 2\theta + 2(1 - \cos\theta)] \\
V_1 &= 2\pi har(2\phi_1 + \pi) \\
V_2 &= 2\pi har(2\phi_2 + \pi) \\
V_0 &= har(\phi_1 - \phi_a)(\phi_1 + \phi_a - \pi) + V_c \\
V_c &= hr_a^2\left[\pi - \sin^{-1}\frac{2a}{r_a} - \frac{2a}{r_a}\right] \\
V_{00} &= hr_a\left[r_a\beta - (r_a - w_d)\sin\beta\right] \\
\beta &= \pi - \cos^{-1}\left[\frac{r_a - r + r\cos(\theta - \theta_d)}{r_a - w_d}\right] - \sin^{-1}\left(\frac{2a}{r_a}\right) \\
w_d &= r_a - \sqrt{r^2 + (r_a - r)^2 + 2r(r_a - r)\cos(\theta - \theta_d)} \\
V_{01} &= V_0 - V_{00}
\end{aligned}
\tag{3.4}
$$

With the listed volumes above, the theoretical suction volume (V_s) can be determined by setting $\phi_1 = \phi_e - 2\pi$ in V_1 equation and discharge volume (V_d) by setting $\phi_1 = \phi_a$ in the same equation. Additionally, the build volumetric ratio ($V_r = \frac{V_s}{V_d}$) and swept volume ($V_{sw} = V_s$).

The geometric parameters used to model the compressor are shown in table 3.2 to match the one used in the paper [76]

Table 3.2: Geometric Parameter [76]

Parameter	Symbol	Value [Unit]
Base Circle	a	$3[mm]$
Wrap Thickness	b	$4.6[mm]$
Height	h	$29.4[mm]$
Involute Starting Angle	ϕ_a	$1.09\pi[rad]$
Involute End Angle	ϕ_e	$5.59\pi[rad]$
Discharge Port Diameter	d	$10[mm]$
Suction Pressure	P_s	$5.84[bar]$
Suction Temperature	T_s	$15[^\circ C]$
Rotation Speed	Ω	$3500[RPM]$
Flow Coefficient	C_d	1
Flank Gap	δ_r	$0 - 20\mu m$
Radial Gap	δ_a	$0 - 20\mu m$
Pressure Ratio	PR	$2.5 - 4$

Volumetric ratio development at each rotation is shown in Figure 3.3a with each volume divided by V_s. At the first rotation, $0-2\pi$ suction occurs where the suction chamber V_n increases until it reaches its maximum at around $\theta = 1.8\pi$ then it starts to decrease at the end of the suction process locking the fluid in the chamber. From $2\pi - \theta_d$, compression occurs where the volume of the chamber V_1 decreases almost linearly followed by further compression at chamber V_2. After the discharge angle is reached and until the end of rotation $\theta_d - \theta_{end}$, the flow discharge through $V_0 \& V_{00}$ until the end of the process.

Following the fluid from the inlet to the outlet over the entire rotation, the volume development can be seen in figure 3.3b.

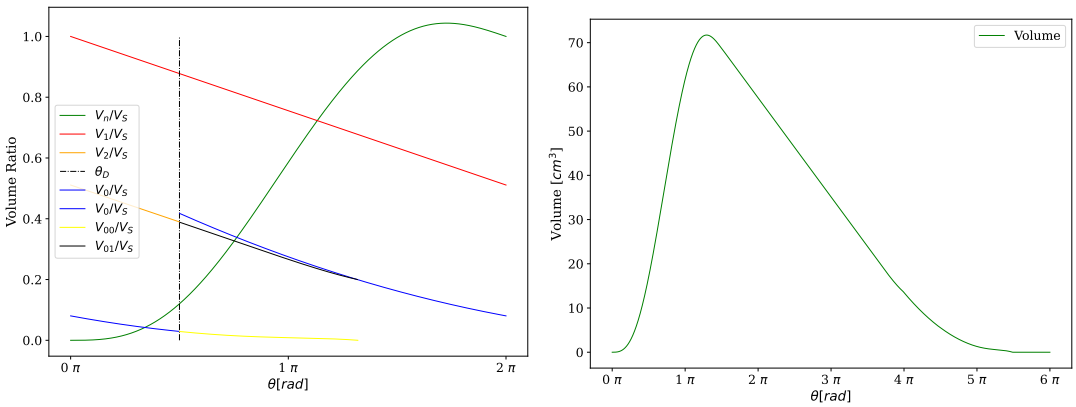

(a) Scroll Volumetric Ratio $\frac{V_i}{V_s}$

(b) Volume Development Over Entire Rotation

Figure 3.3: Scroll Volume Development Through the Compression Process

3.1.1.2. Area Development

The area at which the working fluid enters the compressor is referred to as the intake area A_n while the area at which the flow out of the compressor is called the exit area A_d. Additionally, the discharge port is referred to as A_p which represents the exhaust pipe section out of the compressor. These are modeled through equation 3.5 [76].

$$\begin{aligned} A_p &= \frac{\pi D^2}{4} \\ A_d &= 2hW_d \\ A_n &= 2hW_s \\ W_s &= r(1-\cos\theta) \end{aligned} \tag{3.5}$$

3.1.1.3. Gaps

There are two types of gaps in the scroll compressor which are the radial and flank gaps as can be seen in figure 3.4 [44]. The radial gap is the gap between the tip of one of the two involutes and the base plate of the other as represented by δ_a in figure 3.4 (b) while the flank gap is the gap between the two walls of the scroll compressor as represented by δ_r in figure 3.4 (a). Through the radial and flank gaps, leaks from the higher pressure chamber to the lower pressure chamber occur which impacts the performance of the compressor. The radial line length l_r represents the tip length between two adjacent chambers through which the leak occurs. The radial and flank areas are represented in equation 3.6 [76].

$$\begin{aligned} l_a &= \pi a(\phi_i - \frac{\pi}{2}) \\ A_a &= l_a \delta_a \\ A_r &= h\delta_r \end{aligned} \tag{3.6}$$

3.1.2. Thermodynamic Model

In this section, the thermodynamic model governing the scroll compressor will be described. This includes the continuity equation, energy equation, and generalized isentropic relations.

3.1.2.1. Mass Flowrate

The working fluid enters the compressor at the beginning of the intake cycle which takes 2π to complete and exits the compressor at the discharge cycle which occurs at $\theta_d - \theta_{d,end}$. The mass flow rate in $\dot{m}_{in}$ and out $\dot{m}_{out}$ of the compressor is expressed by equation 3.7 where $\dot{m}_{leak}$ is the mass leaking from one chamber to the other through the compressor gaps:

$$\begin{aligned} \dot{m}_{in} &= \frac{\mathrm{d}m_{in}}{\mathrm{d}t} - \frac{\mathrm{d}m_{leak}}{\mathrm{d}t} \\ \dot{m}_{out} &= \frac{\mathrm{d}m_{out}}{\mathrm{d}t} - \frac{\mathrm{d}m_{leak}}{\mathrm{d}t} \end{aligned} \tag{3.7}$$

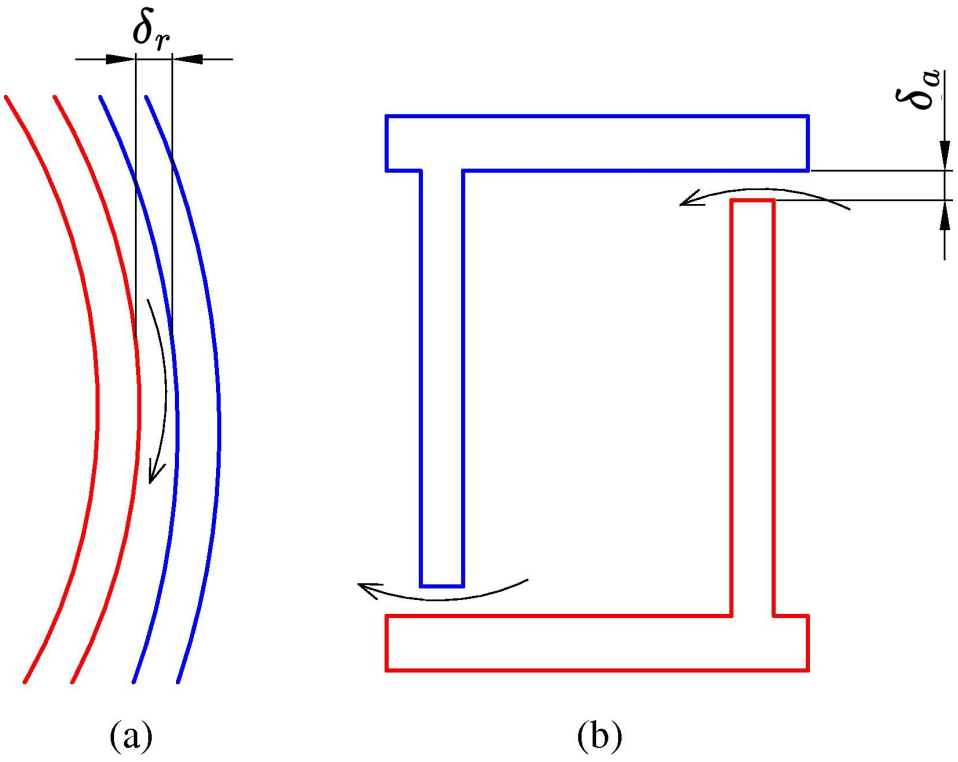

Figure 3.4: Types of Scroll Compressor Gaps (a) Flank Gap δ_r (b) Radial Gap δ_a [44]

It is advantageous to represent the mass flow rate in terms of the rotating angle θ with total mass m as can be seen in equation 3.8

$$\begin{aligned} \frac{\mathrm{d}m}{\mathrm{d}t} &= \frac{\mathrm{d}m}{\mathrm{d}\theta}\frac{\mathrm{d}\theta}{\mathrm{d}t} \\ \frac{\mathrm{d}m}{\mathrm{d}t} &= \frac{\mathrm{d}m}{\mathrm{d}\theta}\omega \\ \frac{\mathrm{d}m}{\mathrm{d}\theta} &= \frac{\dot{m}}{\omega} \\ m &= \int_0^{\theta} \frac{\mathrm{d}m}{\mathrm{d}\theta}\, d\theta \end{aligned} \tag{3.8}$$

The mass flow in and out as well as leakage flow is represented by flow through a one-dimensional isentropic compressible nozzle following equation 3.9 where A is the cross-sectional area, C_d is a flow correction factor based on experiment, R is the universal gas constant, k is the isentropic exponent [71]. The condition shows the choking limit of the flow through the nozzle.

$$\dot{m} = \begin{cases} C_d A P_{up} \left\{ \frac{2k}{R(k-1)T_{up}} \left[\left(\frac{P_{down}}{P_{up}} \right)^{\frac{2}{k}} - \left(\frac{P_{down}}{P_{up}} \right)^{\frac{k+1}{k}} \right] \right\}^{\frac{1}{2}} & , \left(\frac{P_{down}}{P_{up}} \right) \geq \left(\frac{2}{k+1} \right)^{\frac{k}{k-1}} \\ C_d A P_{up} \left\{ \frac{k}{RT_{up}} \left(\frac{2}{k+1} \right)^{\frac{k+1}{k-1}} \right\}^{\frac{1}{2}} & , \left(\frac{P_{down}}{P_{up}} \right) < \left(\frac{2}{k+1} \right)^{\frac{k}{k-1}} \end{cases} \tag{3.9}$$

3.1.2.2. Energy Equation

The first law of thermodynamics governs the energy model of the compressor as described in equation 3.10 [56]. The following assumptions were made for the model:

- Kinetic and potential energy are negligible.
- The compressor is assumed to be adiabatic where the loss to the environment is negligible $\dot{Q} = 0$.
- The model is assumed to be at a steady state which means $\dot{U} = 0$

With equation 3.10, the work enthalpy difference will be negative which indicates the work enters the system.

$$\begin{aligned} \dot{U} &= \dot{Q} - \dot{W} + \dot{m}_{in} h_{in} - \dot{m}_{out} h_{out} + K.E + P.E \\ 0 &= -\dot{W} + \dot{m}_{in} h_{in} - \dot{m}_{out} h_{out} \\ \dot{W} &= \dot{m}_{in} h_{in} - \dot{m}_{out} h_{out} \\ \dot{W} &= \dot{m}(h_{in} - h_{out}) \end{aligned} \tag{3.10}$$

Additionally, the shaft power can be expressed in terms of instantaneous torque τ driving the shaft with a rotating speed ω as can be seen in equation 3.11 [76]. The force exerted by the pressure on the scroll is shown in Figure 3.5.

$$\begin{aligned} \dot{W}_{shaft\ power} &= \frac{\omega}{2\pi} \int_0^{2\pi} \tau \, d\theta \\ \tau &= har \left\{ (2\phi_1 - \pi)(P_d - P_s) + 4\pi \sum_{j=1}^{n-1} (P_j - P_s) \right\} \end{aligned} \tag{3.11}$$

3.1.2.3. General Isentropic Model

Compression is generally modeled as an isentropic process where the process is adiabatic and reversible. This implied that the entropy doesn't change from inlet to outlet $\Delta s = 0$ and an isentropic efficiency is determined based on deviation from the isentropic compression work. For an ideal gas, the compressibility factor $(Z = \frac{Pv}{RT} = 1)$ and the isentropic exponent coefficient $\gamma = \frac{c_p}{c_v}$ is constant which is used to derive the isentropic relations for an ideal gas as can be seen in equation 3.12 [49]

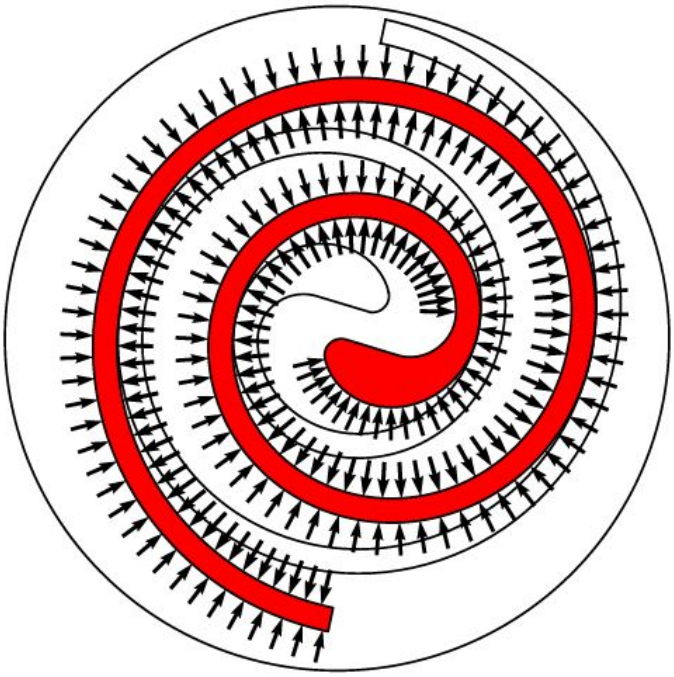

Figure 3.5: Radial Force[6]

$$Pv^{\gamma} = constant$$
$$\frac{P_2}{P_1} = \left(\frac{T_2}{T_1}\right)^{\frac{\gamma}{\gamma-1}} = \left(\frac{V_1}{V_2}\right)^{\gamma} = \left(\frac{\rho_2}{\rho_1}\right)^{\gamma} \tag{3.12}$$

However, for real gas, the ideal gas model fails especially at high-pressure ratios where γ can't be assumed to be constant anymore. A general isentropic model describing the behavior of real gas was demonstrated by [49] where the isentropic exponent is replaced by $\gamma_{Pv}, \gamma_{Tv}, \; and \; \gamma_{PT}$. The exponents can be calculated from equation 3.13 where (α) is thermal expansion coefficient, (β) is the isothermal compressibility factor, (c_p) is the isobaric specific heat capacity, and (c_v) is the isochoric specific heat capacity.

$$\gamma_{Pv} = \frac{\gamma}{P\beta}$$
$$\gamma_{Tv} - 1 = \frac{v\alpha}{c_v\beta} \tag{3.13}$$
$$\frac{\gamma_{PT} - 1}{\gamma_{PT}} = \frac{Pv\alpha}{c_p}$$

Hence the isentropic relations become as shown in equation 3.14

$$Pv^{\gamma_{Pv}} = constant$$
$$\frac{P_2}{P_1} = \left(\frac{T_2}{T_1}\right)^{\frac{\gamma_{PT}}{\gamma_{PT}-1}} = \left(\frac{v_1}{v_2}\right)^{\gamma_{Pv}} = \left(\frac{\rho_2}{\rho_1}\right)^{\gamma_{Pv}} \tag{3.14}$$

With this, a new equation for isentropic nozzle flow based on the general isentropic model can be seen in equation 3.15 [49] where the condition shows the choking limit of the flow through the nozzle.

$$\dot{m} = \begin{cases} C_d A P_{up} \left\{ \frac{2\gamma_{Pv}}{R(\gamma_{Pv}-1)T_{up}} \left[\left(\frac{P_{down}}{P_{up}} \right)^{\frac{2}{\gamma_{Pv}}} - \left(\frac{P_{down}}{P_{up}} \right)^{\frac{\gamma_{Pv}+1}{\gamma_{Pv}}} \right] \right\}^{\frac{1}{2}} & , \left(\frac{P_{down}}{P_{up}} \right) \geq \left(\frac{2}{\gamma_{Pv}+1} \right)^{\frac{\gamma_{Pv}}{\gamma_{Pv}-1}} \\ C_d A P_{up} \left\{ \frac{\gamma_{Pv}}{RT_{up}} \left(\frac{2}{\gamma_{Pv}+1} \right)^{\frac{\gamma_{Pv}+1}{\gamma_{Pv}-1}} \right\}^{\frac{1}{2}} & , \left(\frac{P_{down}}{P_{up}} \right) < \left(\frac{2}{\gamma_{Pv}+1} \right)^{\frac{\gamma_{Pv}}{\gamma_{PV}-1}} \end{cases} \tag{3.15}$$

Additionally, the specific work Δh for isentropic real gas is shown in equation 3.16 [49] [49]

$$\Delta h = h_2 - h_1 = \frac{P_1}{\rho_1} \frac{\gamma_{Pv}}{\gamma_{Pv}-1} \left[\left(\frac{P_2}{P_1} \right)^{\frac{\gamma_{Pv}-1}{\gamma_{Pv}}} - 1 \right] \tag{3.16}$$

In order to check the behavior of the general isentropic model for the refrigerants that would be used in the cycle, the enthalpy predicted by the general isentropic model was compared to the properties from REFPROP. The results are shown in figure 3.6. It can be seen the enthalpy prediction of the general isentropic model is very accurate where the error percentage was below 1% 3.6b. The main advantages of using the general isentropic model are:

- Reducing computing time by using the general isentropic model as compared to calling the properties through REFPROP
- More accurate than the ideal gas model especially in a high-pressure ratio where the ratio of specific heats is not constant which is the case for transcritical cycles.

Hence, the general isentropic model will be used for the compressor and expander models.

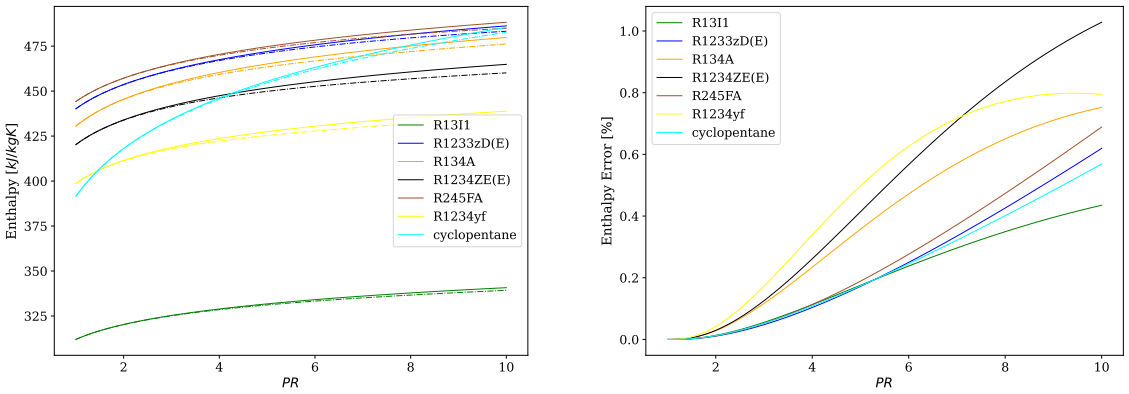

(a) Enthalpy Predicted by the General Model γ_{Pv} (Continuous Line), and REFPROP (Dashed Line)

(b) Enthalpy Error Percentages of the General Model γ_{Pv}, compared to REFPROP

Figure 3.6: Enthalpy Predicted by the General Isentropic Model γ_{Pv}, Ideal Gas Model γ, and REFPROP

3.1.2.4. Compressor Losses

Several loss models need to be accounted for in order to accurately predict the compressor's overall isentropic efficiency $\eta_{c,is}$. These losses are applied to the isentropic work which are the leak losses, heat losses, mechanical losses, and motor losses as can be seen in figure 3.7. This means the electrical work input to the motor driving the compressor will be higher than the required thermodynamic work to compress the fluid from P_1 to P_2.

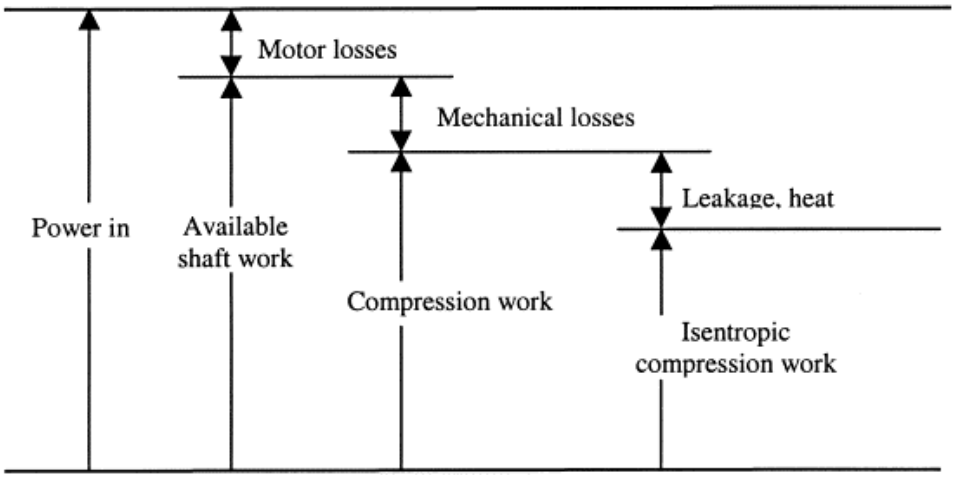

Figure 3.7: Compressor Losses [10]

The isentropic work is derived for the general isentropic model's specific work demonstrated earlier as seen in equation 3.17

$$\dot{W}_{c,is} = \dot{m}(h_{2,is} - h_1) = \dot{m}\frac{P_1}{\rho_1}\frac{\gamma_{Pv}}{\gamma_{Pv} - 1}\left[\left(\frac{P_2}{P_1}\right)^{\frac{\gamma_{Pv}-1}{\gamma_{Pv}}} - 1\right] \tag{3.17}$$

An empirical relation was developed by Park et al. [56] provided an empirical relation for motor and mechanical efficiencies in relation to frequency f based on experimental work done on variable scroll compressor in air conditioning unit as shown by equation 3.18

$$\begin{aligned}\eta_{mechanical} &= 0.8680 + 0.0048f - 4.4444 \times 10^{-5} f^2 \\ \eta_{motor} &= 0.6980 + 0.0013f + 4.1235 \times 10^{-5} f^2 - 4.8781 \times 10^{-7} f^3 + 1.4206 \times 10^{-9} f^4\end{aligned} \tag{3.18}$$

Additionally, the leak gaps that were introduced earlier will result in additional mass than ideal inside the compressor chambers. This additional mass increases the pressure inside the compression chambers which in turn increases the torque and therefore increases the shaft power required to drive the compressor. This will be demonstrated later in the Results and Discussion Section 3.1.4.

Finally, flow restriction occurs at the intake and discharge section of the compressor due to the opening and closing of the suction and discharge chamber geometry. The opening area is parabolic as will be described later which act as an orifice restricting the flow in the isentropic nozzle equation 3.15. In the discharge, the restriction of the flow results in an over-compression of the gas beyond the required discharge pressure which results in additional shaft power required.

With this, the overall isentropic efficiency is calculated based on the shaft power as shown in equation 3.29

$$\eta_{c,is} = \eta_{mechancial} \times \eta_{motor} \frac{\dot{W}_{c,is}}{\dot{W}_{shaft\ power}} \tag{3.19}$$

3.1.2.5. Compressor Logic

Compressor logic was developed to help understand how the compressor model works which can be seen in Figure 3.8. The logic starts with the rotation angle $\theta = 0$ along with the input parameter listed in table 3.2 where the geometric model is applied to build the compressor geometry. An assumption of the chamber pressure is made to find the flow and leakage model from which the mass inside the chamber is calculated followed by the chamber pressure. The chamber pressure is iterated over until the tolerance criteria are met. A new rotation angle is used where the logic repeats until the final rotation angle is reached $\theta = \theta_{end}$.

Since the discharge process is complex, a discharge logic was developed as can be seen in Figure 3.9. At the start of the discharge process, two discharge chambers exist which are V_{00} & V_{01} as mentioned earlier. The pressure in these two chambers is different which is noted as P_{00} & P_{01} that would also be different from the discharge pressure P_d. Based on these three pressure, the flow and leak model would apply to determine the mass flow rate in and out of the chambers. Pressure P_{00} doesn't change much because it is connected with the compressor discharge P_d. However, the pressure P_{01} would vary significantly and would be the source for the overshoot in pressure at the discharge process. Eventually, the pressure P_{00} would equalize with the pressure P_{01} to form one pressure which is P_0.

3.1.3. Model Validation

In order to ensure that the model provides accurate results, the model has to be validated which was done by comparing the results obtained from the model against the one from the original paper [76] in addition to results obtained using Bell et.al [6] open source Positive Displacement compressor model (PDSim). Throughout the validation, the paper values are shown in (circle) marks while the model one is the (line) ones.

3.1.3.1. Parameters

The paper was modeled using a refrigerant (R22) as the working fluid with the parameters shown in table 3.2. The results obtained by the model compared to the results from the paper are shown in table 3.3.

Table 3.3: Geometric Model Validated Parameters

Parameter	Symbol	Paper [76] [Unit]	Model
Theoretical Suction Volume	V_s	$68.7[cm^3]$	$68.7[cm^3]$
Theoretical Discharge Pressure	V_d	$26.7[cm^3]$	$26.7[cm^3]$
Radius of Starting Circular Arc	r_a	$7.2[mm]$	$7.2[mm]$
Clearance Volume	V_c	$2[cm^3]$	$2[cm^3]$
Operating Pressure Ratio	ϵ_p	2.83	2.83
Built In Volumetric Ratio	V_r	2.573	2.572

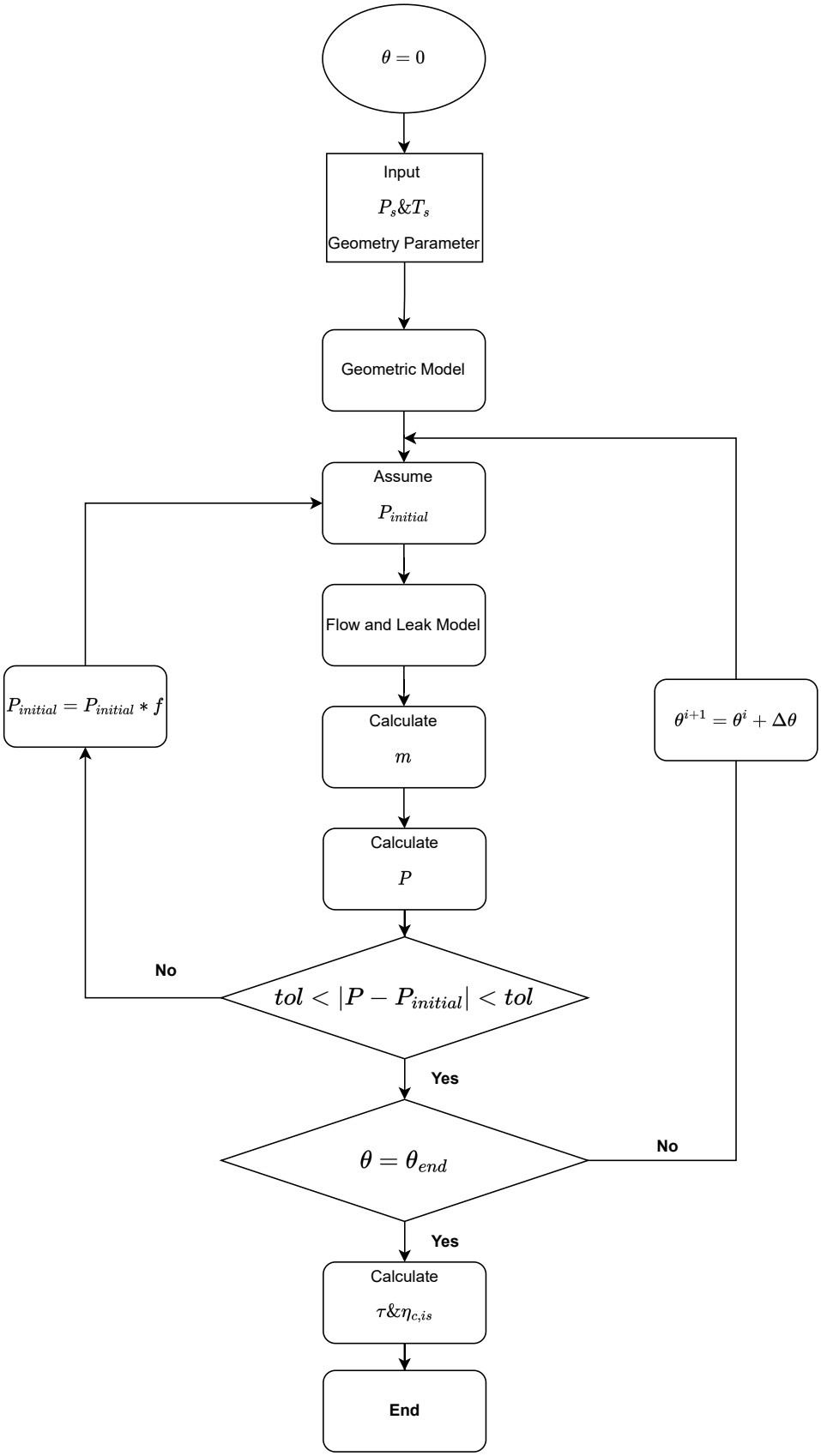

Figure 3.8: Scroll Compressor Logic

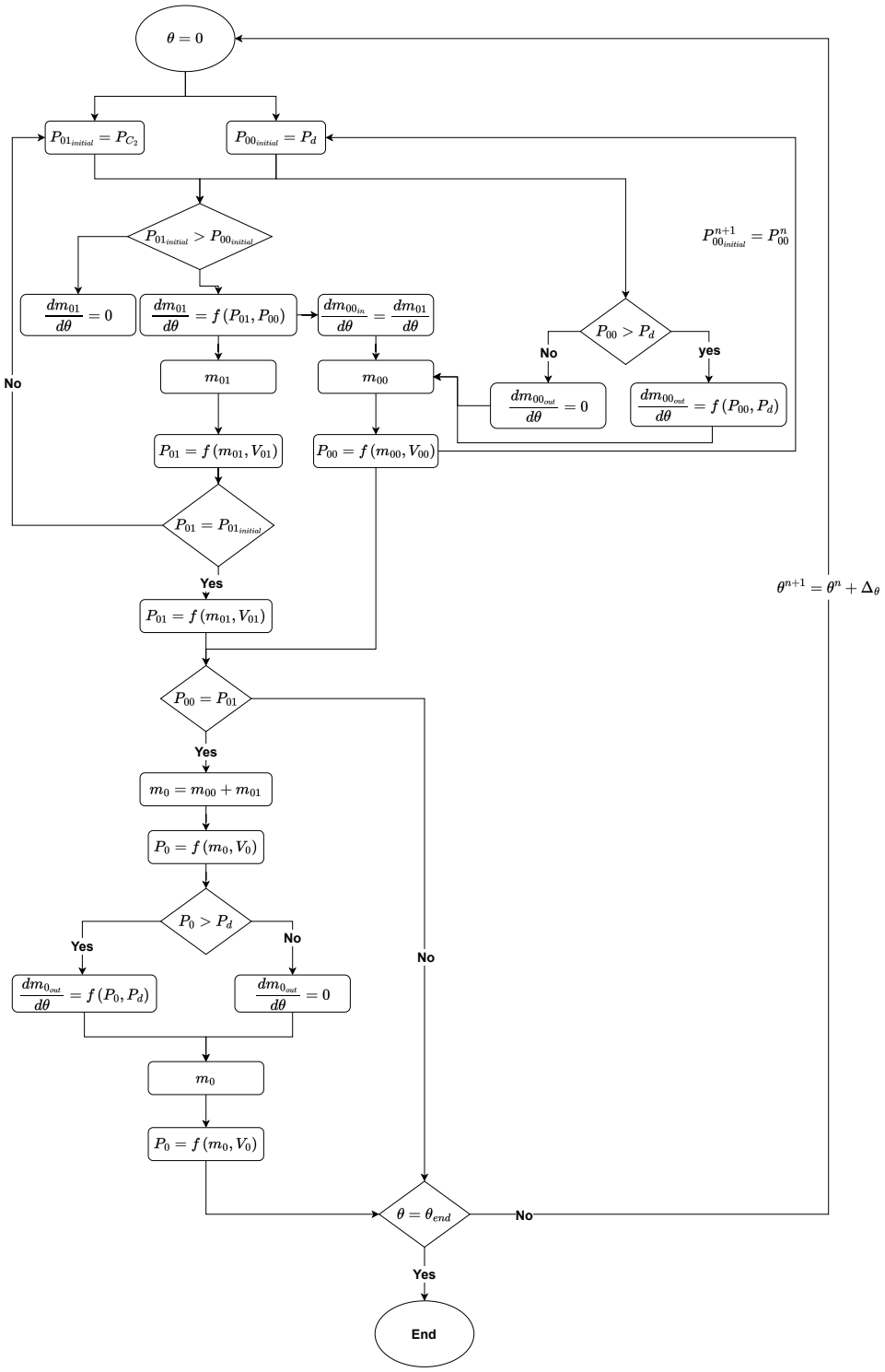

Figure 3.9: Scroll Compressor Discharge Logic

3.1.3.2. Volume and Areas

The chamber volumes were validated against the paper which develops over the entire rotation starting from the suction chamber to the discharge chamber as can be seen in figure 3.10. The volume of each chamber is divided by the suction volume.

The inlet area A_n, discharge exit area A_d, and discharge port area A_p are validated against

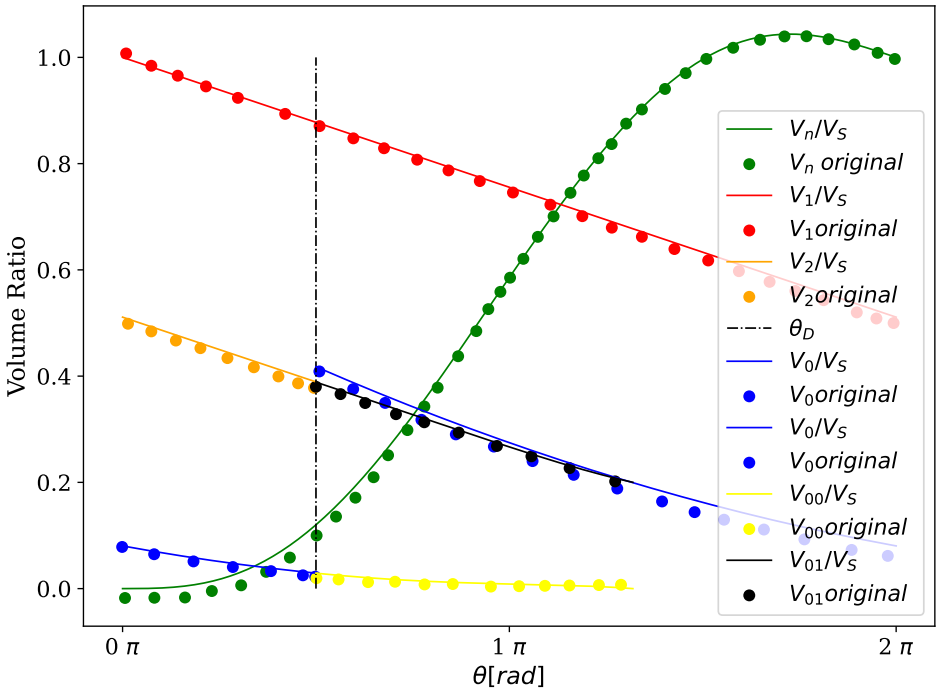

Figure 3.10: Validation of Compressor Volumes

the paper where the areas divided by hr as can be seen in figure 3.11

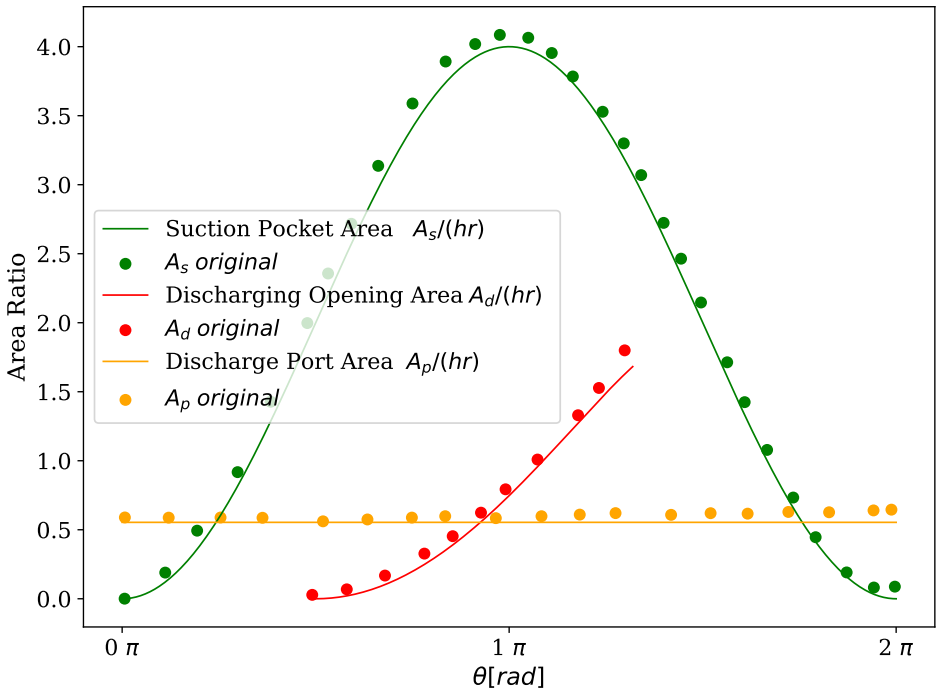

Figure 3.11: Validation of Compressor Area

3.1.3.3. Pressure and Torque

The developed pressure in the compressor chamber was validated without and with the leak model as can be seen in Figure 3.12a and 3.12b respectively.

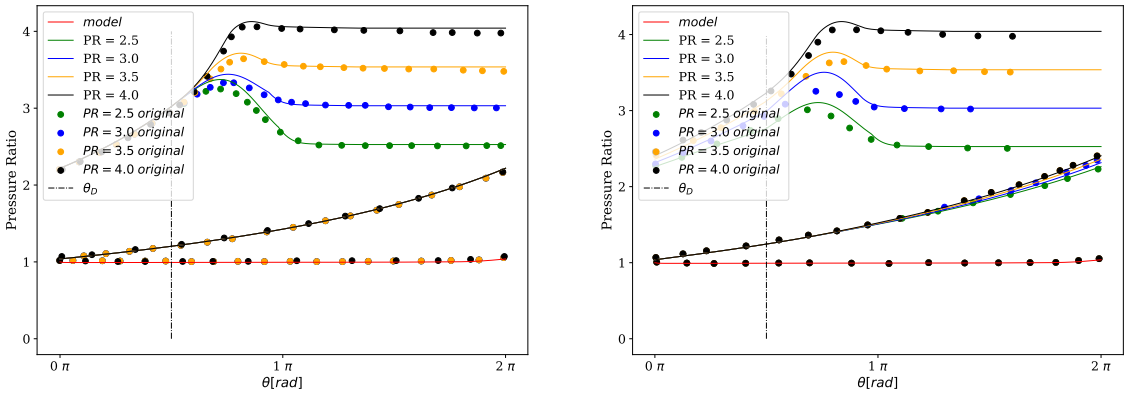

(a) Validation of Compressor Pressure without Leak

(b) Validation of Compressor Pressure with Leak

Figure 3.12: Validation of Compressor Pressure with and without Leak

The torque generated by the pressure inside the volume is validated as can be seen in figure 3.13. With this, the required shaft power is calculated as described earlier.

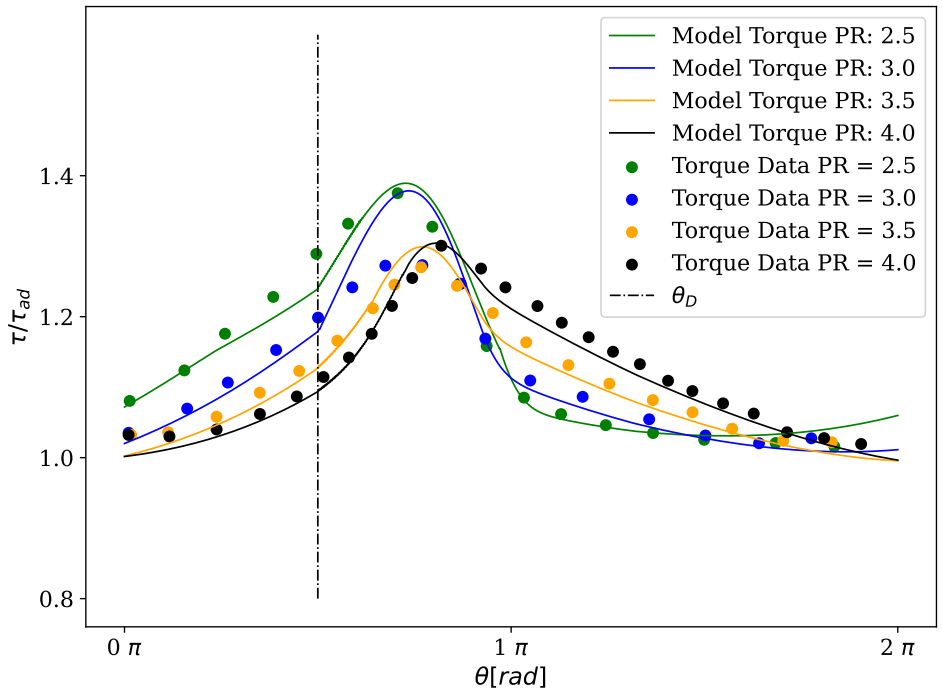

Figure 3.13: Validation of Compressor Torque

3.1.3.4. Isentropic Efficiency

The main parameter of the compressor model is the isentropic efficiency of the model. Therefore, the model was validated considering multiple gaps as can be seen in Figure 3.14a as well as rotation speed as can be seen in Figure 3.14b.

Additionally, the compressor was also modeled with (PDSim) which is an open-source software developed by Bell et al. [6]. With the model, motor and mechanical efficiency were

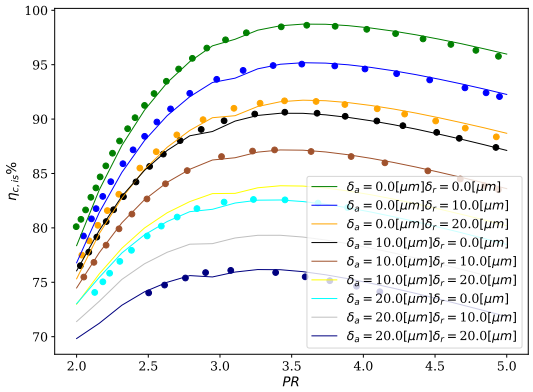

(a) Validation of Compressor Isentropic Efficiency for Multiple Gaps. The Dots Represent The Paper Values While The Continuous Line Represents The Model Ones

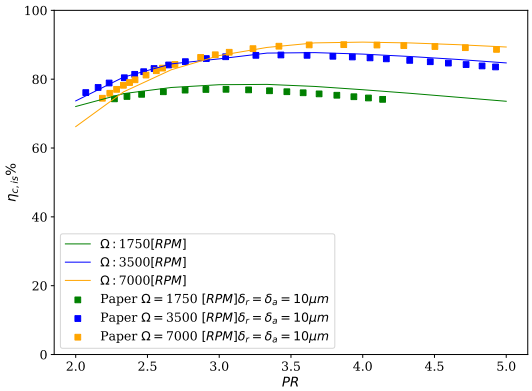

(b) Validation of Compressor Isentropic Efficiency with Rotation Speed

Figure 3.14: Validation of Compressor Efficiency with Gaps and Rotation Speed

taken into consideration since the software accounted for them. However, the PDSim model account for adiabatic losses while the model doesn't. The efficiency was modeled under multiple rotation speeds as can be seen in Figure 3.15

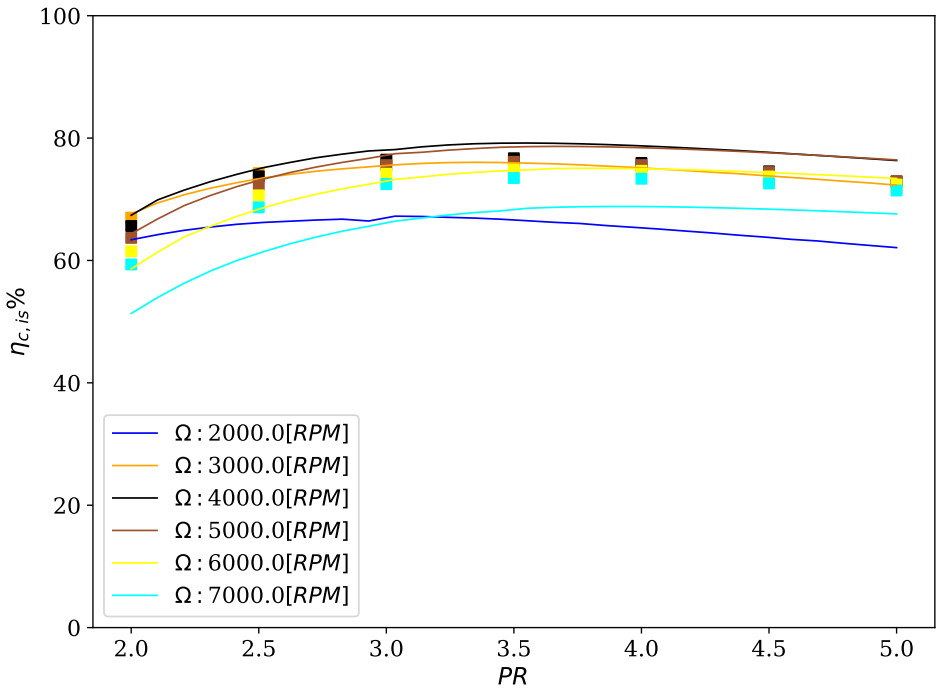

Figure 3.15: Validation of Compressor Isentropic Efficiency with PDSim [6] Where the Continuous Lines Represent the Model Values while the Squares Represent the PDSim ones

3.1.4. Results and Discussion

In this section, the results attained from the model will be detailed and discussed to better understand the performance of the compressor. This will be done by describing the volume and pressure development, mass and mass flow, losses, fluids effect, and efficiency.

3.1.4.1. Volume and Pressure Development

As shown earlier, the volume starts increasing from the inlet until it reaches a maximum value and then starts to decrease slightly by the end of the intake cycle. Because of this decrease, the pressure inside the intake chamber starts to increase above the suction pressure as can be seen in 3.16. Beyond the suction chamber, the compression process starts where the volume starts to decrease almost linearly which results in an increase of the pressure. Ideally, the built-in pressure ratio ϵ_p should match the operating pressure ratio PR in order to avoid over or under-compression losses at the end of the compression process. This means that the pressure at the end of the compression matches the discharge pressure. However, this is not always the case, and additional compression or expansion is required to reach the outlet pressure. This can be seen in figure 3.16b where multiple pressure ratios were demonstrated by having the inlet pressure fixed. Additionally, the temperature develops in a similar manner to pressure from suction to discharge as can be seen in Figure 3.16c.

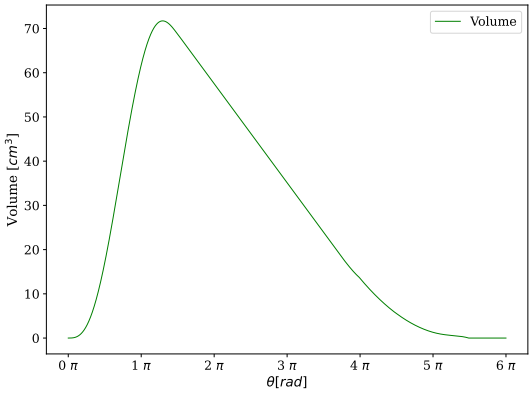

(a) Volume Development Over the Compressor Rotation Angle

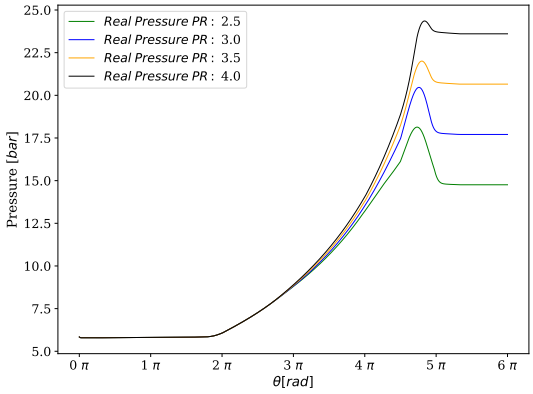

(b) Pressure Development Over the Compressor Rotation Angle Where Inlet Pressure is Fixed and PR is Varied. Discharge Over-compression is Demonstrated

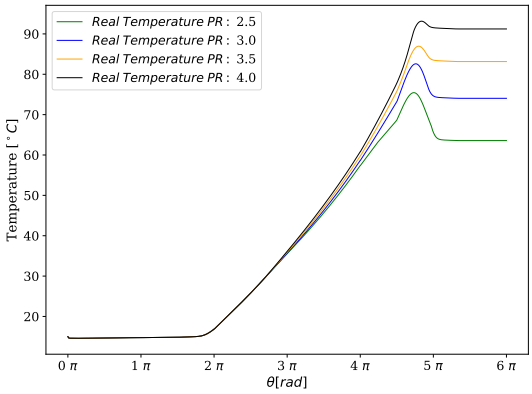

(c) Temperature Development Over the Compressor Rotation Angle

Figure 3.16: Pressure, Temperature, and Volume Development Over the Compressor Rotation Angle. (a) Volume Development with Rotation Angle. (b) Pressure Development with Rotation Angle. (c) Temperature Development with Rotation Angle

3.1.4.2. Losses

The main losses in the compressor are mechanical, motor, leaks, and flow restrictions. The losses labeled as 'others' contain the leak as well as the flow restriction losses. It can be seen in Figure 3.17 that the main sources of losses are the leaks and flow restrictions and the

adiabatic losses which contribute to $30-50\%$ of the losses while mechanical account for the other major part. It also can be seen from the breakdown that the losses change with rotation speed where at a low rotation speed of around $\Omega = 3000RPM$, motor losses are low while they increase at a higher rotation speed of $\Omega = 7000RPM$. Finally, as anticipated, the leak and flow restriction losses (other losses) would be lower close to the build-in pressure ratio while they increase away from the build-in pressure ratio.

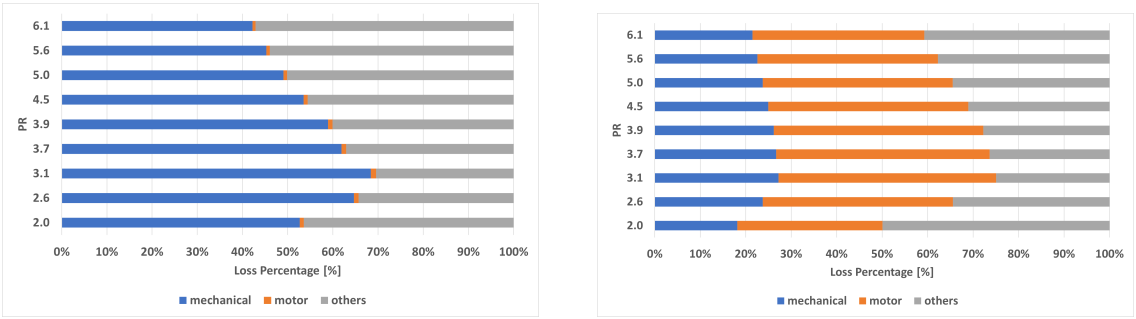

(a) Compressor Losses with $\delta_r = \delta_a = 15\mu m$ and $\Omega = 3000RPM$

(b) Compressor Losses with $\delta_r = \delta_a = 15\mu m$ and $\Omega = 7000RPM$

Figure 3.17: Compressor Losses Breakdown for Mechanical, Motor, and Other Losses for rotation speed (a) $\Omega = 3000RPM$ (b) $\Omega = 7000RPM$ with Gap $\delta_a = \delta_r = 15\mu m$

3.1.4.3. Isentropic Efficiency

Isentropic Efficiency is the parameter that is mostly looked at in the compressor model. It has been shown that isentropic efficiency is impacted by multiple factors including rotation speed, pressure ratio, and leakage gaps.

From Figure 3.14a, it can be seen that gaps negatively impact the isentropic efficiency where higher gaps will result in more leaks which will result in lower isentropic efficiency. Additionally, it can be seen radial gap δ_a has a higher impact on isentropic efficiency than flank gap δ_r which is attributed to the radial area being higher than the flank area which will result in more leaks as compared to the flank one. Multiple models are found in the literature to try and quantify the gap in a scroll compressor with multiple values presented. For the purpose of this paper, a gap of $\delta_r = \delta_a = 15\mu m$ will be used.

3.1.4.4. Fluid Effects

With the compressor model, multiple fluids were tested which would be used in the system. The results are demonstrated in Figure 3.18. It can be seen in the figures that there is an optimum pressure ratio of around $PR = 3$ which is attributed to the build-in pressure ratio where the isentropic efficiency is maximum. Additionally, increasing the rotation speed will result in higher isentropic efficiency up until a point where the effect becomes less apparent which is around $\Omega = 3000RPM$ while at a higher rotation speed of around $\Omega = 7000RPM$ where isentropic efficiency drops due to the additional losses in the motor and mechanical. Additionally, the rotation speed has an effect on the best operating pressure ratio where a higher rotation speed results in a higher optimum operating pressure ratio evidenced by the shift of the highest efficiency point to the right in the figure. Finally, fluids don't have a huge effect on isentropic efficiency as they all have a maximum efficiency of around $\eta_{c,is} = 70-80\%$.

3.2. Expander Model

Similar to the compressor model, an expander model was developed to account for the expander in the heat engine cycle of the pumped thermal energy storage. A geometric ex-

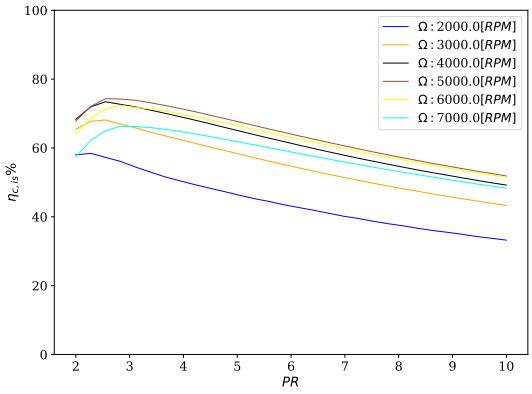

(a) R290 Compressor Isentropic Efficiency Variation with Rotation Speed and Pressure Ratio

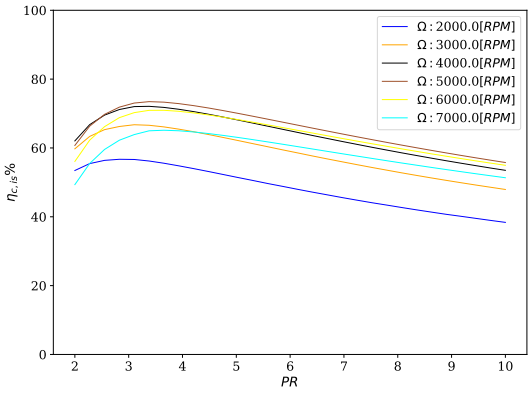

(b) R1233ZD(E) Compressor Isentropic Efficiency Variation with Rotation Speed and Pressure Ratio

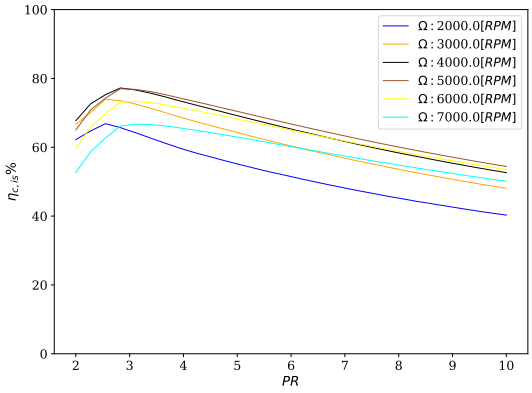

(c) R1234yf Compressor Isentropic Efficiency Variation with Rotation Speed and Pressure Ratio

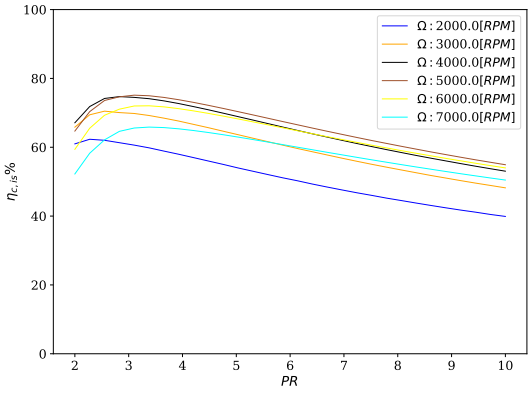

(d) R1234ZE(E) Compressor Isentropic Efficiency Variation with Rotation Speed and Pressure Ratio

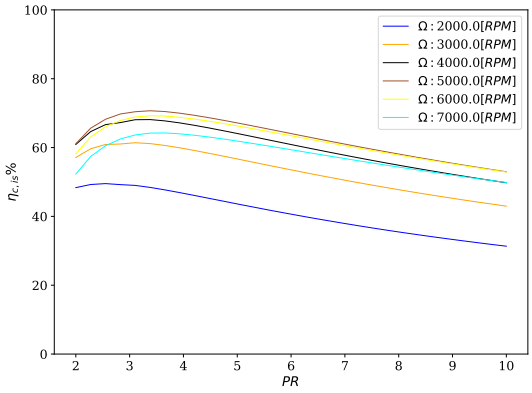

(e) Cyclopentane Compressor Isentropic Efficiency Variation with Rotation Speed and Pressure Ratio

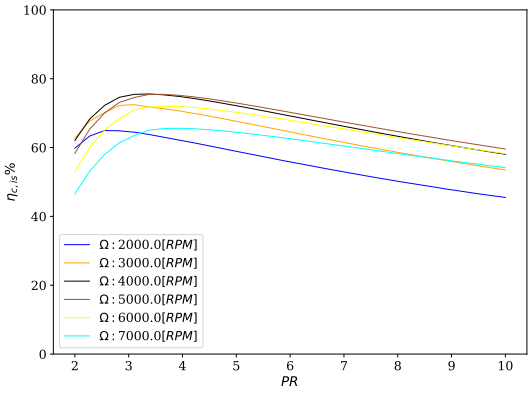

(f) R13I1 Compressor Isentropic Efficiency Variation with Rotation Speed and Pressure Ratio

Figure 3.18: Compressor Isentropic Efficiency Variation with Rotation Speed and Pressure Ratio for Different Fluids (a) R290. (b) R1233ZD(E). (c) R1234yf. (d) R1234ZE(E). (e) Cyclopentane. (f) R13I1

pander model using a modified compressor to work as an expander. Since the expander uses the same geometry as the compressor, then the geometric model would work in the same manner just in reverse. In order to do so, first the scroll geometry will be demonstrated. Secondly, the governing thermodynamic equation for mass, and energy will be detailed. Thirdly, model validation will be discussed. Finally, results and discussion will be provided.

3.2.1. Geometry

The geometric model of the scroll compressor was used to develop the geometric model of the expander by reversing the rotation. This was achieved through the inclusion of $2\pi - \theta)$ in the compressor model to account for the expander rotation in the opposite direction. Additionally, the discharge port of the compressor will work as an inlet to the expander while the inlet to the compressor will work as the discharge to the expander. The chambers' volumes will be the same as that of the compressor. However, there are a few modifications that need to account for the development of the volumes with respect to rotation speed.

Similar to the compressor, the number of contact points needs to be determined in order to identify the number of expansion chambers. With the rotation of the involute, the number of pairs of contact points (n) where the stationary meets the rotating involute is determined through equation 3.20. Through the number of contact points, the number of pairs of compression chambers (N) can also be determined.

$$\begin{aligned} n &= INT\left[\frac{\phi_{end} - (2\pi - \theta) - \phi_a}{2\pi} + 1\right] \\ N &= n - 1 \end{aligned} \tag{3.20}$$

The involute angle for the contact points (ϕ_i) is determined by equation 3.21 where i is the index of the contact point starting from the center of the scroll.

$$\phi_i = \phi_{end} - (2\pi - \theta) - 2\pi(n - i) \tag{3.21}$$

3.2.1.1. Volume Development

Considering all the previous parameters for the compressor, there are three types of chambers with each chamber having its own volume. The volume numbering is maintained similarly to those of the compressor to avoid confusion. However, with the expander, the intake volumes would be the discharge volume of the expander, and so on. Therefore, the intake volume V_0 would split into two chambers $V_{00}\ and\ V_{01}$. Next the expansion chambers $V_1, V_2 \& V_3$ will follow. Three expansion chambers are demonstrated here to match the one from the validation model [41]. Finally, the discharge chamber will be V_n. The intake process end with the expansion angle of (θ_e) after which there are three pairs of expansion chambers $V_1, V_2 \& V_3$ and one intake chamber V_0 and before which there is only two expansion $V_1 \& V_2$ and two intake $V_{00} \& V_{01}$. This is summarized in table 3.4 and can be seen in figure 3.19.

Table 3.4: Scroll Expander Chambers

	Chambers Numbers						
Condition	V_n	V_1	V_2	V_3	V_0	V_{00}	V_{01}
Before θ_e	X	X	X	-	-	X	X
After θ_e	X	X	X	X	X	-	-

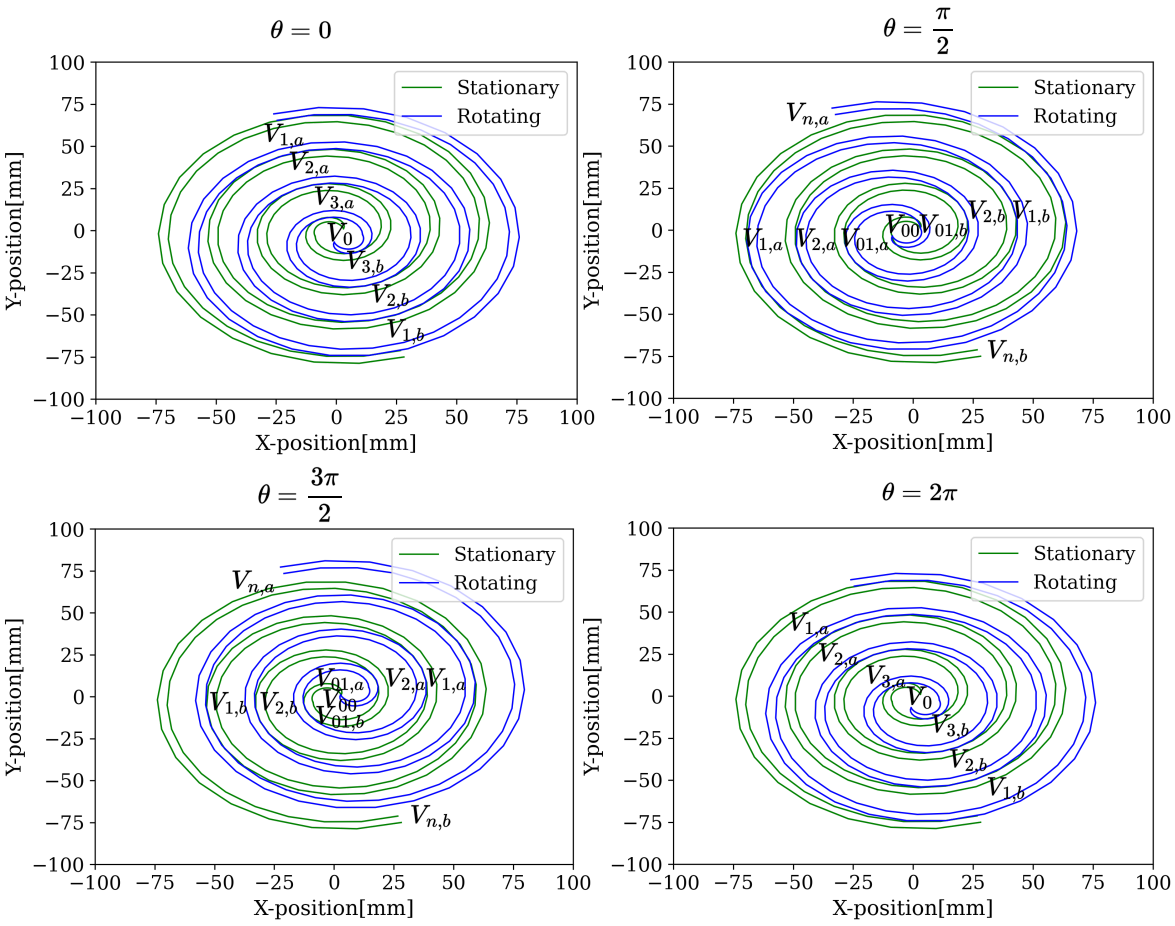

Figure 3.19: Scroll Expander Chambers at Different Rotation Angle θ

$$
\begin{aligned}
V_n &= har[(2\pi-\theta)(2\phi_{end}-\theta-\pi)-2(\phi_{end}-\pi+\alpha)\sin(2\pi-\theta) \\
&\quad -(\frac{\pi}{2}-\alpha)\sin 2(2\pi-\theta)+2(1-\cos(2\pi-\theta))] \\
V_1 &= 2\pi har(2\phi_1+\pi) \\
V_2 &= 2\pi har(2\phi_2+\pi) \\
V_3 &= 2\pi har(2\phi_3+\pi) \\
V_0 &= har(\phi_1-\phi_a)(\phi_1+\phi_a-\pi)+V_c \\
V_c &= hr_a^2\left[\pi-\sin^{-1}\frac{2a}{r_a}-\frac{2a}{r_a}\right] \\
V_{00} &= hr_a\left[r_a\beta-(r_a-w_d)\sin\beta\right] \\
\beta &= \pi-\cos^{-1}\left[\frac{r_a-r+r\cos(\theta-\theta_d)}{r_a-w_d}\right]-\sin^{-1}\left(\frac{2a}{r_a}\right) \\
w_d &= r_a-\sqrt{r^2+(r_a-r)^2+2r(r_a-r)\cos(\theta-\theta_d)} \\
V_{01} &= V_0-V_{00}
\end{aligned}
\tag{3.22}
$$

With the listed volumes above, the theoretical discharge volume (V_d) can be determined by setting $\phi_i = \phi_e - 2\pi$ in V_1 equation and suction volume (V_s) by setting $\phi_i = \phi_a$ in the same

equation. Additionally, the build-in volumetric ratio ($V_r = \frac{V_d}{V_s}$) and swept volume ($V_{sw} = V_d$).

The geometric parameters used to model the compressor are shown in table 3.5 to match the one used in the paper [41]

Table 3.5: Expander Geometric Parameter [41]

Parameter	Symbol	Value [Unit]
Base Circle	a	$3.264[mm]$
Wrap Thickness	b	$4.08[mm]$
Height	h	$28.65[mm]$
Involute Starting Angle	ϕ_a	$3.5[rad]$
Involute End Angle	ϕ_{end}	$23.92[rad]$
Suction Port Diameter	d	$10[mm]$
Suction Pressure	P_s	$7[bar]$
Suction Temperature	T_s	$145.6[°C]$
Rotation Speed	Ω	$1771 - 2660[RPM]$
Flow Coefficient	C_d	0.66
Flank Gap	δ_r	$70\mu m$
Raidal Gap	δ_a	$0\mu m$
Pressure Ratio	PR	$2 - 10$
Fluid	[-]	R123

Volumetric ratio development at each rotation is shown in Figure 3.20a with each volume divided by V_d. At the first rotation, suction occurs where the suction chamber $V_{00}\&V_{01}$ starts increasing to allow for fluid to enter the chamber until the end of the suction process where $\theta = \theta_d$. After which expansion starts from V_3 followed by V_2 and finally V_1. Finally, the discharge process starts with V_n at maximum volume and it starts decreasing discharging the fluid.

Following the fluid from the inlet to the outlet over the entire rotation, the volume development can be seen in figure 3.20b.

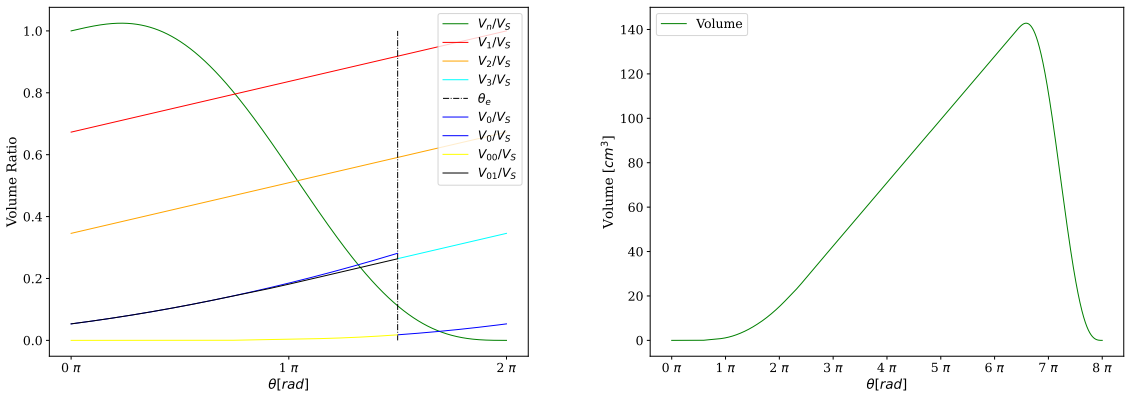

(a) Scroll Expander Volumetric Ratio

(b) Expander Volume Development Over Entire Rotation

Figure 3.20: Scroll Expander Volume Development Through the Expansion Process

3.2.1.2. Area Development and Gap

The area and gap for the expander are similar to that of the compressor. The suction pocket area A_s is the area at which the fluid enters the compressor while the discharge area A_d is the area at which the fluid exit the expander. The suction port area A_p is the port area of the inlet pipe. The development of the different areas with the rotation angle can be seen

in Figure 3.21. The lower value between the suction port area A_p and suction pocket area A_s will govern the area since that would be the area restricting the flow the most.

For the gap, it is exactly as the one described for the compressor where the flank is the gap between the two scroll walls and the radial is the gap at the tip.

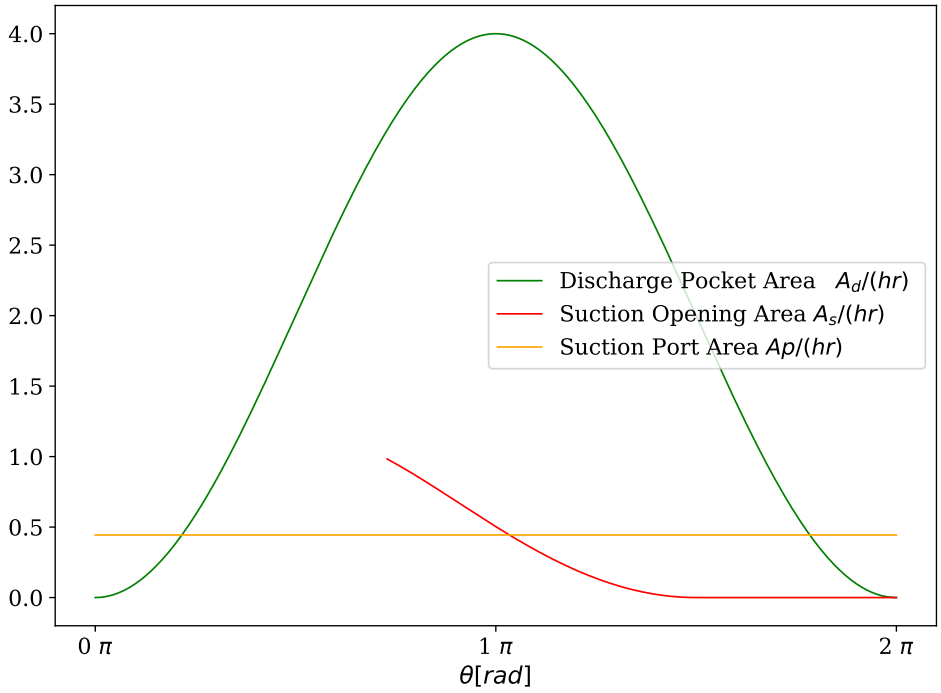

Figure 3.21: Scroll Expander Area Development

3.2.2. Thermodynamic Model

In this section, the governing thermodynamic equation will be detailed. The general isentropic equation will be followed as described earlier in the compressor section. This will be done by first detailing the mass conservation. Secondly, the governing energy equations will be provided. Thirdly, the expander losses will be discussed. Finally, the logic followed in the expander model will be provided.

3.2.2.1. Mass Flowrate

The mass flow rate in $\dot{m}_{in}$ and out $\dot{m}_{out}$ of the expander is expressed by equation 3.23 where $\dot{m}_{leak}$ is the mass leaking from one chamber to the other through the expander gaps:

$$\begin{aligned} \dot{m}_{in} &= \frac{\mathrm{d}m_{in}}{\mathrm{d}t} - \frac{\mathrm{d}m_{leak}}{\mathrm{d}t} \\ \dot{m}_{out} &= \frac{\mathrm{d}m_{out}}{\mathrm{d}t} - \frac{\mathrm{d}m_{leak}}{\mathrm{d}t} \end{aligned} \tag{3.23}$$

The mass flow in and out as well as leakage flow is represented by flow through a one-dimensional isentropic compressible nozzle following equation 3.24 where A is the cross-sectional area, C_d is a flow correction factor based on the experiment, R is the universal gas

constant, γ_{Pv} is general isentropic exponent [49] which is similar to that used in the compressor model where the condition shows the choking limit of the flow through the nozzle.

$$\dot{m} = \begin{cases} C_d A P_{up} \left\{ \frac{2\gamma_{Pv}}{R(\gamma_{Pv}-1)T_{up}} \left[\left(\frac{P_{down}}{P_{up}} \right)^{\frac{2}{\gamma_{Pv}}} - \left(\frac{P_{down}}{P_{up}} \right)^{\frac{\gamma_{Pv}+1}{\gamma_{Pv}}} \right] \right\}^{\frac{1}{2}} & , \left(\frac{P_{down}}{P_{up}} \right) \geq \left(\frac{2}{\gamma_{Pv}+1} \right)^{\frac{\gamma_{Pv}}{\gamma_{Pv}-1}} \\ C_d A P_{up} \left\{ \frac{\gamma_{Pv}}{RT_{up}} \left(\frac{2}{\gamma_{Pv}+1} \right)^{\frac{\gamma_{Pv}+1}{\gamma_{Pv}-1}} \right\}^{\frac{1}{2}} & , \left(\frac{P_{down}}{P_{up}} \right) < \left(\frac{2}{\gamma_{Pv}+1} \right)^{\frac{\gamma_{Pv}}{\gamma_{PV}-1}} \end{cases} \tag{3.24}$$

3.2.2.2. Energy Equation

The energy model followed in the expander model is the same as that followed in the compressor one derived from the first law of thermodynamics with the following assumptions:

- Kinetic and potential energy are negligible.
- The expander is assumed to be adiabatic where the loss to the environment is negligible $\dot{Q} = 0$.
- The model is assumed to be at a steady state which means $\dot{U} = 0$

Unlike in the compressor, the enthalpy difference will be positive which indicates output power as can be seen in equation 3.25.

$$\begin{aligned} \dot{U} &= \dot{Q} - \dot{W} + \dot{m}_{in} h_{in} - \dot{m}_{out} h_{out} + K.E + P.E \\ 0 &= -\dot{W} + \dot{m}_{in} h_{in} - \dot{m}_{out} h_{out} \\ \dot{W} &= \dot{m}_{in} h_{in} - \dot{m}_{out} h_{out} \\ \dot{W} &= \dot{m}(h_{in} - h_{out}) \end{aligned} \tag{3.25}$$

Additionally, the shaft power can be expressed in terms of instantaneous torque τ driving the shaft with a rotating speed ω as can be seen in equation 3.26.

$$\begin{aligned} \dot{W}_{shaft\ power} &= \frac{\omega}{2\pi} \int_0^{2\pi} \tau \, d\theta \\ \tau &= har \left\{ (2\phi_1 - \pi)(P_s - P_d) + 4\pi \sum_{j=1}^{n-1} (P_j - P_d) \right\} \end{aligned} \tag{3.26}$$

The specific work for the isentropic expander model using the general isentropic exponent can be derived similarly to that of the compressor as seen in Equation 3.27. With that, the isentropic power of the expander is shown in eqution

$$\Delta h = (h_2 - h_1) = -\frac{P_1}{\rho_1} \frac{\gamma_{Pv}}{\gamma_{Pv} - 1} \left[\left(\frac{P_2}{P_1} \right)^{\frac{\gamma_{Pv}-1}{\gamma_{Pv}}} - 1 \right] \tag{3.27}$$

$$\dot{W}_{t,is} = \dot{m}(h_1 - h_{2,is}) = -\dot{m} \frac{P_1}{\rho_1} \frac{\gamma_{Pv}}{\gamma_{Pv} - 1} \left[\left(\frac{P_2}{P_1} \right)^{\frac{\gamma_{Pv}-1}{\gamma_{Pv}}} - 1 \right] \tag{3.28}$$

3.2.2.3. Expander Losses

Similar to the compressor model, the expander experience similar losses which impact the overall isentropic efficiency $\eta_{t,is}$. These losses are applied to the isentropic work which are the leak losses, heat losses, mechanical losses, and generator losses as can be seen in figure 3.22. This means the electrical work output of the generator driven by the scroll expander will be lower than that of the isentropic power.

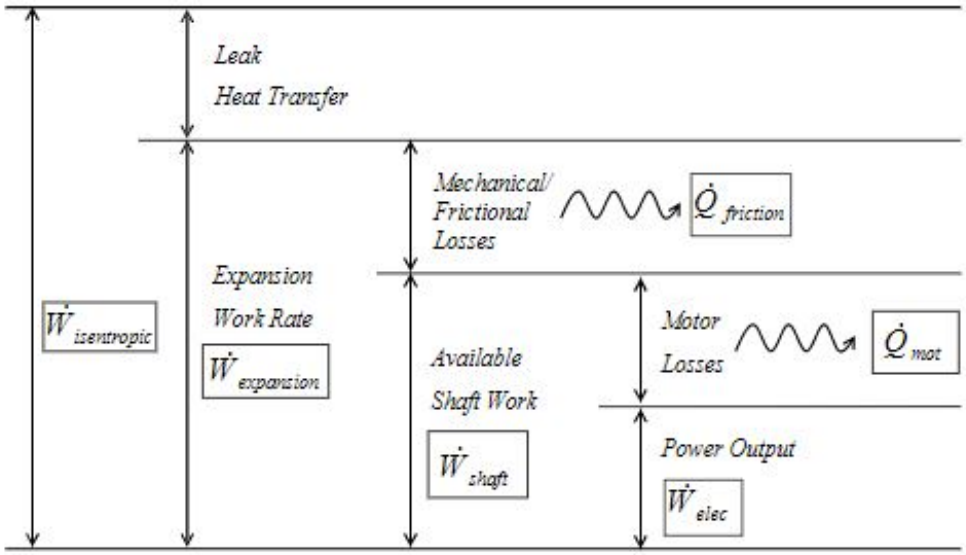

Figure 3.22: Scroll Expander Losses [41]

The empirical relation that was developed by Park et al. [4] to calculate the mechanical and motor efficiency of scroll compressors based on the frequency f of the compressor shown earlier in equation 3.18 will also be used for the expander model since the motor can also operate as a generator.

Additionally, the leak gaps that were introduced earlier will result in lower mass than ideal inside the expander chambers which will result in lower torque and therefore lower power output.

Finally, flow restriction as well as operating at a different pressure ratio than the build-in one result in additional losses which need to be accounted for to have an accurate prediction of the efficiency.

With this, the overall isentropic efficiency is calculated based on the shaft power as shown in equation 3.29

$$\eta_{T,is} = \eta_{mechancial} \times \eta_{generator} \times \frac{\dot{W}_{shaft\ power}}{\dot{W}_{t,is}} \tag{3.29}$$

3.2.2.4. Expander Logic

The logic followed in the expander is the same one followed in the compressor where inlet parameters including the geometry and suction pressure and temperature along with discharge pressure are specified as can be seen in Figure 3.8. An assumption of the pressure

inside the expander chamber is assumed and is used for the flow and leak models to calculate the chamber mass. The mass is used to determine the chamber pressure which is compared with the assumed one and iterated over until tolerance is reached. Finally, the torque along with power and efficiency are determined based on the losses model.

3.2.3. Model Validation

The model is mainly validated using the model developed under [41] where an expander working with refrigerant R123 was demonstrated experimentally. The geometric parameters shown in table 3.5 are used in the simulation. The validation is made by comparing the results of the model isentropic efficiency with the one shown in the paper which can be seen in Figure 3.23. From the results, it can be seen that the model overestimates the expander isentropic efficiency slightly due to the adiabatic assumption of the model.

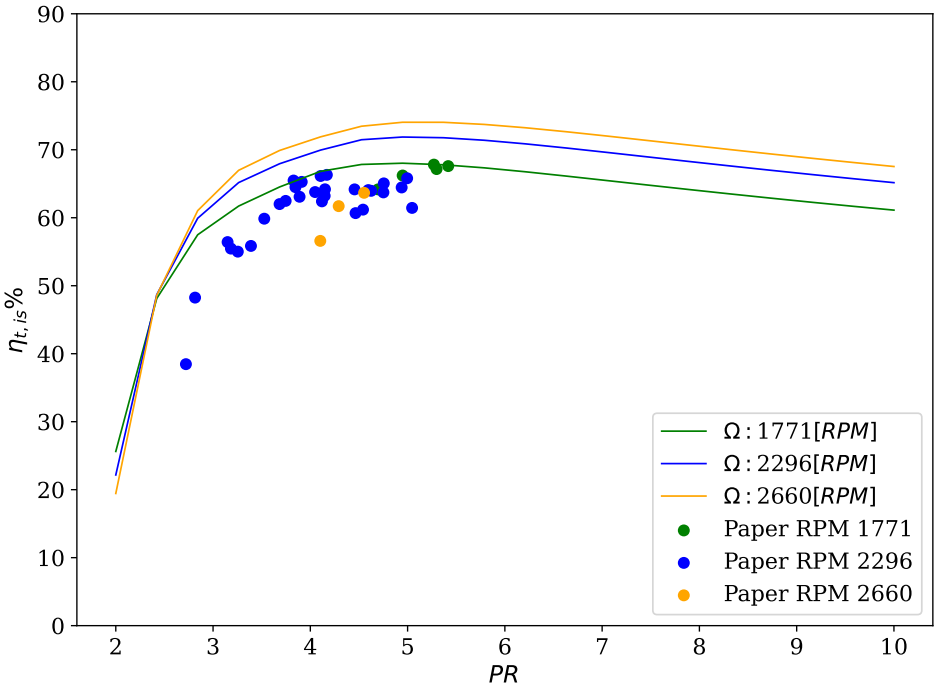

Figure 3.23: Validation of Expander Efficiency

3.2.4. Results and Discussion

In this section, the results attained from the model will be detailed and discussed to better understand the performance of the expander. This will be done by describing the volume and pressure development, mass and mass flow, torque and power, fluids effect, and efficiency.

3.2.4.1. Volume and Pressure Development

As shown earlier, the volume starts increasing from the inlet through the intake until the end of the intake cycle. Afterward, the expansion process starts where the volume starts increasing almost linearly until the discharge angle is reached. At the discharge, the pressure starts decreasing to expel the fluid out of the discharge chamber as can be seen in Figure 3.24a.

For the pressure, from the intake, the pressure drops slightly below intake due to the expansion of the intake chamber and flow restriction until the expansion angle is reached. After which, the expansion process starts where the pressure drops due to the gradual decrease

of the chamber volume. Depending on the discharge pressure, under or over-expansion occurs which would result in losses as will be explained later. Under expansion occurs when the pressure at the end of the last expansion chamber is above the discharge pressure while over expansion occurs when the pressure at the end of the expansion chamber is below the discharge pressure. This is a result of a mismatch between the build-in pressure ratio and the operating pressure ratio as can be seen in Figure 3.24b.

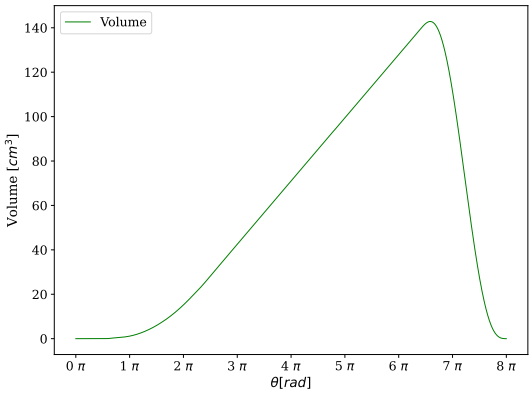

(a) Expander Volume Development with Rotation Angle

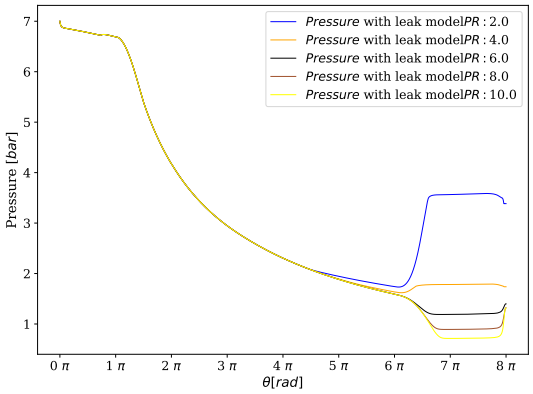

(b) Expander Pressure Development with Rotation Angle Where Inlet Pressure Is Fixed and PR is Varied

Figure 3.24: Pressure and Volume Development Over the Expander Rotation Angle

3.2.4.2. Losses

Similar to the compressor model, losses for the expander are shown in Figure 3.25 for rotation speeds of $\Omega = 4000RPM$ and $\Omega = 7000RPM$. The breakdown shows similar behavior which is to be expected since the motor and mechanical losses were simulated using the same losses models prescribed in equation 3.18.

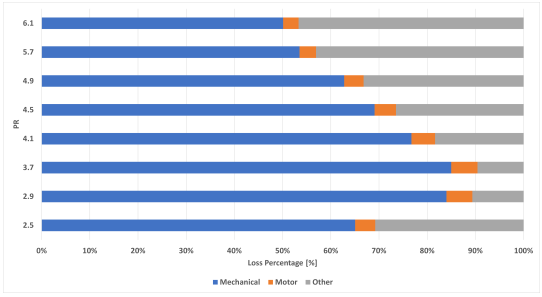

(a) Expander Losses with $\delta_r = \delta_a = 15\mu m$ and $\Omega = 4000RPM$

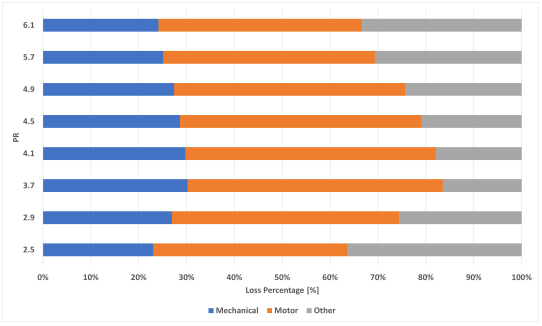

(b) Expander Losses with $\delta_r = \delta_a = 15\mu m$ and $\Omega = 7000RPM$

Figure 3.25: Expander Losses Breakdown for Mechanical, Motor, and Other Losses for rotation speed (a) $\Omega = 4000RPM$ (b) $\Omega = 7000RPM$ with Gap $\delta_r = \delta_a = 15\mu m$

3.2.4.3. Torque and Power

Variations of torque and power generator by the expander can be seen in Figure 3.26a and 3.26b respectively. It can be seen that both the torque and power increase with increasing pressure ratio. However, the rate of increase decreases as the pressure ratio increases. Additionally, the rotation speed doesn't seem to have a high effect on the torque while it has a great effect on the power where the power increases as the rotation speed increase.

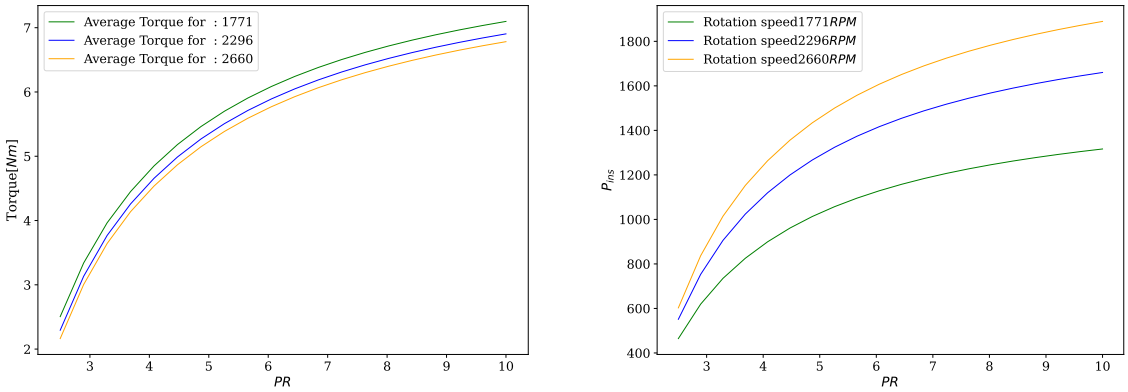

(a) Expander Average Torque Variation with Pressure Ratio and Rotation Speed

(b) Expander Instantaneous Power Variation with Pressure Ratio and Rotation Speed

Figure 3.26: Expander (a) Average Torque and (b) Instantaneous Power Variation with Pressure Ratio and Rotation Speed

3.2.4.4. Efficiency

The expander efficiency was modeled based on the geometric parameter provided in table 3.5 where the effect of flank leaks where only considered without radial leaks as stated by the paper [41]. Additionally, a range of rotation speeds were considered $\Omega = 2000 - 5000RPM$ with pressure ratio of $PR = 2 - 10$. Finally, the effect of mechanical and generator losses were taken into consideration.

It can be seen in Figure 3.27 that the efficiency is low at low-pressure ratio $PR < 3$ which is attributed to the huge over-expansion. As the pressure ratio approaches the build-in pressure ratio, the maximum efficiency is attained before it starts decreasing slightly with an increasing pressure ratio.

Additionally, increasing the rotation speed from $\Omega = 2000RPM$ to $\Omega = 4000RPM$ results in higher expander isentropic efficiency since the generated power increases with increasing rotation speed. However, increasing the rotation speed beyond that point will have negative effect as the losses in mechanical will be high. Moreover, the rotation speed has an effect on the best operating pressure ratio where a higher rotation speed results in a higher optimum operating pressure ratio evidenced by the shift of the highest efficiency point to the right in Figure 3.27

3.2.4.5. Fluid Effects

The effect of working fluid on the expansion performance was studied by simulating the expander with the same geometric parameters used in the compressor model shown in table 3.2. The radial, as well as the flank, were considered to be $(\delta_r = \delta_a = 15\mu m)$ with rotation speed $(\Omega = 2000 - 7000RPM)$. The overall isentropic efficiency can be seen in Figure 3.28. It can be seen in the figures that there is an optimum pressure ratio of around $PR = 3$ which matches the build-in pressure ratio of the compressor model. Additionally, increasing the pressure ratio will result in a drop in efficiency attributed to operating the expander away from the build-in pressure ratio. Moreover, there seems to be an optimum rotation speed for the expander which is around $\Omega = 4000RPM$ where a higher rotation speed will result in lower efficiency attributed to the increase in the mechanical and generator losses. Finally, fluids don't have a huge effect on the efficiency as they all have a maximum efficiency of around $\eta_{c,is} = 80 - 85\%$.

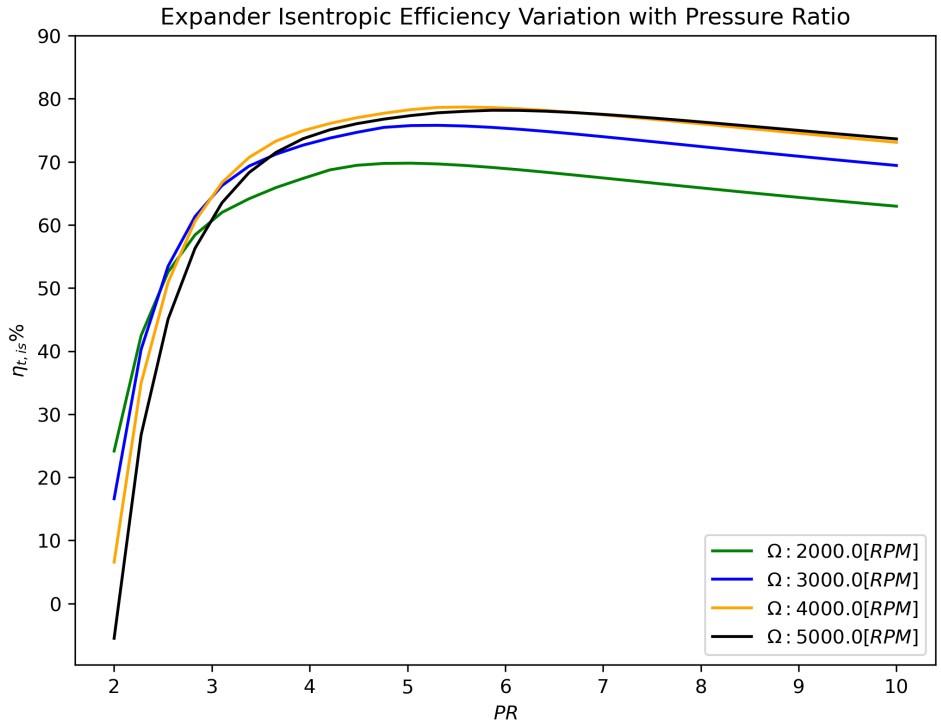

Figure 3.27: Expander Efficiency

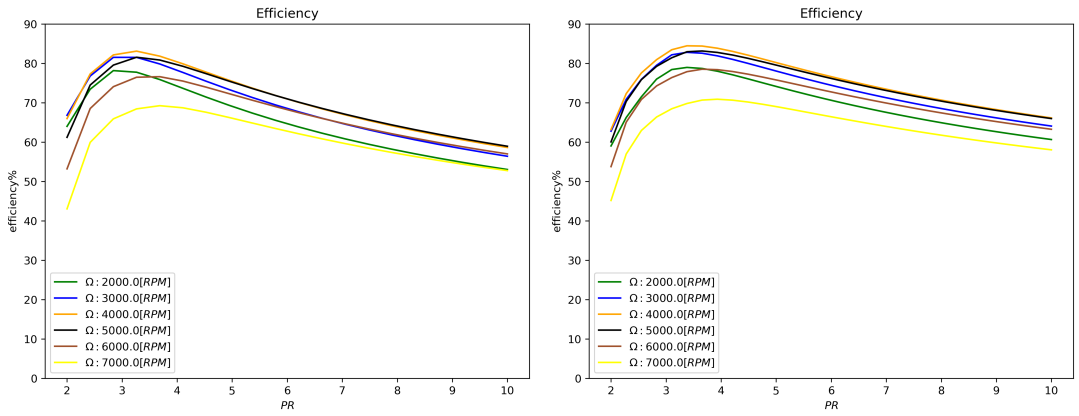

(a) R1234ZE(E) Expander Efficiency

(b) R1233ZD(E) Expander Efficiency

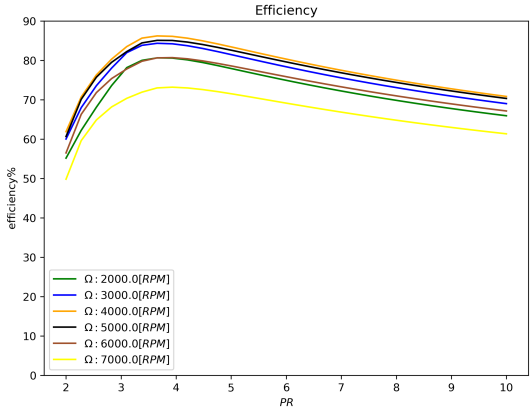

(c) Cyclopentane Expander Efficiency

Figure 3.28: Expander Efficiency for Different Fluids (a) R1234ZE(E) (b) R1233ZD(E) (c) Cyclopentane

4

Pumped Thermal Energy Storage Systems Model

The previous chapter detailed components models in the pumped thermal energy storage systems. In this chapter, the modeling of the pumped thermal energy storage system will be detailed. This will be approached by firstly detailing the governing equations used to measure the performance of the system. Secondly, thermodynamic cycles will be detailed for the heat pump and heat engine cycles along with their sensitivity to different parameters. Thirdly, different fluids will be analyzed in order to select the most appropriate fluid for the selected application. Finally, optimization criteria will be presented to govern the selection of the optimum cycle.

4.1. Governing Equations

For PTES, parameters can be introduced for the performance of the different cycles which are heat pump Coefficient of Performance COP_{hp} and heat engine efficiency η_{he} as can be seen in equation 4.1.

$$\begin{aligned} COP_{hp} &= \frac{\dot{Q}_{hp_{out}}}{\dot{W}_c} && \text{Heat Pump COP} \\ \eta_{he} &= \frac{\dot{W}_t - \dot{W}_p}{Q_{he,in}} && \text{Heat Engine Efficiency} \end{aligned} \tag{4.1}$$

The main parameter used to measure energy storage performance is the round trip efficiency η_{rt} which is the ratio of the output net energy from the heat engine cycle $W_t - W_p$ to the input energy in the heat pump cycle W_c. Other important parameters used in evaluating energy storage are energy and power density ρ_{en} and ρ_{pw} which are the ratio of output energy and power to the storage volume which indicate the compactness of the system and therefore higher values are desirable. Round trip efficiency can also be expressed in terms of heat pump COP and heat engine efficiency η_{he} as can be seen in equation 4.2.

$$\eta_{rt} = \frac{W_t - W_p}{W_c} = COP_{hp} \times \eta_{he} \quad \text{Round Trip Efficiency}$$
$$\rho_{en} = \frac{W_t - W_p}{V_{tes}} \quad \text{Energy Density} \qquad (4.2)$$
$$\psi_{ex} = \frac{\eta_{rt}}{\eta_{rt,Carnot}} \quad \text{Power Density}$$

Where $\eta_{rt,Carnot}$ is the round trip efficiency of a Carnot-based heat pump and heat engine cycles as described in equation 4.3 [37]

$$COP_{hp,Carnot} = \frac{T_H}{T_H - T_C} \quad \text{Carnot Heat Pump COP}$$
$$\eta_{he,Carnot} = \frac{T_H - T_C}{T_H} \quad \text{Carnot Heat Engine Efficiency} \qquad (4.3)$$
$$\eta_{rt,Carnot} = COP_{hp,Carnot} \times \eta_{he,Carnot} \quad \text{Carnot Round Trip Efficiency}$$

4.2. Thermodynamic Cycles Models

The thermodynamic cycles employed in the pumped thermal energy storage system are the heat pump and heat engine cycles. The heat pump cycle uses electrical power to upgrade the temperature of the working fluid from low temperature to high temperature as described earlier. While the heat engine cycle consumes the heat energy on the working fluid to generate electrical energy. In the following subsection, both cycles will be detailed. The following assumptions were made for the modeling of pumped thermal energy storage:

- The effect of potential energy and kinetic energy were assumed to be negligible.
- The system was assumed to be perfectly insulated and therefore heat loss to the environment was assumed to be negligible.
- Pressure drop across different systems was assumed to be negligible.
- Charging and discharging times were assumed to be the same. This is done during the fluid selection process to have comparable parameters among all fluids. However, in the integrated cycle, they will be decoupled.
- Sensible heat storage working with pressurized water will be modeled since the storage temperature will not exceed $T_{st} = 200°C$ which is within the operating range of pressurized water as indicated in Section 2.30.

By specifying the source and storage temperatures, a heat pump and heat engine cycles are constructed to fit the specified parameters. It was assumed that the discharging time τ_{dis} is equal to the charging time τ_{ch} to facilitate using the same heat exchanger in the charging and discharging cycles and therefore improve the economical aspect which comes at the cost of exergy loss as detailed in [67]. The model inputs and outputs are listed in table 4.1. In the following sections, more details will be provided on the modeling of the heat pump and the heat engine cycles.

Table 4.1: Model Input and Output Parameters

Input Parameter			Output Parameter	
Description	**Parameter**	**Value [Unit]**	**Description**	**Parameter**
Waste heat temperature	T_{source}	50-80[$^{\circ}C$]	Heat Pump Mass Flow	$\dot{m}_{hp}$
Ambient temperature	$T_{ambient}$	15 [$^{\circ}C$]	Waste Heat Input	$\dot{Q}_{hp,in}$
Degree of heat pump superheat, ($\Delta T_{hp,sup}$)	$T_1 - T_4$	2 [K]	Heat Pump Output Heat	$\dot{Q}_{hp,out}$
Storage temperature	$T_{storage}$	90-140 [$^{\circ}C$]	Storage Mass Flowrate	$\dot{m}_{st}$
Compressor efficiency	$\eta_{is,comp}$	80 [%]	Storage Volume	V_{st}
Turbine efficiency	$\eta_{is,turb}$	88 [%]	Heat Engine Mass Flow	$\dot{m}_{he}$
Pump efficiency	$\eta_{is,pump}$	80 [%]	Heat Engine Input Heat	$\dot{Q}_{he,in}$
Pinch across each heat exchanger	ΔT_{pinch}	2 [K]	Turbine Output Power	$\dot{W}_{turb}$
Charging-discharging duration	t_{ch}, t_{dch}	1 [hrs]	Heat Engine Output Heat	$\dot{Q}_{he,out}$
Compressor Input Power	$\dot{W}_{comp}$	1 [kW]	Pump Input Power	$\dot{W}_{pump}$
Degree of Heat Engine Subcool $\Delta T_{he,supc}$	$T_2" - T_1"$	5 [K]	Heat Pump Coefficient of Performance	COP_{hp}
Degree of Heat Engine Superheat $\Delta T_{he,suph}$	$\Delta T_{he,suph}$	10 [K]	Heat Engine Efficiency	η_{he}
			Round Trip Efficiency	η_{rt}
			Energy Density	ρ_{en}
			Exergy Efficiency	ψ_{ex}

4.2.1. Heat Pump Cycle

The Heat pump cycle is used to upgrade the heat from low temperature T_{source} to high temperature $T_{storage}$ where heat from the high-temperature heat exchanger $\dot{Q}_{hp,out}$ is used to store heat in the storage system. A single-stage heat pump cycle was modeled as depicted in figure 4.1 with a (red) line going in a counterclockwise direction. The heat pump modeling logic is demonstrated in Figure 4.2.

The start of the heat pump model is by specifying the source temperature T_{source} and storage temperature $T_{storage}$ along with the super-heat $\Delta T_{hp,sup}$ and pinch temperature ΔT_{pinch}. The super-heat is required to avoid condensation at the compressor outlet. With these specified the saturation temperature of the heat pump evaporator can be calculated using equation 4.4. This is done because the pinch point will be at the source temperature inlet point as can be seen in Figure 4.3.

$$T_{hp,evap} = T_{source} - \Delta T_{pinch} - \Delta T_{hp,sup} \tag{4.4}$$

By determining the evaporator saturation temperature, then the compressor inlet pressure is a function of the evaporator temperature $T_{hp,evap}$ and quality for saturated vapor $x = 1$ can be seen in equation 4.5:

$$P_{hp,evap} = fn\left(T_{hp,evap}, x = 1\right) \tag{4.5}$$

With this, the inlet condition of the compressor is known and therefore the specific enthalpy and specific entropy can be determined through equation 4.6.

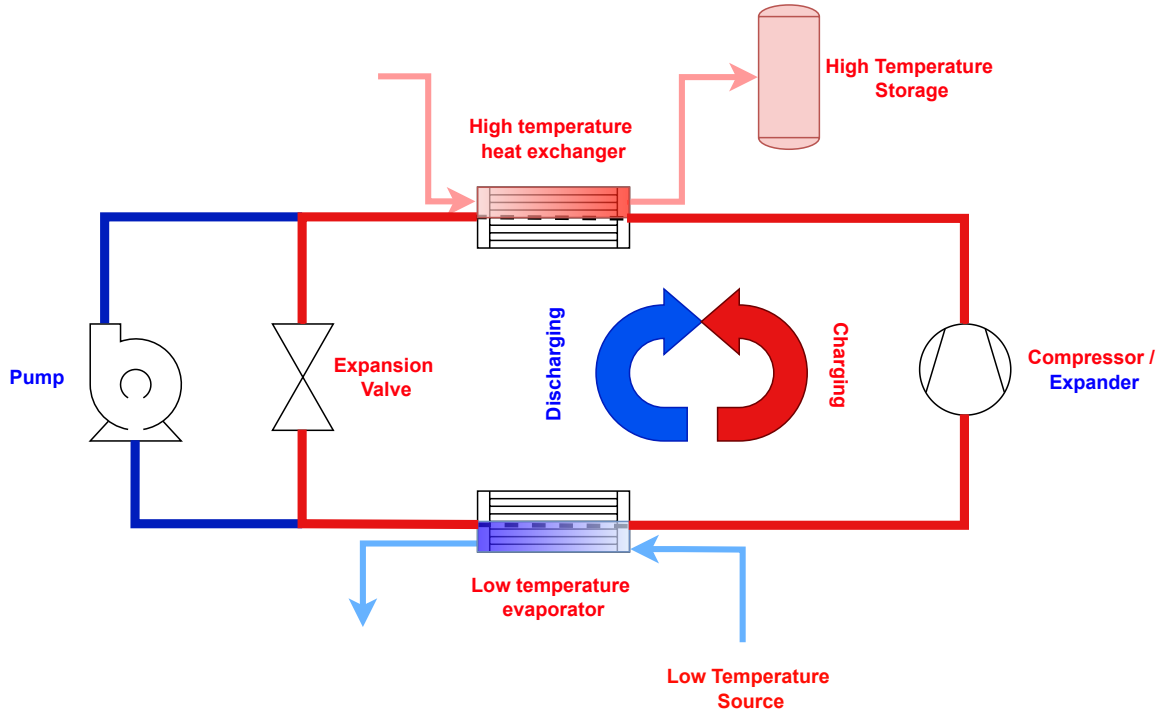

Figure 4.1: Heat Pump (Red) and Heat Engine (Blue) Cycle Configuration

$$\begin{aligned} T_{comp,in} &= T_{hp,evap} + \Delta T_{hp,sup} \\ h_{comp,in}, s_{comp,in} &= fn\left(P_{hp,evap}, T_{comp,in}\right) \end{aligned} \tag{4.6}$$

The compressor outlet pressure is then assumed to be $P_{comp,out}$ which provides a means to carry out the rest of the modeling. With the outlet pressure and compressor isentropic efficiency $\eta_{is,comp}$, the compressor outlet condition can be determined as per equation 4.7

$$\begin{aligned} s_{is,comp,out} &= s_{comp,in} \\ h_{is,comp,out} &= fn\left(P_{comp,out}, s_{is,comp,out}\right) \\ h_{real,comp,out} &= \frac{h_{is,comp,out} - h_{comp,in}}{\eta_{is,comp}} + h_{comp,in} \end{aligned} \tag{4.7}$$

After determining the outlet condition of the compressor, the heat pump working fluid mass flowrate can be calculated from equation 4.8 using compressor work input $\dot{W}_{comp}$

$$\dot{m}_{hp} = \frac{\dot{W}_{comp}}{h_{real,comp,out} - h_{comp,in}} \tag{4.8}$$

In order to maximize the output heat (duty) of the heat pump, the condenser outlet enthalpy $h_{hp,cond_out}$ shall equal the evaporator saturated liquid enthalpy $h_{hp,evap,sat,liq}$. With this, the duty of the heat pump can be determined per equation 4.9.

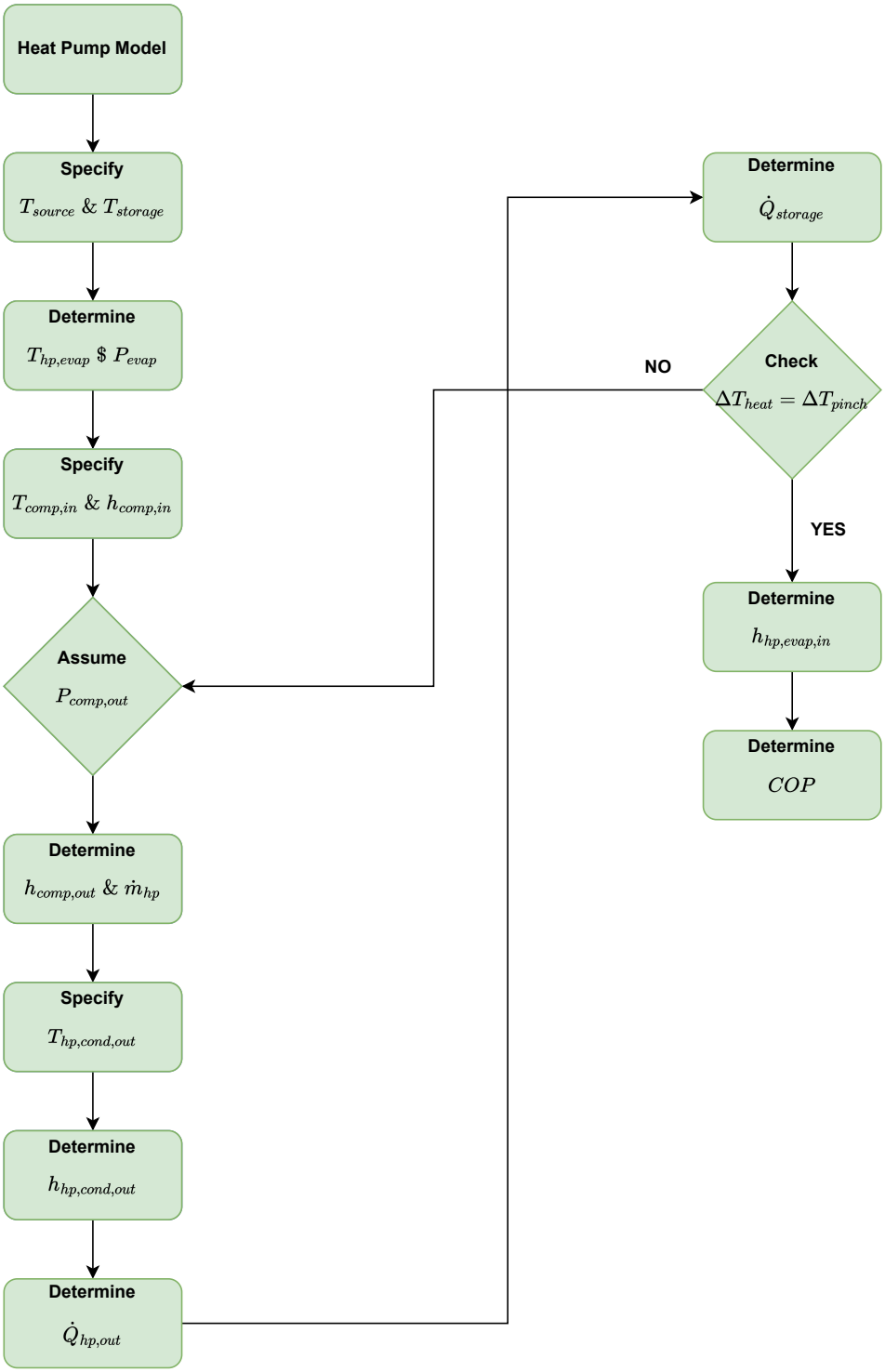

Figure 4.2: Heat Pump Modeling Logic

$$
\begin{aligned}
h_{hp,cond,in} &= h_{real,comp,out} \\
h_{hp,cond,out} &= h_{hp,evap,sat,liq} \\
\dot{Q}_{hp,out} &= \dot{m}_{hp}\left(h_{hp,cond,out} - h_{hp,cond,in}\right) \\
Q_{hp,out} &= \dot{Q}_{hp,out} * charging
\end{aligned}
\tag{4.9}
$$

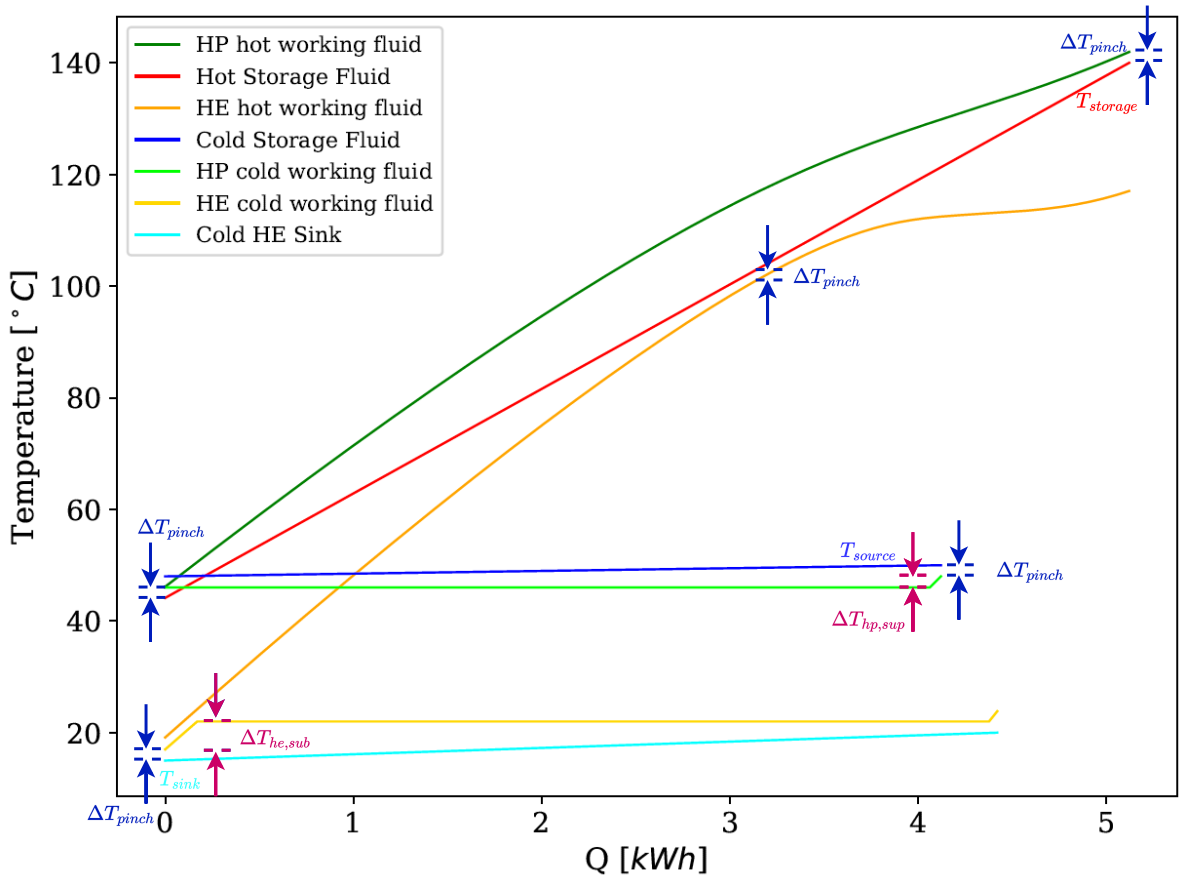

Figure 4.3: Heat Flow in the Heat Pump and Heat Engine Cycles.
(Green) Heat Pump High Pressure (Lime) Heat Pump Low Pressure
(Red) Storage Fluid (Blue) Source Fluid (Sky Blue) Sink Fluid
(Orange) Heat Engine High Pressure (Light Orange) Heat Engine Low Pressure

The duty of the heat pump is the same as the storage heat. The inlet temperature of the storage fluid was determined by having a pinch point at the inlet to minimize exergy destruction as can be seen in figure 4.3 using the following relation ($T_{storage,in} = T_{hp,cond,out} - \Delta T_{pinch}$). With the duty and inlet and storage temperature known, the storage medium flowrate and volume can be determined as per equation 4.10 :

$$\begin{aligned} \dot{Q}_{storage} &= \dot{Q}_{\dot{Q}_{hp,out}} \\ h_{storage,in} &= fn\left(T_{storage,in}, P_{storage}\right) \\ h_{storage} &= fn\left(T_{storage}, P_{storage}\right) \\ \dot{m}_{st} &= \frac{\dot{Q}_{storage}}{h_{storage} - h_{storage,in}} \\ V_{storage} &= \frac{\dot{m}_{st}\tau_{ch} * 3600}{\rho_{storage}} \end{aligned} \tag{4.10}$$

With these parameters known, the heat energy and storage energy lines shown in Figure 4.3 (Green) and (Red) respectively can be determined. And the difference between the two temperatures can be evaluated to ensure that the pinch point at the right side is satisfied. The

compressor output pressure will be iterated until this pinch is satisfied. Finally, the evaporator inlet will be determined as the enthalpy across the expansion valve doesn't change as per equation 4.11:

$$\begin{aligned} h_{hp,evap,in} &= h_{hp,cond,out} \\ P_{hp,evap,in} &= P_{comp,in} \\ T_{hp,evap,in} &= fn\left(h_{hp,evap,in}, P_{hp,evap,in}\right) \end{aligned} \tag{4.11}$$

The heat pump Coefficient of Performance can be calculated as the ratio of the heat pump duty to the power input as per equation 4.12

$$COP = \frac{\dot{Q}_{hp,out}}{\dot{W}_{comp}} \tag{4.12}$$

With this, the heat pump cycle is determined and T-s diagram can be generated as per Figure 4.4.

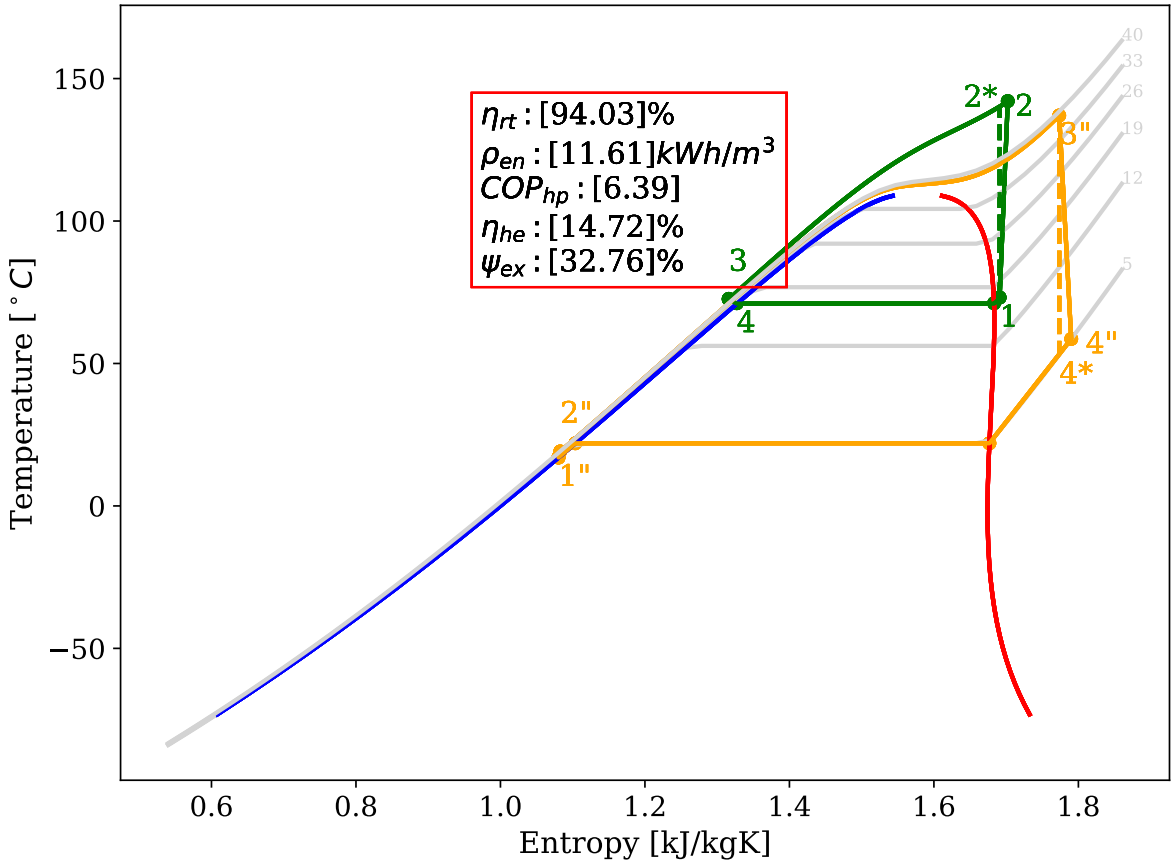

Figure 4.4: Heat Pump (Green) and Heat Engine (Orange) T-s Diagram. (Gray) are isobar lines, (Blue) is Saturated Liquid, and (Red) is Saturated Vapor.
(1) Compressor Inlet (2) Real Compressor Outlet (2*) Isentropic Compressor Outlet (3) Expansion Valve Inlet (4) Expansion Valve Outlet.
(1") Pump Inlet (2") Real Pump Outlet (3") Expander Inlet (4") Real Expander Outlet (4*) Isentropic Expander Outlet

4.2.2. Heat Engine Cycle

Similar to the heat pump, heat engine states can be determined. The heat engine modeling steps can be seen in Figure 4.5. Atmospheric condition is considered to be the sink temperature $T_{he,sink}$ with a subcool of $(\Delta T_{he,subc} = 5K)$. By doing so, the saturation temperature at the heat engine condenser can be determined based on equation 4.13 which then can be used to calculate pump inlet temperature, pressure, specific enthalpy, and specific entropy based on the fluid quality x as can be seen in Figure 4.3. Low-pressure side of the heat engine $P_{he,LP}$ and high-pressure side of the heat engine $P_{he,HP}$ will be used for the pump inlet and outlet pressures respectively.

$$\begin{aligned} T_{he,cond,sat} &= T_{sink} + \Delta T_{pinch} + T_{he,subc} \\ P_{hp,LP} &= fn\left(T_{he,cond,sat}, x = 0\right) \\ T_{pump,in} &= T_{he,cond,sat} - T_{he,subc} \\ h_{pump,in}, s_{pump,in} &= fn\left(T_{pump,in}, P_{he,LP}\right) \end{aligned} \tag{4.13}$$

The high pressure is first assumed $P_{he,HP}$ and with this and pump isentropic efficiency $\eta_{is,pump}$, the outlet condition can be calculated through equation 4.14

$$\begin{aligned} s_{is,pump,out} &= s_{pump,in} \\ h_{is,pump,out} &= fn\left(s_{is,pump,out}, P_{he,HP}\right) \\ h_{real,pump,out} &= \frac{h_{is,pump,out} - h_{pump,in}}{\eta_{is,pump}} + h_{pump,in} \\ T_{real,pump,out} &= fn\left(h_{real,pump,out}, P_{he,HP}\right) \end{aligned} \tag{4.14}$$

The duty of the heat engine's heat input was assumed to be equal to the duty of the storage system previously calculated. Additionally, a superheat equal to $(\Delta T_{he,suph} = 10K)$ was assumed to avoid going through a two-phase region during expansion. From this, the turbine inlet condition can be determined which is then used to calculate the mass flowrate of the heat engine working fluid through the equation 4.15. The mass flowrate is used to determine the pump inlet power.

$$\begin{aligned} T_{turb,in} &= T_{he,evap,sat} + \Delta T_{he,suph} \\ h_{turb,in} &= fn\left(s_{is,pump,out}, T_{turb,in}\right) \\ \dot{Q}_{he,in} &= \dot{Q}_{storage} \\ \dot{m}_{he} &= \frac{\dot{Q}_{he,in}}{h_{turb,in} - h_{real,pump,out}} \\ \dot{W}_{pump} &= \dot{m}_{he}\left(h_{real,pump,out} - h_{pump,in}\right) \end{aligned} \tag{4.15}$$

With these parameters known and similar to the heat pump storage, the heat engine hot working fluid line (Orange) and hot storage line (Red) in Figure 4.3 can be determined with the difference between the two lines can be evaluated. The heat engine high pressure $P_{he,HP}$ is then optimized to reach pinch point.

The outlet of the turbine is then determined with equation 4.16 that is used to calculate the power output by knowing the turbine isentropic efficiency $\eta_{is,turb}$

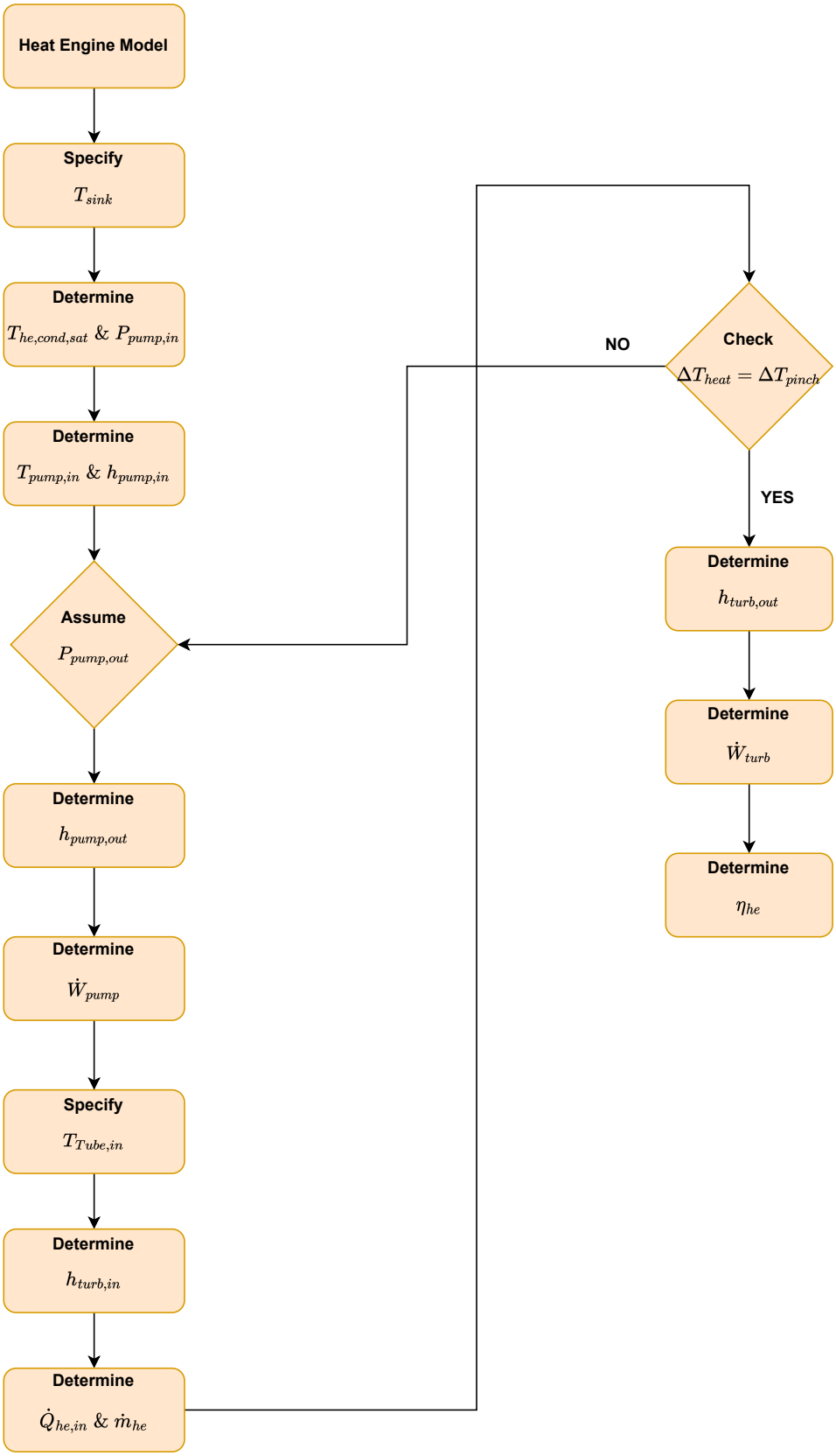

Figure 4.5: Heat Engine Modeling Steps

$$
\begin{aligned}
s_{turb,in} &= fn\left(P_{he,HP}, T_{turb,in}\right) \\
s_{is,turb,out} &= s_{turb,in} \\
h_{is,turb,out} &= fn\left(P_{he,LP}, s_{is,turb,out}\right) \\
h_{real,tube,out} &= \eta_{is,turb}\left(h_{is,turb,out} - h_{turb,in}\right) + h_{turb,in} \\
\dot{W}_{turb} &= \dot{m}_{he}\left(h_{turb,in} - h_{real,tube,out}\right)
\end{aligned}
\tag{4.16}
$$

With this, the heat engine performance can be determined using equation 4.17

$$
\eta_{he} = \frac{\dot{W}_{turb} - \dot{W}_{pump}}{\dot{Q}_{he,in}} \tag{4.17}
$$

4.2.3. Sensitivity Analysis

Different sensitivity analyses need to be conducted in order to understand the effect of different input parameters like source, storage, compressor, and expander isentropic efficiencies among others on the performance of the system in terms of round trip efficiency, energy density, and exergy efficiency.

4.2.3.1. Source Temperature

By increasing the source temperature while keeping the storage temperature fixed, the heat pump pressure ratio decreases as can be seen in Figure 4.6a. Even though the results are shown for $R1234ZE(E)$, the effect is similar in other fluids.

For the heat engine cycle, increasing the source temperature while keeping the storage temperature constant results in an increase in pressure ratio across the heat engine which is not very intuitive. The sink temperature of the heat engine was fixed at $T_{sink} = 15°C$ to match atmospheric conditions. Therefore, fixing the storage temperature $T_{storage}$ intuitively should fix the pressure ratio but this is not the effect seen in Figure 4.6b. This is attributed to the fact that increasing the source temperature would increase the hot storage stream starting temperature which will facilitate a higher pressure ratio on the heat engine cycle. For the last (yellow) line where the storage temperature $T_{storage} = 140°C$, the pressure ratio remains constant beyond the source temperature of $T_{source} = 65°C$. This is attributed to not being able to satisfy the pinch requirement by increasing the pressure ratio in the heat engine cycle therefore the pressure ratio was limited to slightly higher than critical pressure to limit equipment cost.

Variation of round trip efficiency and energy density with source and storage temperature can be seen in Figures 4.7a and 4.7b respectively. It can be seen in the figures that increasing the source temperature T_{source} while keeping the storage temperature fixed increases the round trip efficiency η_{rt} while the energy density ρ_{en} decreases. This produces a competing result where maximizing the round-trip efficiency will result in minimizing the energy density. Additionally, it can be seen that small heat pump lift temperature $\Delta_{hp,lift}$ favor round trip efficiency η_{rt} while having the opposite effect on energy density ρ_{en} which is in line with the conclusion made by [19] and [23].

4.2.3.2. Storage Temperature

Increasing the storage temperature while maintaining the source temperature constant will result in increasing the pressure ratio across the heat pump as well as the heat engine cycles which are attributed to the increase in lift temperature $\Delta T_{hp,lift}$ and $\Delta T_{he,lift}$ which can be seen in Figure 4.6a and 4.6b respectively.

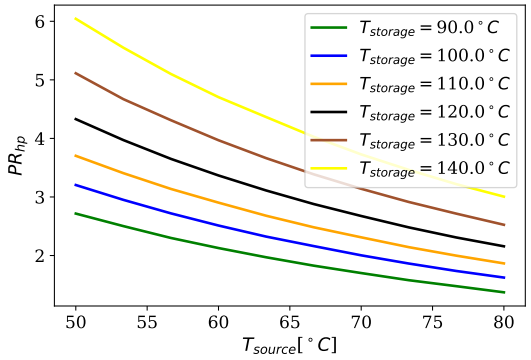

(a) Variation of Heat Pump Pressure Ratio PR_{hp} with T_{source} & $T_{storage}$ for R1234ZE(E)

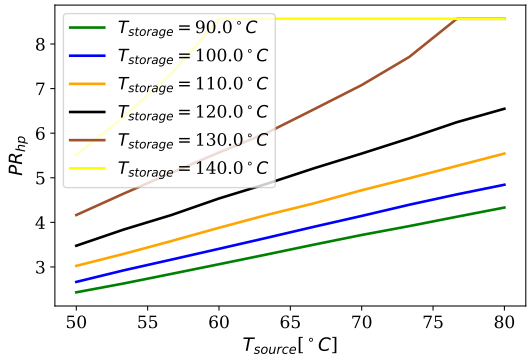

(b) Variation of Heat Pump Pressure Ratio PR_{he} with T_{source} & $T_{storage}$ for R1234ZE(E)

Figure 4.6: Variation of heat pump and heat engine pressure ratios with T_{source} & $T_{storage}$ for R1234ZE(E). (a) Variation of Heat Pump Pressure Ratio PR_{hp} with T_{source} & $T_{storage}$ for R1234ZE(E). (b) Variation of Heat Engine Pressure Ratio PR_{he} with T_{source} & $T_{storage}$ for R1234ZE(E)

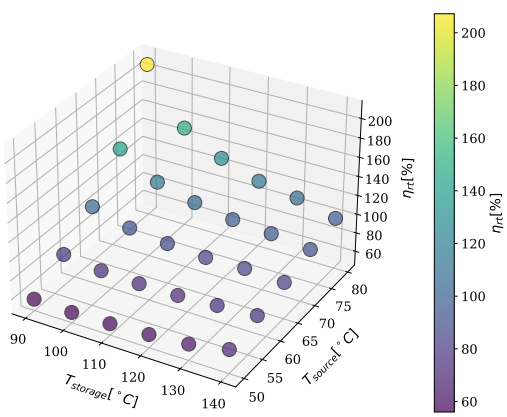

(a) Variation of η_{rt}, $with\ T_{source}$ & $T_{storage}$ for R1234ZE(E)

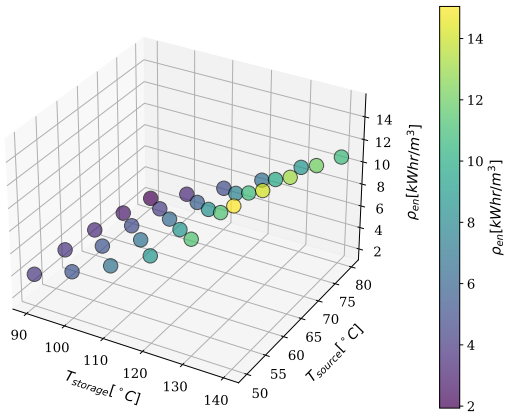

(b) Variation of ρen, $with\ T_{source}$ & $T_{storage}$ for R1234ZE(E)

Figure 4.7: Variation of η_{rt} & ρ_{en} with T_{source} & $T_{storage}$ for R1234ZE(E) Where Low Heat Pump Lift Temperature Favor Round Trip Efficiency η_{rt}. (a) Variation of η_{rt} with T_{source} & $T_{storage}$. (b) Variation of ρen with T_{source} & $T_{storage}$

For round-trip efficiency η_{rt}, increasing the storage temperature result in a decrease in round-trip efficiency which is attributed to the increase in lift temperature in the heat pump cycle as can be seen in Figure 4.7a. On the other hand, energy density will increase as the storage temperature increases as can be seen in Figure 4.7b.

4.2.3.3. Compressor and Expander Isentropic Efficiency

Variations of the system round trip efficiency η_{rt} and energy density ρ_{en} with the compressor and expander isentropic efficiency are shown in Figure 4.8 where compressor and expander isentropic efficiency were varied from $50 - 90\%$.

It can be seen that round trip efficiency η_{rt} linearly increase with the increase of the compressor and expander isentropic efficiency. Moreover, it can be seen that the expander isentropic efficiency $\eta_{t,is}$ has a higher impact over round trip efficiency η_{rt} than compressor isotopic efficiency $\eta_{c,is}$ where round trip efficiency increased $2\times$ over the expander range while it increased $1.5\times$ over the compressor range.

For energy density ρ_{en}, it can be seen that compressor isentropic efficiency $\eta_{c,is}$ has a low

effect over energy density which is attributed to the fact that compressor isentropic efficiency has no impact over storage temperature. However, energy density ρ_{en} linearly increase over expander isentropic efficiency $\eta_{t,is}$.

Therefore, compressor and expander isentropic efficiencies are crucial in the performance of the storage system with the expander isentropic efficiency being more influential on the performance of the storage system as it positively affects both round trip efficiency and energy density. Additionally, more realistic compressor and expander models are required to provide a better understanding of the performance of the system.

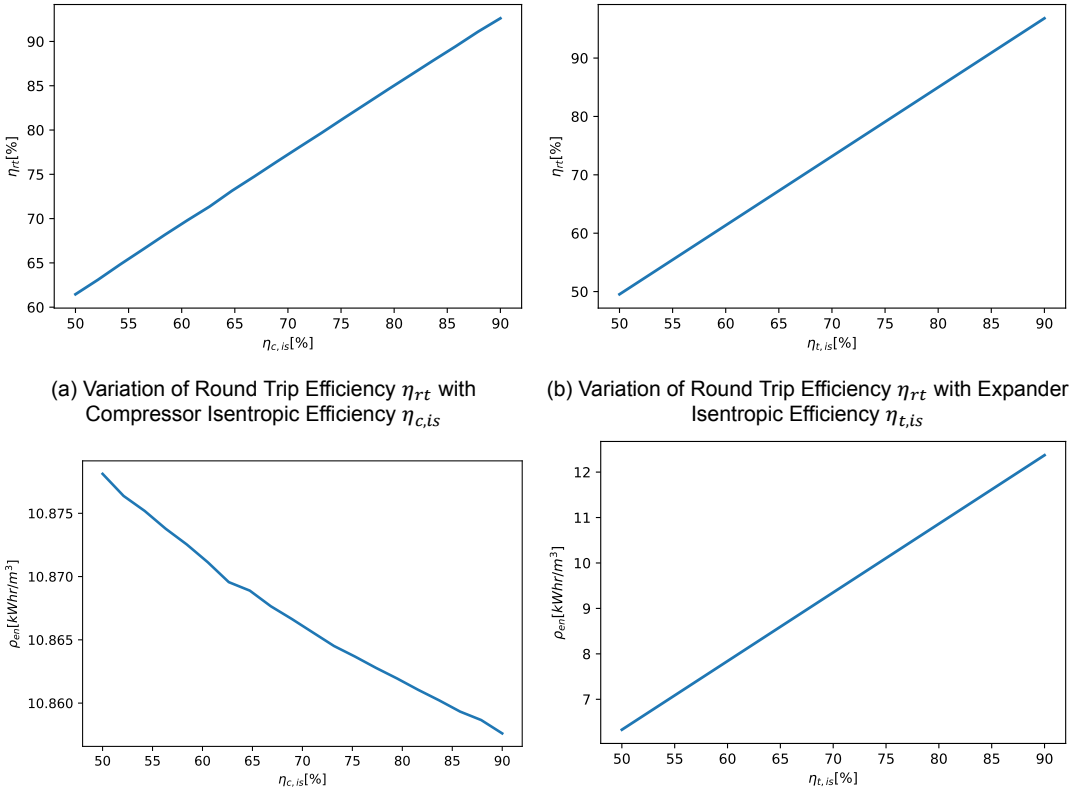

(a) Variation of Round Trip Efficiency η_{rt} with Compressor Isentropic Efficiency $\eta_{c,is}$

(b) Variation of Round Trip Efficiency η_{rt} with Expander Isentropic Efficiency $\eta_{t,is}$

(c) Variation of Energy Density ρ_{en} with Compressor Isentropic Efficiency $\eta_{c,is}$

(d) Variation of Energy Density ρ_{en} with Expander Isentropic Efficiency $\eta_{t,is}$

Figure 4.8: Variation of η_{rt} & ρ_{en} with Compressor and Expander Isentropic Efficiency. (a) η_{rt} Variation with Compressor Isotopic Efficiency $\eta_{c,is}$. (b) η_{rt} Variation with Expander Isotopic Efficiency $\eta_{t,is}$. (c) ρ_{en} Variation with Compressor Isotopic Efficiency $\eta_{c,is}$. (a) ρ_{en} Variation with Expander Isotopic Efficiency $\eta_{t,is}$

4.2.3.4. Heat Pump Superheat

The impact of increasing heat pump superheat $\Delta T_{hp,sup}$ from $2°C - 20°C$ on round trip efficiency η_{rt} and energy density ρ_{en} can be seen in Figure 4.9. It can be seen that a low degree of superheat is advantageous to improve round trip efficiency η_{rt} while having the opposite impact on energy density ρ_{en}. Therefore, a low degree of superheat of $\Delta T_{hp,sup} = 2°C$ will be selected to favor round-trip efficiency.

4.2.3.5. Heat Engine Subcool

The impact of increasing heat engine subcool $\Delta T_{he,sub}$ at pump inlet from $2°C - 20°C$ on round trip efficiency η_{rt} and energy density ρ_{en} can be seen in Figure 4.10. It can be seen that a low degree of subcooling is advantageous as it improves both round-trip efficiency and energy density. Therefore, a low degree of subcool of $\Delta T_{he,sub} = 5°C$ will be selected.

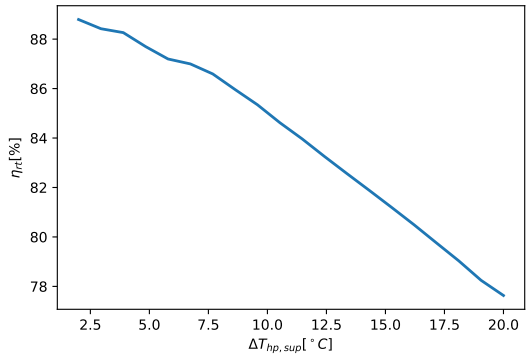

(a) Variation of Round Trip Efficiency η_{rt} with Heat Pump Superheat $\Delta T_{hp,sup}$

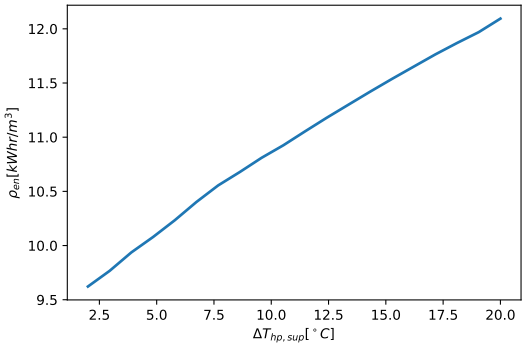

(b) Variation of Energy Density ρ_{en} with Heat Pump Superheat $\Delta T_{hp,sup}$

Figure 4.9: Variation of η_{rt} & ρ_{en} with Heat Pump Superheat. (a) η_{rt} Variation with Heat Pump Superheat $\Delta T_{hp,sup}$. (b) ρ_{en} Variation with Heat Pump Superheat $\Delta T_{hp,sup}$

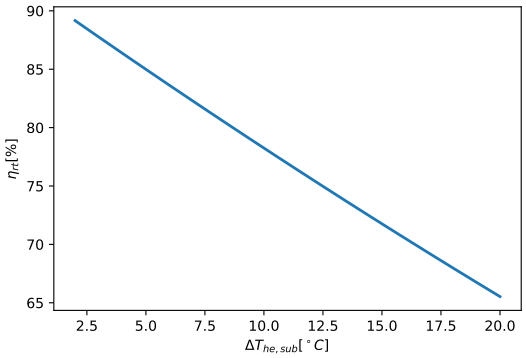

(a) Variation of Round Trip Efficiency η_{rt} with Heat Engine Subcool $\Delta T_{he,sub}$

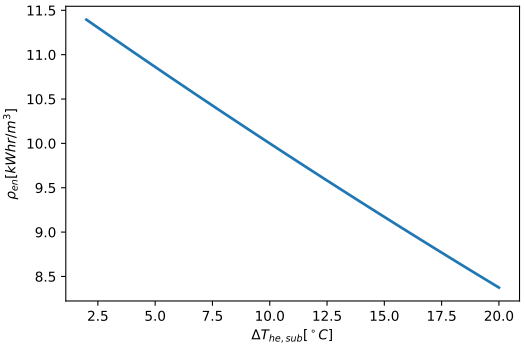

(b) Variation of Energy Density ρ_{en} with Heat Engine Subcool $\Delta T_{he,sub}$

Figure 4.10: Variation of η_{rt} & ρ_{en} with Heat Engine Subcool. (a) η_{rt} Variation with Heat Engine Subcool $\Delta T_{he,sub}$. (b) ρ_{en} Variation with Heat Engine Subcool $\Delta T_{he,sub}$

4.3. Optimization

As mentioned earlier, energy density and round trip efficiency are competing parameters where maximizing one will mandate minimizing the other. Therefore, an optimization scheme was developed where each criterion is given a weight and the storage temperature and source temperature are the optimization variables in order to achieve the objective of maximizing round trip efficiency, energy density, and exergy efficiency. Additionally, the performance of the system heavily depends on the selected working fluids. The fluids mentioned earlier in the literature review part in Table 2.4 will be studied in the system to evaluate their performance. There is no single fluid that satisfies all the required properties and therefore some compromise will have to be made. Therefore, a simple multi-fluid optimization scheme, as well as a multi-objective optimization scheme, were developed to aid the optimization process.

4.3.1. Simple Multi-Fluid Optimization Scheme

It is possible to use different fluids for the heat pump and heat engine cycle. The performance of each system cycle can be evaluated individually through the heat pump COP_{hp} and the heat engine η_{he} which will be reflected in the overall round trip efficiency η_{rt}, energy density ρ_{en}, and exergy efficiency ψ_{ex}. A simple optimization scheme is used to optimize two key parameters ($\boldsymbol{x}$) which are the source and storage temperatures with the objective of maximiz-

Table 4.2: Optimized HP:HE Selection for Scenario 1: $(a = b = c = \frac{1}{3})$

		Source Temperature			
		50	**60**	**70**	**80**
Storage Temperature	**90**	R1234yf : R1234yf	R1234yf : R1234yf	Cyclopentane : R1234yf	Cyclopentane : R1234yf
	100	R1234yf : R1234yf	R1234yf : R1234yf	R1234yf : R1234yf	Cyclopentane : R1234yf
	110	R1234yf : R1234yf	R1234yf : R1234yf	R1234yf : R1234yf	R1234yf : R1234yf
	120	R1234yf : R1234yf	R1234yf : R1234yf	R290 : R1234ZE(E)	R290 : R1234ZE(E)
	130	R1234yf : R1234yf	R290 : R1234ZE(E)	R290 : R1234ZE(E)	R1234ZE(E) : R1234ZE(E)
	140	R290 : R1234ZE(E)	R1234ZE(E) : R1234ZE(E)	R1234ZE(E) : R1234ZE(E)	R1234ZE(E) : R1234ZE(E)

ing round trip efficiency, exergy efficiency, and energy density. Levelized round trip efficiency $(\widetilde{\eta_{rt}})$, levelized energy density $(\widetilde{\rho_{en}})$, and levelized exergy efficiency $(\widetilde{\psi_{ex}})$ were introduced in the objective function $(g(x))$ to facilitate numerical addition of the different parameters. The maximum value used in the levelized parameters is the maximum in the grid based on the source and storage temperatures. The mathematical model used in this optimization can be seen in Equation 4.21 as proposed by [24]:

$$\begin{cases} g(x) & = a\widetilde{\eta_{rt}} + b\widetilde{\rho_{en}} + c\widetilde{\psi_{ex}} \\ x & = [T_{source}, T_{storage}] \end{cases} \tag{4.18}$$

where: (4.19)

$$\widetilde{\eta_{rt}} = \frac{\eta_{rt,i}}{\eta_{max}}; \quad \widetilde{\rho_{en}} = \frac{en,i}{\rho_{max}}; \quad \widetilde{\psi_{ex}} = \frac{\psi_{ex,i}}{\psi_{max}} \tag{4.20}$$

(4.21)

In equation 4.21, $a, b, \& c$ are the weight of each parameter where they take a value from $0 - 1$ where 0 represents the lowest while 1 is the highest. Two scenarios are studied one in which they are equally weighted $(a = b = c = \frac{1}{3})$ and the other where only energy efficiency and round trip efficiency are considered $(a = b = \frac{1}{2}; c = 0)$.

Figures 4.11 shows samples of the optimization result for Scenario 1 where $(a = b = c = \frac{1}{3})$ while Figures 4.12 shows samples of the optimization results for Scenario 2 where $(a = b = \frac{1}{2}; c = 0)$. Considering the different fluids and source and storage temperatures, Table 4.2 and 4.3 shows the heat pump and heat engine fluid selection based on the optimization criteria for scenario 1 $(a = b = c = \frac{1}{3})$ and scenario 2 $(a = b = \frac{1}{2}; c = 0)$ respectively.

The results show that in more than 60% of the cases, it is optimum to use the same fluid for the heat pump and heat engine cycle. Therefore, the same fluid will be considered hereafter.

4.3.2. Multi Objective Optimization Scheme

Following the results from the simple multi-fluid optimization, a more rigorous optimization scheme was implemented based on a single fluid in the heat pump and heat engine cycle to carry out a multi-objective optimization. A Non-Dominated Sorting Genetic Algorithm-II (NSGA-II) scheme was selected due to its wide use in resolving multi-objective optimization problems to find the Pareto Optimal solution to optimize the objective function of maximizing round trip efficiency η_{rt} and energy density ρ_{en} with two variables which are the source T_{source} and storage $T_{storage}$ temperatures.

Optimization formulation is shown in equation 4.22 is the multi-objective function for NSGA-II [77]. The objective function $f(\boldsymbol{x})$ that is minimized is the inverse of the maximize function.

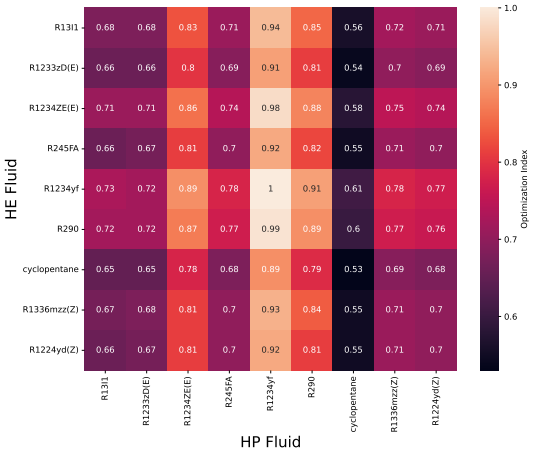

(a) Optimization Index Heat Map Scenario 1 for $T_{source} = 50^{\circ}C$ and $T_{storage} = 110^{\circ}C$

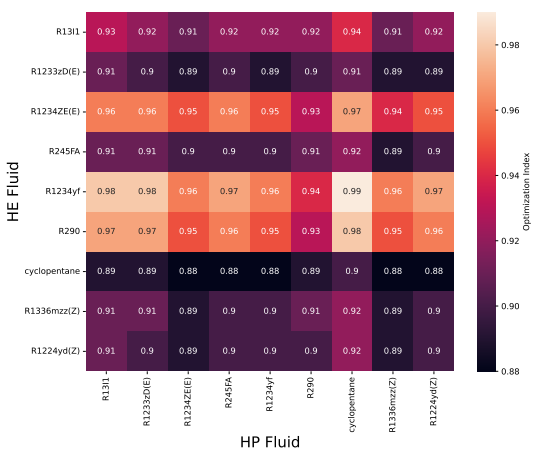

(b) Optimization Index Heat Map Scenario 1 for $T_{source} = 80^{\circ}C$ and $T_{storage} = 110^{\circ}C$

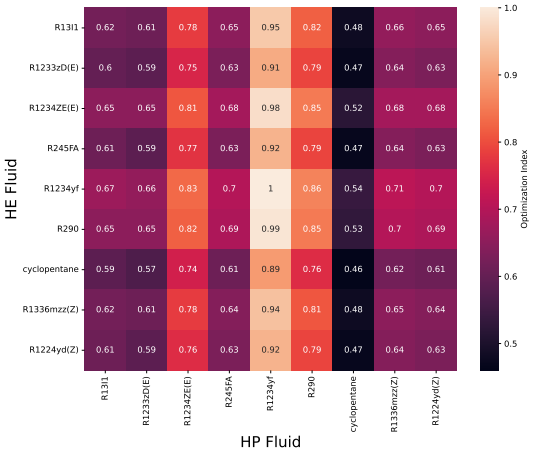

(c) Optimization Index Heat Map Scenario 1 for $T_{source} = 50^{\circ}C$ and $T_{storage} = 120^{\circ}C$

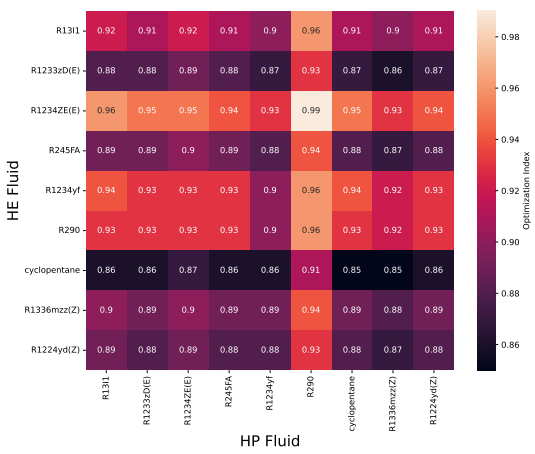

(d) Optimization Index Heat Map Scenario 1 for $T_{source} = 80^{\circ}C$ and $T_{storage} = 120^{\circ}C$

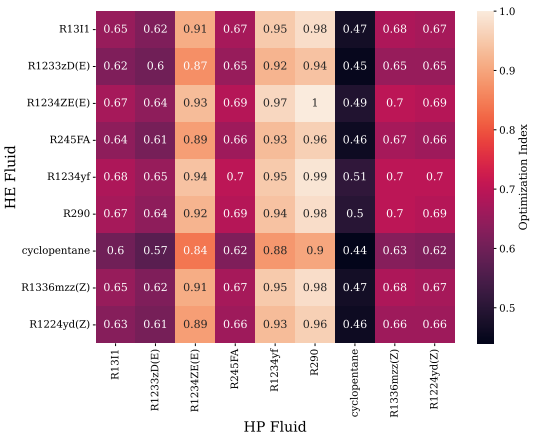

(e) Optimization Index Heat Map Scenario 1 for $T_{source} = 50^{\circ}C$ and $T_{storage} = 140^{\circ}C$

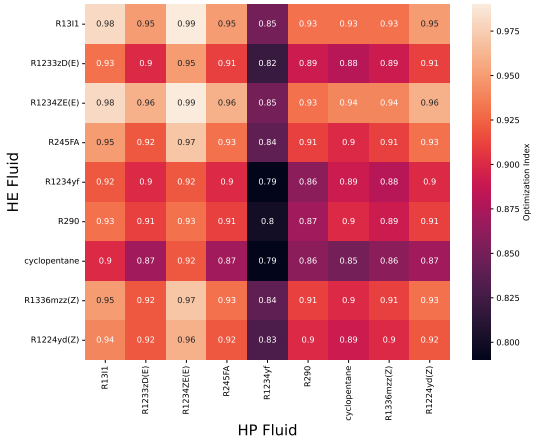

(f) Optimization Index Heat Map Scenario 1 for $T_{source} = 80^{\circ}C$ and $T_{storage} = 140^{\circ}C$

Figure 4.11: Different Fluid Optimization Index Heat Map Scenario 1: $(a = b = c = \frac{1}{3})$

$$
\begin{aligned}
Minimize f(\boldsymbol{x}) &= [f_1(\boldsymbol{x}), f_2(\boldsymbol{x})] \\
f_1(\boldsymbol{x}) &= \frac{1}{\eta_{rt}} \\
f_2(\boldsymbol{x}) &= \frac{1}{\rho_{en}} \\
\boldsymbol{x} &= [T_{source}, T_{storage}] \\
T_{source} &= [50, 80] \\
T_{storage} &= [90, 140]
\end{aligned}
\tag{4.22}
$$

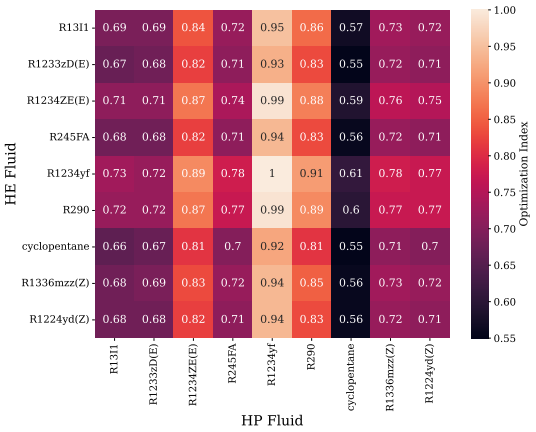

(a) Optimization Index Heat Map Scenario 2 for $T_{source} = 50^{\circ}C$ and $T_{storage} = 110^{\circ}C$

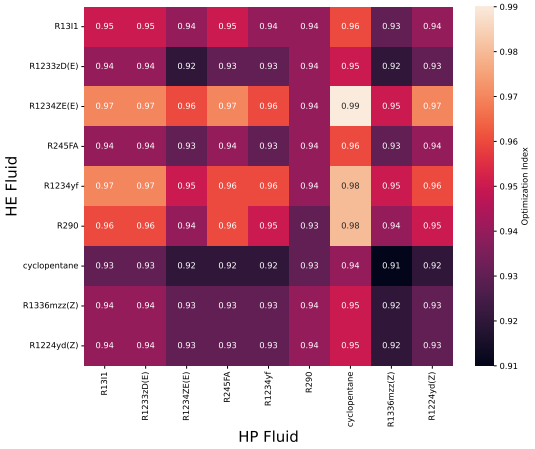

(b) Optimization Index Heat Map Scenario 2 for $T_{source} = 80^{\circ}C$ and $T_{storage} = 110^{\circ}C$

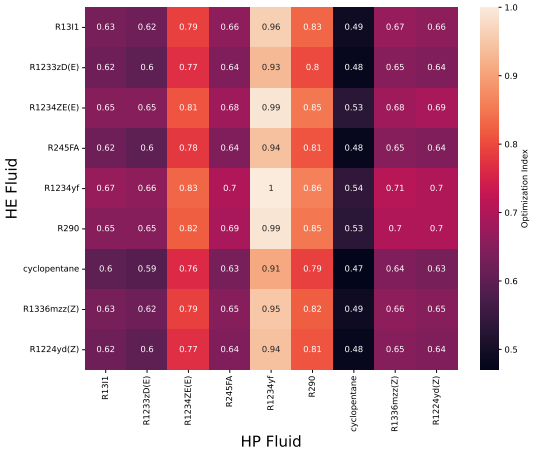

(c) Optimization Index Heat Map Scenario 2 for $T_{source} = 50^{\circ}C$ and $T_{storage} = 120^{\circ}C$

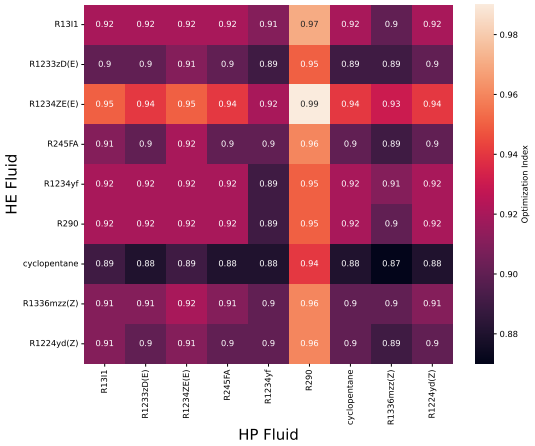

(d) Optimization Index Heat Map Scenario 2 for $T_{source} = 80^{\circ}C$ and $T_{storage} = 120^{\circ}C$

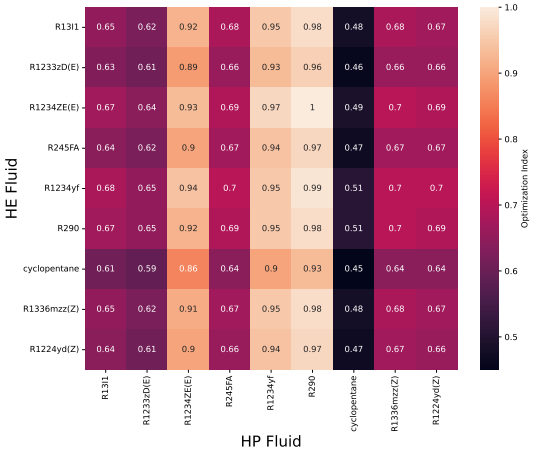

(e) Optimization Index Heat Map Scenario 2 for $T_{source} = 50^{\circ}C$ and $T_{storage} = 140^{\circ}C$

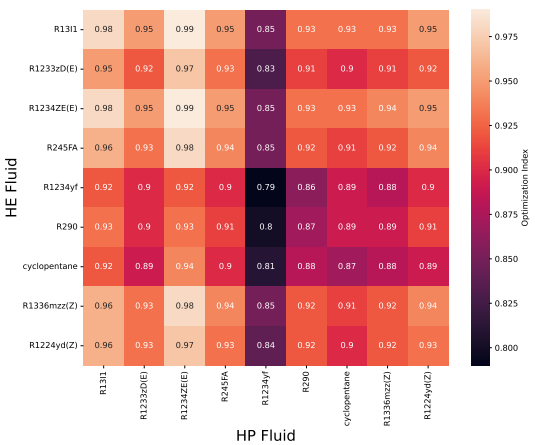

(f) Optimization Index Heat Map Scenario 2 for $T_{source} = 80^{\circ}C$ and $T_{storage} = 140^{\circ}C$

Figure 4.12: Different Fluid Optimization Index Heat Map Scenario 2: $(a = b = \frac{1}{2}); c = 0$

where $\boldsymbol{x}$ is the decision variable which is the source and storage temperature. $\varkappa$ is the variable space and F is the solution space.

If two variables $x_1, x_2 \in \varkappa$ satisfy the objective function, then a solution is said to be domi-

Table 4.3: Optimized HP:HE Selection for Scenario 2: $(a = b = \frac{1}{2}); c = 0$

		Source Temperature			
		50	**60**	**70**	**80**
Storage Temperature	**90**	R1234yf : R1234yf	R1234yf : R1234yf	Cyclopentane : R1234yf	Cyclopentane : Cyclopentane
	100	R1234yf : R1234yf	R1234yf : R1234yf	R1234yf : R1234yf	Cyclopentane : R1234yf
	110	R1234yf : R1234yf	R1234yf : R1234yf	R1234yf : R1234yf	Cyclopentane : R1234ZE(E)
	120	R1234yf : R1234yf	R1234yf : R1234ZE(E)	R290 : R1234ZE(E)	R290 : R1234ZE(E)
	130	R1234yf : R1234ZE(E)	R290 : R1234ZE(E)	R290 : R1234ZE(E)	R1234ZE(E) : R1234ZE(E)
	140	R290 : R1234ZE(E)	R1234ZE(E) : R1234ZE(E)	R1234ZE(E) : R1234ZE(E)	R1234ZE(E) : R1234ZE(E)

nant if $f_i(x_1) \leq f_i(x_2)$ for all values of i and there exists at least one value where $f_i(x_1) < f_i(x_2)$. This is represented mathematically in equation 4.23 [77].

$$[\forall i \in 1, 2, ..., m, f_i(x_1) \leq f_i(x_2)] \cap [\exists i \in 1, 2, ..., m, f_i(x_1) < f_i(x_2)] \tag{4.23}$$

NSGA-II logic is demonstrated in Figure 4.13 [32]. The logic work as follows:

- An initial population is formulated and assigned Gen 1 based on the determined population size.
- If offspring has been generated then new Gen 2 is formulated. Otherwise, ranking and selection have to be done based on the non-dominated solution method
- The offspring population is merged with the parent population to formulate a new mutated population
- Continue the offspring formulation and integration until the termination is reached

With this, a Pareto Front was formed for the heat pump and heat engine cycles for the listed fluids based on 20 population size and 100 number of generations. The objective solutions are shown in Figure 4.14a with the variables shown in Figure 4.14b.

From Figure 4.14a that the solution that maximizes both round trip efficiency η_{rt} and energy density ρ_{en} will be located in the top right corner of the graph. Therefore, the right side of the curves would represent the Pareto Front which is the optimum solution to the optimization problem. From the decision variable of storage and source temperature shown in Figure 4.14b, it can be seen that at low source temperature $T_{source} < 75°C$ the solution population is low compared to higher source temperature of $T_{source} > 75°C$ which shows higher solution population. For storage temperature, the population seems to be concentrated at low storage and high storage temperatures of $T_{storage} \leq 140°C$.

Indeed there is a low population for low source-low storage temperatures since the round trip efficiency, as well as energy density would both be low.

Multiple scenarios were studied depending on the source and storage temperature as well as whether compressor and expander isentropic efficiencies were assumed to be constants or a fit function based on typical compressor and expander models. The fit equations can be seen in Appendix A. The result of the different optimization scenarios can be seen in Table 4.4. The Pareto optimum solution figures for the different scenarios can be seen in Appendix B

The scenario of $T_{source} = [50 : 80]°C$ and $T_{storage} = [90 : 200]°C$ was selected as the basis for the remaining work since the storage temperature limit of pressurized water is $200°C$

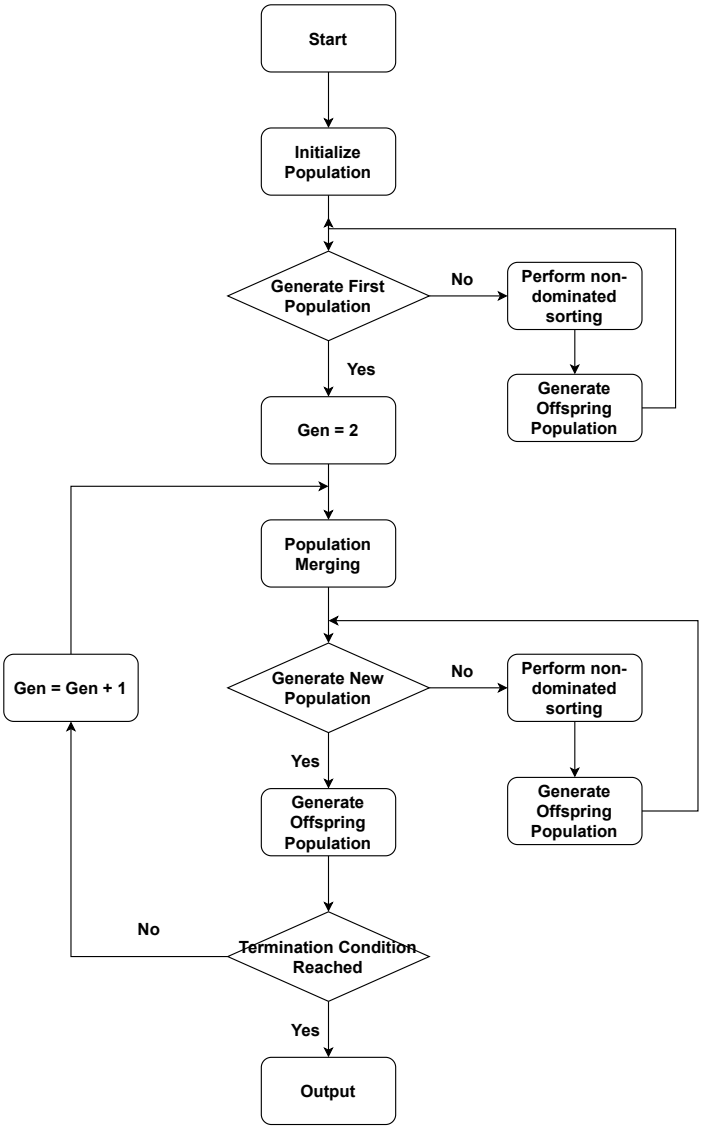

Figure 4.13: NSGA-II Logic [32]

Table 4.4: Multi-Objective Optimization Scenarios

Scenario	Fluid	$T_{source}[^{\circ}C]$	$T_{storage}[^{\circ}C]$	$\eta_{rt}[\%]$	$\rho_{en}[kWhr/m^3]$
$T_{sr}[50:80]; T_{st}[85:100]$	R1233ZD(E)	70	100	104.1%	4.4
$T_{sr}[50:80]; T_{st}[90:140]$	R1234ZE(E)	77	134	100.6%	10.1
$T_{sr}[50:80]; T_{st}[90:200]$	R13I1	79	139	100.2%	10.8
$T_{sr}[50:80]; T_{st}[85:100]; \eta_{is,fit}$	R13I1	79	100	100.6%	3.2
$T_{sr}[50:80]; T_{st}[90:140]; \eta_{is,fit}$	R13I1	78	97	101%	2.9

as mentioned earlier. With this, the optimization region is where a round trip efficiency of $\eta_{rt} \geq 75\%$ with energy density $\rho_{en} > 10kWhr/m^3$ as marked in figure 4.14a. With this in mind then fluid (R13I1) would be the most suitable fluid for this system considering that the

fluid represents the Pareto optimum at that range as can be seen in Figure 4.14a. This was selected to maximize round-trip efficiency in the selection region.

Subsequent to the optimization results, an optimized cycle working with R13I1 with the $T_{source} = 80°C$ & $T_{storage} = 140°C$ was modeled. The optimized cycle is based on the transcritical heat pump cycle and subcritical heat engine cycle as modeled in Figure 4.15a which shows the T-s diagram of the thermodynamic transcritical heat pump and sub-critical heat engine cycles working with these parameters. Figure 4.15b shows the heat flow energy in the heat pump and heat engine heat exchangers.

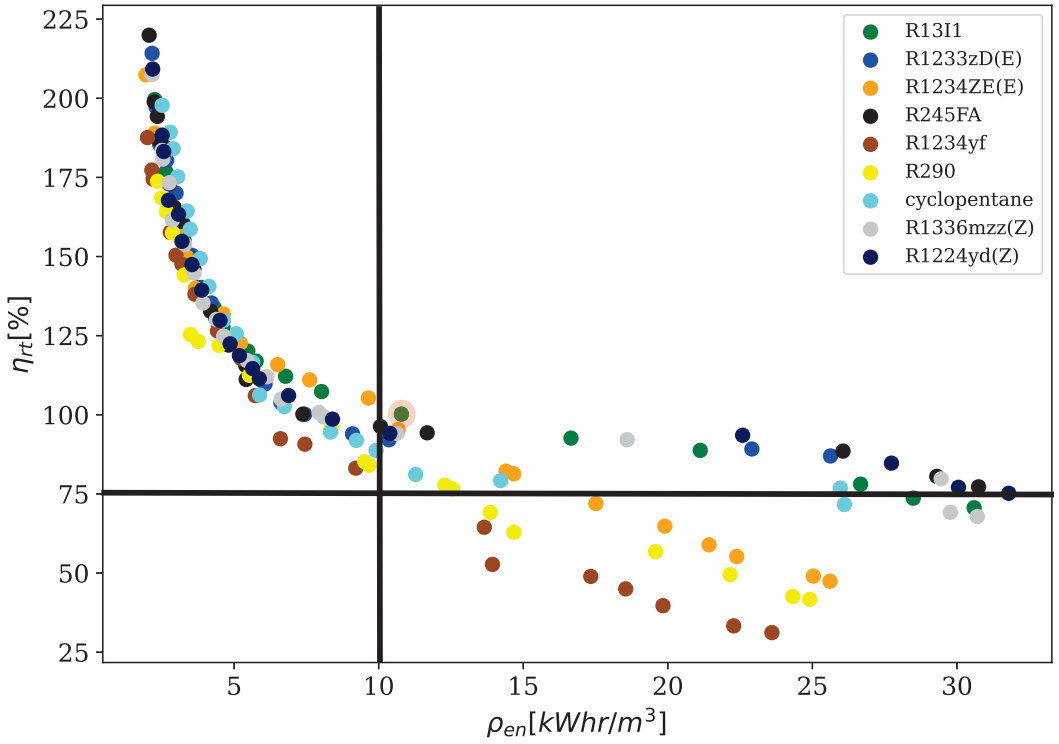

(a) Pareto Front Optimum Solution for Different Fluids of the PTES for $T_{source} = [50 : 80]^{\circ}C$ and $T_{storage} = [90 : 200]^{\circ}C$. The Highlighted Point Represents The Optimum Point

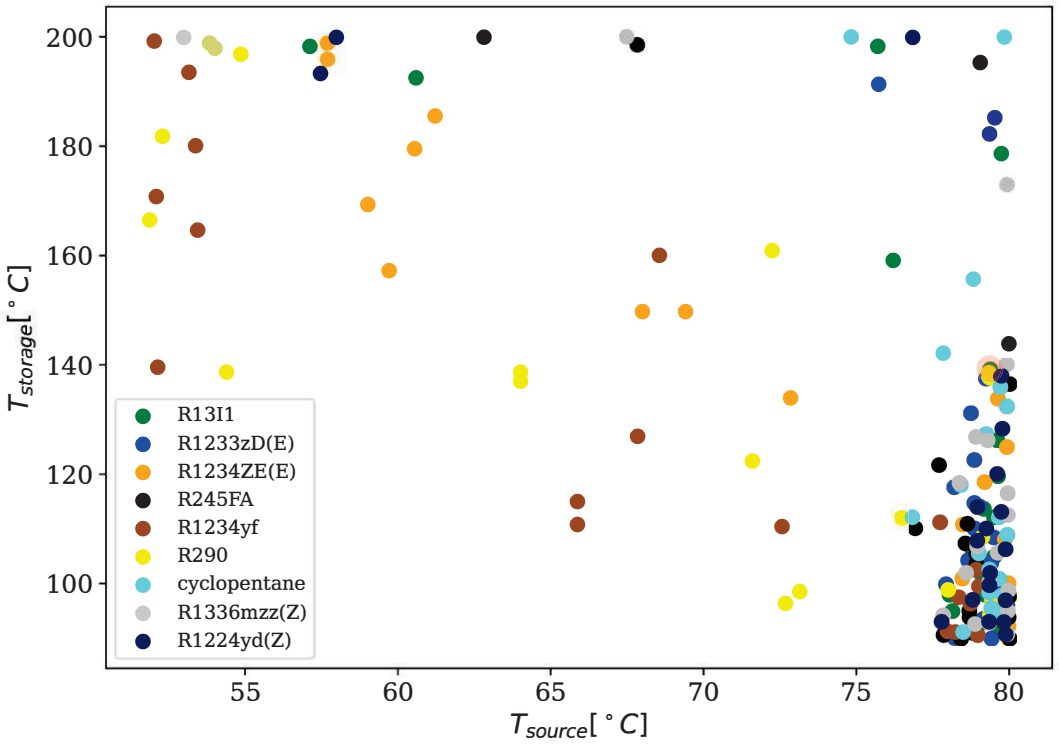

(b) Decision Variables of Source and Storage Temperatures For the Objective Solutions of Different Fluids of the PTES for $T_{source} = [50 : 80]^{\circ}C$ and $T_{storage} = [90 : 200]^{\circ}C$. The Highlighted Point Represents The Optimum Point

Figure 4.14: NSGA-II Pareto Front Optimum Solution for $T_{source} = [50 : 80]^{\circ}C$ and $T_{storage} = [90 : 200]^{\circ}C$. (a) Objective Solutions Pareto Front (b) Decision Variables of the Optimum Solution

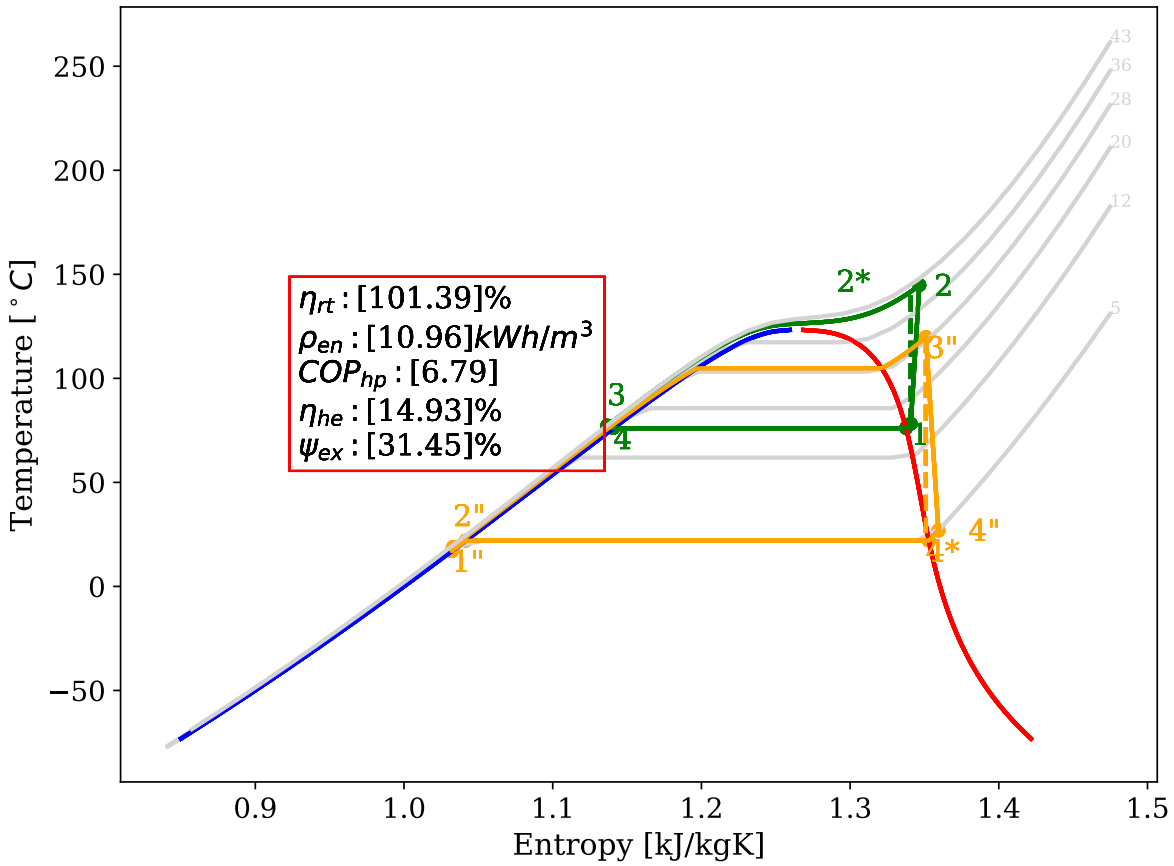

(a) R13I1 Optimized Thermodynamic Cycle (Green) (1 - 4) Charging Heat Pump Cycle (Orange) (1" - 4") Discharging Heat Engine Cycle

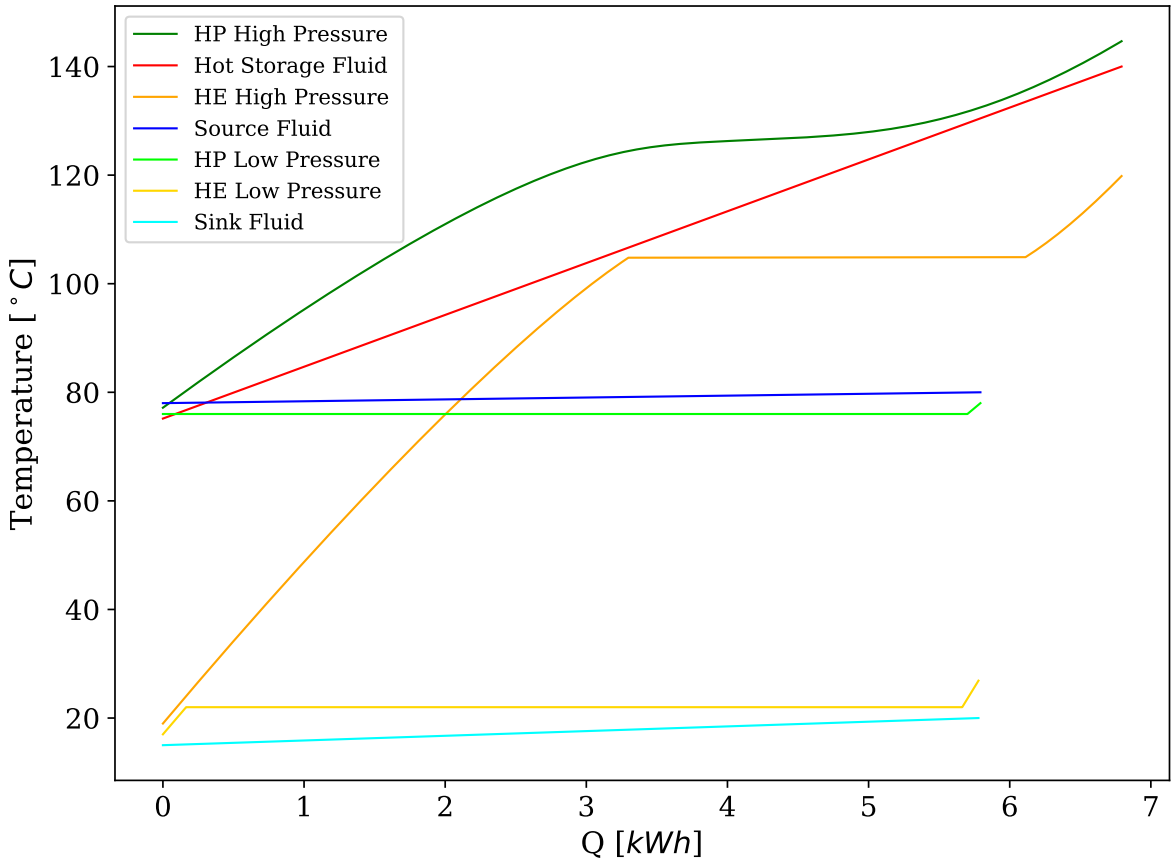

(b) R13I1 Optimized Cycle Heat Flow in (Green) Heat Pump High Pressure (Light Green) Heat Pump Low Pressure (Orange) Heat Engine High Pressure (Light Orange) Heat Engine Low Pressure (Red) Hot Storage Fluid (Blue) Source Fluid (Light Blue) Sink Fluid

Figure 4.15: R13I1 Optimized (a) Thermodynamic Cycle and (b) Heat Flow

5

Models Integration and Case Study

Following the results of the Pumped Thermal Energy Storage and the Component Models in the previous chapters, the models need to be integrated where the output models of the compressor and expander are used in the pumped thermal energy storage model. Additionally, a case study utilizing solar-integrated pumped thermal energy storage will be presented and discussed in this chapter.

5.1. Models Integration

In the previous Pumped Thermal Energy Storage section, the compressor and expander efficiencies were assumed to be constants while in reality, they are not. Hence, the three models namely the Pumped Thermal Energy Storage, Compressor, and Expander models were integrated to provide a more reliable result where the compressor and expander geometry as well as their isentropic efficiency can be determined and used in the Pumped Thermal Energy Storage Model.

In order to do so, the compressor model is used in the heat pump cycle while the expander is used in the heat engine cycle. The heat pump cycle set the geometry of the compressor which is then used as an expander in the heat engine cycle. Therefore, the pressure ratio across the heat pump cycle PR_{hp} set the build-in volumetric ratio VR_{comp} through equation 5.1.

$$VR_{comp} = PR_{hp}^{\frac{1}{\gamma_{pv}}} \tag{5.1}$$

Subsequently, the compressor start angle ϕ_a, base circle a, and thickness b are used as inputs to find the compressor swept volume V_s, end angle ϕ_e, and height h. This is achieved by assuming a swept volume $V_{swept,ass}$ and finding the height based on equation 5.2 and iterating over the model power $\dot{W}_{c,model}$ in comparison with cycle power $\dot{W}_{c,cycle}$. The logic of the integration can be seen in Figure 5.1

$$\phi_e = \frac{VR_{comp}\,(2\phi_a + \pi) + 3\pi}{2}$$
$$h = \frac{V_{swept}}{2\pi VR_{comp} ar\,(2\phi_a + \pi)} \tag{5.2}$$

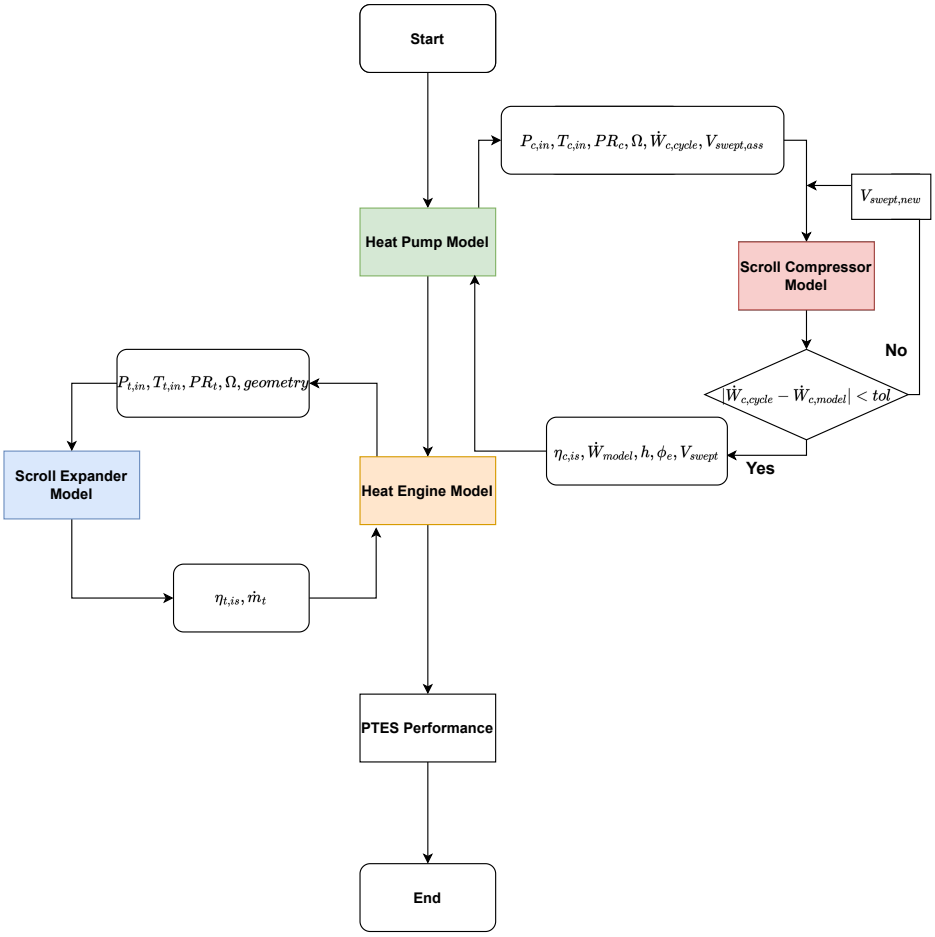

Figure 5.1: Integrated Model Logic

With these parameters, the compressor's built-in volumetric ratio is ensured to match the heat pump volumetric ratio to have the best efficiency possible for the compressor. The same geometry is then used for the expander model to determine the efficiency of the expander in the heat engine cycle.

In doing so, the following cycle was achieved for the source and storage temperature determined in the earlier chapter. Additionally, the charging time and discharging time were decoupled to have the discharging time as an output as supposed to an input. By integrating the two models, the cycle round trip efficiency, energy density, and exergy efficiency were found to be $\eta_{rt} = 93\%, \rho_{en} = 11.55 kWh/m^3$, and $\psi_{ex} = 29\%$ respectively as can be seen in Figure 5.2a with Table 5.1 summarizing the cycle results.

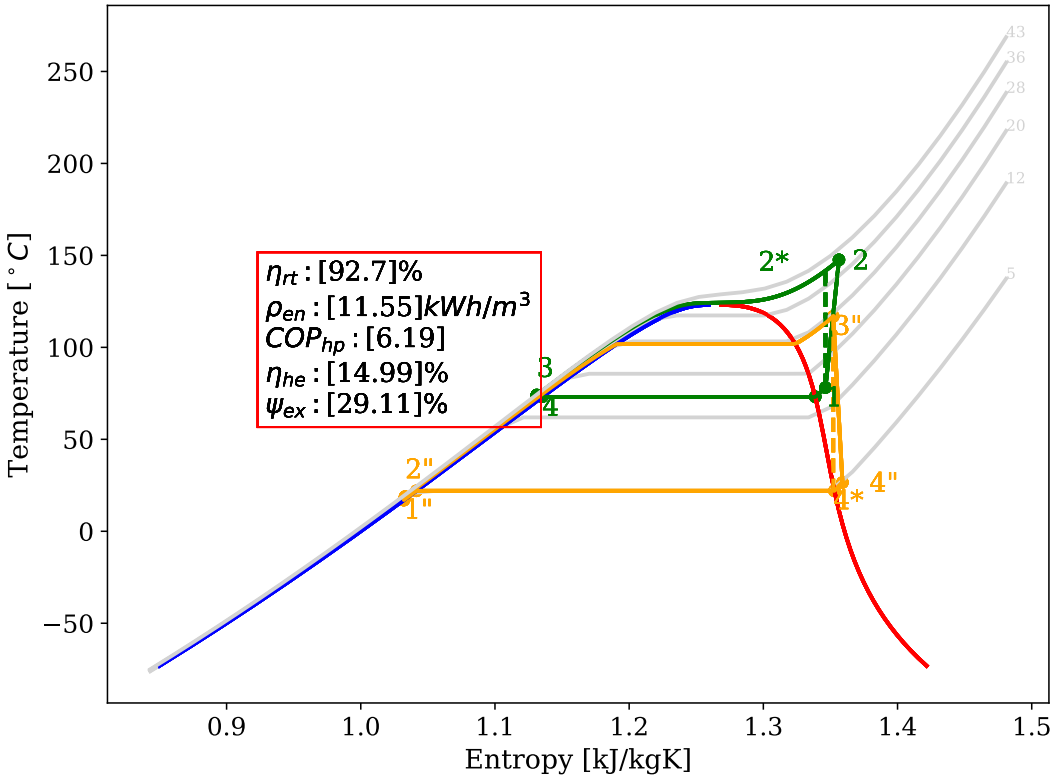

(a) T-s Diagram of R13I1 Integrated Model in the Optimized Cycle

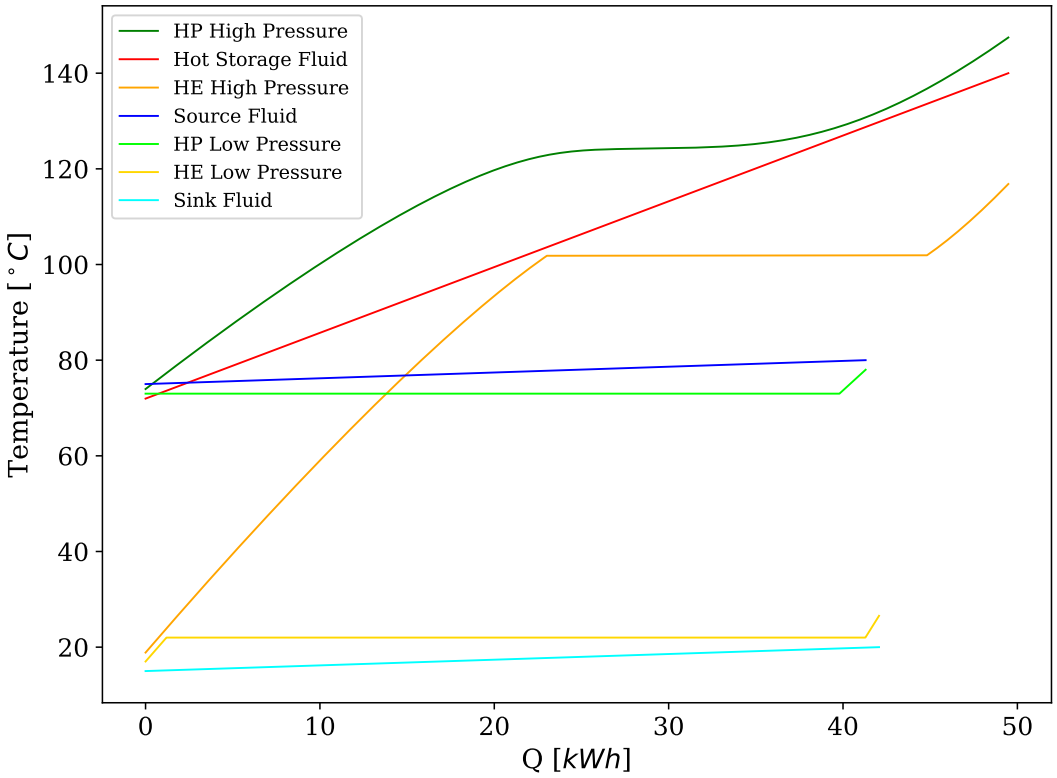

(b) Heat Flow of R13I1 Integrated Model in the Optimized Cycle

Figure 5.2: R13I1 Integrated Cycle (a) T-s Diagram (b) Heat Flow

Table 5.1: Integrated Cycle Results working with R13I1 with $T_{source} = 80^{\circ}C$ & $T_{storage} = 140^{\circ}C$

Input Parameter			Output Parameter		
Description	**Parameter**	**Value [Unit]**	**Description**	**Parameter**	**Value [Unit]**
Waste heat temperature	T_{source}	80[°C]	Heat Pump Mass Flow	$\dot{m}_{hp}$	0.07 $[kg/s]$
Ambient temperature	$T_{ambient}$	15 [°C]	Waste Heat Input	$\dot{Q}_{hp,in}$	5.16 $[kW]$
Degree of heat pump superheat, $(\Delta T_{hp,suph})$	$T_1 - T_4$	5 $[K]$	Heat Pump Output Heat	$\dot{Q}_{hp,out}$	6.19 $[kW]$
Storage temperature	$T_{storage}$	140 [°C]	Storage Mass Flowrate	$\dot{m}_{st}$	0.022 $[kg/s]$
Pump efficiency	$\eta_{is,pump}$	80 [%]	Heat Engine Input Heat	$\dot{Q}_{he,in}$	5.57 $[kW]$
Pinch across each heat exchanger	ΔT_{pinch}	2 $[K]$	Turbine Output Power	$\dot{W}_{turb}$	0.9 $[kW]$
Charging duration	t_{ch}	8 $[hr]$	Heat Engine Output Heat	$\dot{Q}_{he,out}$	4.7 $[kW]$
Compressor Input Power	$\dot{W}_{comp}$	1 $[kW]$	Pump Input Power	$\dot{W}_{pump}$	0.07 $[kW]$
Degree of Heat Engine Subcool $\Delta T_{he,supc}$	$T_2" - T_1"$	5 $[K]$	Heat Pump Coefficient of Performance	COP_{hp}	6.19 $[-]$
Degree of Heat Engine Superheat $\Delta T_{he,suph}$	$\Delta T_{he,suph}$	15 $[K]$	Heat Engine Efficiency	η_{he}	15 [%]
Base Circle	a	2.5 $[mm]$	Storage Volume	V_{st}	642 $[L]$
Involute Thickness	b	4.6 $[mm]$	Heat Engine Mass Flow	$\dot{m}_{he}$	0.05 $[kg/s]$
Rotation Speed	Ω	3000 $[RPM]$	Discharging Time	t_{dch}	8.9 $[hr]$
Involute Starting Angle	ϕ_a	0.9 π $[rad]$	Round Trip Efficiency	η_{rt}	93 [%]
Gap	$\delta_r; \delta_a$	15 μm	Energy Density	ρ_{en}	11.55 $[kWhr^3]$
			Exergy Efficiency	ψ_{ex}	29.11 [%]
			Compressor Isentropic Efficiency	$\eta_{c,is}$	71 [%]
			Expander Isentropic Efficiency	$\eta_{t,is}$	90 [%]
			Involute End Angle	ϕ_e	16.3 $[rad]$
			Involute Height	h	15 $[mm]$

5.2. Integrated Vs Constant Isentropic Efficiency Cycles

The integrated cycle model is compared with the constant isentropic efficiency model with equal charging and discharging time as can be seen in Table 5.2. It can be seen that due to the integration of the compressor and expander model, a more realistic isentropic efficiency of $\eta_{c,is} = 71\%$ can be realized which resulted in a drop in heat pump coefficient of performance by 9%. Consequently, the round trip efficiency of the system dropped by 8%. However, the energy density improved by 5% which is mainly attributed to the slight improvement in expander isentropic efficiency.

Table 5.2: Integrated Vs Constant Isentropic Model Compression

Parameter	Symbol	Constant Isentropic Model	Integrated Model	Difference
Compressor Isentropic Efficiency	$\eta_{c,is}$	80 [%]	71[%]	(11) [%]
Expander Isentropic Efficiency	$\eta_{t,is}$	88 [%]	90 [%]	2 [%]
Heat Pump Coefficient of Performance	COP_{hp}	6.79 $[-]$	6.19 $[-]$	(9) [%]
Heat Engine Efficiency	η_{he}	14.9 [%]	15 [%]	1 [%]
Round Trip Efficiency	η_{rt}	101 [%]	93 [%]	(8) [%]
Energy density	ρ_{en}	10.96 $[kWhr]$	11.55 $[kWhr]$	5 [%]
Exergy Efficiency	ψ_{ex}	31.45 [%]	29.11 [%]	(7) [%]

5.3. Solar Integrated Pumped Thermal Energy Storage

Weather data for South Holland were collected from [1] to assess the solar irradiation throughout the year as can be seen in Figure 5.3. The maximum direct irradiation was reported to be $\dot{Q}_{ir} = 413.05 W/m^2$. Additionally, the annual household energy consumption in the Netherlands was reported to be $\dot{E}_{cons} = 2772.5 kWhr$ [51]. These values will serve as the basis for the solar system calculations. A hybrid system capable of delivering both electrical and thermal energy based on solar irradiation can be utilized. The solar panel data was based on the one manufactured by (DUALSUN) [16] with the panel properties shown in table 5.3.

The number of electrical panels required to supply the required load is calculated based

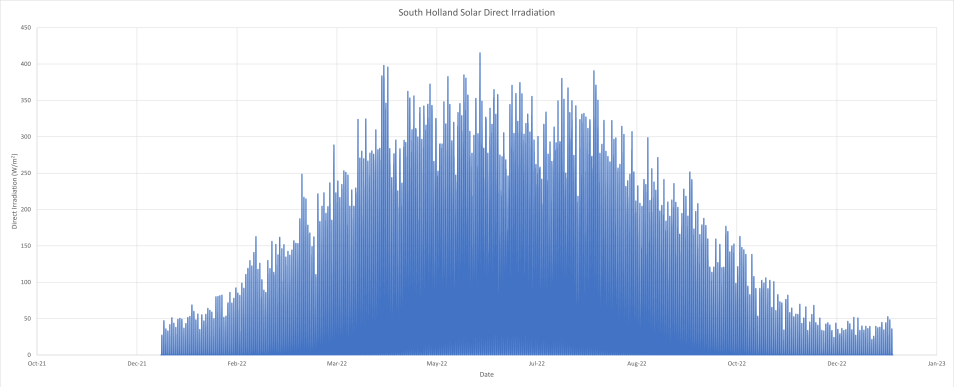

Figure 5.3: South Holland Solar Direct Irradiation Variation Throughout the Year [1]

Table 5.3: Hybrid Solar Panel Data [16]

Photovoltaic Characteristics		Thermal Characteristics	
Parameter	**Value [Unit]**	**Parameter**	**Value [Unit]**
Nominal Power	$400[W/Panel]$	Thermal Power	$1238[W/Panel]$
Electrical Efficiency	$21.3[\%]$	Thermal Efficiency	$65.93[\%]$
Collector Area	$1.876[m^2]$		

on the annual energy consumption E_{con} and the solar hours in a day h_{solar} by determining the solar array output SAO and the solar array size SAS. These are calculated from equation 5.3:

$$\begin{aligned} SAO &= \frac{E_{con}}{365 \times h_{solar}} \\ SAS &= SAO\frac{B_{off}}{a_{env}} \\ N_{panel} &= \frac{SAS \times 1000}{\dot{E}_{panel}} \end{aligned} \tag{5.3}$$

Where B_{off} is the bill offset which is normally 90%, a_{env} is the environmental factor which is normally 80%, $\dot{E}_{panel}$ is the typical panel output power which is normally between $150-300W$ as per [64] with a value of $150W$ was selected for this calculation.

With this in mind, table 5.4 shows the solar system sizing based on a maximum irradiation day.

Subsequently, the daily performance of the system can be seen in Figure 5.4. The charging cycle starts when excess electrical energy (blue line) is stored in the form of heat (brown line) during day time with the peak stored value at noon time. The stored heat is then consumed in the heat engine discharging cycle to produce electrical energy (red line) during night time.

An overall layout of the system can be seen in Figure 5.5. It is noticeable that the source outlet temperature and the storage fluid inlet temperature are similar and therefore using the outlet of the source as an inlet to the storage will reduce the number of storage tanks which increases the energy density.

Table 5.4: Solar System Results

Parameter	Value [Unit]
Solar Irradiation	$413.05[W/m^2]$
Storage Hours	$8[hr]$
Electrical Power Production	$166[W/Panel]$
Thermal Power Production	$511[W/Panel]$
Number of Electrical Panel	$8[Panels]$
Total Electrical Production	$11[kWhr]$
Total Thermal Production	$33[kWhr]$
Total Energy Consumption for 8 Hours	$2.5[kWhr]$
Storage	$8[kWhr]$
Total Thermal Energy Required	$42[kWhr]$
Additional Thermal Panel Required	$3[Panels]$

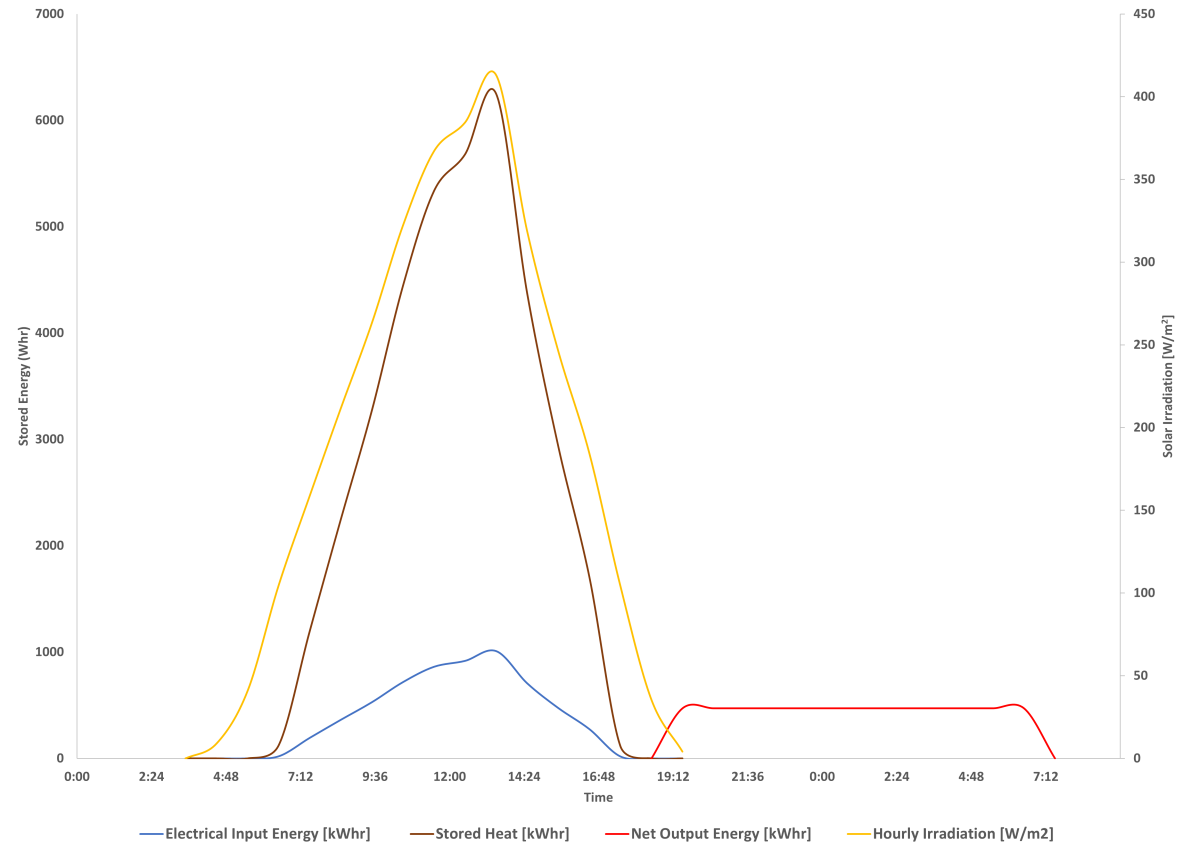

Figure 5.4: Daily Solar Integrated Storage System Performance

5.4. Components Sizing

5.4.1. Heat Exchanger

For a heat exchanger, a plate heat exchanger was selected due to its compactness, suitability for low flows, wide temperature and pressure operating range, and small approach temperature as mentioned earlier.

A chevron-type plate heat exchanger was selected to enhance the heat transfer coefficient capabilities as can be seen in Figure 5.6a where B_p is the plate width, L_p is the plate length, ϕ is the inclination angle, $2\hat{a}$ is the gap between the two plats, and A is the wavelength.

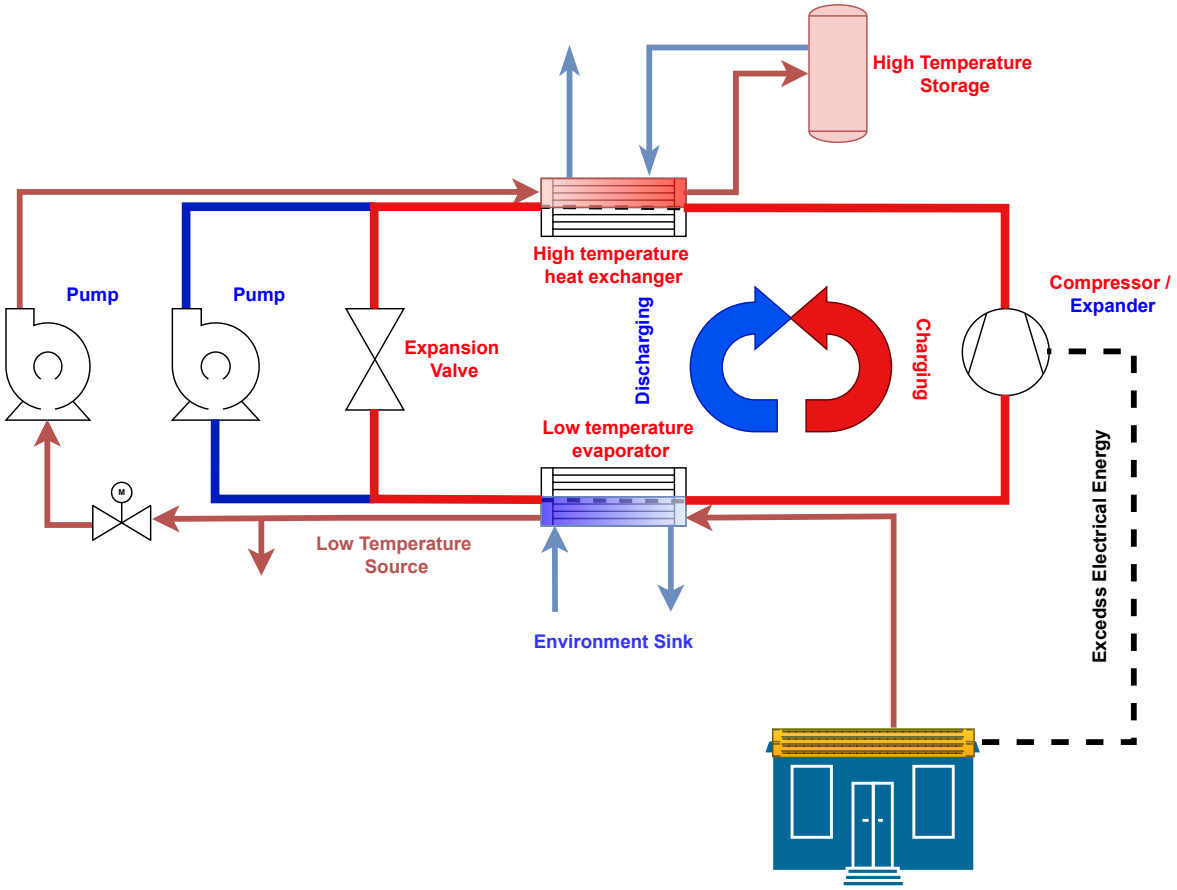

Figure 5.5: Solar Integrated Pumped Thermal Energy Storage System Daily Performance

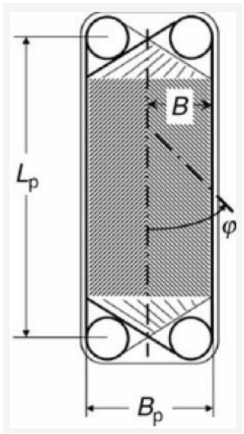

(a) Chevron Type Plate Design [22]

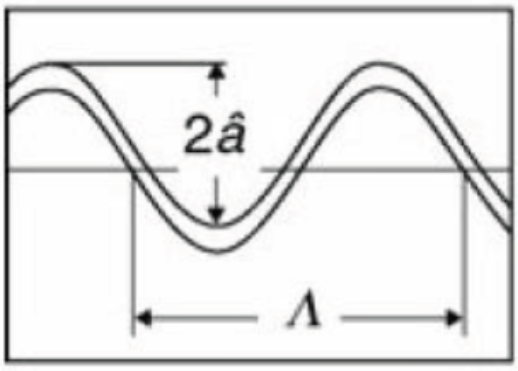

(b) Chevron Type Plate Gap [22]

Figure 5.6: Chevron Type Plate Design [22]

With this, a counter-current parallel flow would be used with a single pass as can be seen in figure 5.7.

ASPEN Exchanger Design and Rating V12 software was used to size the heat exchanger based on the process parameters. The duty of the heat pump high-pressure heat exchanger is similar to the high-pressure heat engine. Additionally, the low-pressure heat pump and low-pressure heat engine heat exchangers are also similar which facilitates re-usability which is

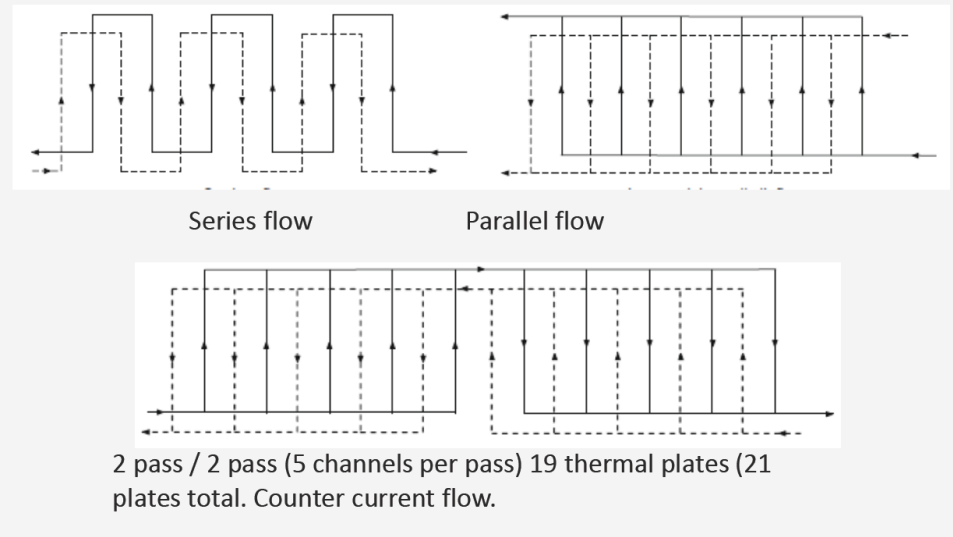

Figure 5.7: Flow Arrangement [70]

achieved by decoupling charging and discharging time while maintaining the energy balance over the high-pressure heat exchanger. Therefore the following table 5.5 shows the high-pressure and low-pressure heat exchangers.

Table 5.5: Sizing of the High-Pressure and Low-Pressure Heat Exchangers

Parameter	HP Heat Exchange	LP Heat Exchanger
Duty $[\dot{Q}]$	5.9 $[kW]$	5.4 $[kW]$
Process Temperatures $[T_{in}; T_{out}]$	147 ; 74 $[°C]$	73 ; 76 $[°C]$
Water Temperatures $[t_{in}; t_{out}]$	72 ; 140 $[°C]$	80 ; 75 $[°C]$
Process Pressure $[P_{wf}]$	40 $[bar]$	16 $[bar]$
Water Pressure $[P_{water}]$	5 $[bar]$	1 $[bar]$
Heat Transfer Area $[A_o]$	19.5 $[m^2]$	13.6 $[m^2]$
Overall Heat Transfer Coefficient $[U_o]$	33.3 $[W/m^2K]$	110 $[W/m^2K]$
Number of Passes $[N_{ps}]$	1 $[-]$	1 $[-]$
Number of Plates $[N_{pl}]$	341 $[-]$	239 $[-]$
Plates Length $[L_p]$	463 $[mm^2]$	463 $[mm^2]$
Plates Width $[B_p]$	133 $[mm^2]$	133 $[mm^2]$
Chevron Angle $[\phi]$	30 [°]	60 [°]

5.4.2. Pump

The pump in the heat engine cycle has to be selected based on the required flow rate and pressure head. Positive displacement pumps are suitable for low-flow/high-pressure applications as recommended by [50]. Figure 5.8 shows that gear pumps are the most suitable pump for the given volumetric flow rate and discharge pressure with table 5.6 showing the pump parameters.

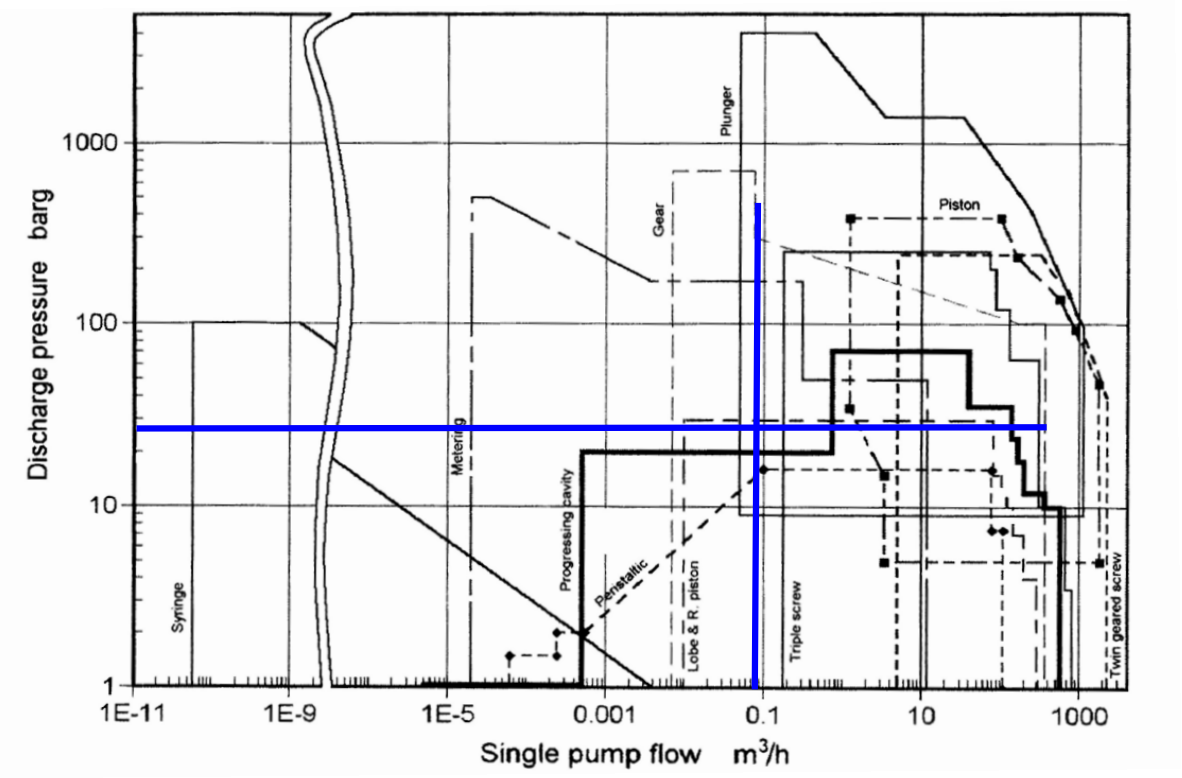

Figure 5.8: Positive Displacement Pump Selection for the Heat Engine Cycle [50]

Table 5.6: Heat Engine Pump Sizing

Parameter	Value
Pump Power $[\dot{Q}]$	67 $[W]$
Pressure Ratio $[PR_{pump}]$	6 $[-]$
Discharge Pressure $[P_{dis}]$	27 $[bar]$
Mass Flowrate $[\dot{m}_{he}]$	49 $[g/s]$
Volumetric Flowrate $[\dot{V}_{he}]$	0.09 $[m^3/h]$

6

Conclusion and Recommendations

6.1. Conclusion

The main objective of this work was to model and optimize a small-scale thermally integrated pumped thermal energy storage with integrated compressor and expander models. This was achieved by analyzing multiple fluids in the heat pump and heat engine cycle through simple multi-fluid optimization schemes and single-fluid multi-objective optimization schemes based on a non-dominated sorting genetic algorithm (NSGA-II). Through the optimization model, $R13I1$ was selected as the optimum fluid with a transcritical heat pump and subcritical heat engine cycles with source temperature and storage temperature of $T_{source} = 80°C$ and $T_{storage} = 140°C$ respectively.

Additionally, scroll compressor and expander models were developed to predict the overall isentropic efficiency of the compressor and expander based on different operating conditions like pressure ratio, rotation speed, and gap. Through the models, an optimum pressure ratio for the compressor and expander was identified to be around $PR = 3$ which depends on the compressor and expander geometry. While increasing the rotation speed increases the isentropic efficiency, there is a limit beyond which the efficiency decreases with increasing rotation speed which was identified to be $\Omega = 4000RPM$.

Moreover, the compressor and expander models were integrated into the pumped thermal energy storage model. The compressor geometry is determined based on the cycle volumetric ratio which resulted in a more realistic compressor isentropic efficiency of $\eta_{c,is} = 71\%$. With the interchangeable need to use the compressor as an expander, the expander isentropic efficiency was determined to be $\eta_{t,is} = 90\%$. This in turn impacted the overall performance of the storage system in terms of round trip efficiency, energy density, and exergy efficiency as the integrated model result are $\eta_{rt} = 93\%, \rho_{en} = 12kWhr/m^3$ and $\psi_{ex} = 29\%$ respectively.

Finally, a case study utilizing the result of the integrated model in a solar system was presented. Dual electrical and heat panels were modeled to maximize the output energy of the solar system. The excess electrical energy generated by the solar system is stored in a $1kW$ pumped thermal energy storage system. A total of 11 panels are needed for the system where 8 are used for electrical power generation and 3 are used for additional thermal energy input.

6.2. Recommendation

The present work demonstrated the validity of using thermally integrated small scale pumped thermal energy storage by modeling the cycle along with the compressor and expander. The following recommendations for future work will enhance the understanding of the system.

- Experimental validation of the storage system. The current work focused on modeling the storage system with integrated compressor and expander models. However, experimental validation of the performance of the cycle under different operating conditions will provide a better understanding of the storage system.
- Including heat transfer in the compressor and expander model. The compressor and expander models were assumed to be adiabatic and heat exchange between two adjacent chambers is negligible which overestimated the isentropic efficiency. Therefore, including heat transfer models will provide a more reliable isentropic efficiency of the compressor and expander.
- Integrating the compressor and expander models into the multi-objective optimization scheme. Currently, the optimization assumed a constant isentropic efficiency for the compressor and expander or a variable one based on the fit equation. However, the fit equation is dependent on the geometry and therefore it will tend to favor the pressure ratio associated with its built-in volumetric ratio. Therefore, integrating the compressor and expander model into the optimization scheme will provide a more realistic understanding of the system.
- The entire model assumes a steady state where no time dependence was considered. Therefore, a dynamic analysis should be carried out to understand the behavior of the system under transient conditions.
- Cost benefit should be carried out to validate the proposed case study. The current model was based on maximizing the performance of the thermodynamic cycles without considering the overall cost impact of the system.

A

Compressor and Expander Fit Equation

The outcome of the compressor and expander models was to generate the variation of efficiency with pressure ratio and rotation speed. This was achieved for multiple fluids as demonstrated in the components chapter 3. With this model, fit equations were generated for the different rotation speeds as shown in Figure A.1. Equation A.1 for rotation speed $\Omega = 3000RPM$ was used in the simulation of the optimization cases with the variation of rotation speed. It is worth noting that these fit equations are geometric specific and therefore they tend to favor the pressure ratio associated with their built-in volumetric ratio.

$$\begin{aligned}\eta_{c,is} = &-0.0000324071PR^6 + 0.0012880077PR^5 - 0.0208218119PR^4 + 0.1751410700PR^3 \\ &- 0.8063194844PR^2 + 1.8740061799PR - 0.9524107129 \\ \eta_{t,is} = &-0.0000451090PR^6 + 0.0018509869PR^5 - 0.0309759252PR^4 + 0.2701006278PR^3 \\ &- 1.2892141206PR^2 + 3.1367418978PR - 2.1884281655\end{aligned} \tag{A.1}$$

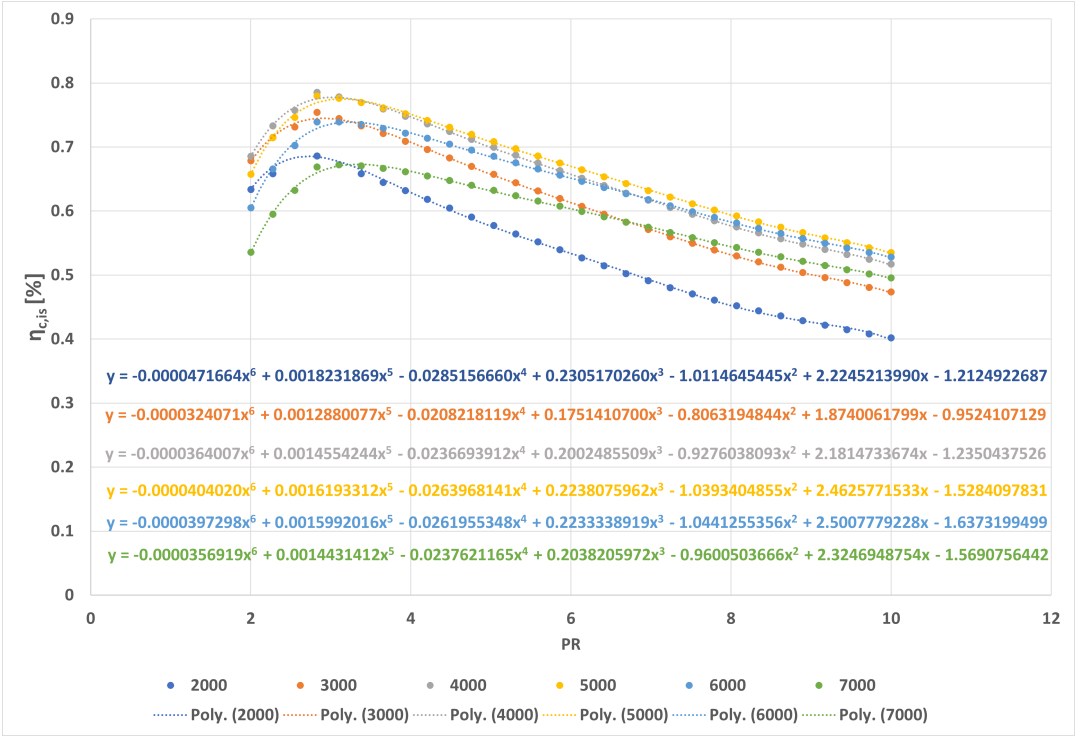

(a) Compressor Fit Equations Efficiency Variation with Pressure Ratio and Rotation Speed

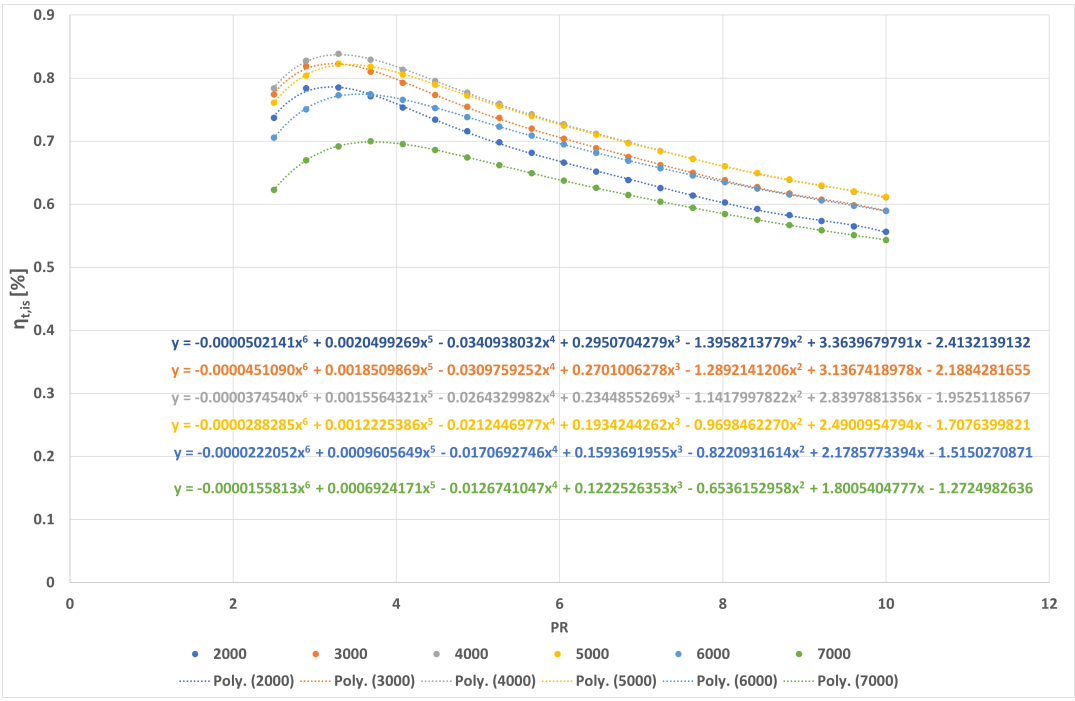

(b) Expander Fit Equations Efficiency Variation with Pressure Ratio and Rotation Speed

Figure A.1: Fit Equations Efficiency Variation with Pressure Ratio and Rotation Speed for (a) Compressor (b) Expander

B

Pumped Thermal Energy Storage

B.1. Pareto Optimum Solution Multiple Scenarios

Several scenarios were studied to determine the Pareto optimum solution for pumped thermal energy storage. This was done to determine the most optimum fluid along with the source and storage temperature that would maximize round trip efficiency η_{rt} and energy density ρ_{en}. With this in mind, the following scenarios were studied:

- Low storage temperature scenario where source temperature $T_{sr} = [50 : 80]$ and storage temperature $T_{st} = [85 : 100]$ with constant compressor and expander isentropic efficiencies.
- Mid storage temperature scenario where source temperature $T_{sr} = [50 : 80]$ and storage temperature $T_{st} = [90 : 140]$ with constant compressor and expander isentropic efficiencies.
- High storage temperature scenario where source temperature $T_{sr} = [50 : 80]$ and storage temperature $T_{st} = [90 : 200]$ with constant compressor and expander isentropic efficiencies.
- Low storage temperature scenario where source temperature $T_{sr} = [50 : 80]$ and storage temperature $T_{st} = [85 : 100]$ with fit equation compressor and expander isentropic efficiencies.
- Mid storage temperature scenario where source temperature $T_{sr} = [50 : 80]$ and storage temperature $T_{st} = [90 : 140]$ with fit equation compressor and expander isentropic efficiencies.

The following Figure B.1 showcases the results of the Pareto Optimum solution using NSGA-II for the different scenarios.

The following Figure B.2 show the Pareto optimum cycles:

The following Figure B.3 show the Pareto optimum heat flow:

B.2. Exergy Analysis

Exergy refers to the theoretical amount of work that could be extracted from a reversible process aimed at attaining thermodynamic equilibrium between a flow and its surrounding environment [37]. The exergy of a flow of state (i) can be calculated from Equation B.1:

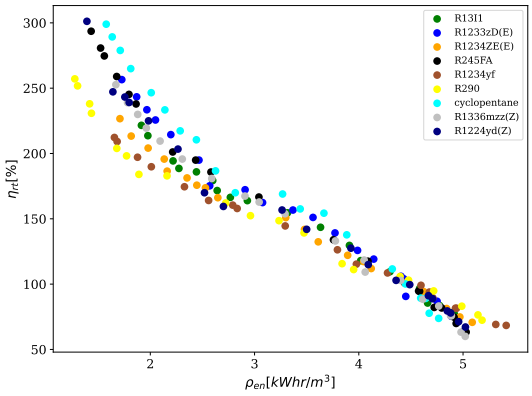

(a) Low Storage Temperature Scenario $T_{source} = [50:80]^\circ C$ and $T_{storage} = [85:100]^\circ C$ with Constant Isentropic Efficiency

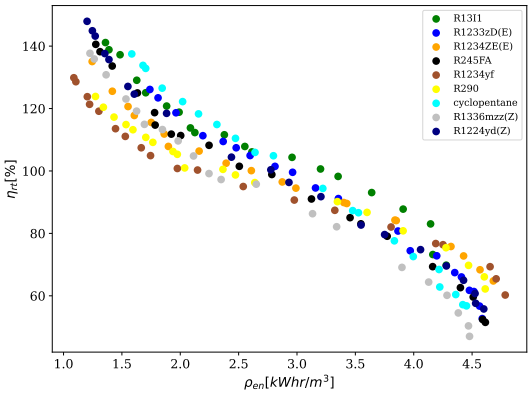

(b) Low Storage Temperature Scenario $T_{source} = [50:80]^\circ C$ and $T_{storage} = [85:100]^\circ C$ with Fit Isentropic Efficiency

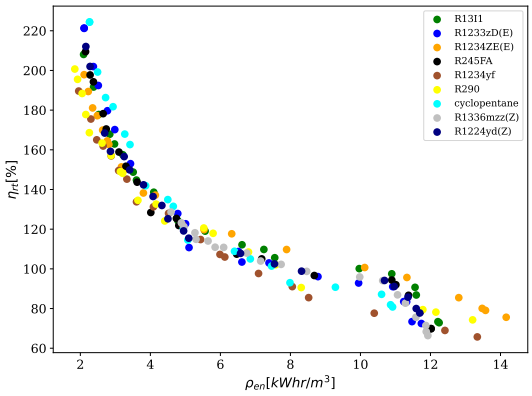

(c) Mid Storage Temperature Scenario $T_{source} = [50:80]^\circ C$ and $T_{storage} = [90:140]^\circ C$ with Constant Isentropic Efficiency

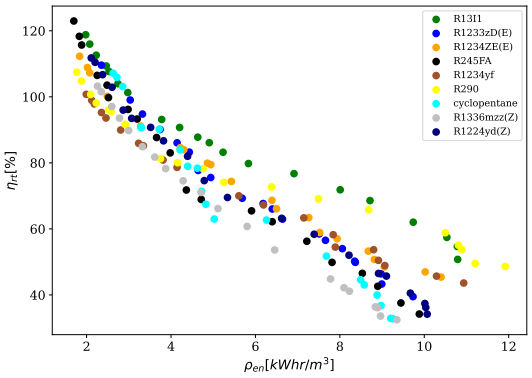

(d) Mid Storage Temperature Scenario $T_{source} = [50:80]^\circ C$ and $T_{storage} = [90:140]^\circ C$ with Fit Isentropic Efficiency

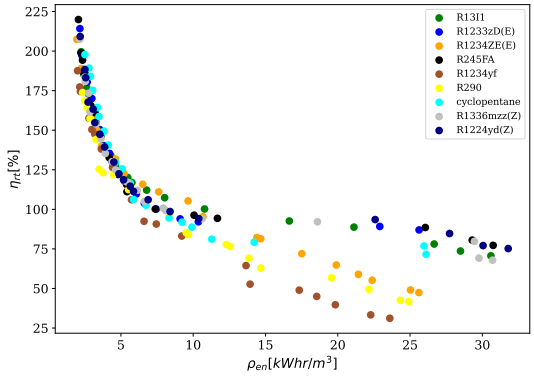

(e) High Storage Temperature Scenario $T_{source} = [50:80]^\circ C$ and $T_{storage} = [90:200]^\circ C$ with Constant Isentropic Efficiency

Figure B.1: NSGA-II Pareto Front Optimum Solution for (a) Low Storage temperature with Constant Isentropic Efficiency (b) Low Storage temperature with Fit Isentropic Efficiency (c) Mid Storage temperature with Constant Isentropic Efficiency (d) Mid Storage temperature with Fit Isentropic Efficiency (e) High Storage temperature with Constant Isentropic Efficiency

$$\dot{Ex}_i = \dot{m}\left[(h_i - h_{env}) - T_{env}(s_i - s_{env}) + \frac{1}{2}c_i^2 + gz_i\right]$$

Neglecting Kinetic and Potential:

$$\dot{Ex}_i = \dot{m}\left[(h_i - h_{env}) - T_{env}(s_i - s_{env})\right] \tag{B.1}$$

An exergy analysis was done to quantify exergy destruction on each component of the cycle to try and understand where energy is lost around the system. The following Table B.1 shows the exergy destruction formulation in each component of the system. A reference environmental value of $T_{env} = 15°C, P_{env} = 1.01[bar]$ was used to find the reference environmental thermodynamic properties like specific enthalpy, specific entropy, density, ..., etc.

Table B.1: Exergy Destruction Formulations [21]

Component	Energy Relation	Exergy Relation
Turbine	$W_{turb} = \dot{m}_{he}\eta_{is,turb}(h_{turb,in} - h_{turb,out})$	$\dot{Ex}_{D,turb} = \dot{Ex}_{turb,in} - \dot{Ex}_{turb,out} - \dot{W}_{turb}$
Pump	$\dot{W}_{pump} = \frac{\dot{m}_{he}}{\eta_{is,pump}}(h_{pump,out} - h_{pump,in})$	$\dot{Ex}_{D,pump} = \dot{Ex}_{pump,in} - \dot{Ex}_{pump,out} + \dot{W}_{pump}$
Heat Engine Cold Heat Exchanger	$\dot{Q}_{he,out} = \dot{m}_{he}(h_{he,coldhex,wf,out} - h_{he,coldhex,wf,in})$	$\dot{Ex}_{D,he,coldhex} = \dot{Ex}_{he,coldhex,wf,out} - \dot{Ex}_{he,coldhex,wf,in} + \dot{Ex}_{coldhex,colant,out} - \dot{Ex}_{coldhex,colant,in}$
Heat Engine Hot Heat Exchanger	$\dot{Q}_{he,in} = \dot{m}_{he}(h_{he,hothex,wf,out} - h_{he,hothex,wf,in})$	$\dot{Ex}_{D,he,hothex} = \dot{Ex}_{he,hothex,wf,out} - \dot{Ex}_{he,hothex,wf,in} + \dot{Ex}_{hothex,colant,out} - \dot{Ex}_{hothex,colant,in}$
Heat Pump Hot Heat Exchanger	$\dot{Q}_{hp,out} = \dot{m}_{hp}(h_{hp,hothex,wf,out} - h_{hp,hothex,wf,in})$	$\dot{Ex}_{D,hp,hothex} = \dot{Ex}_{hp,hothex,wf,out} - \dot{Ex}_{hp,hothex,wf,in} + \dot{Ex}_{hothex,colant,out} - \dot{Ex}_{hothex,colant,in}$
Heat Pump Cold Heat Exchanger	$\dot{Q}_{hp,in} = \dot{m}_{hp}(h_{hp,coldhex,wf,out} - h_{hp,coldhex,wf,in})$	$\dot{Ex}_{D,hp,coldhex} = \dot{Ex}_{hp,coldhex,wf,out} - \dot{Ex}_{hp,coldhex,wf,in} + \dot{Ex}_{coldhex,colant,out} - \dot{Ex}_{coldhex,colant,in}$
Compressor	$\dot{W}_{comp} = \frac{\dot{m}_{hp}}{\eta_{is,comp}}(h_{comp,out} - h_{comp,in})$	$\dot{Ex}_{D,comp} = \dot{Ex}_{comp,in} - \dot{Ex}_{comp,out} + \dot{W}_{comp}$
Expansion Valve	–	$\dot{Ex}_{D,EV} = \dot{Ex}_{EV,in} - \dot{Ex}_{EV,out}$

Performing the analysis on the integrated cycle yields the exergy loss and exergy destruction percentage in each component of the system as seen in Figure B.4. It can be seen that most exergy is lost in the HE hot heat exchanger with (31%) due to the large mismatch between the working fluid temperature and the storage. Followed by the compressor with (20%) due to its low isentropic efficiency.

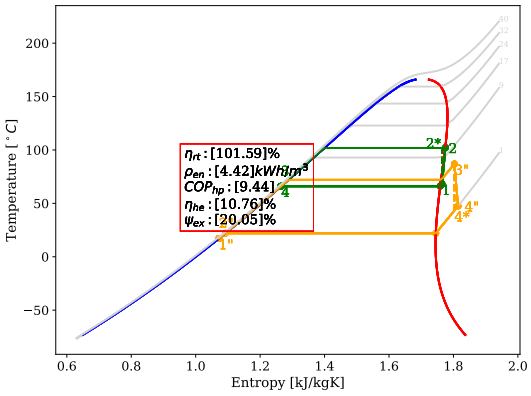

(a) R1233ZD(E) Low Storage Temperature Scenario $T_{source} = 70°C$, $T_{storage} = 100°C$, $PR_{hp} = 2.4$, and $PR_{he} = 4.6$ with Constant Isentropic Efficiency

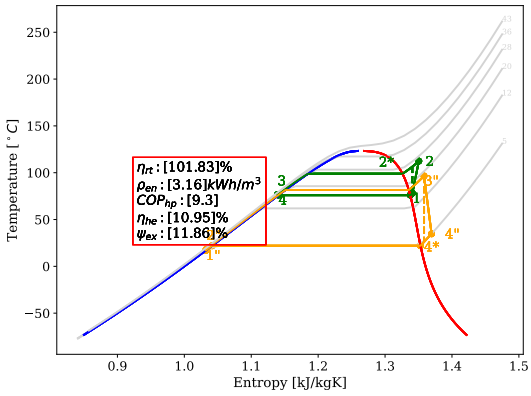

(b) R13I1 Low Storage Temperature Scenario $T_{source} = 80°C$, $T_{storage} = 100°C$, $PR_{hp} = 1.6$, and $PR_{he} = 4.1$ with Fit Isentropic Efficiency

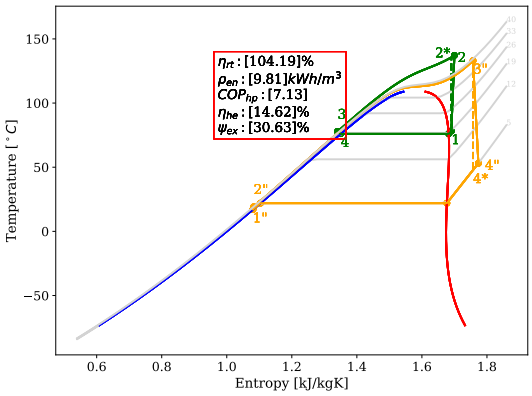

(c) R1234ZE(E) Mid Storage Temperature Scenario $T_{source} = 80°C$, $T_{storage} = 135°C$, $PR_{hp} = 2.8$, and $PR_{he} = 8.6$ with Constant Isentropic Efficiency

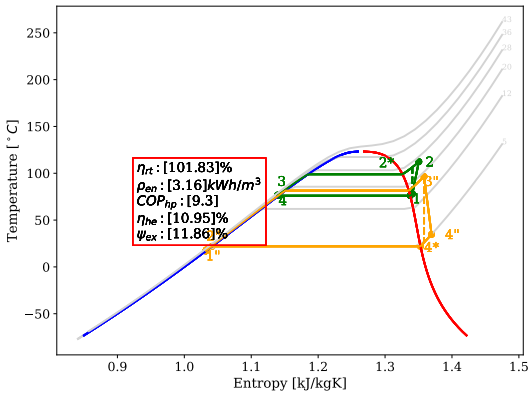

(d) R13I1 Mid Storage Temperature Scenario $T_{source} = 80°C$, $T_{storage} = 100°C$, $PR_{hp} = 1.6$, and $PR_{he} = 4.1$ with Fit Isentropic Efficiency

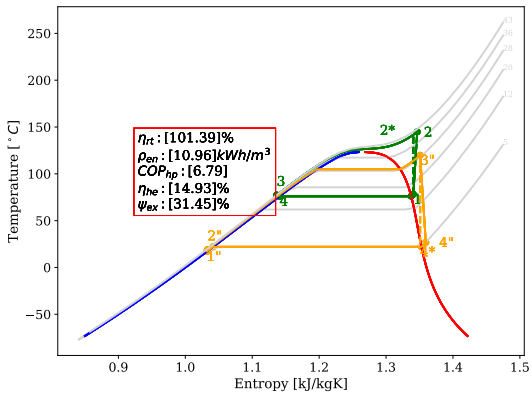

(e) R13I1 High Storage Temperature Scenario $T_{source} = 80°C$, $T_{storage} = 140°C$, $PR_{hp} = 2.5$, and $PR_{he} = 6.3$ with Constant Isentropic Efficiency

Figure B.2: Optimized Cycles Results for:
(a) R1233ZD(E) Low Storage Temperature Scenario $T_{source} = 70°C$ and $T_{storage} = 100°C$ with Constant Isentropic Efficiency
(b) R13I1 Low Storage Temperature Scenario $T_{source} = 80°C$ and $T_{storage} = 100°C$ with Fit Isentropic Efficiency
(c) R1234ZE(E) Mid Storage Temperature Scenario $T_{source} = 80°C$ and $T_{storage} = 135°C$ with Constant Isentropic Efficiency
(d) R13I1 Mid Storage Temperature Scenario $T_{source} = 80°C$ and $T_{storage} = 100°C$ with Fit Isentropic Efficiency
(e) R13I1 High Storage Temperature Scenario $T_{source} = 80°C$ and $T_{storage} = 140°C$ with Constant Isentropic Efficiency

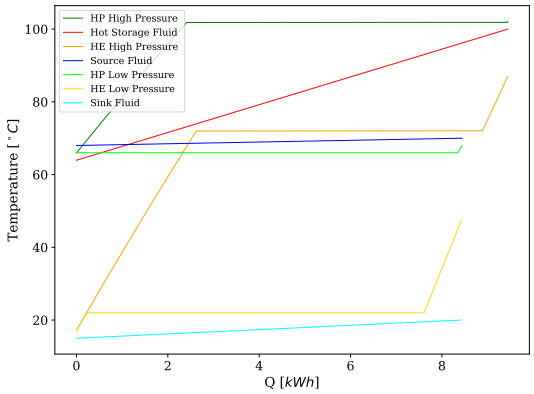

(a) R1233ZD(E) Low Storage Temperature Scenario $T_{source} = 70°C$, $T_{storage} = 100°C$, $PR_{hp} = 2.4$, and $PR_{he} = 4.6$ with Constant Isentropic Efficiency

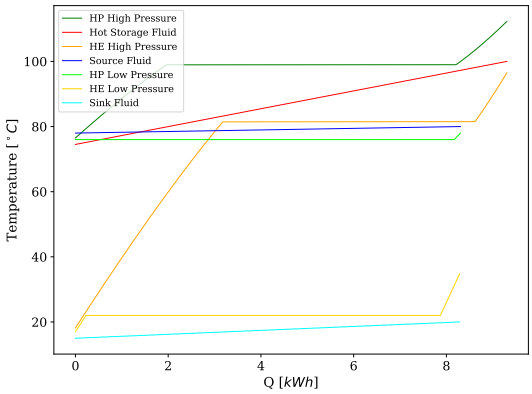

(b) R13I1 Low Storage Temperature Scenario $T_{source} = 80°C$, $T_{storage} = 100°C$, $PR_{hp} = 1.6$, and $PR_{he} = 4.1$ with Fit Isentropic Efficiency

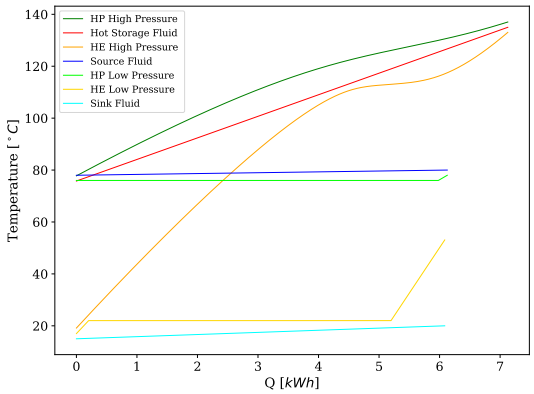

(c) R1234ZE(E) Mid Storage Temperature Scenario $T_{source} = 80°C$, $T_{storage} = 135°C$, $PR_{hp} = 2.8$, and $PR_{he} = 8.6$ with Constant Isentropic Efficiency

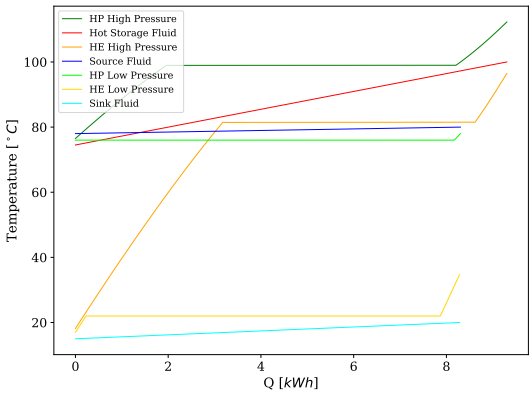

(d) R13I1 Mid Storage Temperature Scenario $T_{source} = 80°C$, $T_{storage} = 100°C$, $PR_{hp} = 1.6$, and $PR_{he} = 4.1$ with Fit Isentropic Efficiency

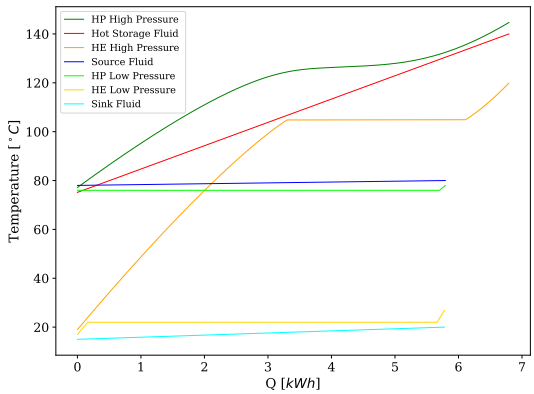

(e) R13I1 High Storage Temperature Scenario $T_{source} = 80°C$, $T_{storage} = 140°C$, $PR_{hp} = 2.5$, and $PR_{he} = 6.3$ with Constant Isentropic Efficiency

Figure B.3: Optimized Cycles Heat Flow for:
(a) R1233ZD(E) Low Storage Temperature Scenario $T_{source} = 70°C$ and $T_{storage} = 100°C$ with Constant Isentropic Efficiency
(b) R13I1 Low Storage Temperature Scenario $T_{source} = 80°C$ and $T_{storage} = 100°C$ with Fit Isentropic Efficiency
(c) R1234ZE(E) Mid Storage Temperature Scenario $T_{source} = 80°C$ and $T_{storage} = 135°C$ with Constant Isentropic Efficiency
(d) R13I1 Mid Storage Temperature Scenario $T_{source} = 80°C$ and $T_{storage} = 100°C$ with Fit Isentropic Efficiency
(e) R13I1 High Storage Temperature Scenario $T_{source} = 80°C$ and $T_{storage} = 140°C$ with Constant Isentropic Efficiency

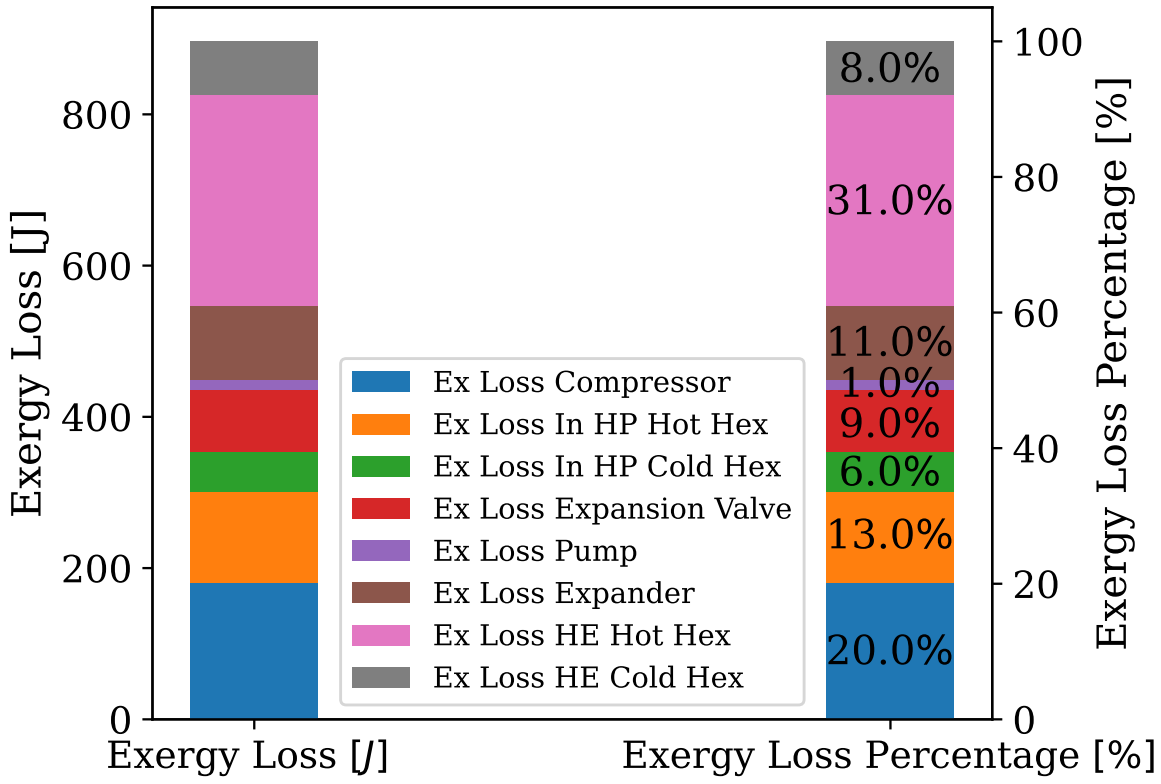

Figure B.4: Exergy Analysis for The Integrated Cycle Working with $T_{source} = 80^{\circ}C$ and $T_{storage} = 140^{\circ}C$

C

Heat Exchanger Sizing

The heat exchanger model is done through Aspen Exchanger Design and Rating V12 which follow the logerethmic mean temperature difference method (LMTD) to size the heat exchanger. The method is described in Sinnott and Towler [70] which will be descibed here:

C.1. Duty

The duty of the heat exchanger is determined based on the process or coolant heat transfer:

$$\dot{Q} = \dot{m}(h_{out} - h_{in}) = UA_o\Delta T_{lm} \tag{C.1}$$

Additionally, the logarithmic mean temperature difference ΔT_{lm} can be determined based on the following with temperatures shown in Figure C.1 for counter current flow:

$$\Delta T_{lm} = \frac{(T_1 - t_2) - (T_2 - t_1)}{\ln \frac{T_1 - t_2)}{(T_2 - t_1)}} \tag{C.2}$$

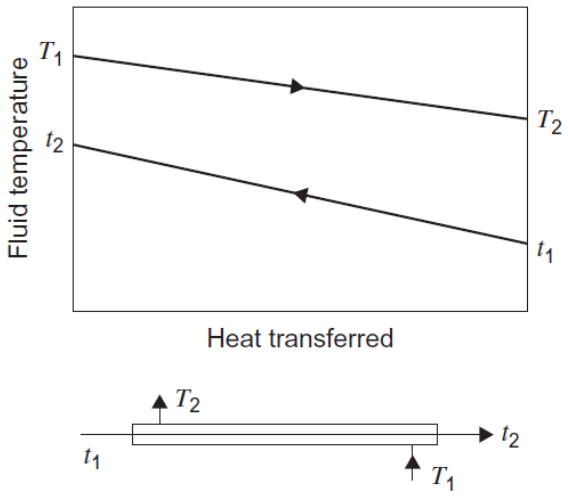

Figure C.1: Counter Current Temperature Profile [70]

Consequently the overall heat transfer area A_o can be calculated by assuming a value for the overall heat transfer coefficient $U_{o,ass}$:

$$A_o = \frac{\dot{Q}}{U_{o,ass}\Delta T_{lm}} \tag{C.3}$$

The number of plates required can be determined by determining the plate area A_p :

$$n_p = \frac{A_o}{A_p} \tag{C.4}$$

The overall heat transfer coefficient is then calculated based on the the process heat transfer coefficient h_o, the coolant heat transfer coefficient h_i, thermal conductivity k and fouling factor h_f as can be seen in equation C.5 :

$$\frac{1}{U_o} = \frac{1}{h_o} + \frac{1}{h_i} + \frac{t}{k} + \frac{1}{h_f} \tag{C.5}$$

For plate heat exchanger, the hydraulic diameter d_e is calculated based on amplitude $\hat{a}$, wave number X, wave length Λ , and plate chevron angle Φ as can be seen in equation C.6 [22] as can be seen in Figure C.2 :

$$\begin{aligned} d_e &= \frac{4\hat{a}}{\Phi} \\ X &= \frac{2\pi\hat{a}}{\Lambda} \\ \Phi &= \frac{1}{6}\left(1 + \sqrt{1+X^2} + 4\sqrt{1+\frac{X^2}{2}}\right) \end{aligned} \tag{C.6}$$

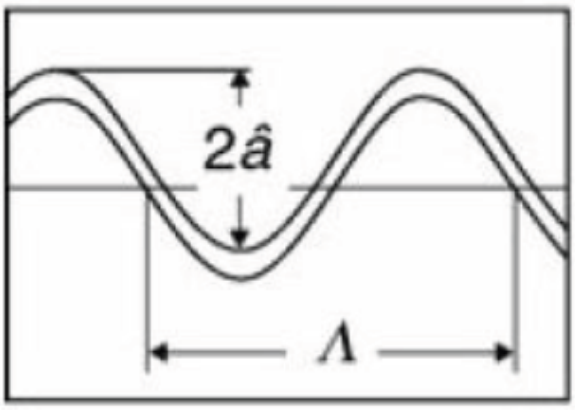

Figure C.2: Chevron Type Plate Gap [22]

The hydraulic diameter is used in calculating the Reynolds number Re and Nusselt number Nu as shown in equation C.7

$$\begin{aligned} Re &= \frac{\rho w_p d_e}{\mu} \\ Nu &= \frac{h d_e}{k} \end{aligned} \tag{C.7}$$

Where:

- w_p : is the velocity through the channel plate
- ρ : is the density of the fluid
- μ : is the dynamic viscosity
- h : is the convective heat transfer coefficient
- k : is the thermal conductivity

The velocity through the plate is determined based on the volumetric flow through the gap $\dot{V}_{gap}$ and the plate width B_p as seen in equation C.8 and Figure C.3:

$$w_p = \frac{\dot{V}_{gap}}{4\hat{a}B_p} \tag{C.8}$$

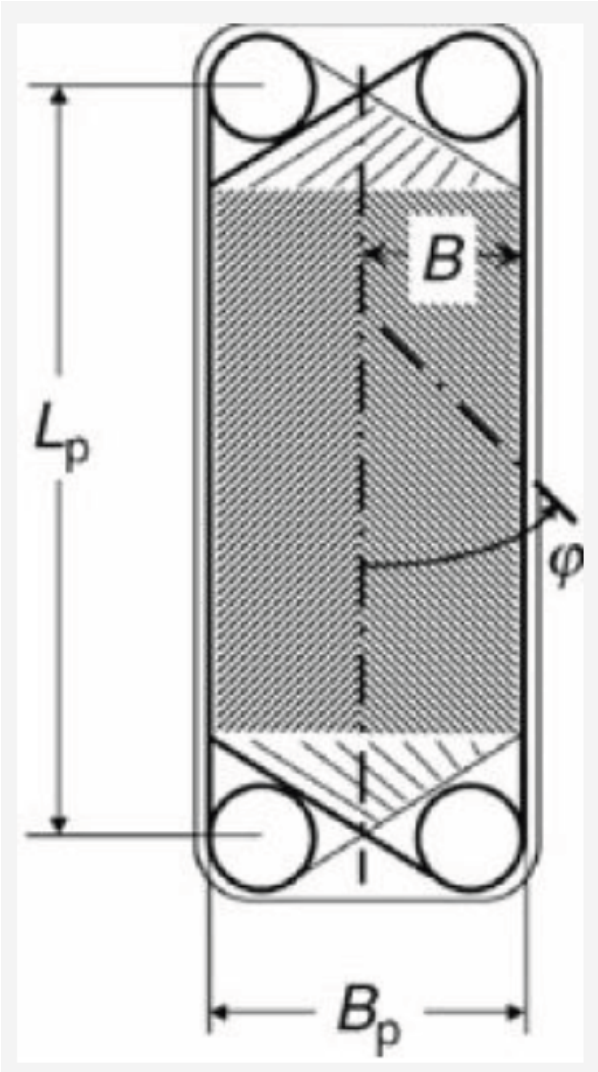

Figure C.3: Chevron Plate Dimensions [22]

The pressure drop across the heat exchanger is then determined based on the flow velocity w_p, correction factor ξ, plate length L_p as follows:

$$\Delta P = \xi \frac{1}{2} \rho w_p^2 \frac{L_p}{d_e} \tag{C.9}$$

The Nu number is determined based on Re and Prandtl number Pr as follows

$$Nu = A Re^B Pr^C \tag{C.10}$$

where A, B, C are factors depending on tabulated experimental relations.

The reader is directed to [22] for the specific correlation for Nu and Ξ to determine the pressure drop and heat transfer coefficient based on different parameter.

The overall heat transfer coefficient and the pressure drop are then iterated until the tolerance is satisfied as can be seen in figure C.4

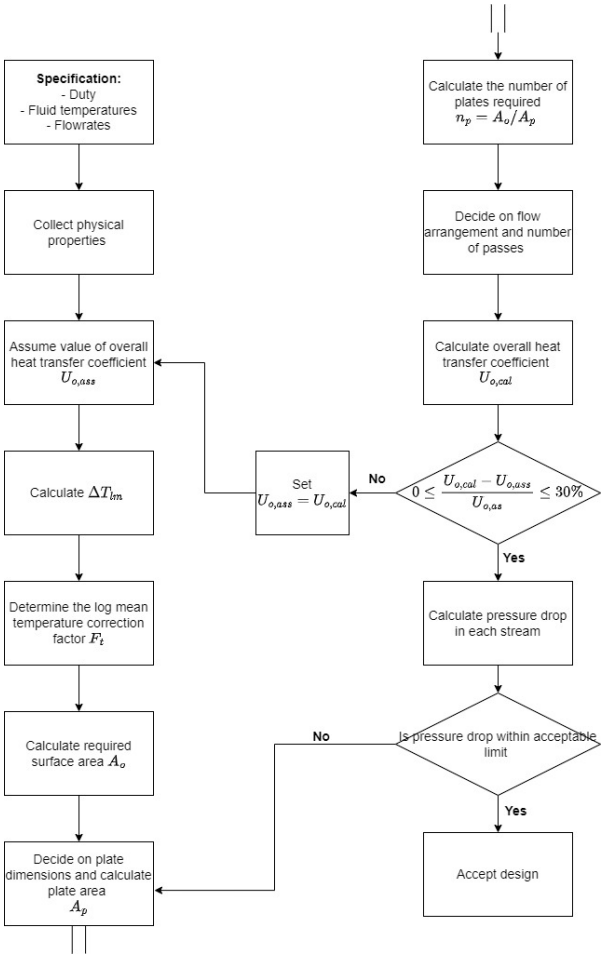

Figure C.4: Heat Exchanger Design Logic [22] [70]

D

Economic Analysis

An economic analysis to quantify the total investment cost (TIC) can be conducted to determine the feasibility of such system. This was done by estimating the purchasing equipment cost (PEC) based on cost models provided by [43] or estimation provided by companies as shown in Table D.1.

Table D.1: Pumped Thermal Energy Storage Cost Models [43]

Component	PEC Model	Currency and Year/[Price]	Parameter
Compressor	$PEC_{comp} = k_r \beta_c \dot{V}$	£2016	k_r = 8000 ; $\beta_c = PR$
Pump	$PEC_{pump} = 1120X^{0.8}$	$ 2009	$X = \dot{W}_{pump}\ [kW]$
High Pressure Heat Exchanger	[-]	$ [6346]	
Low Pressure Heat Exchanger	[-]	$ [4639]	
Storage Tank	$PEC_{storage} = 141X^{0.667}$	$ 2017	$X = Q_{duty}\ [kWhr]$
Hybrid Solar Panels		€[809]	
Motor	$PEC_{motor} = 60X^{0.95}$	$ 2009	$X = \dot{W}_{motor}\ [kW]$

The PEC model are used to calculate the cost of the corresponding year which has to be corrected for inflation using chemical engineering plant cost index (CEPCI) as shown in equation D.1 [9] where year 2022 was used due to availability of data from that year.

$$PEC_{2022} = PEC_{year}\left(\frac{CEPCI_{2022}}{CEPCI_{year}}\right) \tag{D.1}$$

Considering the models provided in table D.1 along with the correction CEPCI, purchasing equipment cost was calculated for each component of the system and shown in table D.2. The total investment cost (TIC) for the system would be around $€22,000$. This gives a return on investment (ROI) in 30 years based on an electricity cost of $0.4€/kWhr$ [61].

Considering the results shown in Table D.2 the cost breakdown for each component is shown in Figure D.1

Table D.2: Pumped Thermal Energy Storage Purchasing Equipment Cost (PEC)

Component	Purchased Equipment Cost €
Compressor	142
Pump	175
High Pressure Heat Exchanger	5774
Low Pressure Heat Exchanger	4221
Storage Tank	2708
Hybrid Solar Panels	8899
Motor	95

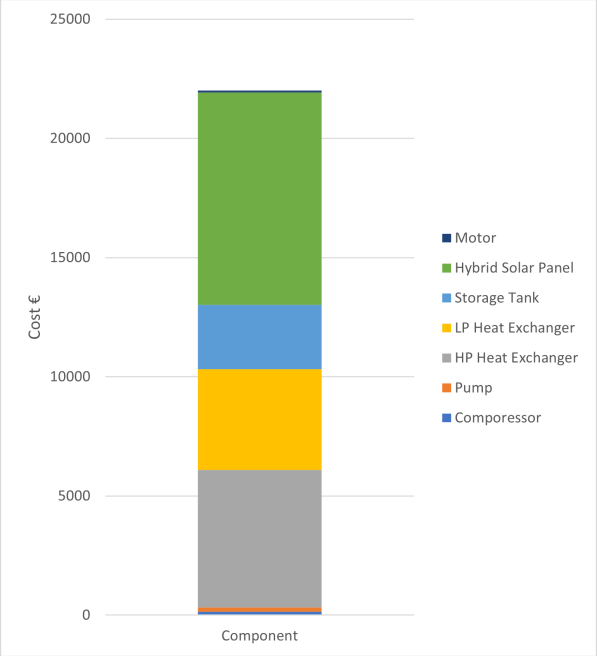

Figure D.1: PTES Components Cost Breakdown

Bibliography

[1] URL: https://pvportal-3.ewi.tudelft.nl/PVP3.1/Meteo/DataPortal.php.

[2] amechieneer. “Thinking How a Roots Blower Works?? It’s Time to Stop”. In: (). URL: https://amechieneer.com/roots-blower/.

[3] ASHRAE and UNEP Cooperation. *Update on New Refrigerants Designations and Safety Classifications*. Apr. 2020. URL: http://tiny.cc/9193vz.

[4] Kevin Attonaty et al. “Thermodynamic analysis of a 200 MWh electricity storage system based on high temperature thermal energy storage”. In: *Energy* 172 (2019), pp. 1132–1143. ISSN: 0360-5442. DOI: https://doi.org/10.1016/j.energy.2019.01.153. URL: https://www.sciencedirect.com/science/article/pii/S0360544219301690.

[5] Junjiang Bao and Li Zhao. “A review of working fluid and expander selections for organic Rankine cycle”. In: *Renewable and Sustainable Energy Reviews* 24 (2013), pp. 325–342. ISSN: 1364-0321. DOI: https://doi.org/10.1016/j.rser.2013.03.040. URL: https://www.sciencedirect.com/science/article/pii/S1364032113001998.

[6] Ian Bell. *Theoretical and experimental analysis of liquid flooded compression in scroll compressors*. Apr. 2011. URL: https://docs.lib.purdue.edu/herrick/2/.

[7] Mechanical Engineering Blog. “Centrifugal Compressor: Principle, Construction, Working, Types, Advantages, Disadvantages with its Application”. In: (). URL: https://www.mech4study.com/uncategorized/centrifugal-compressor.html/.

[8] M.P. Boyce. “2 - Advanced industrial gas turbines for power generation”. In: *Combined Cycle Systems for Near-Zero Emission Power Generation*. Ed. by Ashok D. Rao. Woodhead Publishing Series in Energy. Woodhead Publishing, 2012, pp. 44–102. ISBN: 978-0-85709-013-3. DOI: https://doi.org/10.1533/9780857096180.44. URL: https://www.sciencedirect.com/science/article/pii/B978085709013350002X.

[9] “Capturing green opportunities”. In: (2022). URL: https://www.nxtbook.com/accessintelligence/ChemicalEngineering/chemical-engineering-june-intl-2022/index.php?startid=48#/p/48.

[10] Yu Chen et al. “Mathematical modeling of scroll compressors — part II: overall scroll compressor modeling”. In: *International Journal of Refrigeration* 25.6 (2002), pp. 751–764. ISSN: 0140-7007. DOI: https://doi.org/10.1016/S0140-7007(01)00072-X. URL: https://www.sciencedirect.com/science/article/pii/S014070070100072X.

[11] *CO Emissions by Fuel Type, World*. 2021. URL: https://ourworldindata.org/grapher/co2-by-source.

[12] Group Communications and Jan Hoppe. *Press release MAN and ABB introduce unique Energy Storage Solution*. 2018. URL: https://www.man-es.com/docs/default-source/press-releases-new/180626-man-press-release_etes_en.pdf?sfvrsn=d169f4a1_2.

[13] Atlas Copco. “SCROLL COMPRESSORS”. In: (). URL: https://www.atlascopco.com/content/dam/atlas-copco/compressor-technique/industrial-air/documents/leaflets/compressors/sf1-22/SF1-22_antwerp_leaflet_EN_2935084448.pdf.

[14] T. Desrues et al. “A thermal energy storage process for large scale electric applications”. In: *Applied Thermal Engineering* 30.5 (2010), pp. 425–432. ISSN: 1359-4311. DOI: https://doi.org/10.1016/j.applthermaleng.2009.10.002. URL: https://www.sciencedirect.com/science/article/pii/S1359431109002932.

[15] I. Dinçer and M.A. Rosen. *Thermal Energy Storage: Systems and Applications*. Wiley, 2011. ISBN: 9781119956624. URL: https://www.researchgate.net/file.PostFileLoader.html?id=574d5d57f7b67eba9d4c929f&assetKey=AS:367742109667314646879593 19.

[16] *dualsun datasheet spring 400 shingle black*. 2023. URL: https://dualsun.com/wp-content/uploads/2023/05/dualsun-en-datasheet-spring-400-shingle-black.pdf.

[17] Olivier Dumont et al. “Carnot battery technology: A state-of-the-art review”. In: *Journal of Energy Storage* 32 (2020), p. 101756. ISSN: 2352-152X. DOI: https://doi.org/10.1016/j.est.2020.101756. URL: https://www.sciencedirect.com/science/article/pii/S2352152X20315930.

[18] Olivier Dumont et al. “Experimental investigation and optimal performance assessment of four volumetric expanders (scroll, screw, piston and roots) tested in a small-scale organic Rankine cycle system”. In: *Energy* 165 (2018), pp. 1119–1127. ISSN: 0360-5442. DOI: https://doi.org/10.1016/j.energy.2018.06.182. URL: https://www.sciencedirect.com/science/article/pii/S0360544218312477.

[19] Olivier Dumont et al. *Experimental Investigation Of A Thermally Integrated Carnot Experimental Investigation Of A Thermally Integrated Carnot Battery Using A Reversible Heat Pump/Organic Rankine Cycle Battery Using A Reversible Heat Pump/Organic Rankine Cycle Experimental investigation of a thermally integrated Carnot battery using a reversible heat pump/organic Rankine cycle*. 2021. URL: https://docs.lib.purdue.edu/iracc/2085/.

[20] Jan Rudolf Eggers et al. “Design and performance of a long duration electric thermal energy storage demonstration plant at megawatt-scale”. In: *Journal of Energy Storage* 55 (2022), p. 105780. ISSN: 2352-152X. DOI: https://doi.org/10.1016/j.est.2022.105780. URL: https://www.sciencedirect.com/science/article/pii/S2352152X22017686.

[21] Ruoxuan Fan and Huan Xi. “Exergoeconomic optimization and working fluid comparison of low-temperature Carnot battery systems for energy storage”. In: *Journal of Energy Storage* 51 (2022), p. 104453. ISSN: 2352-152X. DOI: https://doi.org/10.1016/j.est.2022.104453. URL: https://www.sciencedirect.com/science/article/pii/S2352152X22004753.

[22] Carlos Infante Ferreira. *Lecture 6: Equipment for Heat Transfer*. Feb. 2022.

[23] Guido Francesco Frate, Marco Antonelli, and Umberto Desideri. “A novel Pumped Thermal Electricity Storage (PTES) system with thermal integration”. In: *Applied Thermal Engineering* 121 (2017), pp. 1051–1058. ISSN: 1359-4311. DOI: https://doi.org/10.1016/j.applthermaleng.2017.04.127. URL: https://www.sciencedirect.com/science/article/pii/S135943111634114X.

[24] Guido Francesco Frate, Lorenzo Ferrari, and Umberto Desideri. “Multi-criteria investigation of a pumped thermal electricity storage (PTES) system with thermal integration and sensible heat storage”. In: *Energy Conversion and Management* 208 (2020), p. 112530. ISSN: 0196-8904. DOI: https://doi.org/10.1016/j.enconman.2020.112530. URL: https://www.sciencedirect.com/science/article/pii/S0196890420300662.

[25] Marguerre Fritz. *Thermodynamic Energy Storage*. 1936. URL: https://patents.google.com/patent/US2065974.

[26] S. Furbo. “2 - Using water for heat storage in thermal energy storage (TES) systems”. In: *Advances in Thermal Energy Storage Systems*. Ed. by Luisa F. Cabeza. Woodhead Publishing Series in Energy. Woodhead Publishing, 2015, pp. 31–47. ISBN: 978-1-78242-088-0. DOI: https://doi.org/10.1533/9781782420965.1.31. URL: https://www.sciencedirect.com/science/article/pii/B978178242088050002X.

[27] Divyansh Gautam. “Thermodynamic Modelling And Optimization Of Waste Heat Integrated Rankine PTES System”. In: (2023). URL: https://repository.tudelft.nl/islandora/object/uuid:b6f478c3-0335-4c48-91ff-616263c7617d.

[28] Emeline Georges et al. “Design of a small-scale organic Rankine cycle engine used in a solar power plant”. In: *International Journal of Low Carbon Technologies* 8 (June 2013). DOI: 10.1093/ijlct/ctt030.

[29] *Global Primary Energy Consumption by Source*. 2021. URL: https://ourworldindata.org/grapher/global-energy-substitution.

[30] Said Attia al Hagrey, Daniel Köhn, and Wolfgang Rabbel. “Geophysical assessments of renewable gas energy compressed in geologic pore storage reservoirs”. In: *SpringerPlus* 3.1 (2014). DOI: 10.1186/2193-1801-3-267.

[31] Stephen Hall. “2 - Heat Exchangers”. In: *Branan’s Rules of Thumb for Chemical Engineers (Fifth Edition)*. Ed. by Stephen Hall. Fifth Edition. Oxford: Butterworth-Heinemann, 2012, pp. 27–57. ISBN: 978-0-12-387785-7. DOI: https://doi.org/10.1016/B978-0-12-387785-7.00002-5. URL: https://www.sciencedirect.com/science/article/pii/B9780123877857000025.

[32] Jian Hao et al. “An Improved NSGA-II Algorithm Based on Adaptive Weighting and Searching Strategy”. In: *Applied Sciences* 12.22 (2022). ISSN: 2076-3417. DOI: 10.3390/app122211573. URL: https://www.mdpi.com/2076-3417/12/22/11573.

[33] S.M. Hasnain. “Review on sustainable thermal energy storage technologies, Part I: heat storage materials and techniques”. In: *Energy Conversion and Management* 39.11 (1998), pp. 1127–1138. ISSN: 0196-8904. DOI: https://doi.org/10.1016/S0196-8904(98)00025-9. URL: https://www.sciencedirect.com/science/article/pii/S0196890498000259.

[34] Wei He and Jihong Wang. “Optimal selection of air expansion machine in Compressed Air Energy Storage: A review”. In: *Renewable and Sustainable Energy Reviews* 87 (2018), pp. 77–95. ISSN: 1364-0321. DOI: https://doi.org/10.1016/j.rser.2018.01.013. URL: https://www.sciencedirect.com/science/article/pii/S1364032118300170.

[35] Henning Jockenhöfer, Wolf-Dieter Steinmann, and Dan Bauer. “Detailed numerical investigation of a pumped thermal energy storage with low temperature heat integration”. In: *Energy* 145 (2018), pp. 665–676. ISSN: 0360-5442. DOI: https://doi.org/10.1016/j.energy.2017.12.087. URL: https://www.sciencedirect.com/science/article/pii/S0360544217321308.

[36] Siemens Wind Power GmbH Co. KG. *Electric Thermal Energy Storage (ETES)*. Nov. 2017. URL: https://windenergietage.de/wp-content/uploads/sites/2/2017/11/26WT0811_F11_1120_Dr_Barmeier.pdf.

[37] Anton Kiss and Carlos Ferreira. *Heat Pumps in Chemical Process Industry*. Sept. 2016. ISBN: 978-1-4987-1895-0. DOI: 10.1201/9781315371030.

[38] Antoine Koen, Pau Farres Antunez, and Alexander White. “A study of working fluids for transcritical pumped thermal energy storage cycles”. In: *2019 Offshore Energy and Storage Summit (OSES)*. 2019, pp. 1–7. DOI: 10.1109/OSES.2019.8867217.

[39] Robert B. Laughlin. “Pumped thermal grid storage with heat exchange”. In: *Journal of Renewable and Sustainable Energy* 9.4 (2017), p. 044103. DOI: 10.1063/1.4994054. eprint: https://doi.org/10.1063/1.4994054. URL: https://doi.org/10.1063/1.4994054.

[40] Alfa Laval. *Seven benefits of replacing a shell-and-tube with a gasketed plate heat exchanger, using only dimensional data*. 2019. URL: https://pragyaassociates.net/wp-content/uploads/2020/12/shell-and-tube_replacement.pdf.

[41] Vincent Lemort. “Contribution to the Characterization of Scroll Machines in Compressor and Expander Modes”. English. PhD thesis. ULiège - Université de Liège, 19 December 2008.

[42] Vincent Lemort et al. “Testing and modeling a scroll expander integrated into an Organic Rankine Cycle”. In: *Applied Thermal Engineering* 29.14 (2009), pp. 3094–3102. ISSN: 1359-4311. DOI: https://doi.org/10.1016/j.applthermaleng.2009.04.013. URL: https://www.sciencedirect.com/science/article/pii/S1359431109001173.

[43] Ting Liang et al. “Key components for Carnot Battery: Technology review, technical barriers and selection criteria”. In: *Renewable and Sustainable Energy Reviews* 163 (2022), p. 112478. ISSN: 1364-0321. DOI: https://doi.org/10.1016/j.rser.2022.112478. URL: https://www.sciencedirect.com/science/article/pii/S1364032122003823.

[44] Zhiwei Ma, Huashan Bao, and Anthony Paul Roskilly. “Dynamic modelling and experimental validation of scroll expander for small scale power generation system”. In: *Applied Energy* 186 (2017). Sustainable Thermal Energy Management (SusTEM2015), pp. 262–281. ISSN: 0306-2619. DOI: https://doi.org/10.1016/j.apenergy.2016.08.025. URL: https://www.sciencedirect.com/science/article/pii/S0306261916311126.

[45] Joshua D. McTigue, Alexander J. White, and Christos N. Markides. “Parametric studies and optimisation of pumped thermal electricity storage”. In: *Applied Energy* 137 (2015), pp. 800–811. ISSN: 0306-2619. DOI: https://doi.org/10.1016/j.apenergy.2014.08.039. URL: https://www.sciencedirect.com/science/article/pii/S0306261914008423.

[46] Harald Mehling and Luisa F. Cabeza. *Heat and Cold Storage with PCM: An Up to Date Introduction Into Basics and Applications*. Jan. 2008. ISBN: 978-3-540-68556-2 (Print) 978-3-540-68557-9 (Online). DOI: 10.1007/978-3-540-68557-9.

[47] Mehmet Mercangöz et al. “Electrothermal energy storage with transcritical CO2 cycles”. In: *Energy* 45.1 (2012). The 24th International Conference on Efficiency, Cost, Optimization, Simulation and Environmental Impact of Energy, ECOS 2011, pp. 407–415. ISSN: 0360-5442. DOI: https://doi.org/10.1016/j.energy.2012.03.013. URL: https://www.sciencedirect.com/science/article/pii/S0360544212002046.

[48] Matteo Morandin et al. “Conceptual design of a thermo-electrical energy storage system based on heat integration of thermodynamic cycles – Part A: Methodology and base case”. In: *Energy* 45.1 (2012). The 24th International Conference on Efficiency, Cost, Optimization, Simulation and Environmental Impact of Energy, ECOS 2011, pp. 375–385. ISSN: 0360-5442. DOI: https://doi.org/10.1016/j.energy.2012.03.031. URL: https://www.sciencedirect.com/science/article/pii/S0360544212002228.

[49] Pim Nederstigt and Rene Pecnik. “Generalised Isentropic Relations in Thermodynamics”. In: *Energies* 16.5 (2023). ISSN: 1996-1073. DOI: 10.3390/en16052281. URL: https://www.mdpi.com/1996-1073/16/5/2281.

[50] “15 - Pump selection”. In: *Handbook of Pumps and Pumping*. Ed. by Brian Nesbitt. Oxford: Elsevier Science Ltd, 2006, pp. 329–339. ISBN: 978-1-85617-476-3. DOI: https://doi.org/10.1016/B978-185617476-3/50017-2. URL: https://www.sciencedirect.com/science/article/pii/B9781856174763500172.

[51] Statistics Netherlands. *Energy consumption private dwellings; type of dwelling and regions*. Oct. 2022. URL: https://www.cbs.nl/en-gb/figures/detail/81528ENG.

[52] Vaclav Novotny et al. “Review of Carnot Battery Technology Commercial Development”. In: *Energies* 15.2 (2022). ISSN: 1996-1073. DOI: 10.3390/en15020647. URL: https://www.mdpi.com/1996-1073/15/2/647.

[53] Andreas V. Olympios et al. *Progress and prospects of thermo-mechanical energy storage-a critical review*. Mar. 2020. DOI: 10.1088/2516-1083/abdbba.

[54] Emre Oralli, C. Zamfirescu, and Ibrahim Dincer. “A study on scroll compressor conversion into expander for Rankine cycles”. In: *International Journal of Low-Carbon Technologies* 6 (Aug. 2011). DOI: 10.1093/ijlct/ctr008.

[55] Michael Papapetrou et al. “Industrial waste heat: Estimation of the technically available resource in the EU per industrial sector, temperature level and country”. In: *Applied Thermal Engineering* 138 (2018), pp. 207–216. ISSN: 1359-4311. DOI: https://doi.org/10.1016/j.applthermaleng.2018.04.043. URL: https://www.sciencedirect.com/science/article/pii/S1359431117347919.

[56] Youn Cheol Park, Yongchan Kim, and Honghyun Cho. “Thermodynamic analysis on the performance of a variable speed scroll compressor with refrigerant injection”. In: *International Journal of Refrigeration* 25.8 (2002), pp. 1072–1082. ISSN: 0140-7007. DOI: https://doi.org/10.1016/S0140-7007(02)00007-5. URL: https://www.sciencedirect.com/science/article/pii/S0140700702000075.

[57] Richard B. Peterson. “A concept for storing utility-scale electrical energy in the form of latent heat”. In: *Energy* 36.10 (2011), pp. 6098–6109. ISSN: 0360-5442. DOI: https://doi.org/10.1016/j.energy.2011.08.003. URL: https://www.sciencedirect.com/science/article/pii/S0360544211005330.

[58] Mario Petrollese et al. “Pumped thermal energy storage systems integrated with a concentrating solar power section: Conceptual design and performance evaluation”. In: *Energy* 247 (2022), p. 123516. ISSN: 0360-5442. DOI: https://doi.org/10.1016/j.energy.2022.123516. URL: https://www.sciencedirect.com/science/article/pii/S0360544222004194.

[59] Mario Petrollese et al. “Pumped thermal energy storage systems integrated with a concentrating solar power section: Conceptual design and performance evaluation”. In: *Energy* 247 (2022), p. 123516. ISSN: 0360-5442. DOI: https://doi.org/10.1016/j.energy.2022.123516. URL: https://www.sciencedirect.com/science/article/pii/S0360544222004194.

[60] PNEUMOFORE. “Rotary Vane Technology”. In: (). URL: https://www.pneumofore.com/rotary-vane-tech/.

[61] *Price cap for energy*. [Accessed 11-08-2023]. URL: https://www.energievergelijk.nl/english/price-cap-energy.

[62] Sylvain Quoilin. “Sustainable energy conversion through the use of Organic Rankine Cycles for waste heat recovery and solar applications”. PhD thesis. Jan. 2011, p. 183. URL: https://www.researchgate.net/publication/261696692_Sustainable_energy_conversion_through_the_use_of_Organic_Rankine_Cycles_for_waste_heat_recovery_and_solar_applications.

[63] Sylvain Quoilin, Sébastien Declaye, and Vincent Lemort. “Expansion Machine and fluid selection for the Organic Rankine Cycle”. In: July 2010. URL: https://www.researchgate.net/publication/261696695_Expansion_Machine_and_fluid_selection_for_the_Organic_Rankine_Cycle.

[64] Madhumathi Raman and Michael Darcy. *Solar Panel calculator*. June 2023. URL: https://www.omnicalculator.com/ecology/solar-panel.

[65] Shafiqur Rehman, Luai M. Al-Hadhrami, and Md. Mahbub Alam. “Pumped hydro energy storage system: A technological review”. In: *Renewable and Sustainable Energy Reviews* 44 (2015), pp. 586–598. ISSN: 1364-0321. DOI: https://doi.org/10.1016/j.rser.2014.12.040. URL: https://www.sciencedirect.com/science/article/pii/S1364032115000106.

[66] *Renewable energy generation, World*. 2021. URL: https://ourworldindata.org/grapher/modern-renewable-energy-consumption.

[67] Luis Sanz Garcia, Emmanuel Jacquemoud, and Philipp Jenny. “THERMO-ECONOMIC HEAT EXCHANGER OPTIMIZATION FOR ELECTRO-THERMAL ENERGY STORAGE BASED ON TRANSCRITICAL CO2 CYCLES”. In: Sept. 2019. DOI: 10.17185/duepublico/48917.

[68] Ioan Sarbu and Calin Sebarchievici. “A Comprehensive Review of Thermal Energy Storage”. In: *Sustainability* 10.1 (2018). ISSN: 2071-1050. DOI: 10.3390/su10010191. URL: https://www.mdpi.com/2071-1050/10/1/191.

[69] W.D. Steinmann. “The CHEST (Compressed Heat Energy STorage) concept for facility scale thermo mechanical energy storage”. In: *Energy* 69 (2014), pp. 543–552. ISSN: 0360-5442. DOI: https://doi.org/10.1016/j.energy.2014.03.049. URL: https://www.sciencedirect.com/science/article/pii/S0360544214003132.

[70] Gavin Towler and Ray Sinnott. “Chapter 19 - Heat-Transfer Equipment”. In: *Chemical Engineering Design (Second Edition)*. Ed. by Gavin Towler and Ray Sinnott. Second Edition. Boston: Butterworth-Heinemann, 2013, pp. 1047–1205. ISBN: 978-0-08-096659-5. DOI: https://doi.org/10.1016/B978-0-08-096659-5.00019-5. URL: https://www.sciencedirect.com/science/article/pii/B9780080966595000195.

[71] Baolong Wang, Xianting Li, and Wenxing Shi. “A general geometrical model of scroll compressors based on discretional initial angles of involute”. In: *International Journal of Refrigeration* 28.6 (2005), pp. 958–966. ISSN: 0140-7007. DOI: https://doi.org/10.1016/j.ijrefrig.2005.01.015. URL: https://www.sciencedirect.com/science/article/pii/S0140700705000484.

[72] Liang Wang et al. “Analytic optimization of Joule–Brayton cycle-based pumped thermal electricity storage system”. In: *Journal of Energy Storage* 47 (2022), p. 103663. ISSN: 2352-152X. DOI: https://doi.org/10.1016/j.est.2021.103663. URL: https://www.sciencedirect.com/science/article/pii/S2352152X21013384.

[73] Alexander White, Geoff Parks, and Christos N. Markides. “Thermodynamic analysis of pumped thermal electricity storage”. In: *Applied Thermal Engineering* 53.2 (2013). Includes Special Issue: PRO-TEM Special Issue, pp. 291–298. ISSN: 1359-4311. DOI: https://doi.org/10.1016/j.applthermaleng.2012.03.030. URL: https://www.sciencedirect.com/science/article/pii/S1359431112002141.

[74] Eric Winandy, Claudio Saavedra O, and Jean Lebrun. “Experimental analysis and simplified modelling of a hermetic scroll refrigeration compressor”. In: *Applied Thermal Engineering* 22.2 (2002), pp. 107–120. ISSN: 1359-4311. DOI: https://doi.org/10.1016/S1359-4311(01)00083-7. URL: https://www.sciencedirect.com/science/article/pii/S1359431101000837.

[75] S. Wu. “4 - Heat energy storage and cooling in buildings”. In: *Materials for Energy Efficiency and Thermal Comfort in Buildings*. Ed. by Matthew R. Hall. Woodhead Publishing Series in Energy. Woodhead Publishing, 2010, pp. 101–126. ISBN: 978-1-84569-526-2. DOI: https://doi.org/10.1533/9781845699277.1.101. URL: https://www.sciencedirect.com/science/article/pii/B9781845695262500049.

[76] T. Yanagisawa et al. *Optimum operating pressure ratio for scroll compressor*. URL: https://docs.lib.purdue.edu/icec/732/.

[77] Xin-She Yang. “Chapter 14 - Multi-Objective Optimization”. In: *Nature-Inspired Optimization Algorithms*. Ed. by Xin-She Yang. Oxford: Elsevier, 2014, pp. 197–211. ISBN: 978-0-12-416743-8. DOI: https://doi.org/10.1016/B978-0-12-416743-8.00014-2. URL: https://www.sciencedirect.com/science/article/pii/B9780124167438000142.